

AN ABSTRACT OF THE DISSERTATION OF

Peng Jiang for the degree of Doctor of Philosophy in Chemistry presented on August 28, 2012.

Title: Structure-property Relationships of Oxides with Hexagonal AMO_3 and Brownmillerite Related Structures

Abstract approved:_____

Munirpallam A. Subramanian

Transition metal oxides exhibit potential in various application fields due to the special *d*-electrons. Solid state chemistry focuses on discovering the structure-property relationships. The work in this thesis mainly discusses compounds with hexagonal or brownmillerite-type structure and their practical properties.

Hexagonal $\text{YIn}_{1-x}\text{Fe}_x\text{O}_3$ ($x = 0-0.3, 0.7-1.0$) phases have been prepared and characterized. All phases appear to have the ferroelectric structure known for YInO_3 . The color of the phases changes from yellow to orange to dark red with increasing Fe content. Magnetic measurements confirm high-spin Fe^{3+} for all phases. Similarly, solid solution $\text{YAl}_{1-x}\text{Fe}_x\text{O}_3$ ($x = 0-0.4, 0.7-1.0$) phases were successfully synthesized through the sol-gel method. The Al-rich compounds present paraelectric YAlO_3 structure while the Fe-rich side samples exhibit YFeO_3 structure. The color of the

compounds appear to be yellow with small Fe content and change to brown which has higher Fe content.

Brownmillerite-type oxides $\text{Ba}_2\text{In}_{2-x}\text{Mn}_x\text{O}_{5+x}$ ($x = 0.1-0.7$) have been prepared and characterized. Magnetic measurements confirm that Mn in as prepared samples is substituting as Mn^{5+} for all values of x with observed paramagnetic spin-only moments close to values expected for two unpaired electrons. Neutron diffraction structure refinements show Mn^{5+} occupies tetrahedral sites for orthorhombic ($x = 0.1$) and tetragonal ($x = 0.2$) phases. For $\text{Mn} \geq 0.3$ samples, neutron refinements show the phases are cubic with disordered cations and oxygen vacancies. The colors of the phases change from light yellow ($x = 0$) to intense turquoise ($x = 0.1$), to green ($x = 0.2$, 0.3) or dark green ($x \geq 0.4$). Solid solution $\text{Ba}_2\text{In}_{2-x}\text{Fe}_x\text{O}_{5+y}$ ($x = 0.1-1.5$) also exhibit brownmillerite-type structure. The color of the compounds appear to be green with small Fe content and change to black with higher Fe content ($x \geq 0.3$). Magnetic measurements and Mössbauer spectroscopy conclude the mixed valence of $\text{Fe}^{3+}/\text{Fe}^{4+}$ for all the phases.

Nonstoichiometry compound $\text{YCu}_{0.6}\text{Ti}_{0.4}\text{O}_{3-\delta}$ has been prepared and characterized. Structure study indicates that oxygen vacancy is favored under the synthesis condition. This change in oxygen content was further studied in the Mn-doped system. And the effect of stoichiometric difference in the Mn-doped samples was not as obvious as the initial compound. The disorder in the cation site enhanced the tolerance of the structure in the aspect of oxygen content. The hexagonal phases $\text{LnCu}_{0.5}\text{Ti}_{0.5}\text{O}_3$ ($\text{Ln} = \text{Y}, \text{Tb-Lu}$) phases were prepared by the traditional solid state

reactions. The prepared compounds were reduced at high temperature in the reduction atmosphere created by the H_2/N_2 gas mixture. Study on the structure and properties changes by reduction was conducted by X-ray diffraction, optical measurement, magnetic measurement and thermalgravimetric analysis. And we observed some evidence of the presence of Cu^+ in the reduced phase by these characterization methods.

Solid solution $\text{YMn}_x\text{Ti}_y\text{O}_{3-\delta}$ ($y = 0.1-0.4$) was successfully prepared through conventional solid state approach. All the samples showed hexagonal structure. But the structure transition from ferroelectric $P6_3cm$ to paraelectric $P6_3/mmc$ occurred when Ti amount is higher than 0.2. Based on the neutron diffraction refinement, the lattice expanded in the ab plane but contracted along the c axis direction.

©Copyright by Peng Jiang

August 28, 2012

All Rights Reserved

Structure-property Relationships of Oxides with Hexagonal AMO_3 and
Brownmillerite Related Structures

by

Peng Jiang

A DISSERTATION

submitted to

Oregon State University

In partial fulfillment of
the requirements for the
degree of

Doctor of Philosophy

Presented August 28, 2012

Commencement June 2013

Doctor of Philosophy dissertation of Peng Jiang presented on August 28, 2012.

APPROVED:

Major Professor, representing Chemistry

Chair of the Department of Chemistry

Dean of the Graduate School

I understand that my dissertation will become part of the permanent collection of Oregon State University libraries. My signature below authorizes release of my dissertation to any reader upon request.

Peng Jiang, Author

ACKNOWLEDGEMENTS

I was so fortunate to do research in the department of Chemistry, Oregon State University. While I was pursuing my doctor degree here, I got the chance to learn knowledge from the most excellent professors and use the state-of-art instruments, which was a valuable experience for me. I got numerous help from a lot of people during the last three years. And I need to express my great thankfulness to those who helped me getting through.

None of the thesis would be completed without the help of my thesis advisor Dr. M. A. Subramanian. I would like to thank him for providing such a great lab in which I can do almost all the measurements in solid state chemistry. He gave me all the freedom and encouragement to try anything I wanted. His brilliant scientific thinking and profound knowledge always guided me when I came across with problems. I learned the passion for science from him, and I will be benefitted for that lifelong.

It was also a priceless experience to work with Dr. Arthur. W. Sleight who is a brilliant scientist in solid state chemistry. He offered important knowledge in understanding the structure in detail and related properties. I would also thank all the rest of the graduate committee members: Dr. Wei Kong, Dr. Michael Lerner, Dr. Paul Cheong and Dr. John Wager. I really appreciate their support and commitment.

Special thanks to Dr. Jun Li who helped me with the refinements of the structure and her valuable discussion regarding structures. Thanks to Dr. Alain

Wattiaux for the measurement and analysis of all the Mössbauer spectroscopy in this thesis. Thanks to Dr. Andrew Ozarowski for his collaboration on the EPR measurement. Dr. Judith Stalick and Dr. Jason Hodges helped with collecting neutron diffraction data. I also need to thank Dr. Andrew Smith for introducing the general lab techniques patiently to me and Dr. Krishnendu Biswas for discussion. I really appreciate the help from Dr. Romain Berthelot on the $\text{LnCu}_{0.5}\text{Ti}_{0.5}\text{O}_3$ reduction project. Thanks to Dr. Theeranun Siritanon who was a nice officemate and gave me great help and insight discussions all the time. And thanks to Dr. James Eilertsen, Dr. Sean Muir, Dr. Alvin Gatimu, Geneva Luarita-Plankis, Rosa Grajczyk, Whitney Schmidt, and all the other members of Dr. Subramanian research group for all their help and support.

I sincerely thank the department of Chemistry for the support. And I got great teaching experience while working with excellent instructors and lab coordinators. I also thank Dr. Lerner research group and Dr. Keszler research group for the help.

Thanks to all my friends who helped me whenever they can, and their companion always gave me support and encouragement. Last and most importantly, I thank my parents who brought me to this lovely world. Thanks to my mom who was nurturing my body and mind and provide a pleasant home. Thanks for my dad for teaching me the rightness and leading me to the scientific world.

CONTRIBUTION OF AUTHORS

I acknowledge and sincerely appreciate all those who have contributed in this thesis. Dr. M. A. Subramanian and Dr. Arthur W. Sleight have contributed to all the chapters in this thesis. Dr. Jun Li contributed to the neutron diffraction refinement of $\text{YIn}_{1-x}\text{Fe}_x\text{O}_3$ and $\text{Ba}_2\text{In}_{2-x}\text{Mn}_x\text{O}_{5+x}$. She was very helpful with the use of the GSAS software as well as numerous productive discussions.

Dr. Alain Wattiaux contributed to all the Mössbauer data collection and analysis in this thesis. Dr. Andrew Ozarowski and his colleagues contributed to the EPR measurement and analysis of $\text{Ba}_2\text{In}_{2-x}\text{Mn}_x\text{O}_{5+x}$. Dr. Judith Stalick in NIST collected neutron diffraction data for $\text{YIn}_{1-x}\text{Fe}_x\text{O}_3$. Dr. Jason Hodges in ORNL collected the rest of neutron diffraction data shown in this thesis.

Dr. Andrew Smith helped with the some of the characterizations of $\text{YIn}_{1-x}\text{Fe}_x\text{O}_3$ solid solution. Dr. Romain Berthelot assisted with the synthesis and reduction study of $\text{Ln}_{0.5}\text{Ti}_{0.5}\text{O}_3$ phases. He also provided insight discussions of the project. Dr. Krishnendu Biwas gave a lot of help in the general synthesis method. Dr. Theeranun Siritanon assisted with the use of some software.

TABLE OF CONTENTS

	<u>Page</u>
Chapter 1	1
Introduction	1
1.1 Transition metal oxides	1
1.2 Crystal structures.....	2
1.3 Properties and practical applications.....	7
1.2.1 Electronic property.....	7
1.2.2 Magnetic property	10
1.2.3 Optical properties	16
1.2.3.1 Color in transition metal oxides	17
1.2.3.2 Luminescence.....	21
1.2.4 Dielectric and thermoelectric property.....	22
1.4 References	26
Chapter 2	29
Experimental Methods of Analysis	29
2.1 X-Ray Diffraction: MiniFlex II diffractometer.....	29
2.2 Neutron Diffraction (Center for Neutron Research, National Institute of Science and Technology; Oak Ridge National Laboratory Neutron Science):.....	32
2.3 Quantum Design Physical Property Measurement System.....	35
2.3.1 Magnetometry	36

TABLE OF CONTENTS

	<u>Page</u>
2.3.2 DC Electrical Resistivity	39
2.4 Optical measurements	41
2.5 Thermogravimetric analysis (TGA)	42
2.6 Mössbauer spectroscopy	43
2.7 References	47
Chapter 3	48
Structure and Physical Properties of $YM_{1-x}Fe_xO_3$ Hexagonal Structure System (Mn = In, Al)	48
3.1 Introduction	50
3.2 Hexagonal $YIn_{1-x}Fe_xO_3$ phases: Structural, Optical, and Magnetic Studies	55
3.2.1 Introduction	55
3.2.2 Synthesis	57
3.2.3 Result and discussion	58
3.2.4 Conclusion	74
3.3 Effect of Iron substitution in $YAlO_3$ ceramics	75
3.3.1 Introduction	75
3.3.2 Synthesis	77
3.3.3 Result and discussion	78
3.3.4 Conclusion	85
3.4 References	85

TABLE OF CONTENTS

	<u>Page</u>
Chapter 4	88
Structure and Physical Properties of $\text{Ba}_2\text{In}_{2-x}\text{M}_x\text{O}_{5+y}$ Brownmillerite-type Structure System (M=Mn, Fe)	88
4.1 Introduction	90
4.2 Intense Turquoise and Green Colors in Brownmillerite-type Oxides Based on Mn^{5+} in $\text{Ba}_2\text{In}_{2-x}\text{Mn}_x\text{O}_{5+y}$	95
4.2.1 Introduction	95
4.2.2 Synthesis	96
4.2.3 Result and discussion	97
4.2.4 Conclusion	116
4.3 Study on Brownmillerite-type solid solution $\text{Ba}_2\text{In}_{2-x}\text{Fe}_x\text{O}_{5+y}$	116
4.3.1 Introduction	116
4.3.2 Synthesis	118
4.3.3 Result and discussion	118
4.3.4 Conclusion	130
4.4 References	130
Chapter 5	133
Study on $\text{LnCu}_{0.5}\text{Ti}_{0.5}\text{O}_3$ hexagonal system (Ln=Y, Tb-Lu)	133
5.1 Introduction	134

TABLE OF CONTENTS

	<u>Page</u>
5.2 Study on structure and properties of the compounds $\text{YCu}_{0.6}\text{Ti}_{0.4}\text{O}_3$, $\text{YMn}_{0.5}\text{Cu}_{0.25}\text{Ti}_{0.25}\text{O}_3$ and $\text{YMn}_{0.5}\text{Cu}_{0.3}\text{Ti}_{0.2}\text{O}_3$	136
5.2.1 Introduction	137
5.2.2 Synthesis	137
5.2.3 Results and discussion	138
5.2.4 Conclusion	148
5.3 Study on the reduction of $\text{LnCu}_{0.5}\text{Ti}_{0.5}\text{O}_3$ (Ln=Y, Eu-Lu)	148
5.3.1 Introduction	148
5.3.2 Synthesis	150
5.3.3 Results and discussions	150
5.3.4 Conclusion	161
5.4 References	162
Chapter 6	164
Structural and magnetic property study on the cation vacancy system: $\text{YMn}_x\text{Ti}_y\text{O}_{3-\delta}$ ($y = 0.1-0.4$)	164
6.1 Introduction	165
6.2 Synthesis	167
6.3 Results and discussion	167
6.4 Conclusion	172
6.5 References	173

TABLE OF CONTENTS

	<u>Page</u>
General conclusion and future work	174
Bibliography.....	177

LIST OF FIGURES

<u>Figure</u>	<u>Page</u>
Figure 1.1 A close packed layer of spheres with the same size (a), three close packed layers in hexagonal close packing sequence (b) and three close packed layers in cubic close packing sequence (c) [3].	4
Figure 1.2 Simplified diagram of the electronic band structure of metals, semiconductors, and insulators.	9
Figure 1.3 Arrangement of magnetic dipoles for different magnetic behavior.	11
Figure 1.4 The magnetization of diamagnetic material, paramagnetic material and ferromagnetic material.	12
Figure 1.5 Temperature dependence of the inverse magnetic susceptibility for different materials.	14
Figure 1.6 Graphical representations of d orbital shapes.	19
Figure 1.7 Illustration of splitting of d orbital diagrams of V^{4+} in octahedral O_h , square-pyramidal C_{4v} , and distorted square-pyramidal C_{2v} geometry. The latter geometry appears in the V^{4+} environment in the reduced V_2O_5 . (ΔE is the energy gap between d_{xz} and d_{xy} orbitals) [39]	20
Figure 1.8 Polarization of dielectric material in capacitors.	23
Figure 1.9 Dimensionless figure of merit [49].	26
Figure 2.1 Rigaku MiniFlex II diffractometer (a) and the inner workings with x-ray tube, sample platform and detector labeled (b).	30
Figure 2.2 Derivation of Bragg's Law for X-ray diffraction	31
Figure 2.3 Illustration of neutron generator (left) and high resolution powder diffractometer BT-1 [6].	34
Figure 2.4 Quantum Design Physical Property Measurement System set up for ACMS measurements.	36

LIST OF FIGURES (Continued)

<u>Figure</u>	<u>Page</u>
Figure 2.5 Representation of the ACMS coil set and tube assemblage (left), expanded view with labels of the ACMS coil set detection unit (center), and mounted ‘as prepared’ sample (right). ACMS coil set illustrations taken and modified from Quantum Design application notes [8].....	38
Figure 2.6 PPMS resistivity puck with a bar sample connected to position 1 using the four probe contact technique. Notice the labeled voltage and current contacts... 39	39
Figure 2.7 Representation of DC electrical resistivity tube assemblage (left) and detail (right) [9]......	40
Figure 2.8 Illustration of fiber optics system used in diffuse reflectance measurements (a) and light source on white reference BaSO ₄ (b).	42
Figure 2.9 Elements of the periodic table which have known Mössbauer isotopes (shown in red font). Elements which are used the most are shaded with black [12].	44
Figure 2.10 Simple Mössbauer spectrum from identical source and absorber [12].....	45
Figure 2.11 Isomer shift (a), quadrupole splitting (b) and magnetic splitting (c) of the nucleus energy levels and the corresponding Mössbauer spectrum [15].	46
Figure 3.1 The cubic structure for AMO ₃ perovskite oxide. Blue spheres are A cations, light blue spheres are M cations, grey spheres are O ²⁻ anions.	51
Figure 3.2 Structure field map of A ³⁺ B ³⁺ O ₃ perovskite.	52
Figure 3.3 Summary of AMnO ₃ phases with Ln ³⁺ as A cation.....	53
Figure 3.4 Hexagonal YMnO ₃ powders with ferroelectric structure (Y: blue spheres; Mn: dark yellow spheres; O: turquoise spheres).....	53
Figure 3.5 Lattice parameter versus radii in YMO ₃ group (M=Fe, In, Ga, Mn).	54
Figure 3.6 Illustration of the structure of YInO ₃ with space group P6 ₃ /mmc (a) and P6 ₃ cm (b). O is shown in red sphere and Y is turquoise sphere. And In which is indicated in grey spheres is in the center of the grey trigonal bipyramid [reproduction of reference 25].	56

LIST OF FIGURES (Continued)

<u>Figure</u>	<u>Page</u>
Figure 3.7 Thermal Gravimetric Analysis of YFeO_3 from a dehydrated citrate gel....	59
Figure 3.8 XRD patterns of the $\text{YIn}_{1-x}\text{Fe}_x\text{O}_3$ powder samples.	60
Figure 3.9 Hexagonal $\text{YIn}_{1-x}\text{Fe}_x\text{O}_3$ powders with ferroelectric structure (Y: blue spheres; In, Fe: dark yellow spheres; O: turquoise spheres).	61
Figure 3.10 Morphology of $\text{YIn}_{1-x}\text{Fe}_x\text{O}_3$ powders by SEM. (a) $x = 0.9$; (b) $x = 0.1$. Scale is the same for a and b	62
Figure 3.11 Low temperature neutron powder diffraction patterns of YFeO_3 . Peaks due to magnetic ordering are labeled with crosses.	63
Figure 3.12 Hexagonal lattice parameters vs x in $\text{YIn}_{1-x}\text{Fe}_x\text{O}_3$. Both X-ray (open symbols) and neutron data (solid symbols) are plotted.	64
Figure 3.13 Diffuse-reflectance spectra for $\text{YIn}_{1-x}\text{Fe}_x\text{O}_3$ with colors of the samples with varying x . Spectra for $x = 0$ (hexagonal YInO_3 : white color) are shown for comparison.	66
Figure 3.14 Inverse magnetic susceptibility of $\text{YIn}_{1-x}\text{Fe}_x\text{O}_3$ for $x = 0.1, 0.2, 0.3$ (left) and $x = 0.7, 0.8, 0.9$ (right).	67
Figure 3.15 Magnetic susceptibility and inverse magnetic susceptibility of YFeO_3 . ..	68
Figure 3.16 Illustration of magnetic frustration in triangular lattice [38].	69
Figure 3.17 Mössbauer spectrum of $\text{YIn}_{0.3}\text{Fe}_{0.7}\text{O}_3$	70
Figure 3.18 Mössbauer spectrum of $\text{YIn}_{0.7}\text{Fe}_{0.3}\text{O}_3$	71
Figure 3.19 Mössbauer spectrum of YFeO_3	72
Figure 3.20 Thermal Gravimetric Analysis of $\text{YFe}_{0.1}\text{In}_{0.9}\text{O}_3$ (a) and YFeO_3 (b). The heating rate is 300°C/h in both figures.	73
Figure 3.21 Illustration of YAlO_3 with ferrielectric structure. Al is indicated in blue sphere; Y is demonstrated by grey sphere and O is omitted.	76
Figure 3.22 Ferrielectric YAlO_3 (left) and ferroelectric YMnO_3 (right).	77

LIST OF FIGURES (Continued)

<u>Figure</u>	<u>Page</u>
Figure 3.23 XRD patterns of the $\text{YAl}_{1-x}\text{Fe}_x\text{O}_3$ powder samples.	79
Figure 3.24 Hexagonal lattice parameters vs x in $\text{YAl}_{1-x}\text{Fe}_x\text{O}_3$	80
Figure 3.25 Cell volume vs. x in $\text{YAl}_{1-x}\text{Fe}_x\text{O}_3$	81
Figure 3.26 Pictures (above) (value for Fe content is below the sample) and diffuse-reflectance spectra (below) for $\text{YAl}_{1-x}\text{Fe}_x\text{O}_3$ with colors of the samples with varying x . Spectra for $x = 0$ (hexagonal YAlO_3 : white color) are shown for comparison.	82
Figure 3.27 Inverse magnetic susceptibility versus temperature plot for $\text{YAl}_{1-x}\text{Fe}_x\text{O}_3$	83
Figure 4.1 Structure of YFeO_3 perovskite structure (a) and $\text{Ca}_2\text{Fe}_2\text{O}_5$ brownmillerite structure (b).	90
Figure 4.2 stacking sequence in perovskite-brownmillerite family: “Perovskite space” in the oxygen-deficient axis, $2.5 < \text{O/A} < 3.0$ [4].	91
Figure 4.3 The $Pnma$ version of the brownmillerite structure where the two chains shown have different configurations. Octahedra are turquoise and tetrahedral are green.	93
Figure 4.4 Chains of tetrahedra along the a axis in the $Pnma$ orthorhombic structure	94
Figure 4.5 The formation of five-fold coordination in $\text{Ba}_2\text{In}_{2-x}\text{Mn}_x\text{O}_{5+y}$ system.	96
Figure 4.6 Powder X-ray diffraction patterns of $\text{Ba}_2\text{In}_{2-x}\text{Mn}_x\text{O}_{5+y}$ samples ($x = 0 - 0.6$).	97
Figure 4.7 Cell edges for $\text{Ba}_2\text{In}_{2-x}\text{Mn}_x\text{O}_{5+y}$ phases as a function of x	98
Figure 4.8 Cell volume for $\text{Ba}_2\text{In}_{2-x}\text{Mn}_x\text{O}_{5+y}$ phases as a function of x	99
Figure 4.9 Inverse magnetic susceptibility of $\text{Ba}_2\text{In}_{2-x}\text{Mn}_x\text{O}_{5+y}$ for $x = 0.1 - 0.7$	100
Figure 4.10 Thermal Gravimetric Analysis of $\text{Ba}_2\text{In}_{1.5}\text{Mn}_{0.5}\text{O}_{5+y}$ with a heating rate of $5^\circ\text{C}/\text{min}$, and the maximum temperature is 1000°C in N_2 atmosphere.	102

LIST OF FIGURES (Continued)

<u>Figure</u>	<u>Page</u>
Figure 4.11 Colors of powders for $\text{Ba}_2\text{In}_{2-x}\text{Mn}_x\text{O}_{5+y}$ samples, left to right, $x = 0, 0.1, 0.2$ and 0.3	104
Figure 4.12 Diffuse reflectance spectra for $\text{Ba}_2\text{In}_{2-x}\text{Mn}_x\text{O}_{5+y}$ with colors of the sample with varying x	105
Figure 4.13 Reflection spectra of Mn (V)-doped (1 mol 7%) spodiosite-type compounds $\text{Ca}_2(\text{PO}_4)\text{Cl}$ (I), $\text{Ca}_2(\text{VO}_4)\text{Cl}$ (II), and $\text{Sr}_2(\text{VO}_4)\text{Cl}$ (111). (Reproduction of reference 13)	106
Figure 4.14 Reflection spectra of $\text{Ba}_2\text{In}_{2-x}\text{Mn}_x\text{O}_{5+x}$ for as prepared samples (above) and reduced samples (below).	107
Figure 4.15 TOF neutron data of orthorhombic $\text{Ba}_2\text{In}_{1.9}\text{Mn}_{0.1}\text{O}_{5.1}$ are shown with Rietveld fit. The observed pattern displayed is from the highest-resolution bank (Bank 2) with d-spacing range $0.60 - 3.2 \text{ \AA}$	108
Figure 4.16 TOF neutron data of tetragonal $\text{Ba}_2\text{In}_{1.8}\text{Mn}_{0.2}\text{O}_{5.2}$ are shown with Rietveld fit. The observed pattern displayed is from the highest-resolution bank (Bank 2) with d-spacing range $0.60 - 3.2 \text{ \AA}$	110
Figure 4.17 Ellipsoids for tetragonal $\text{Ba}_2\text{In}_{1.8}\text{Mn}_{0.2}\text{O}_{5.2}$: green Ba, red In, blue Mn and turquoise O.	112
Figure 4.18 TOF neutron data of cubic $\text{Ba}_2\text{In}_{1.6}\text{Mn}_{0.4}\text{O}_{5.4}$ are shown with Rietveld fit. The observed pattern displayed is from the highest-resolution bank (Bank 2) with d-spacing range $0.60 - 3.2 \text{ \AA}$	113
Figure 4.19 High-field EPR spectra for $\text{Ba}_2\text{In}_{1.98}\text{Mn}_{0.02}\text{O}_{5.02}$	115
Figure 4.20 Powder X-ray diffraction patterns of $\text{Ba}_2\text{In}_{2-x}\text{Fe}_x\text{O}_{5+y}$ samples ($x = 0.1 - 1.5$).	119
Figure 4.21 Cell edges for $\text{Ba}_2\text{In}_{2-x}\text{Fe}_x\text{O}_{5+y}$ phases as a function of x	120
Figure 4.22 Cell volume data for $\text{Ba}_2\text{In}_{2-x}\text{Fe}_x\text{O}_{5+y}$ phases. The volume of orthorhombic phases are multiplication of the converted a , b and c value.	121

LIST OF FIGURES (Continued)

<u>Figure</u>	<u>Page</u>
Figure 4.23 TOF neutron data of orthorhombic $\text{Ba}_2\text{In}_{1.8}\text{Fe}_{0.2}\text{O}_{5+y}$ are shown with Rietveld fit. The observed pattern displayed is from the highest-resolution bank (Bank 2) with d-spacing range 0.60 – 3.2 Å.	122
Figure 4.24 TOF neutron data of cubic $\text{Ba}_2\text{In}_{1.5}\text{Fe}_{0.5}\text{O}_{5+y}$ are shown with Rietveld fit. The observed pattern displayed is from the highest-resolution bank (Bank 2) with d-spacing range 0.60 – 3.2 Å.	123
Figure 4.25 Pictures of prepared samples (above) and diffuse reflectance spectra (below) for $\text{Ba}_2\text{In}_{2-x}\text{Fe}_x\text{O}_{5+y}$ samples. Spectra for $x = 0$ ($\text{Ba}_2\text{In}_2\text{O}_5$; pale yellow color) is shown for comparison.	124
Figure 4.26 Inverse magnetic susceptibility data of $\text{Ba}_2\text{In}_{2-x}\text{Fe}_x\text{O}_{5+y}$ for $x = 0.1$ -1.5.	125
Figure 4.27 Thermogravimetric Analysis of $\text{Ba}_2\text{InFeO}_{5+y}$ in N_2 atmosphere with the maximum temperature of 1000 °C.	129
Figure 5.1 Illustration of ferroelectric structure of $\text{YCu}_{0.5}\text{Ti}_{0.5}\text{O}_3$. Grey sphere: Y^{3+} ; Green sphere: $\text{Cu}^{2+}/\text{Ti}^{4+}$; light green sphere: O^{2-}	136
Figure 5.2 X-ray patterns of $\text{YCu}_{0.5}\text{Ti}_{0.5}\text{O}_3$ and $\text{YCu}_{0.6}\text{Ti}_{0.4}\text{O}_3$. $\text{Y}_2\text{Ti}_2\text{O}_7$ pyrochlore impurity peaks are indicated in arrow.	139
Figure 5.3 NIST constant wavelength neutron diffraction data of $\text{YCu}_{0.6}\text{Ti}_{0.4}\text{O}_3$ are shown with Rietveld fit.	140
Figure 5.4 Structure of $\text{YCu}_{0.6}\text{Ti}_{0.4}\text{O}_{3-\delta}$. Cu/Ti ions are indicated with yellow sphere; Y ions are represented by green octahedras; O ions are omitted.	142
Figure 5.5 Thermal ellipsoid of $\text{YCu}_{0.6}\text{Ti}_{0.4}\text{O}_{3-\delta}$. Cu/Ti: green sphere; O-1 and O-2: yellow sphere; Y: red sphere; O-3: blue sphere; O-4: light blue sphere.	143
Figure 5.6 Diffuse reflectance spectra of $\text{YCu}_{0.5}\text{Ti}_{0.5}\text{O}_3$ and $\text{YCu}_{0.6}\text{Ti}_{0.4}\text{O}_3$	144
Figure 5.7 Magnetic susceptibility (a) and inverse susceptibility (b) versus temperature plot of $\text{YCu}_{0.6}\text{Ti}_{0.4}\text{O}_3$ and $\text{YCu}_{0.5}\text{Ti}_{0.5}\text{O}_3$	145
Figure 5.8 XRD patterns of $\text{YMn}_{0.5}\text{Cu}_{0.25}\text{Ti}_{0.25}\text{O}_3$ and $\text{YMn}_{0.5}\text{Cu}_{0.3}\text{Ti}_{0.2}\text{O}_3$	146

LIST OF FIGURES (Continued)

<u>Figure</u>	<u>Page</u>
Figure 5.9 Magnetic susceptibility and inverse magnetic susceptibility versus temperature for $\text{YMn}_{0.5}\text{Cu}_{0.3}\text{Ti}_{0.2}\text{O}_3$ and $\text{YMn}_{0.5}\text{Cu}_{0.25}\text{Ti}_{0.25}\text{O}_3$	147
Figure 5.10 Illustration of the structure of delaffosite CuYO_2 (grey sphere: Y^{3+} ; green sphere: Cu^{2+} ; yellow sphere: O^{2-}).....	149
Figure 5.11 X-ray pattern of $\text{YCu}_{0.5}\text{Ti}_{0.5}\text{O}_3$ reduced at 400 °C for various time periods.	152
Figure 5.12 X-ray patterns of $\text{YCu}_{0.5}\text{Ti}_{0.5}\text{O}_3$ sample reduced at various temperatures.	153
Figure 5.13 Cell edges <i>a</i> and <i>c</i> (above figure) and cell volume (below figure) at various reduction temperature.....	154
Figure 5.14 Colors of $\text{LnCu}_{0.5}\text{Ti}_{0.5}\text{O}_3$ (Ln= Y, Tb-Lu) before and after reduction....	156
Figure 5.15 Cell edge <i>a</i> and <i>c</i> versus ionic radius of Ln^{3+} (Ln=Y, Tb-Lu) (green: initial phase; black: reduced phase).....	157
Figure 5.16 Cu^{2+} in octahedral coordination and TBP coordination (reproduction of reference 10).....	158
Figure 5.17 Diffuse reflectance spectra of $\text{YCu}_{0.5}\text{Ti}_{0.5}\text{O}_3$ as prepared (left) and reduced in H_2/N_2 gas mixture (right).	159
Figure 5.18 Magnetic susceptibility versus temperature plot of $\text{YCu}_{0.5}\text{Ti}_{0.5}\text{O}_3$ as prepared (indicated in black square) and reduced (indicated in red dot).	160
Figure 5.19 Thermal Gravimetric Analysis of $\text{YCu}_{0.5}\text{Ti}_{0.5}\text{O}_3$ in H_2/N_2 gas mixture. The maximum temperature is 400 °C with a heating rate of 5 °C/h and 6 hours dwell time.....	161
Figure 6.1 Illustration of the structure of YMnO_3 (a): Mn^{3+} is indicated in blue sphere; Y^{3+} is represented by red sphere. The figure on the right (b) is the MnO_5 trigonal bipyramidal layer from <i>c</i> axis direction.	166
Figure 6.2 X-ray patterns of $\text{YMn}_x\text{Ti}_y\text{O}_{3-\delta}$ ($y = 0-0.4$).	168

LIST OF FIGURES (Continued)

<u>Figure</u>	<u>Page</u>
Figure 6.3 TOF neutron data of $\text{YMn}_{0.73}\text{Ti}_{0.2}\text{O}_{3-\delta}$ are shown with La Bail fit. The observed pattern displayed is from the highest-resolution bank (Bank 2) with d -spacing range 0.60 – 3.2 Å.....	169
Figure 6.4 Lattice parameter a (above) and c (below) versus the Ti content. The value of YMnO_3 is from neutron diffraction data of reference 18.	170
Figure 6.5 Magnetic susceptibility (above) and inverse magnetic susceptibility (below) versus temperature for $\text{YMn}_x\text{Ti}_y\text{O}_{3-\delta}$	171

LIST OF TABLES

<u>Table</u>	<u>Page</u>
Table 1.1 Magnetic susceptibilities of different types of materials	13
Table 3.1 Magnetic data of hexagonal $\text{YIn}_{1-x}\text{Fe}_x\text{O}_3$	69
Table 3.2 Mössbauer parameters of $\text{YIn}_{0.3}\text{Fe}_{0.7}\text{O}_3$	70
Table 3.3 Mössbauer parameters of $\text{YIn}_{0.7}\text{Fe}_{0.3}\text{O}_3$	70
Table 3.4 Mössbauer parameters of YFeO_3	71
Table 3.5 Summary of magnetic data of $\text{YAl}_{1-x}\text{Fe}_x\text{O}_3$	84
Table 4.1 Summary of magnetic data (as prepared) (Observed magnetic moments (μ_B , Bohr magnetons) per Mn for $\text{Ba}_2\text{In}_{2-x}\text{Mn}_x\text{O}_{5+x}$ as prepared)	101
Table 4.2 Summary of magnetic data (as prepared and after reduction).	103
Table 4.3 Structural summary for orthorhombic $\text{Ba}_2\text{In}_{2-x}\text{Mn}_x\text{O}_{5+x}$ phases*	107
Table 4.4 TOF Neutron structural refinement of orthorhombic $\text{Ba}_2\text{In}_{1.9}\text{Mn}_{0.1}\text{O}_{5.1}$	108
Table 4.5 TOF neutron structural refinement of tetragonal $\text{Ba}_2\text{In}_{1.8}\text{Mn}_{0.2}\text{O}_{5.2}$	110
Table 4.6 TOF neutron structural refinement of cubic $\text{Ba}_2\text{In}_{1-x}\text{Mn}_x\text{O}_{5+x}$ samples	113
Table 4.7 Structural parameters of $\text{Ba}_2\text{In}_{2-x}\text{Fe}_x\text{O}_{5+y}$ solid solution	120
Table 4.8 Magnetic moments of $\text{Ba}_2\text{In}_{2-x}\text{Fe}_x\text{O}_{5+y}$ for $x = 0.1-1.5$	126
Table 4.9 Summary of Mössbauer data of $\text{Ba}_2\text{In}_{2-x}\text{Fe}_x\text{O}_{5+y}$	127
Table 5.1 Lattice parameters summary of $\text{YCu}_{0.5}\text{Ti}_{0.5}\text{O}_3$ and $\text{YCu}_{0.6}\text{Ti}_{0.4}\text{O}_{3-\delta}$	139
Table 5.2 NIST Neutron structural refinement of $\text{YCu}_{0.6}\text{Ti}_{0.4}\text{O}_{3-\delta}$	140
Table 5.3 Summary of magnetic data of $\text{YCu}_{0.5}\text{Ti}_{0.5}\text{O}_3$ and $\text{YCu}_{0.6}\text{Ti}_{0.4}\text{O}_{3-\delta}$	145
Table 5.4 Summary of magnetic data of $\text{YMn}_{0.5}\text{Cu}_{0.3}\text{Ti}_{0.2}\text{O}_3$ and $\text{YMn}_{0.5}\text{Cu}_{0.25}\text{Ti}_{0.25}\text{O}_3$	147

LIST OF TABLES (Continued)

<u>Table</u>	<u>Page</u>
Table 5.5 Cell edges of $\text{YCu}_{0.5}\text{Ti}_{0.5}\text{O}_3$ for different treatment	155
Table 5.6 Summary of cell edges and conductivity of $\text{LnCu}_{0.5}\text{Ti}_{0.5}\text{O}_3$ (Tb - Lu, Y) for samples as prepared and reduced	156
Table 5.7 Calculated magnetic moment of $\text{LnCu}_{0.5}\text{Ti}_{0.5}\text{O}_3$ (Ln=Tb-Lu, Y)	159
Table 6.1 Summary of magnetic data of $\text{YMn}_x\text{Ti}_y\text{O}_{3-\delta}$	172

Chapter 1

Introduction

1.1 Transition metal oxides

Followed by the discovery of high temperature superconductor by Bednorz and Muller, transition metal oxides went back into the center of people's attention [1]. Transition metal oxides constitute one of the most attractive materials as they exhibit a wide range of structure types, which as a result, show a variety of properties and phenomena. The specialty of transition metal oxides is rooted in the unique nature of outer d electrons. As a result, the metal-insulator transition can be observed in some transition metal oxides.

Transition metal oxides present complex types of structures, which has been characterized by diffraction and microscopic methods. The most common families are perovskite, spinel and pyrochlore and so on. Some relatively rare structure types such as octahedral tunnel structures and three-dimensional mixed frame works are equally interesting [2]. Properties of oxides were realized to be strongly correlated to the faults or defects in the structure, ultramicrostructures, too.

It can be seen in many applied fields that many transition metal oxides are already used: thermoelectric materials are installed in the hybrid cars to convert heat loss to electric energy. High T_c superconductors, are used in MRI/NMR machines,

mass spectrometers etc. Besides, many high performance pigments are made from transition metal oxides. Transition metal oxides can produce various intense colors because of the specialty of crystal field splitting from *d*-electrons.

1.2 Crystal structures

The variety in structure of transition metal oxides is one of the most fascinating facts which attract attention. Structure is of great importance in the aspect of designing and synthesizing new materials. And chemical bonding between metal and oxide can range from ionic to metallic due to the *d*-electrons in the outer shell. With the progress in the analytical techniques, we can have a better understanding of the structures by X-ray and neutron diffraction. Also, with the help of electronic microscope, local structure can be examined and more information is provided.

The structure of crystals includes several topics such as: the description and classification of different crystal structures. Understanding the structure of the crystal is fundamental in solid state chemistry as it is concerned with the correlation between the factors which determine the structure and the chemical composition, and the relationship between the structure and chemical or physical properties. Thus, information of crystal structure is of great importance in material design.

Various ways can be used to describe crystal structures. The most common approach is to refer the structure to the unit cell and it contains all the information needed. The unit cell is defined by several parameters such as the size, shape and the

positions of the atoms inside the cell. However, the arrangement of atoms relative to each other, the coordination numbers, interatomic distances and types of bonding are also important in revealing picture of the structure in three dimensions as information of the unit cell alone is often insufficient. Alternative ways of describing structures are the close packing approach and space filling polyhedron approach. They provide a greater insight into the structure of crystals than unit cell alone.

The guiding factor in the concept of close packing is that the structure needs to have the maximum density. The way of close packing in two dimensions is that each sphere is surrounded by six touching spheres (Figure 1.1), and this is referred as a closed packed layer. In three dimensions, the most efficient way of packing atoms is to stack close packed layers on top of each other and the resulting structure is closed packed. Hexagonal close packed and cubic closed packed structures are two categories in close packing. Figure 1.1 illustrated the arrangement of the two closed packed structures. The difference between these two approaches is the arrangement of the close packed layers. After the first layer A is set, the atoms on the second layer B occupy the position between three A atoms, and this is true for both close packed methods. The difference lies in the position of the third layer. In hexagonal close packed structures, the spheres on the third layer will be seated exactly the same positions as A layer. Thus, the stacking sequence is:

...ABABAB...

If the spheres on the third layer are placed between three spheres on B layer but not the same positions as A layer, then all the three layers are staggered relative to each other and the stacking sequence arises as:

...ABCABCABC...

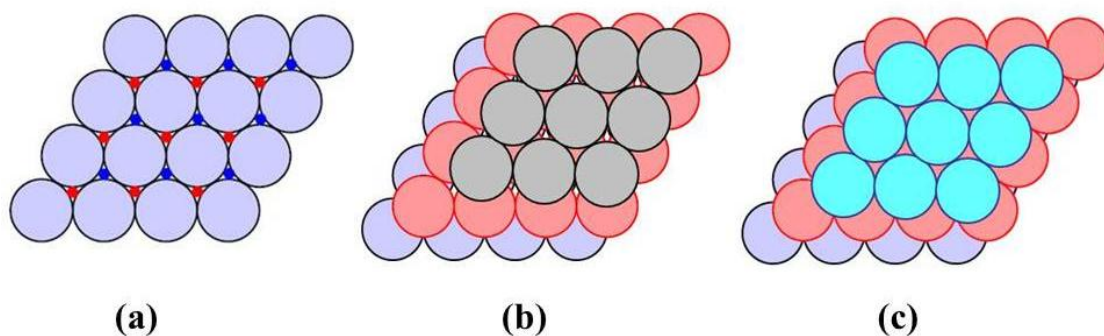


Figure 1.1 A close packed layer of spheres with the same size (a), three close packed layers in hexagonal close packing sequence (b) and three close packed layers in cubic close packing sequence (c) [3].

The other approach, space filling polyhedral, emphasizes the coordination number of the cations. The structure is considered to be built up by polyhedra which are connected together by sharing corners, edges or faces. The structure of the crystal is obtained by the linkage between the neighbouring octahedral in three dimensions. And even in this three dimensional framework, not all the available space is filled and thus it is not legitimate to estimate the efficiency of space filling. The space filling polyhedron has the advantage that it exhibits the topology or linkage of a framework structure and reveals clearly the location of empty interstitial sites [4]. A variety of polyhedral can be found in crystal structures and the most common ones are tetrahedra and octahedra [5]. The transition metal ions sometimes prefer one polyhedron over the other due to the crystal field stabilization energy [6]. Adjacent polyhedra which share

the corners, edges and faces are not necessarily the same type and the corners can be shared by more than two polyhedra, too.

In considering the types of polyhedral connection that are likely to appear in crystal structures, Pauling's third rule for the structure of complex ionic crystals provides a helpful guideline [7,8]. This rule points out that the stability of the structure is decreased with the presence of shared edges and particularly shared faces. And when the cations show large valences and small coordination number, the effect is particularly true. For tetrahedra which contain cations of high charge, edge sharing turned to be unacceptable in energy concern and only corner sharing occurs.

Many complicated structures can be derived from the basic structures, so it is very meaningful to understand the simple structures. Several structures are considered as the fundamental ones such as rock salt, rutile, fluorite, ReO_3 and so on.

For binary compounds, Rock salt (NaCl), Zinc Blende (ZnS) and antifluorite (Na_2O) can be put into one category as they are all binary cubic close packed structures. The simplest structure type is rock salt which is also common in binary transition metal oxides. It can be considered as a cubic close pack of anions in which all the octahedral holes filled with cations. MgO , NaCl , CaO all crystalize in this structure. Wurtzite (ZnS) and nickel arsenide (NiAs) belong to the hexagonal close packed structures.

ReO_3 structure another symbolic structure with vacancies. Anions are closed packed in the cubic structure and cations fill 1/4 of the octahedral holes. Examples are AF_3 etc. And this structure is the mother structure of perovskite.

Among all the transition metal oxides which have the formula ABO_3 , perovskite and its relatives are big family in which a lot of functional materials belong to. The structure can be considered as a derivative of ReO_3 structure, and in perovskite, A cation sits in the center of corner-sharing BO_6 octahedral cages. The formula allows the combination of the cation oxidation states to be 6. So the structure also exhibits various stoichiometries and cation ordering. So many transition metal oxides can be found in this structure and a variety of properties are shown from these oxides. $CaTiO_3$ is a good dielectric material, $BaTiO_3$ shows prominent ferroelectric property, and ABO_{3-x} gives giant magnetoresistance effect [9].

Perovskite structure is well known for the toleration of oxygen vacancies [10]. The brownmillerite family, which has the formula $A_2B_2O_5$ or $(ABO_3)_nABO_2$, is widely used as solid electrolyte. In this structure, two of the oxygens are removed from the BO_6 octahedras, and tetrahedral coordination is formed. Some more complicated structures can also find the root in perovskite. Such as three-dimensional mixed frameworks in oxygen-deficient perovskite, and layered cuprates like $YBa_2Cu_3O_7$.

In compounds which have ABO_3 formula, if the structure is built up by hexagonal arrangement of anions, then it belongs to another category: hexagonal structure. The occurrence of hexagonal compounds is rare compared to perovskite. In some conditions, compounds appear in both depending on the synthesis condition. Other than perovskite and hexagonal, structures like ilmenite, skutterudite, calcite are also well known.

1.3 Properties and practical applications

Transition metal oxides exhibit interesting and prominent properties such as electrical, magnetic, dielectric and optical properties. And applications can be found correlated to these properties. With the comprehensive understanding of the properties, solid state chemists can get the desired materials; manipulate the properties to better performance.

1.2.1 Electronic property

Electronic properties are important because they are the basis for integrated circuits, lasers, magnetic recording tape, and solar energy converters and so on. The basic principles involved in studying and understanding the electronic structure of the compounds helped to improve rational design of functional materials. The multiple types of chemical bonding in transition metal oxides and partially filled *d* orbitals give rise to the special electronic behavior of transition metal oxides. Plenty of examples can be found as metallic materials, semiconductors, metals showing nonmetal-metal transition, and superconductors.

The symbol of electronic property of a compound is that whether it is conductive. The difference between metallic solids and non-metallic solids is that whether it conducts down to low temperature. The conductivity (σ) is defined by the equation: $\sigma = n e \mu$, and n is the number of the charge carriers, e the charge and μ the

mobility of the charge carriers. The conductivity temperature dependence of different materials can find root in the properties of n , e , and μ . For metals, n is large and e is constant. The mobility term (μ) normally decreases with the increase of the temperature as the moving electrons collides with phonons due to the lattice vibration or other conditions. Therefore, the conductivity of metals will decrease as temperature increases. For semiconductors and insulators, the number of charge carriers usually increases with the temperature. And it will exceed the effect of the decrease in mobility. Thus, conductivity increases with elevating temperature. Insulators can be considered as the extreme of semiconductors as n is very small in that. And the phenomena that insulators become semiconducting at high temperatures and semiconductors behave similar to insulators at low temperature are observed.

The variety in behavior of electronic conductivity of solids can be explained by the electronic structure which is described by the band theory, which is illustrated below. The conductivity is related to the motions of electrons in the band. So if the bands are filled, the net motion of electrons is zero. And the band gap existed between the filled band and empty band, so the solid will not conduct at its ground state. The metallic compounds, by contrast, have a partially filled band, in which there is no energy gap for electrons which filled the top-occupied levels. Applied electric field will push the electrons to move into the orbitals where they generate a net motion of charge in the solid and electric current flows [11].

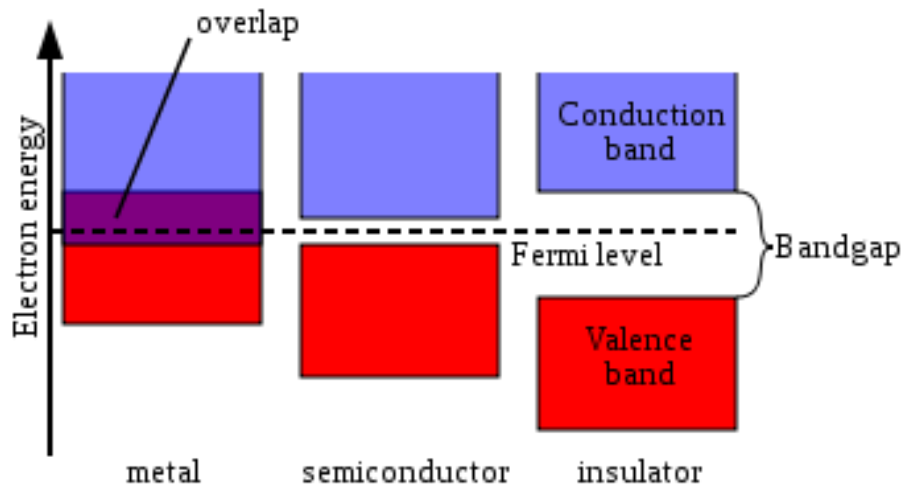


Figure 1.2 Simplified diagram of the electronic band structure of metals, semiconductors, and insulators.

Semiconductors have electronic conductivity between the conductivity of insulators and metallic compounds. The electronic states in semiconductors are developed by the properties of periodicity of the structure [12]. In the semiconductors, there are no electronic states available for a given interval of energies, which is called the energy gap (E_g). The valence band (E_v) appears to be in the upper edge and the conduction band (E_c) in the lower edge, and this is demonstrated in figure 1.2. The resistivity of semiconductor is decreasing with increase of temperature. The conductivity at room temperature is due to the presence of mobile charge carriers which are either electrons in the conduction band or holes in the valence band. Two types of semiconductors exist: intrinsic and extrinsic semiconductors. Several factors such as stoichiometry and defects can affect the semiconducting phenomena [13]. Semiconductors are widely applied in many fields such as solar cell, diode including light-emitting diode (LED).

Solids with a large band gap are not able to generate current flow under normal conditions. But at high temperatures, conductivity is observed in some solids because of the migration of ions. And this phenomenon is referred as ion conductivity. The photoconductivity is another example of excitation which was produced by absorption of a photon of energy greater than the band gap.

1.2.2 Magnetic property

Magnetism is one of the most studied properties because of the wide applications. Magnetic effects which a property of all substances are characterized by having unpaired electrons. The unfilled *d* and *f* electrons and the capability of different oxidation states of transition metal ions in the compounds make them especially attractive. And many magnetic oxides, especially ferrites such as MgFe_2O_4 , can be applied in various fields like hard disk recorder, information storage devices and MRI [14-16]. In addition, magnetic measurement serves as a helpful method in structural determination and explanation.

Generally the magnetic behaviors of all substances can be categorized into diamagnetic and paramagnetic, and both of them will generate magnetic moment. If the material has unpaired electrons, then it will show paramagnetic behavior. The unpaired electrons may be oriented randomly in the paramagnetic materials. The direction of unpaired electrons may be aligned to be in parallel fashion, and the material possesses an overall magnetic moment which is referred to ferromagnetic. If

the unpaired electrons are all aligned antiparallel to each other, making the total magnetic moment to be zero, in this case it is antiferromagnetic behavior. If the alignment happens in antiparallel but with unequal number of electrons in both directions, a net magnetic moment appears and the behavior is ferromagnetic. The schematic representation of magnetic ordering is showed below in figure 1.3.

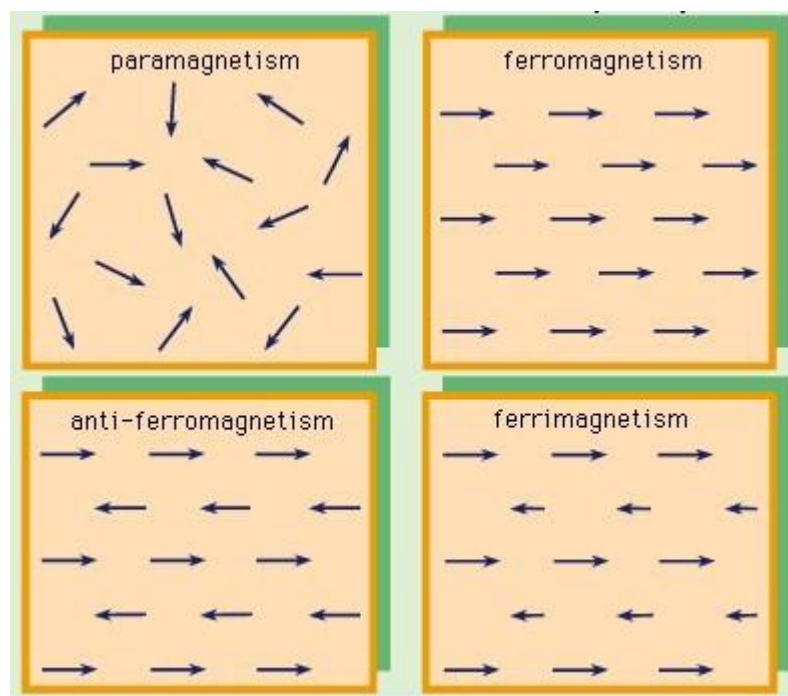


Figure 1.3 Arrangement of magnetic dipoles for different magnetic behavior.

When an external magnetic field is applied to the compounds, diamagnetic material will have a repulsive interaction whereas paramagnetic show an attractive force. If the interaction is very strong (the magnetic permeability is much higher than 1), the compounds exhibit ferromagnetism. The interaction is illustrated below. And the relationship of the magnetic induction (B), applied field (H) and magnetization intensity (I) can be expressed as the following equation:

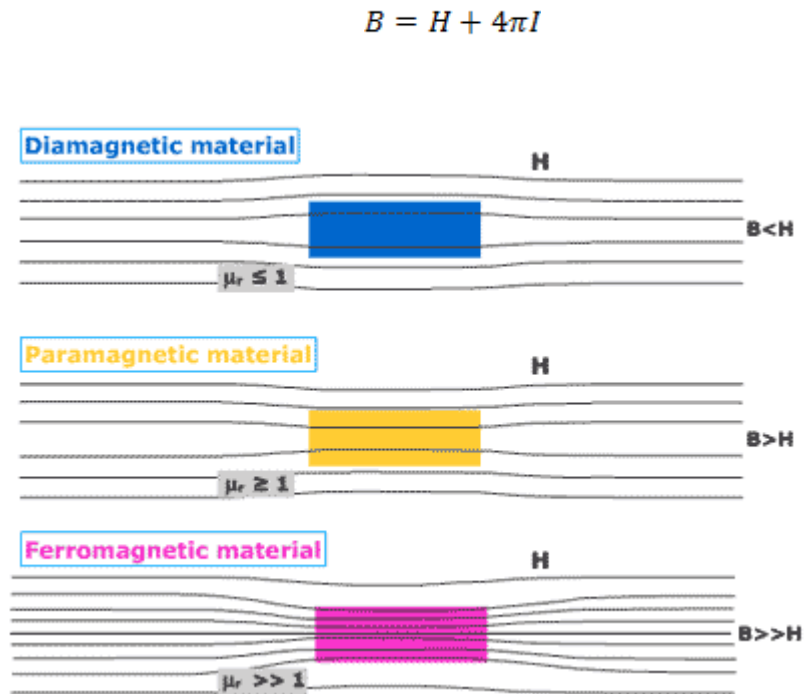


Figure 1.4 The magnetization of diamagnetic material, paramagnetic material and ferromagnetic material.

The permeability (P) is defined as the ratio B/H , and this is an extrinsic property of the material.

$$P = \frac{B}{H} = 1 + \frac{4\pi I}{H} = 1 + 4\pi\chi$$

The intrinsic property volume susceptibility (χ) is thus obtained by the ratio of induced magnetic moment and applied field (I/H). Diamagnetic materials exhibit a low or negative magnetic susceptibility whereas the paramagnetic susceptibility is usually positive and higher [17, 18].

Diamagnetic materials tend to have closed shells which shield the interior part from the external magnetic field. For diamagnetic materials, $P < 1$ and χ is small and slightly negative. The mechanism of induced diamagnetic moment is similar to

electromagnetism explained by Lenz's Law [19]: when external magnetic flux is applied to an electrical circuit, an electromotive force which is opposite to the original direction of external flux is induced. Thus diamagnetic moment will exist only if material is under external magnetic field [20]. Diamagnetism is a general phenomenon because all electrons will give weak signal of diamagnetic moment. However, in compounds which show other magnetism such as paramagnetism and ferromagnetism, diamagnetism is always overshadowed. The magnetic susceptibilities of different types of materials are summarized in table 1.1.

Table 1.1 Magnetic susceptibilities of different types of materials

Bahavior	Typical χ Value	P	Change of χ with T increase	Field dependence
Diamagnetism	-10^{-6}	<1	None	No
Paramagnetism	0 to 10^{-2}	>1	Decreases	No
Ferromagnetism	10^{-2} to 10^6	$\gg 1$	Decreases	Yes
Antiferromagnetism	0 to 10^{-2}	>1	Increases	Yes

Besides the absolute magnitudes of different magnetic materials, temperature dependence can be another judgement to determine the type of magnetism. Many paramagnetic substances obey the Curie Law, which states that the magnetic susceptibility is inversely proportional to temperature:

$$\chi_m = \frac{C}{T}$$

C is the Curie constant. And normally, a better fit is observed with the Curie-Weiss Law:

$$\chi_m = \frac{C}{(T + \theta)}$$

θ is the Weiss constant. The sign of the Weiss constant is correlated to the direction of the spin alignment. The negative Weiss constant indicates the antiferromagnetic behavior whereas the positive value shows the ferromagnetic behavior.

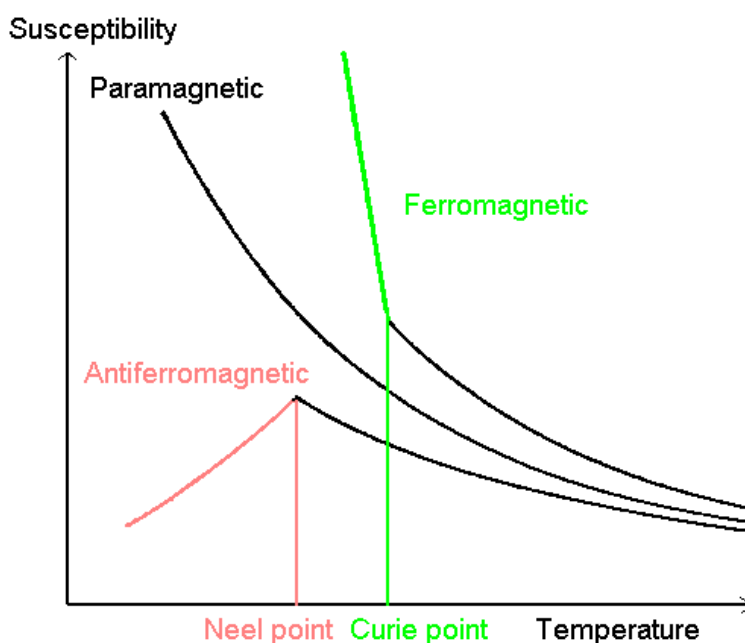


Figure 1.5 Temperature dependence of the inverse magnetic susceptibility for different materials.

For ferromagnetic and antiferromagnetic materials, simple Curie-Weiss Law is not obeyed. Ferromagnetic substances show a great susceptibility at low temperature range and the value decreases with the rising temperature. Above the certain temperature (Curie Temperature T_C), the material bears a magnetic transition from ferromagnetic to paramagnetic and Curie-Weiss Law behavior is observed. The

magnetic susceptibility of antiferromagnetic material increases as the temperature is elevated up to a critical temperature (Néel temperature T_N). And the substance reverts to paramagnetic. The inverse susceptibility versus temperature plot of these different materials is in figure 1.5.

The magnetic properties of materials can be represented by the term of the magnetic moment μ , which is directly related to the unpaired electrons. The relationship between μ and χ is expressed in the equation:

$$\mu = \sqrt{\frac{3kC}{N_A}} = 2.84 \sqrt{C} \mu_B$$

Where N_A is Avogadro's number, k is Boltzmann's constant, C is the Curie constant and μ_B is the Bohr magneton.

Magnetic ordering is observed in metal oxides, metal alloys [21-23]. Two requirements need to be satisfied for the magnetic ordering. The first one is that a uniform magnetic moment is able to be associated with ions in a solid. Applied magnetic field will generate the induced moments and spontaneous moments are produced even without the external field. The second one is that the moments are interacting through quantum mechanical forces, not the ordinary dipole-dipole forces. These exchange forces rely on the factors such as distance of the magnetic ions and geometrical arrangement [24]. Thus, various magnetic orders are observed in solids. The direct exchange is appeared when the distances between the magnetic moments are small. And indirect exchange presents when the distance is greater. Generally, this occurs through a non-magnetic media which is an anion in superexchange in insulators

or itinerant electrons in RKKY interactions in metals [25, 26]. And Goodenough-Kanamori (GK) rules is employed to evaluate the competing interactions (ferromagnetic or antiferromagnetic) [27-29].

Multiferroics are attractive among all the magnetic phenomena. The definition is the materials that exhibit more than one primary ferroic order parameter at the same time. The four basic primary ferroic order parameters are ferromagnetism, ferroelectricity, ferroelasticity and ferrotoroidicity. And the coupling can expand to non-primary order parameters such as antiferromagnetism or ferrimagnetism. In bulk form, multiferroics are generally utilized and explored for novel multifunctional devices such as high-sensitivity magnetic field sensors and electrical tunable microwave devices [30]. In the thin film form, the major application is the development of magnetoelectronic devices which use the coupling between magnetic and ferroelectric orders. Examples are spintronic devices such as tunnel magnetoresistance (TMR) sensors [31].

1.2.3 Optical properties

When optical property is discussed for a material, color and luminescence are the concepts that come out first. Color arises normally because the material is sensitive to the visible light. And the observed color corresponds to the unabsorbed radiation and its range of associated wavelength. Luminescence is the term for the emission of light by a material as a result of energy absorbed. Color and luminescence are often, but not

always, associated with transition metal ions. The specialty of unfilled d and f electrons make them suitable materials for applications such as color pigments, solar cell, lasers.

1.2.3.1 Color in transition metal oxides

The mechanism for light and color observation is known: when energy (light source) is absorbed and released, the substances (object) migrate between excited and ground state. If the energy falls in the visible region, color is observed by the eye which serves as a detector. To further examine the reason for the occurrence of color, principles of quantum mechanics need to be employed. It states that only certain energy levels are legitimate for electrons in ground states. And there are well-calculated energy differences between all these energy levels. Only the wavelengths corresponding to the exact energy differences between different levels are absorbed. Energy absorbed from the electromagnetic radiation is consumed for species excitation from ground state to excited state. It is the transition that gives rise to the color. All substances, color or colorless, all exhibit these behavior. However, only absorption from a strict wavelength results in color, and the appearance of color is determined by the sensitivity of eye [32].

One special property of transition metal oxides is that they always show various colors. The majority of atoms ions in solid and solution do not show the pronounced colors because the energy gap between ground state and nearest excited

state is outside the visible region. But this does not happen to transition metal ions due to the crystal field splitting of d electrons [33].

In order to modify colors, information about the electronic processes in different materials which give rise to color will be helpful. Generally, five types of processes are classified as follows [34, 35]:

- 1) Transitions in conjugated compounds (normally for organic compounds)
- 2) Charge transfer transitions (intermolecular)
- 3) Charge transfer transitions (intramolecular)
- 4) Crystal field transitions
- 5) Band transitions

The first two processes are normally observed organic color compounds and thus not discussed in this work. The intramolecular charge transfer was first observed in NaCl showing photon absorption around 234 nm in the gas form. And it was explained as a transfer of an electron from Cl^- to Na^+ [36]. The iron complex which exhibits color is Fe^{3+} with CNS^- . The thiocyanate is believed to transfer the electron to Fe^{3+} to get to the excited state in which the formula shifts partially to Fe^{2+} , and the energy level difference falls in 500 nm region and gives rise to a red color [37]. Similarly, the molecule or ion can be considered as a ligand bound to a metal. Then the process of charge transfer can be generated as an electron is transferred from an orbital from the ligand to an orbital on the metal. The other direction of transfer also exists. The charge transfer may occur in other materials besides transition metal complexes. Most charge transfer transitions require high energy and thus the

absorption usually situated in the ultraviolet or far ultraviolet region. However, if the metal is easily oxidized and the ligand is easily reduced, the metal to ligand charge transfer transition is possible to happen in the visible region. The reverse condition may shift the ligand to metal charge transfer to the visible region, too [34]. Most intramolecular charge transfer transitions in the visible region take place in compounds containing transition metals especially *d*-block elements. Prussian blue, for example, is used as the pigment. The color arises from the charge transition between $\text{Fe}^{2+}(\text{CN})_6^{4-}$ and Fe^{3+} ions [38].

For inorganic materials, the most intense colors are observed in the compounds of the *d*-block metals and the same ion appears in different colors in different chemical environments. While charge transfer is partially taken account to the colors, a major reason is from the transition of *d* electrons. When the metal ion is in the gaseous form, the *d*-orbitals have particular orientation in space (Figure 1.6).

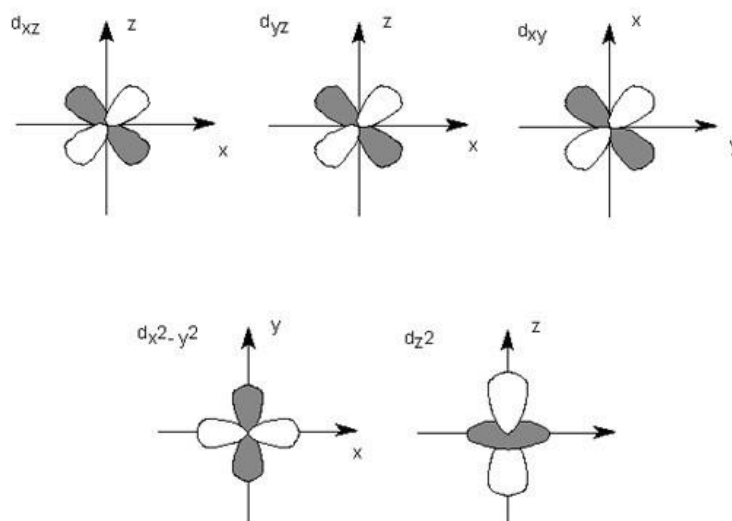


Figure 1.6 Graphical representations of *d* orbital shapes.

In the gaseous free ion, the d electrons are only affected by the interelectronic repulsion force. And this gives rise to a splitting of the energy levels into different sub levels. When the ion is situated in aqueous form or crystal lattice, the nearest neighbor ligands will exert an electric field upon it. And the energy levels are further splitted due to the different geometries of ion and its neighbor ligand. An example of splitting in vanadium in the octrahedral coordination is given in figure 1.7 [39]. The splitting is determined by the number of d electrons and the symmetry of the field.

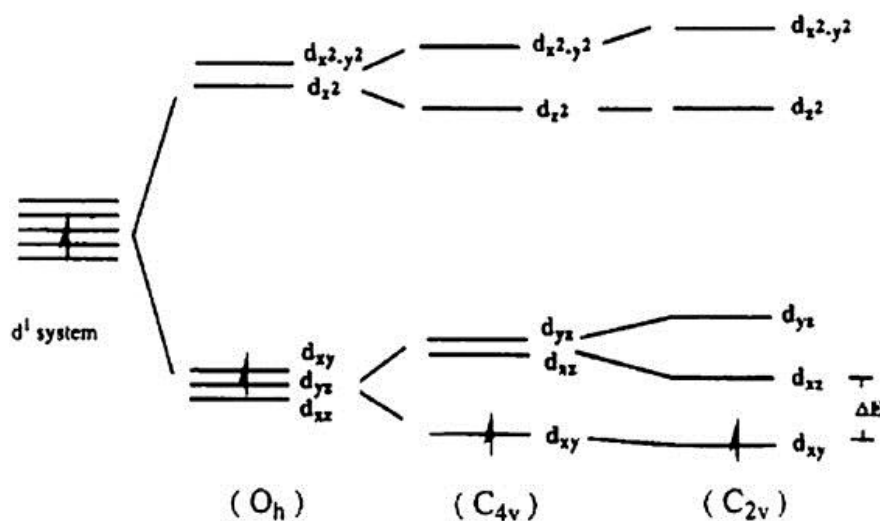


Figure 1.7 Illustration of splitting of d orbital diagrams of V^{4+} in octahedral O_h , square-pyramidal C_{4v} , and distorted square-pyramidal C_{2v} geometry. The latter geometry appears in the V^{4+} environment in the reduced V_2O_5 . (ΔE is the energy gap between d_{xz} and d_{xy} orbitals) [39]

A lot of transition metal oxides in the fourth period exhibit color due to the crystal field transition. And the colors of some minerals and gems can be clarified using this model together with charge transfer. The minerals such as hematite (α - Fe_2O_3), maghemite (γ - Fe_2O_3) and magnetite (Fe_3O_4) all contain iron but exhibit different color. The structure absorption due to crystal field transitions gives the

explanation. The characteristic change of ferric oxides from weak absorption in the near-IR region to near UV region is also considered as a cause for the intense colors [40].

Colors from materials which have no crystal field transition like cadmium sulfide are not yet explained. Semiconductor properties are considered as an alternative approach. In crystals, atoms are close to each other and the allowed energy states are merged into bands. The band gap is the space between bands and is forbidden. For the non-metallic compounds, only photons with great energy which can overcome the band gap and break an electron free from a bonding orbital are able to be absorbed. If the electronic structure of the compound is suitable, the absorption will fall in the visible region. So for CdS, the band gap is 2.4 eV (527nm). It will absorb all the electrical radiation with energy greater than 2.4 eV and the blue region of the visible light is absorbed thus presents in yellow color [41].

In some cases, the color can be modified by other factors such as crystal form, lattice defects, particle size or shape, temperature and dispersing medium [42]. However, even with all the mechanisms, the color prediction of unsynthesized compounds is still a risky task. But the color fascination will become clear as we know more and more.

1.2.3.2 Luminescence

Luminescence is categorized by different excitation sources. Photoluminescence utilizes photons or UV light as a source while electrical energy serves as the energy input in electroluminescence. Similarly, cathodoluminescence uses rays or electrons from cathode for excitation. Based on the time between excitation and emission, two types of luminescence are distinguished. Fluorescence represents for a short time period, normally $\leq 10^{-8}$ second. For any decay time longer than that, the process is known as phosphorescence. And the phenomenon persists for a long time after the source of excitation is removed [4].

Photoluminescent materials are the most attractive materials, and the most common use is for safety applications. The combination of photoluminescent property with other properties will result in a wider range of applications such as liquid-crystal display [43]. Photoluminescent materials require a crystal structure such as ZnS, CaWO_4 as a host matrix. The cation activator such as Sn^{2+} and Eu^{2+} is doped to the host in a small amount. And sometimes, another cation is added as a sensitizer. Inorganic luminescent materials are generally referred as phosphors.

1.2.4 Dielectric and thermoelectric property

Dielectric materials are widely applied in the regions of electronic industries such as circuit boards, wireless communications and especially capacitors for a long time [9]. In capacitors, dielectric materials which are all insulators are inserted between two conducting sheets. When applied with an electric field, the charges that

were fixed are now forced to migrate to the opposite charge. The electron clouds are distorted by the external field and the polarization occurs. And this process generates an opposing electric field which is illustrated below [44].

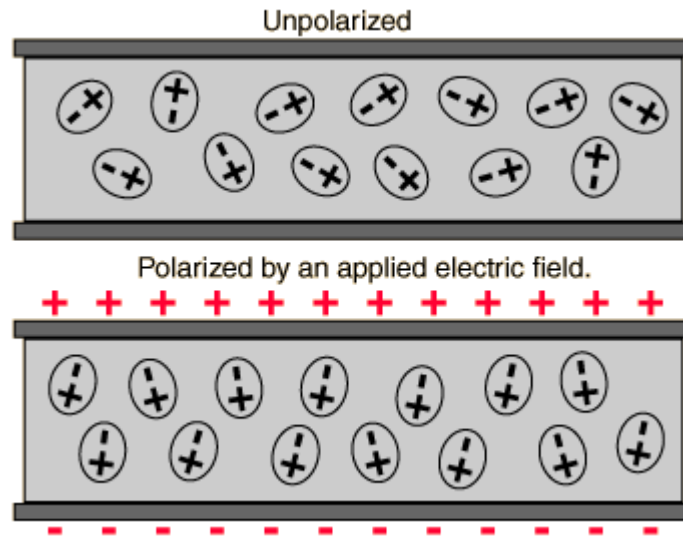


Figure 1.8 Polarization of dielectric material in capacitors.

The measure of the dielectric property is qualified by the dielectric constant and loss. When a certain voltage (V) is applied to the capacitor, a charge (Q) representing the electric field will be measured. The capacitance is defined as:

$$C = \frac{Q}{V}$$

Given the permittivity ϵ_r , surface area of the capacitor A , the thickness of the dielectric material d , the capacity can be expressed by:

$$C = \epsilon_0 \epsilon_r \frac{A}{d}$$

Where ϵ_0 is a constant: the permittivity of free space. The dielectric constant κ can be derived as:

$$\kappa = \frac{Cd}{\epsilon_0 A}$$

The dielectric constant depends on the degree of polarization, or the amount of charge displacement. Transition metal oxides (e.g. BaTiO₃) are prone to have high dielectric constant compared to the other materials. Factors such as temperature, frequency can affect the dielectric constant [9, 44].

The behavior of a dielectric material is evaluated by the dielectric loss (loss tangent) as well. In an ideal dielectric material, electronic current leads the voltage to change by 90° when an alternating current is passed through it. However, most dielectric materials change less than 90° and result in the phase lag. The dielectric loss is referred as $\tan\delta$, where δ is the angle changed by the phase lag from the ideal angle.

Dielectric materials with high dielectric constant and low loss are desired for the electronic industry as it is an effective way to minimize the size of the electronics. CaCu₃Ti₄O₁₂ (CCTO), made by Dr. Subramanian group, was found to have a dielectric constant about 10,000 at 1000 kHz and it was nearly independent of temperature in a temperature range of 120 to 600 K [45].

Thermoelectric property concerns the generation of electricity from the thermal gradient, and this is particularly interesting in heat recovery in automobile exhaust, geothermal or solar heat. Applications of thermoelectric materials will recoup a tremendous amount of energy in current industrial processes [46].

The Seebeck effect should be considered as the starting point of understanding thermoelectric property. The phenomenon was first discovered as a thermal gradient created a voltage across the junctions of two materials. The Seebeck coefficient (α) is

defined as the ratio of the voltage over the temperature difference: $\alpha = \Delta V / \Delta T$. Seebeck coefficient is an intrinsic property of the material, and generally metals have relatively low Seebeck coefficient whereas semiconductors and insulators have higher value. The type of charge carrier can also be derived from the value of Seebeck coefficient. The common application of the Seebeck phenomena is the thermocouple which is used to give precise temperature value [47].

After the discovery of the Seebeck effect, the reverse effect which is named the Peltier effect was reported. Peltier found that when an electrical current was applied to the junction of two dissimilar materials, heat was either given out or absorbed depending on the direction of the current. The Peltier coefficient Π is used to describe this phenomenon:

$$\Pi = \alpha T$$

The Seebeck or Peltier effect alone is not enough to describe the thermoelectric property. A dimensionless figure of merit denoted ZT (figure 1.9) is employed to determine the behavior of a thermoelectric material instead:

$$ZT = \frac{\alpha^2 \sigma T}{\kappa} = \frac{\alpha^2 T}{\rho \kappa}$$

In which α is the Seebeck coefficient, σ is the electrical conductivity, ρ is the electrical resistivity, and κ is the total thermal conductivity. From the definition, the ZT of a material can be enhanced for a higher Seebeck coefficient and conductivity, while the thermal conductivity should be lowered. However, all the factors are correlated. The good thermoelectric material should have the properties of both metals

and insulators, and they are mostly found in semiconductors. And $ZT > 1$ is considered as illegible for industry application [48].

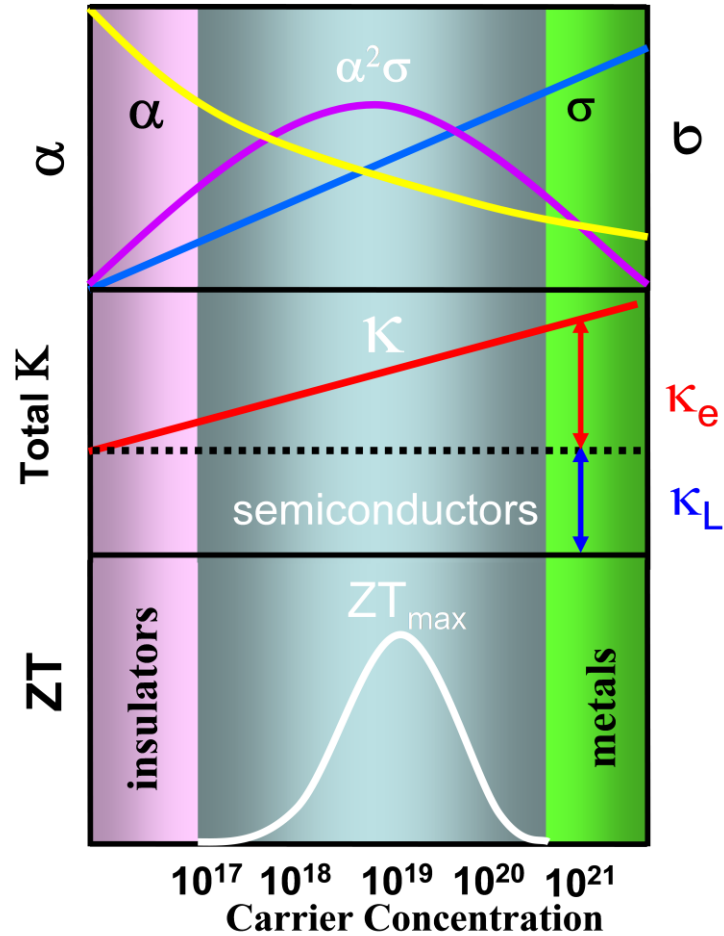


Figure 1.9 Dimensionless figure of merit [49].

1.4 References

1. J. Mannhart; J. G. Bednorz; K. A. Müller; D. G. Schlom, *Zeitschrift für Physik B* 83, 307-311.
2. C.N.R. Rao; B. Reveau. *Transition Metal Oxides: Structure, Properties, and synthesis of Ceramic Oxides*, 2nd edition, John Wiley & Sons: New York, 1998.
3. Dr. Subramanian lecture: *Solid State Chemistry*.

4. A. R. West. *Solid State Chemistry and Its Applications*. John Wiley & Sons Ltd. 1985.
5. R. E. Williams. *Science*. 161, 276-277, 1968.
6. J. D. Dunitz; L. E. Orgel. *J. Phys. Chem. Solids*. 3, 318-323. 1957.
7. L. Pauling. *J. Am. Chem. Soc.* 51, 1010-1026, 1929.
8. J. K. Burdett; T. J. McLarnan. *J. Am. Chem. Soc.* 104, 5229-5230, 1982.
9. A.R.West. *Basic Solid State Chemistry*. 2nd edition, John Wiley & Sons, LTD.
10. D.M. Smyth. *Cryst. Lattice Defects Amorph. Mater.* 18, 355, 1989.
11. P. A. Cox. *The Electronic Structure and Chemistry of Solids*. Oxford University Press, 1987.
12. S. Cattarin; F. Decker. *Electrodes: Semiconductor Electrodes*. Elsevier, 2009.
13. J. Nishizawa. *Mater. Sci. in Semiconductore Processing*. 6, 249-252, 2003.
14. Y. Tokura. *Colossal Magneto-resistive Oxides*. Gordon and Breach Science Publishers, 2000
15. E. De Grave; A. Govaert; D. Chambaere; G. Robbrecht. *Physica B+C*. 96, 103-110, 1979.
16. R. J. Harrison; A. Putnis. *Phys. Chem. Minerals*. 26, 322-332, 1999.
17. P.W. Selwood. *Magnetochemistry*. Interscience Publishers, Inc, New York, 1943.
18. J.B. Goodenough. *Magnetism and the Chemical Bond*. John Wiley & Sons, New York, 1963
19. http://en.wikipedia.org/wiki/Lenz%27s_law.
20. Michael M. Schieber. *Experimental Magnetochemistry Nonmetallic Magnetic Materials*. John Willey & Sons, Inc, New York, 1967
21. P. G. Radaelli; D. E. Cox; M. Marezio; S-W. Cheong. *Phys. Rev. B*. 55, 3015, 1997.
22. V. Cannella; J. A. Mydosh. *Phys. Rev. B*. 6, 4220, 1972.
23. R. J. Elliott. *Phy. Rev.* 124, 346, 1961.
24. C. M. Hurd. *Contemp. Phys.* 23, 469-493, 1982.
25. J. Kanamori. *J. Phys. Chem. Solids* 10, 87-98, 1959.
26. D. N. Aristov. *Phys. Rev. B*. 55, 8064, 1997
27. P. W. Anderson. *Phys. Rev.* 79, 350, 1950.
28. J. B. Goodenough; A. L. Loeb. *Phys. Rev.* 98, 391, 1955.
29. J. Kanamori. *J. Phys. Chem. Solids*. 10, 87, 1959.
30. C-W Nan; M. I. Bichurin; S. Dong; D. Viehland; G. Srinivasan. *J. Appl. Phys.* 103, 031101, 2008.
31. M. Gajek; M. Bibes; S. Fusil; K. Bouzehouane; J. Fontcuberta; A. Barthélémy; A. Fert. *Nature Mater.* 6, 296-302, 2007.
32. E. Coates. *J. Soc. Dyers. Colour.* 83, 95, 1967.
33. Richard J. D. Tilley. *Colour and the Optical Properties of Materials*. Second Edition, John Wiley and Sons, Ltd., Publication,
34. M. V. Orna. *J. Chem. Educ.* 55, 478, 1978.
35. K. Nassau. *Am. Mineral.* 63, 219-229, 1978.
36. K. Z. Prizbram. *Physik*. 20, 196, 1923.
37. E. Robinowitch. *Rev. Mod. Phys.* 14, 127, 1942.

38. M. B. Robin. *Inorg. Chem.* 1, 337-342, 1962.
39. Y. -J. Liu; J. A. Cowen; T. Kaplan; D. C. DeGroot; J. Schindler; C. R. kannewurf; M. G. Kanatzidis. *Chem. Mater.* 7, 1616-1624, 1995
40. R. V. Morris; H. V. Lauer, Jr; C. A. Lawson; E. K. Gibson, Jr; G. A. Nace; C. Stewart. *J. Geophys. Res.* 90, 3126-3144, 1985.
41. P. E. Lippens; M. Lannoo. *Phys. Rev. B.* 39, 10935-10942, 1989.
42. S. Huey. *Color Eng.* 9, 20, 1971.
43. A. Montali; C. bastiaansen; P. Smith; C. Weder. *Nature.* 392, 261-264, 1998.
44. W. D. Kingery; H. K. Bowen; D. R. Uhlmann. *Introduction to Ceramics*. 2nd ed.; John Wiley & Sons: New York, 1976
45. M.A. Subramanian; D. Li; N. Duan; B.A. Reisner; A.W. Sleight. *J. Solid State Chem.* 151, 323, 2000.
46. T. M. Tritt; M. A. Subramanian, *Mat. Res. Soc. Bul.* 31, 188-194, 2006.
47. S.O. Kasap. *Thermoelectric Effects in Metals: Thermocouples*. An e-booklet, 1997-2001.
48. G.D. Mahan; J.O. Sofo. *Proc. Natl. Acad. Sci.* 19, 7436, 1996.
49. Dr. Subramanian, lecture on thermoelectric materials.

Chapter 2

Experimental Methods of Analysis

The evolution of sciences and technologies relies on various factors, among them experimental analysis is crucial as it is the primary approach for acquiring information. The improvement in capabilities of instrumentation including automation, resolution, simultaneous detection and higher sensitivity greatly promotes the quality of research done today [1]. As the acquired data is the basis of all the rational explanations, the measurement must provide useful and reliable information. Thus the discussion of the instrumentation and methodology used for data collecting in this thesis is necessary. The content in this chapter serves as an introduction to the instrumentation and methodology.

For the study of solid state chemistry, X-ray diffraction is the most fundamental technique as it gives information about the essence of the material. However, different instruments are necessary to conduct a comprehensive characterization of the compound.

2.1 X-Ray Diffraction: MiniFlex II diffractometer

The very first step to study the compound is to get information about “what it is” and the structure. X-ray diffraction is the most widely used method of characterization for non-molecular and crystalline materials. Because every crystalline

compound will have unique and fixed X-ray pattern, it is ideal to get the phase identification. Not only single phase can be characterized, in the mixture of several phases, each phase will exhibit its own peaks. And this makes X-ray diffraction a prominent method to do the qualitative phase analysis. By analyzing the positions of lines (which represent d spacing) of a powder pattern, accurate unit cell parameter can be determined. Also, crystal structures can be determined by examining the intensity of peaks and particle size of the sample is solved from the breadth of peaks. [2] Crystal structures were refined by the Rietveld method using the GSAS software package with the EXPGUI Interface [3, 4].

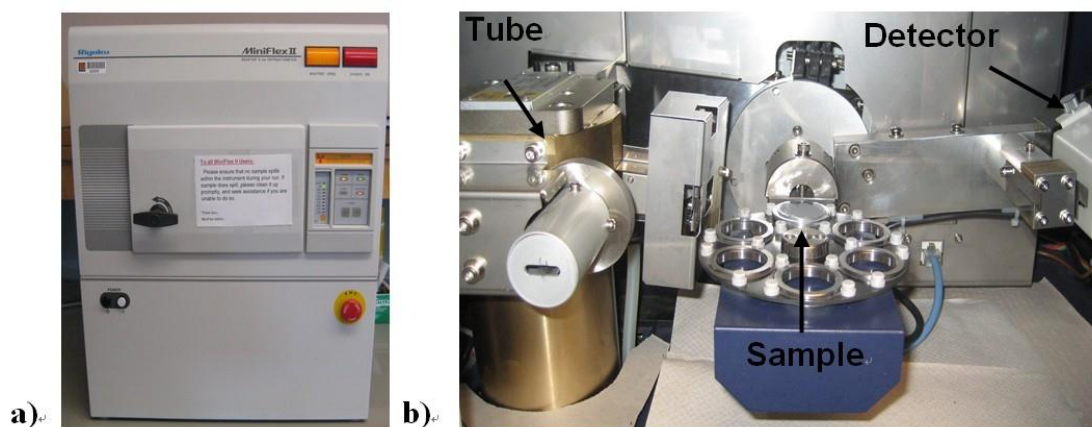


Figure 2.1 Rigaku MiniFlex II diffractometer (a) and the inner workings with x-ray tube, sample platform and detector labeled (b).

The majority of X-ray data was collected from the Miniflex bench top Diffractometer which is shown in figure 2.1 (a) and (b). When the machine is running, the X-ray was produced from X-ray generator tube on the left side. The tube is made from tungsten and has a cathode, which directs the flux of electrons into vacuum, and an anode, which collects the electrons. The stream of electrons generated between the two ends will bombard on the copper target and the energy carried by the electrons

will ionize some of the copper 1s electrons (K shell). The electrons of the outer shell (normally 2p or 3p) will drop and fill in the 1s orbital and the energy for transition is X-radiation. The energy for relaxation is fixed and for copper, radiation from 2p to 1s is called $K\alpha$ with a wavelength of 1.5418\AA ; the one from 3p to 1s is $K\beta$, 1.3922\AA . The K radiation is more desired because of higher intensity, so a filter made from nickel foil is needed to get the monochromatic X-ray source [5]. The X-ray produced from X-ray tube will be shed on the sample held by aluminum holders, which is shown in the center part. The diffracted beam is collected by the detector and transmitted to signals on the computer.

The diffraction of electromagnetic radiation is similar to visible light. And Bragg's law was used to describe the mechanism of X-ray diffraction which is illustrated in figure 2.2. When crystalline sample which has multiple atomic planes is exposed to the X-ray beams A and B, the difference in the radiation pathway will be $GY+YH$. The sum should equal to the integer times of wavelength to obey the condition of diffraction.

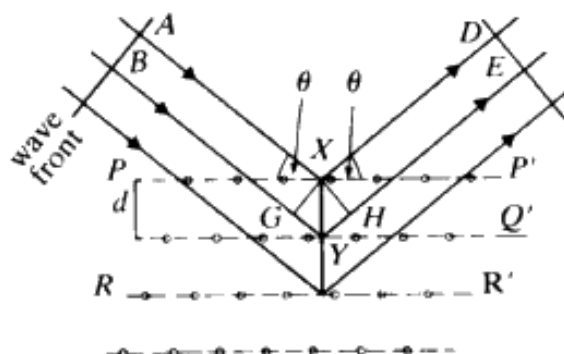


Figure 2.2 Derivation of Bragg's Law for X-ray diffraction

$$GY = YH = d \sin \theta$$

$$GY + YH = 2d \sin \theta = n\lambda \quad \text{Bragg's Law}$$

For a diffractometer using copper as a target material, the wavelength is fixed so diffraction angle can be varied to get a full map of X-ray file. At certain angle, only the d spacing which satisfies Bragg's Law will produce constructive reflected beams and show peaks on the pattern. Other conditions will be destructive and cancel each other. For the real sample which contains more layers, Bragg's Law is still strictly obeyed which means if the d spacing is incorrect for a little extent, cancellation of the reflected beam is usually complete.

For simple phase identification, the diffractometer is set to scan over a range of 2θ values continuously at a fixed angular velocity. If accurate information such as cell parameters and atom positions is desired, a slower and fixed time scan is needed. And in some cases, an internal standard was mixed to the compound to get the accurate d spacing and unit cell edges. A correction factor can be found by comparing the experimental and literature value of the d spacing of the standard.

Two types of sample preparations are normally used in X-ray diffraction: powder or thin film. All the samples in this thesis are powder form.

2.2 Neutron Diffraction (Center for Neutron Research, National Institute of Science and Technology; Oak Ridge National Laboratory Neutron Science):

Neutron diffraction applies neutron as a radiation resource to determine the crystalline structure, especially for magnetic materials. It is an alternative method used for crystallographic work when X-ray diffraction is inadequate. Neutrons are working as a radiation resource the same principle can be applied to neutron diffraction. However, a nuclear reactor is needed to create a sufficiently intense source of neutrons, so it is an expensive method. All the neutron diffraction data in this thesis was collected from NIST Center for Neutron Research and ORNL Neutron Science.

Several differences could be identified between neutron and X-ray diffraction. First, the scattering strength of atoms toward neutrons and X-ray is quite different. For X-ray, atoms react based on the atomic number, so the light atoms will have little signals. And this will be solved in neutron diffraction as light atoms like hydrogen and oxygen are very sensitive to neutron. Accurate oxygen content of oxides can be obtained from neutron diffraction data. Second, atoms with similar x-ray scattering factors will have quite different neutron scattering factor. And this is precious for transition metal oxides. For example, Manganese, iron, cobalt and nickel all have similar scattering power toward X-ray, but giant different respond to neutrons. Although there are no charges on neutrons, they carry magnetic dipole moment. So they will interact with unpaired electrons in magnetic materials and give rise to an additional scattering effect. So it is a reliable technique to analyze the magnetic structure of the compounds.

There are two ways to utilize neutrons. The first one type is similar to X-ray diffraction. A continuous spectrum of neutrons is generated from the nuclear reactor

and a filter is applied to obtain the monochromatic neutron beams. And in the filter process, the majority of energy is wasted. So the beam used is weak and greater amount of sample is always needed ($\sim 1\text{cm}^3$). The instrumentation is shown below.

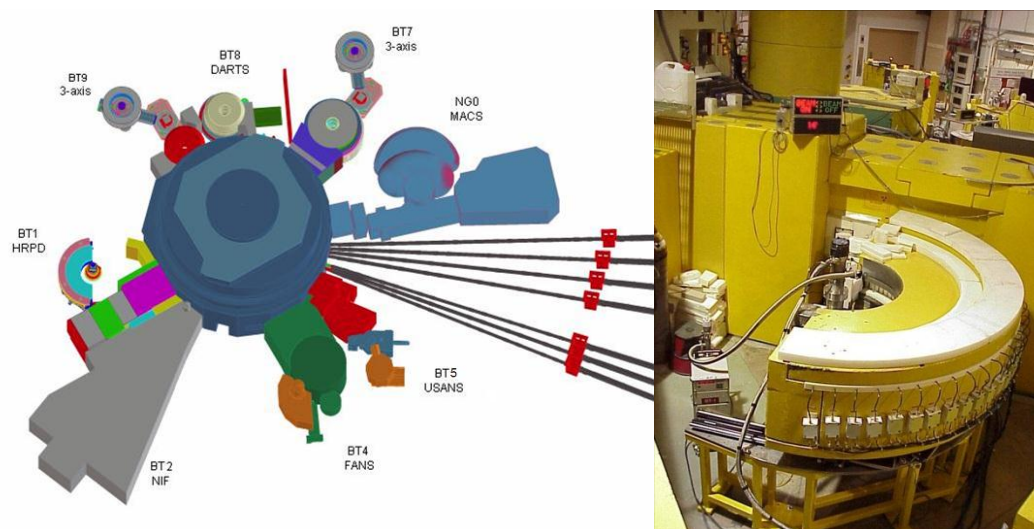


Figure 2.3 Illustration of neutron generator (left) and high resolution powder diffractometer BT-1 [6].

Time of flight is another way to make use of the neutrons. This method uses the entire neutron spectrum with a fixed diffraction angle and a pulsed neutron source is used instead. As neutrons of different wavelength are the radiation resource, the diffracted signals are separated according to the neutrons' time of flight. Bragg's Law is still being obeyed here and in time of flight, diffraction angle is fixed, but θ and d (the d spacing) are the changed accordingly. This method has the advantage of a shorter data collection time. Another good aspect of this one is that it may be applied for studies of short time relaxation phenomena, especially in experiments where samples are subjected to pulsed magnetic fields.

Part of the neutron data in this thesis was collected by this method from Neutron Center of Oak Ridge National Lab. Time-of-flight (TOF) neutron data were collected using the Powgen powder diffractometer at the Spallation Neutron Source (SNS) at Oak Ridge National Laboratory. Samples of about 3.9 g were contained in 10 mm vanadium cans and analyzed over d-spacings 0.6 – 8.3 Å. Constant wavelength neutron data were collected using the BT-1 32-detector high-resolution diffractometer at the NIST Center for Neutron Research at the National Institute of Standards and Technology. A Cu (311) monochromator, which has a takeoff angle of 90°, $\lambda = 1.5401(2)$ Å, was employed. Collimation of 15' of arc was used before the monochromator, 20' before the sample, and 7' before the detectors. The samples were loaded into vanadium containers 15.6 mm in diameter and 50 mm in length. Data were collected at room temperature over a 2θ range of 3-166° with a step size of 0.05°.

Crystal structures were refined by the Rietveld method using the GSAS software package with the EXPGUI Interface [3, 4]. TOF peak-profile function no. 3 (tabulated α , β , and ΔT form) and shifted Chebyshev function were used for modeling the diffraction peaks and background, respectively.

2.3 Quantum Design Physical Property Measurement System

The Physical Property Measurement System (PPMS) built by Quantum Design is a comprehensive instrument which can measure several properties of materials like AC and DC magnetism, DC resistivity and AC transport. The corresponding property

value is recorded as a function of temperature. The system uses liquid helium as cooling agent and thus the measured temperature can be as low as 3K. The PPMS at Oregon State University is equipped with an EverCool liquid helium recycling system, and this essentially allows the instrument to self-replenish liquid helium lost during system venting and regular measurements by use of a condensing unit and external helium gas. This eliminates the need for regular liquid helium transfers.

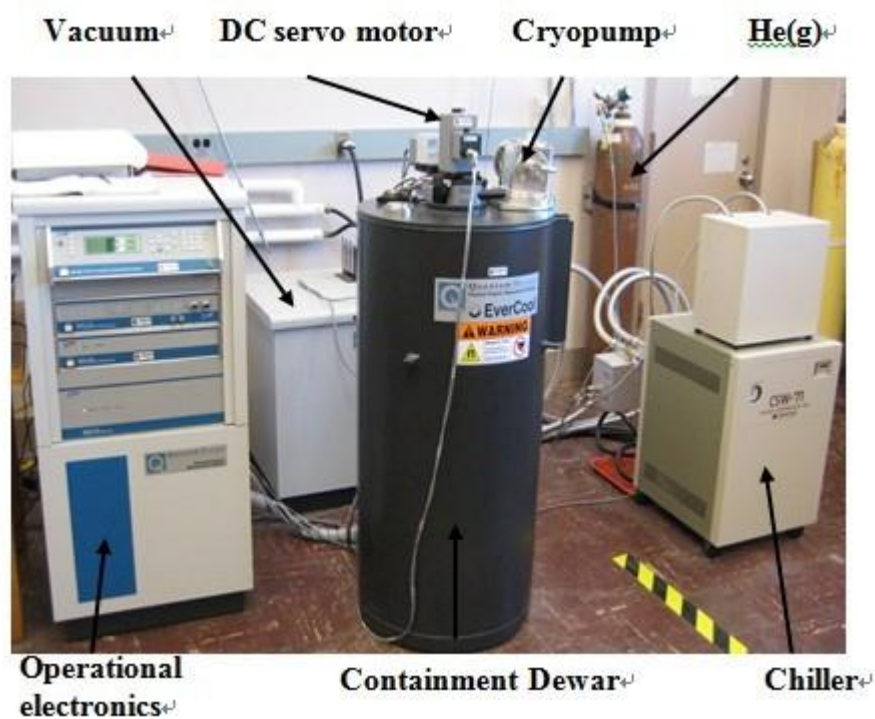


Figure 2.4 Quantum Design Physical Property Measurement System set up for ACMS measurements.

2.3.1 Magnetometry

The AC/DC Magnetometry System (ACMS) is one attachment of the PPMS which measures for AC susceptibility and DC magnetization. All the magnetic

measurements performed in this thesis utilize a technique for DC measurements known as extraction magnetometry. The ACMS coil set, as shown in Figure 2.5, is inserted into the main dewar chamber (shown in Figure 2.4), connected to the instrument through a 12-pin connector at the base of the sample chamber. The sample, held by cotton in a polycarbonate straw is vibrated vertically through the coil set by the DC servo motor. Sample should be fixed at a certain position in the straw as it can affect the measurement process if the sample does not move according to the DC servo motor. Generally, the sample can be measured as a sintered pellet or as a tightly packed powder in a plastic gel. An applied field induces a magnetization in the sample and this signal is detected by the ACMS coil set as an induced voltage. So the amplitude of the voltage signal is related to the magnetic moment and the speed of vertical movement for a given extraction. Although automated, an important aspect of the measurement is the speed in which an extraction is made. A faster speed for an extraction generally results in enhanced signal strength and this will give a more accurate measurement. Another important factor is the samples location with respect to the detection coils. Thus, it is necessary to locate the sample using a single point DC extraction. This allows the instrument to correct for the sample displacement when the DC servo motor is engaged. If the sample has not been centered, the operator runs the risk of inaccurate magnetization measurements. Generally the AC excitation location is more accurate as there is better resolution, but it is recommended to locate the sample using the method employed for actual measurements [7].

An applied field is necessary for DC magnetization measurements. The PPMS at Oregon State University utilizes a superconducting magnet capable of providing magnetic fields as high as 7 Tesla, but an applied field of 0.1 – 1 Tesla is generally sufficient for temperature dependent measurements. It should be noted that if attempting to determine the effective moment, Curie constant and transition temperatures through the Curie-Weiss relationship, a sufficient temperature range above any transition temperature is required. This temperature range would be overlaid into the paramagnetic region. Thus, it is necessary to have some insight into the potential magnetic interactions present for a sample, and may require several measurement runs to resolve temperature discrepancies.

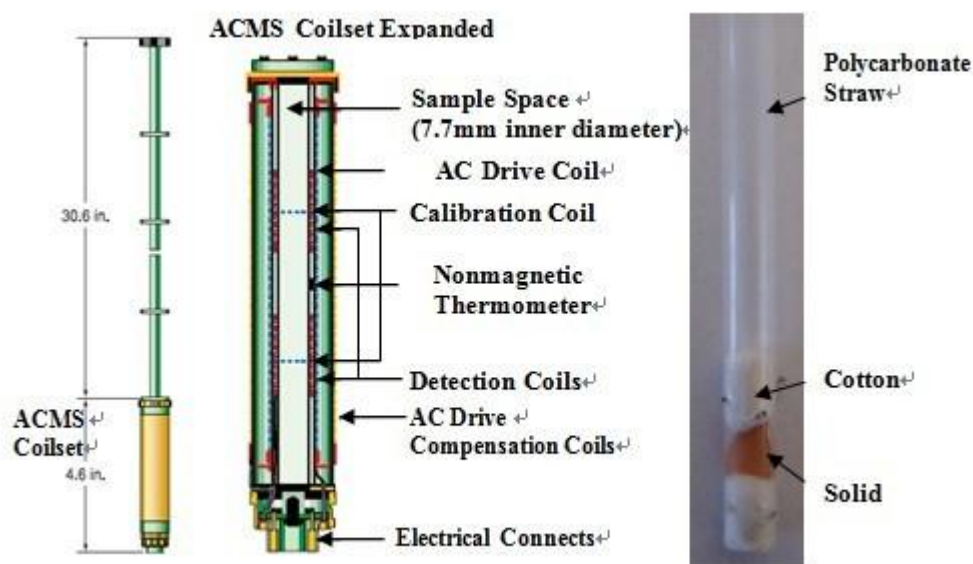


Figure 2.5 Representation of the ACMS coil set and tube assemblage (left), expanded view with labels of the ACMS coil set detection unit (center), and mounted 'as prepared' sample (right). ACMS coil set illustrations taken and modified from Quantum Design application notes [8]

2.3.2 DC Electrical Resistivity

Electrical resistivity is a very useful bulk physical property because it is very sensitive to variations from structural distortions, bond angles and magnetic/structural transitions. Electrical resistivity provides unique insight into the mechanisms present in various samples.

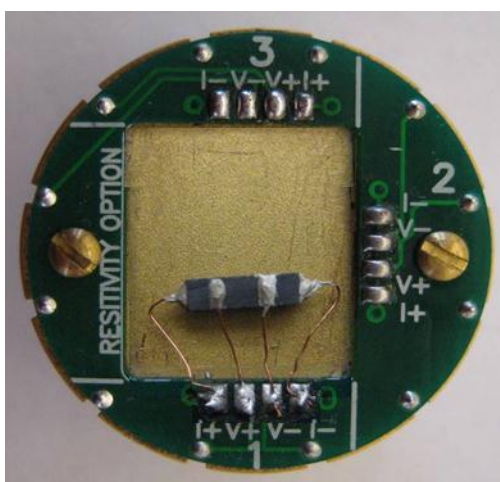


Figure 2.6 PPMS resistivity puck with a bar sample connected to position 1 using the four probe contact technique. Notice the labeled voltage and current contacts.

The PPMS can be easily set up to perform DC resistivity measurements. The resistivity puck (shown in Figure 2.7) uses the same 12-pin connector at the base of the sample chamber as that used for a connection to the ACMS coil set mentioned previously (shown in Figure 2.8). The PPMS resistivity puck is able to measure four probe resistivity on 3 samples independently at the same time. There are two techniques in resistivity measurement: two probe resistivity technique and four probe technique. Four probe resistivity is normally employed when the sample resistivity is less than $10 \text{ } \Omega\text{-cm}$. This method has one advantage because there is no contact

resistance. As the voltage leads and current leads are separated, the contribution of the lead wire and contact resistance are removed. Samples with resistivity above $\rho = 10 \text{ } \Omega\text{-cm}$ can be measured by the two probe technique where the contact and lead wire resistance will affect much on the total resistivity. For samples measured in the PPMS, the four probe technique is the only option. Bar sample with known dimension is ideal and is attached to the resistivity puck by. As shown in Figure 2.7, four contact wires are attached to the sample bar of known dimension by means of silver paste or silver epoxy. When sample are irregularly shaped, or cannot be fashioned into bars, the van der Pauw method can be used in which there are no restrictions on the size or shape of the sample.

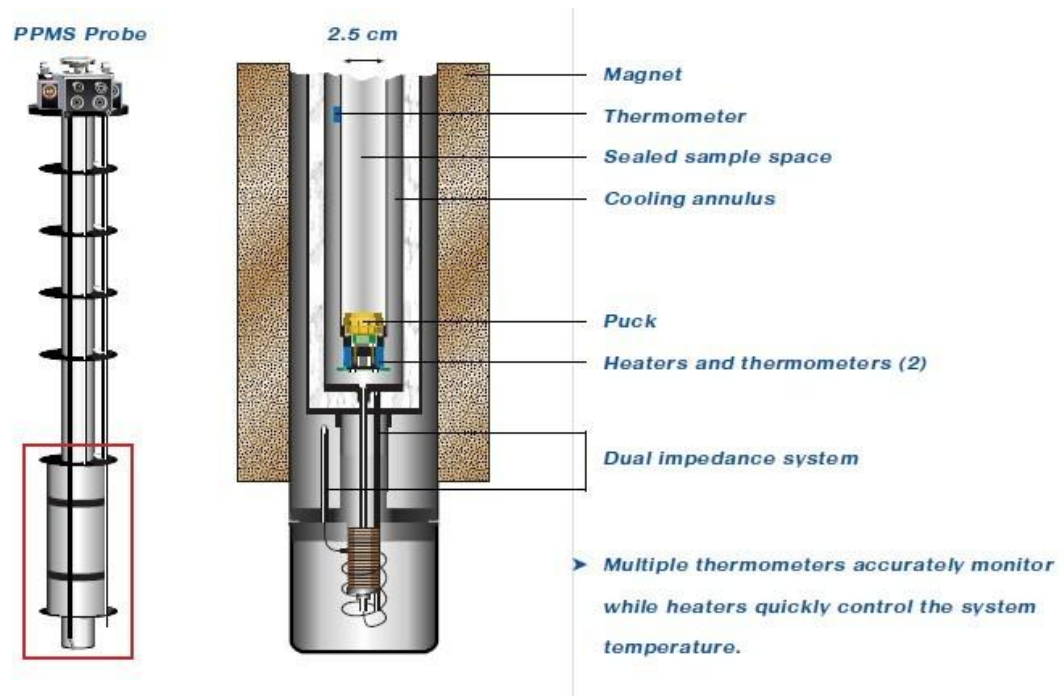


Figure 2.7 Representation of DC electrical resistivity tube assemblage (left) and detail (right) [9].

2.4 Optical measurements

Optical properties were measured in Dr. Janet Tate's group in Department of Physics, OSU. The fiber optics system was used to collect the diffuse reflectance spectrum in the UV-visible region. In this method, light from a light source is passed through a bifurcated (Y-shaped) optical fiber assembly onto the sample, and back into the bifurcate optical fiber (Figure 2.7 (b) inset center white circle) where it is taken to a spectrophotometer [10]. This process is illustrated in figure 2.8 (a). White and black reference must be taken before the measurement. Black paper was used for black reference; MgO or BaSO₄ is always selected for light reference and is also used to coat the inside of the integrating spheres. The Kubelka-Munk function was used to convert reflectance data collected to absorbance value [11]. The plotted absorbance as a function of electron volts, eV, or wavelength, nm, gives a characteristic pattern which is generally dependent on the electron occupation of orbitals and can provide approximate band gap magnitudes. This can give a great deal of insight into the electronic properties and reinforce electrical resistivity assessments.

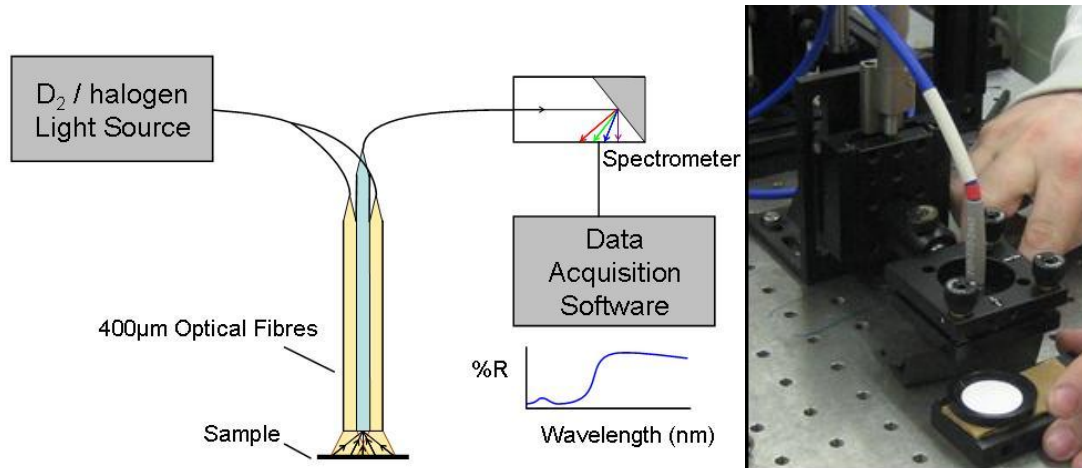


Figure 2.8 Illustration of fiber optics system used in diffuse reflectance measurements (a) and light source on white reference BaSO_4 (b).

2.5 Thermogravimetric analysis (TGA)

Thermogravimetric analysis (TGA) is one of the main thermal analysis techniques. It records the weight of a sample as a function of temperature or time. The phase transition or sample decomposition can be observed from the TGA chart record. The method has wide application in research of determination of degradation temperature of polymers, percentage of absorbed moisture of the sample, etc.

The instrument used for TGA data collection is Metler Toledo TGA 850. The instrument consists of a precise balance and a pan made of platinum to hold the aluminum crucible. Small amount of sample (~30-50 mg) is put into the crucible and a tube furnace outside the platinum pan is used to provide the desired temperature. An accurate thermocouple is also equipped to give the temperature. And all the parts are working under the control of computer program. The sample's mass is constantly

weighed as the sample is heated at a standard rate in a selected atmosphere. The resulting data can then be plotted as a weight percent or mass loss versus temperature.

2.6 Mössbauer spectroscopy

Mössbauer spectroscopy is employed to study the electron clouds surrounding the nuclei (i.e. valance and coordination) of some elements like Fe. The technique is based on Mössbauer effect, which can be interpreted as the gamma fluorescence without recoil.

Electrons in the nuclei in the atoms will move to different energy levels due to excitation and relaxation and this process is always associated with absorption or emission of gamma rays. The energy level is under influence of the electronic and magnetic surrounding environment of the atom. Thus by observing resonance-fluoresce signal from this process, information about atom's the local environment will be obtained. However, two major obstacles make this process not easy to be observed: firstly, the recoil of the nucleus accompanied to the absorption and emission of gamma ray shadowed the resonance; secondly, the interaction between the nucleus and its environment is too small [12]. Mössbauer [13] found that below certain temperature, the recoil energy of the nucleus in a solid will be small enough to prevent the lattice from recoil. For the second obstacle, the element's average halftime of the excited state before it decays should be examined because the limiting resolution is the nature line width of the excited nuclear states. So not all the elements in the periodic

table will produce observable resonance, only some elements like Fe (which has excitation gamma ray of 14.4 KeV) is applicable in Mössbauer Spectroscopy.

H																	He
Li	Be											B	C	N	O	F	Ne
Na	Mg											Al	Si	P	S	Cl	Ar
K	Ca	Sc	Ti	V	Cr	Mn	Fe	Co	Ni	Cu	Zn	Ga	Ge	As	Se	Br	Kr
Rb	Sr	Y	Zr	Nb	Mo	Tc	Ru	Rh	Pd	Ag	Cd	In	Sn	Sb	Te	I	Xe
Cs	Ba	La	Hf	Ta	W	Re	Os	Ir	Pt	Au	Hg	Tl	Pb	Bi	Po	At	Rn
Fr	Ra	Ac															
			Ce	Pr	Nd	Pm	Sm	Eu	Gd	Tb	Dy	Ho	Er	Tm	Yb	Lu	
			Th	Pa	U	Np	Pu	Am	Cm	Bk	Cf	Es	Fm	Md	No	Lr	

Figure 2.9 Elements of the periodic table which have known Mössbauer isotopes (shown in red font). Elements which are used the most are shaded with black [12].

When Mössbauer effect is applied to solids chemistry, balancing the effect of a different environment by a relative shift in the source and absorbing sample is essential to reestablish the resonance [14]. Doppler-Fizeau effect brings a change in the frequency difference which will enlarge the hyperfine interaction between the gamma ray and solid matrix. So oscillating radiation resource is used in Mössbauer spectroscopy and by this way, small increment in gamma ray energy is achievable. When the modulated gamma ray energy matches energy transition in the atom, a peak will show up in the spectrum. A typical spectrum with identical source and absorber is given below.

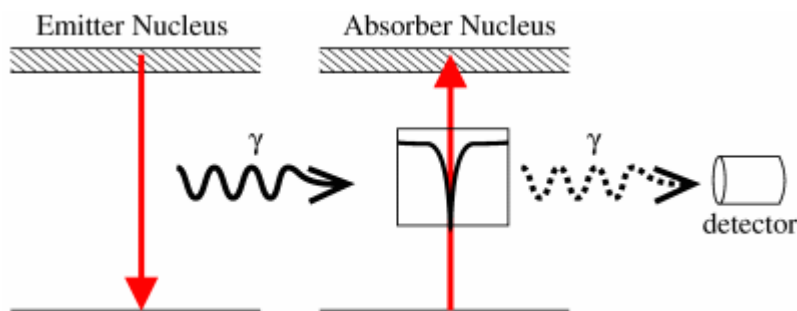


Figure 2.10 Simple Mössbauer spectrum from identical source and absorber [12].

The energy levels in the nuclei in the sample are modified by the environment in three ways: the Isomer Shift, Quadrupole Splitting and Magnetic splitting. The isomer shift is due to the non-zero volume of the nucleus and the electrons within. This gives rise to a Columbic interaction and the energy levels will change accordingly. The isomer shift is measured on the same scale for Fe nucleus in different solids and the value is fixed for different Fe oxidation states. If the nucleus is in the state which has angular momentum quantum number higher than $1/2$, it will have a non-spherical charge distribution. In the presence of an asymmetrical electric field, this splits the nuclear energy levels. Quadrupole splitting is rooted here. And magnetic splitting reflects the interaction between the nucleus and surrounding magnetic field. In the presence of a magnetic field, a nucleus with quantum number I will split into $2I+1$ sub-levels. And this leads to different amount of transition energy and different peaks on the spectrum [15]. Normally, the compound can be analyzed by comparison with known spectra. Additionally, the relative intensities of different peaks can be compared and used for semi-quantitative calculation. The effect of three shifts is shown below.

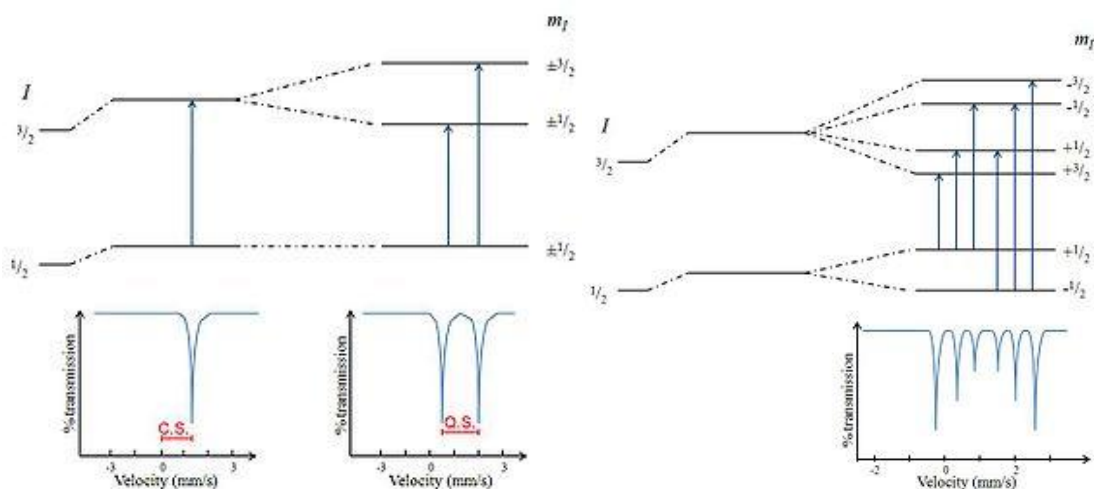


Figure 2.11 Isomer shift (a), quadrupole splitting (b) and magnetic splitting (c) of the nucleus energy levels and the corresponding Mössbauer spectrum [15].

Mössbauer measurements in this thesis were performed with a constant acceleration Halder - type spectrometer using Co^{57} source (Rh matrix) in the transmission geometry at room temperature. The polycrystalline absorbers Containing about $10\text{mg}/\text{cm}^2$ of iron were used to avoid the experimental widening of the peaks. The velocity was calibrated using pure iron metal as the standard material.

The samples were prepared from the finely ground powder. The sample holder assembly is constituted by a waterproof nylon. The powders are inserted in the sample holder. The spectra were recorded from 4.2 K to 293 K.

A first method of calculation was used to adjust the spectra using Lorentzian profile lines. The position, amplitude and width of each line are parameters that can be refined. This first approach allows us to deduce the experimental hyperfine parameters of iron sites.

A second method of calculation was used to strip the spectra in terms of distribution of hyperfine parameters $P(\Delta)$ and $P(B)$ by the method of Hesse and Rubartsch [16]. This method is often used for disordered compounds in which there is a wide distribution of possible environments that results in the experimental spectrum by lines of large width and the shape can deviate from a Lorentzian profile [17].

2.7 References

1. B. Lamp. "Instrumental Analysis." Truman State University. http://www2.truman.edu/~blamp/chem322/pdf/chapter%201%20_9-3%20corrections_.pdf. Accessed May 2010.
2. Anthony R. West, *Solid State Chemistry and Its Applications*, John Wiley & Sons, New York, 1984.
3. A.C. Larson, R.B. Von Dreele, "*General Structure Analysis System (GSAS)*," Los Alamos National Laboratory Report LAUR 86-784, 2004.
4. B.H. Toby, EXPGUI, a graphical user interface for GSAS, *J. Appl. Cryst.* 34, 210, 2001.
5. B.D. Cullity, S.R. Stock. *Elements of X-Ray Diffraction*, 3rd edition; Prentice Hall; New Jersey, 2001.
6. NIST Center of Neutron Research, <http://www.ncnr.nist.gov/instruments/bt1/>.
7. A.E. Smith, Ph.D. thesis, Oregon State University, 2010.
8. Quantum Design. *Physical Property Measurement System Hardware and Operations Manual*, 2nd Edition, Quantum Design, 1999.
9. Quantum Design. <http://www.qdusa.com/products/ppms.html>.
10. R. Kykyneshi. M.S. Thesis, Oregon State University, Corvallis, OR, 2004.
11. M. El. Sherif, O. A. Bayoumi, T. Z. N. Sokkar, *Color Res. App.* 22, 32, 1997.
12. Introduction to Mössbauer Spectroscopy: Part 1. *Royal Soc. Chem.* www.rsc.org.
13. R. L. Mössbauer, *Z. Phys.* 151, 124, 1958.
14. J. P. Suchet, *Crystal Chemistry and Semiconduction in Transition Metal Binary Compounds*, Academic Press, New York and London, 1971.
15. http://en.wikipedia.org/wiki/Mossbauer_spectroscopy.
16. J. Hesse and A. Rubartsch, *J. Phys. E. Sci. instrum.*, 7, 526, 1974.
17. A. Wattaix, private conversation.

Chapter 3

Structure and Physical Properties of $YM_{1-x}Fe_xO_3$ Hexagonal Structure System (Mn = In, Al)

Abstract

Solid solution $YIn_{1-x}Fe_xO_3$ ($x \leq 0.3$, $x \geq 0.7$) and $YAl_{1-x}Fe_xO_3$ ($x \leq 0.4$, $x \geq 0.7$) were successfully prepared by solid state reaction or sol-gel method. Based on both X-ray diffraction data and neutron diffraction data, it was determined that all of the compounds involved exhibited hexagonal structure. The surface texture, structural, magnetic, optical properties were examined.

In solid solution $YIn_{1-x}Fe_xO_3$, bright color was observed from all single phase compounds. The color of $YInO_3$ is pale white. However, small amount of Fe tuned the color to yellow, bright orange, dark red. And finally the color changed to brown color which is shown by the other end member $YFeO_3$. X-ray and neutron diffraction data agreed with the conclusion that the space group of the compounds in this solid solution is $P6_3cm$, which has the ferrielectric structure same as $YInO_3$. The morphology of the compounds was studied by SEM and a clear difference of particle size and surface texture was observed from the SEM images. The compounds showed paramagnetic behavior in the measured temperature range. The Curie-Weiss fit was done for the plot of inverse magnetic susceptibility vs. temperature and magnetic moment of Fe was calculated and compared with different oxidation states. The Fe in this solid solution was confirmed to be Fe^{3+} in high spin state. This was proved by Reitveld refinement and Mössbauer spectroscopy.

The solid solution $\text{YAl}_{1-x}\text{Fe}_x\text{O}_3$ was investigated utilizing structural, optical and magnetic characterizations. A structure transition was observed from X-ray diffraction data. The structure of the Al-rich side phases was ferroelectric structure with space group $\text{P6}_3/\text{mmc}$ while the Fe-rich side phases showed ferrielectric structure with space group $\text{P6}_3\text{cm}$. The color of the phases changed from white (YAlO_3) to yellow and brown (YFeO_3) as the Fe content increased. The increase in the cell volume accompanied with the elevation of Fe component. Magnetic data showed that all the compounds behaved paramagnetically. And Fe^{3+} high spin is confirmed from the Curie-Weiss fit.

3.1 Introduction

AMO₃-type transition metal oxide is an important class of materials and has interesting technical value in many device applications. These oxides display a variety of physical properties of great technical importance such as ferroelectricity, antiferroelectricity, piezoelectricity, insulating behavior, semiconductivity, metallic conductivity, superconductivity etc [1-4]. Different A and M cations can be situated in the AMO₃-type oxides and various structures exist. The biggest and most attractive family is the relatively simple structure of the mineral perovskite (CaTiO₃) with a cubic cell ideally (structure shown in Figure 3.1). The perovskite structure is based on close-packed AO₃ layers with all available octahedral sites filled with M cations. Distortion from the ideal structure is defined by the tolerance factor (t) by Goldshmidt [5]. The radii r_A and r_B are the crucial factor for the structure determination as shown in the expression of tolerance factor: $(r_A + r_O)/\sqrt{2}(r_B + r_O)$. The tolerance factor of ideal perovskite oxide is 1, and different structure appears when the tolerance factor is shifted. GdFeO₃-type structures are found when t is less than unity while polytypic structures are observed when t is greater than unity [6]. More complex structures such as ilmenite, pyrochlore are also found in some oxides. If the basic built-up arrangement of the anions is hexagonal instead of cubic, another category of structure is formed and is known as hexagonal.

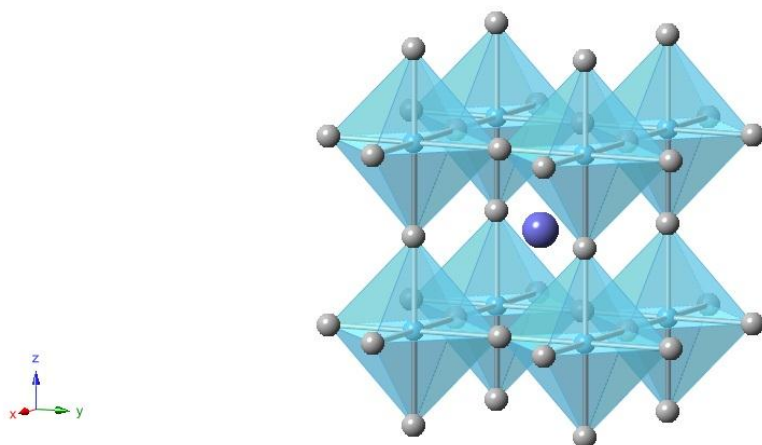


Figure 3.1 The cubic structure for ABO_3 perovskite oxide. Blue spheres are A cations, light blue spheres are M cations, grey spheres are O^{2-} anions.

Hexagonal is another structure exhibited by relatively rare number of ABO_3 -type oxides. The structure is based on hexagonal close packed unit cell. It can be considered as close-packed O layers with a ABACBCA sequence. The A cations occupy all octahedral sites between CA and AC layers, and this site is strongly distorted to a trigonal-antiprismatic coordination. The M cations reside within the BO layers and have a trigonal-bipyramidal coordination. This hexagonal structure is only known for trivalent A cations, which may be In or a small rare earth (Gd to Sc).

The prediction of structures of ABO_3 compounds has been the focus of study and several approaches such as ionic radii and bond ionicities have been discussed and compared [7, 8]. Generally, the ionic radii of A and M cation can be used to justify whether the structure belongs to perovskite or not (shown in Figure 3.2). However, the occurrence of hexagonal phase is not always predictable.

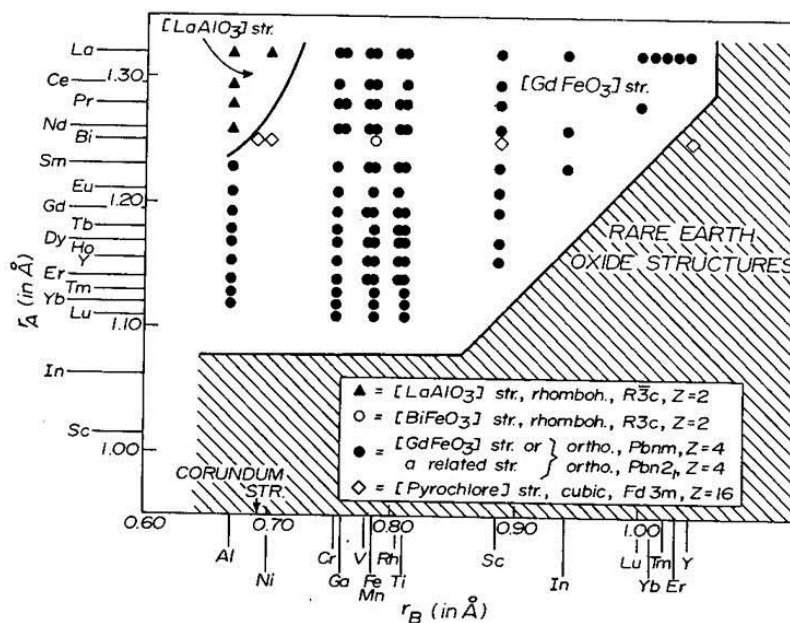


Figure 3.2 Structure field map of $A^{3+}B^{3+}O_3$ perovskite.

For some compounds like $AMnO_3$ group, both hexagonal and perovskite structure existed [9, 10]. For the larger A cation, perovskite phase is more stable than hexagonal phases. Change in physical conditions (e.g. high pressure, temperature, etc.) normally resulted in the phase transition from hexagonal into perovskite in this case. For smaller A cations such as $YMnO_3$, hexagonal phase came as the most stable phase which is achieved by simple solid state reaction in ambient synthesis condition. The general trend of $AMnO_3$ with Ln^{3+} is summarized in figure 3.3. Compounds shown perovskite phase as the most stable phase are indicated with orange color whereas hexagonal compounds are indicated in blue color.

$A =$

58 Ce	59 Pr	60 Nd	61 Pm	62 Sm	63 Eu	64 Gd	65 Tb	66 Dy	67 Ho	68 Er	69 Tm	70 Yb	71 Lu
57 La									39 Y				

Figure 3.3 Summary of $AMnO_3$ phases with Ln^{3+} as A cation.

It is reported that the M cation can be Al, Ga, In, Mn, Fe, 1:1 Cu/Ti, 2:1 Cu/V, or 3:1 Cu/Mo [11-18]. Among these cations, hexagonal $AMnO_3$ compounds have been of interest as multiferroics because these compounds are ferroelectric and magnetically ordered [19]. The ferroelectric Curie temperatures for these hexagonal $AMnO_3$ compounds are usually about 700°C. The ferroelectric version of the hexagonal $AMnO_3$ structure is shown in Figure. 3.4.

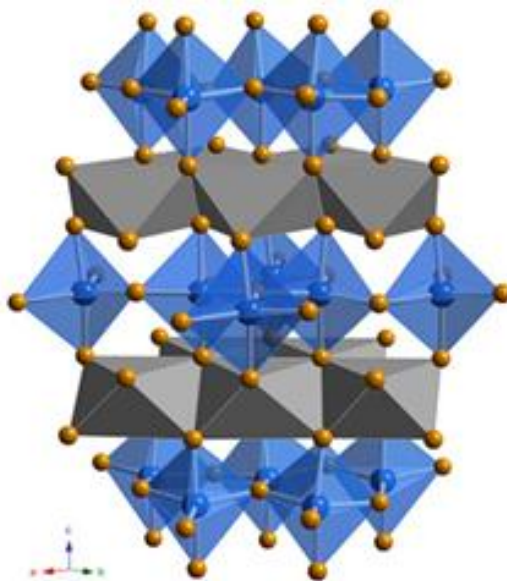


Figure 3.4 Hexagonal $YMnO_3$ powders with ferroelectric structure (Y: blue spheres; Mn: dark yellow spheres; O: turquoise spheres)

The solid solution of YInO_3 - YMnO_3 and other closely related systems has been reported to exhibit brilliant blue color with some compositions [20, 21]. Similar studies have been conducted on the hexagonal $\text{YCu}_{0.5}\text{Ti}_{0.5}\text{O}_3$ systems with substitutions on the Cu/Ti trigonal bipyramidal sites [21]. All these works have prompted us to look into solid solutions between the known hexagonal compounds. Investigation in YMO_3 ($\text{M}=\text{Ga}, \text{Mn}, \text{In}, \text{Fe}$) systems were first taken into consideration. Figure 3.5 showed the relationship of different ions and the ionic radii. Generally Ga, Mn, In and Fe are staying on the trend line (Al is removed from the figure because of the giant ionic radius difference compared to the others). Solid solution of $\text{YMn}_{1-x}\text{Fe}_x\text{O}_3$, $\text{YIn}_{1-x}\text{Mn}_x\text{O}_3$ has been studied thoroughly [23, 20]. However, study on $\text{YIn}_{1-x}\text{Fe}_x\text{O}_3$ and $\text{YAl}_{1-x}\text{Fe}_x\text{O}_3$ was never reported before. The research of this work focused on study into these systems will fulfill the phase diagram of all the YMO_3 compounds.

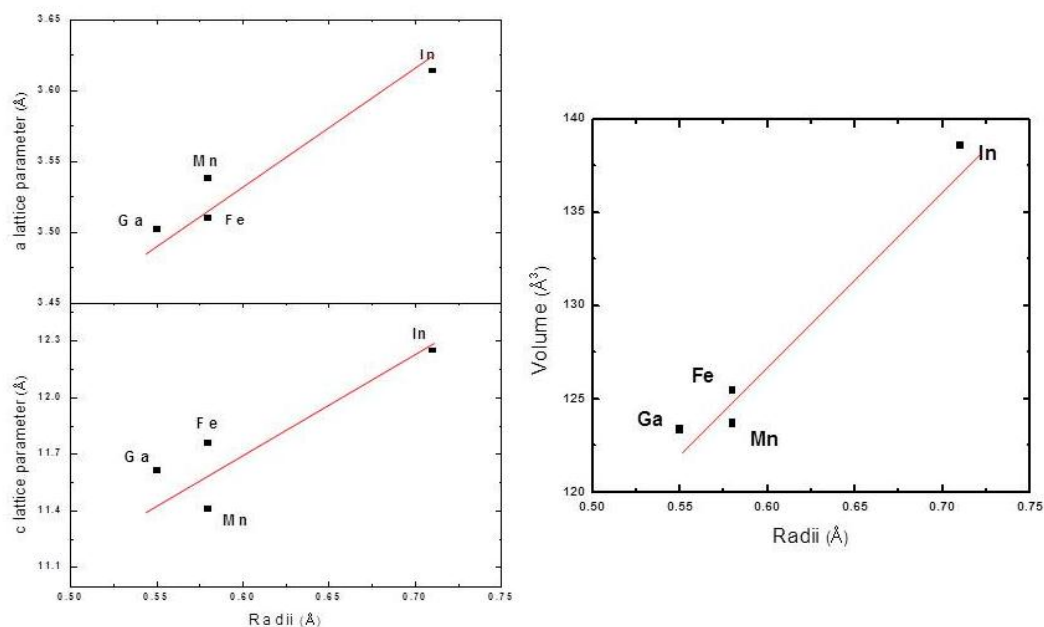


Figure 3.5 Lattice parameter versus radii in YMO_3 group ($\text{M}=\text{Fe}, \text{In}, \text{Ga}, \text{Mn}$).

3.2 Hexagonal $\text{YIn}_{1-x}\text{Fe}_x\text{O}_3$ phases: Structural, Optical, and Magnetic Studies

3.2.1 Introduction

YInO_3 was first reported by Kruger in 1976 and has the hexagonal LuMnO_3 type structure. The structure transformed to cubic structure at temperature above 1000 °C. The In^{3+} is located in the five-fold trigonal bipyramidal site and Y^{3+} is in the seven-fold coordination [24]. The structure bears a ferroelectric transition when the temperature varies and the space group changes from $\text{P6}_3\text{cm}$ to $\text{P6}_3/\text{mmc}$ which is similar to YGaO_3 . Structures with both space groups were shown in figure 3.6. In the paraelectric structure, Y atoms are situated in the inversion center and the coordination of O to Y forms a trigonal antiprism. In atoms are surrounded by five O atoms and the coordination is trigonal bipyramid. The O atoms move a lot along the c axis when paraelectric YInO_3 transformed to ferrielectric structure. The Y-O bond distance is no longer uniform and the coordination of Y increases to 7. Hexagonal structure is maintained in this transition. But the cell edge a is enlarged and cell volume is 3 times larger in $\text{P6}_3\text{cm}$ due to the absence of inversion center [25].

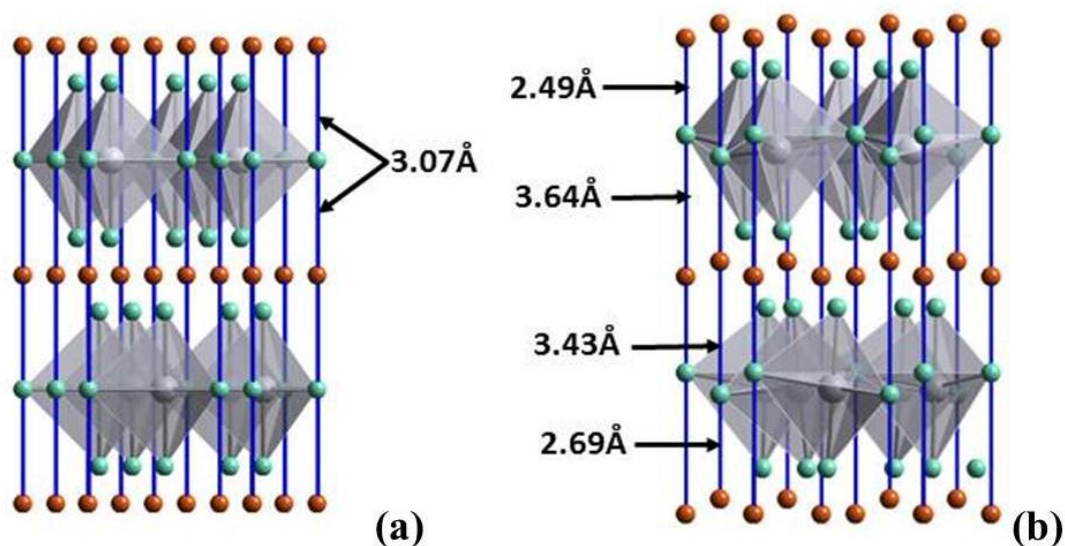


Figure 3.6 Illustration of the structure of YInO_3 with space group $P6_3/mmc$ (a) and $P6_3cm$ (b). O is shown in red sphere and Y is turquoise sphere. And In which is indicated in grey spheres is in the center of the grey trigonal bipyramid [reproduction of reference 25].

YFeO_3 existed in both perovskite and hexagonal structures, depending on the synthesis conditions [26, 27]. And it has the preference of perovskite over hexagonal phases as when the temperature is elevated, hexagonal structure will transform to perovskite structure. The reported hexagonal phase was synthesized by either hydrolysis of yttrium and iron double alkoxides or sol-gel processing. Very few papers were found regarding the structure of hexagonal phase YFeO_3 . X-ray diffraction and neutron diffraction analysis were served as the method of characterization. YMnO_3 (high temperature phase) with space group $P6_3/mmc$, and polar YMnO_3 (low temperature phase) with space group $P6_3cm$ were both used as model in neutron refinement. However, the difference was not obvious and further investigation need to be done to explore the structure of YFeO_3 [28].

Solid solution between YFeO_3 and YInO_3 is never reported and worth investigated because both of the end members can be stabilized as hexagonal structure. It will be interesting to investigate the structures as well as magnetic behavior. The discovery of blue pigment uncovered the truth that Mn^{3+} in five-fold trigonal bipyramidal coordination will give rise to bright color. Thus, other rare earth ions in TBP coordination may also show interesting colors.

3.2.2 Synthesis

A solid state method was used to prepare the In-rich $\text{YIn}_{1-x}\text{Fe}_x\text{O}_3$ phases. Reactants were Fe_2O_3 (JMC, $\geq 99.999\%$), In_2O_3 (Alfa, $\geq 99.99\%$), and Y_2O_3 (Research Chemicals, $\geq 99.99\%$). Appropriate quantities were mixed by grinding together in an agate mortar. The powder mixtures were then pressed into pellets. These were heated for 12 hours at 1200°C in air, reground and pelletized again, and finally heated at 1300°C in air for another 12 hours. Perovskite YFeO_3 was prepared by a similar solid state method, but with a final heating at 1500°C for 3 hours.

The Fe-rich $\text{YIn}_{1-x}\text{Fe}_x\text{O}_3$ phases were prepared starting with solutions. The reactants were $\text{Y}(\text{NO}_3)_3 \cdot 6\text{H}_2\text{O}$ (Alfa Aesar, $\geq 99.9\%$), $\text{In}(\text{NO}_3)_3 \cdot 3\text{H}_2\text{O}$ (Alfa Aesar, $\geq 99.99\%$) and $\text{Fe}(\text{NO}_3)_3 \cdot 9\text{H}_2\text{O}$ (Aldrich, $\geq 99.99\%$). Appropriate quantities were dissolved in deionized water. The orange colored solution was heated to 60°C , and citric acid (Mallinckrodt) was added to the solution in a molar ratio of 2:1 citric acid to Y. The pH of the solution was then adjusted to 7 using aqueous $\text{NH}_3 \cdot \text{H}_2\text{O}$. After

heating for several hours at 90 °C a viscous green gel formed. This gel was heated at 250 °C for 2 hours. The dark brown powder obtained was then ground and heated at 700 °C in air for 18 hours. An additional 20 hours of heating was necessary for the sample with $x = 0.7$.

3.2.3 Result and discussion

The hexagonal YInO_3 phase can be achieved by solid state reaction. However, the preparation of the other end member YFeO_3 is quite different as hexagonal is metastable phase compared to perovskite phase. In the Y-Fe-O group compounds, several structures can be found such as perovskite YFeO_3 (o- YFeO_3), $\text{Y}_3\text{Fe}_5\text{O}_{12}$ (garnet: YIG), and metastable hexagonal YFeO_3 (h- YFeO_3) [29]. Among these compounds, $\text{Y}_3\text{Fe}_5\text{O}_{12}$ was studied most intensively for its superior magnetic properties [30]. Perovskite YFeO_3 was also attractive as a potential material for catalysts, fuel cells and so on [31]. However, for the hexagonal phase, several methods have been reported to successfully synthesize the hexagonal YFeO_3 [28, 32, 33]. The low temperature route is selected to avoid the the ease of impurity formation. Our attempts used the sol-gel route utilizing citric acid as the chelating reagent. Sol-gel method was normally employed to stabilize the metastable phases. As the precursor was prepared by solution, the particle size is relatively smaller compared to conventional solid state approach. Thus this method has the advantage of greater surface area as well as reactivity. Generally the synthesis temperature can be lowered

by this approach. After the precursor was prepared, it went through thermal gravimetric analysis to study the proper reaction temperature. Figure 3.7 illustrated the TGA data of YFeO_3 precursor. When the temperature reached to 700°C - 750°C , a weight loss was observed which indicated the formation of h-YFeO_3 . After that, the drop of weight became mild and the powder X-ray diffraction data showed a major phase of perovskite. Different periods were marked in the figure. Thus 700°C was picked up for the synthesis temperature.

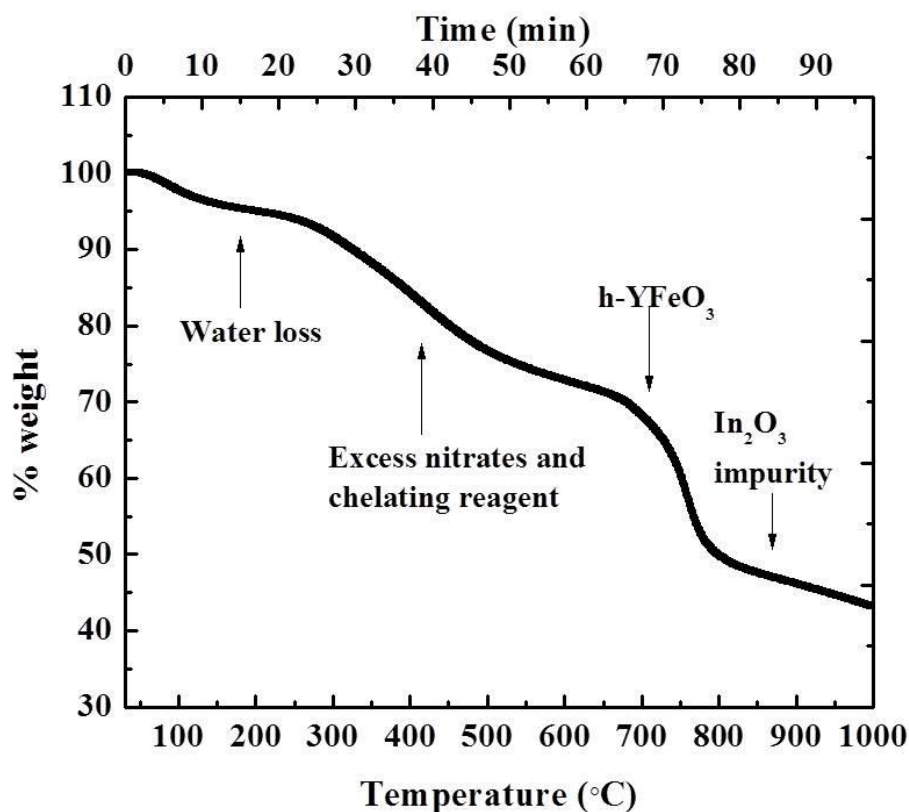


Figure 3.7 Thermal Gravimetric Analysis of YFeO_3 from a dehydrated citrate gel.

The standard solid state synthesis approach was successful for preparing hexagonal $\text{YIn}_{1-x}\text{Fe}_x\text{O}_3$ phases from $x = 0.0$ to 0.3 . The solution route was successful

for $\text{YIn}_{1-x}\text{Fe}_x\text{O}_3$ phases from $x = 0.7$ to 1.0 . Both methods were tried for the compositions in the range between the two ends. However, neither approach was successful for intermediate x values. In_2O_3 impurity peaks with relative high intensity showed up in the sol-gel method. And a coexistence of perovskite and hexagonal phase was observed from the X-ray patterns of samples prepared by solid state approach.

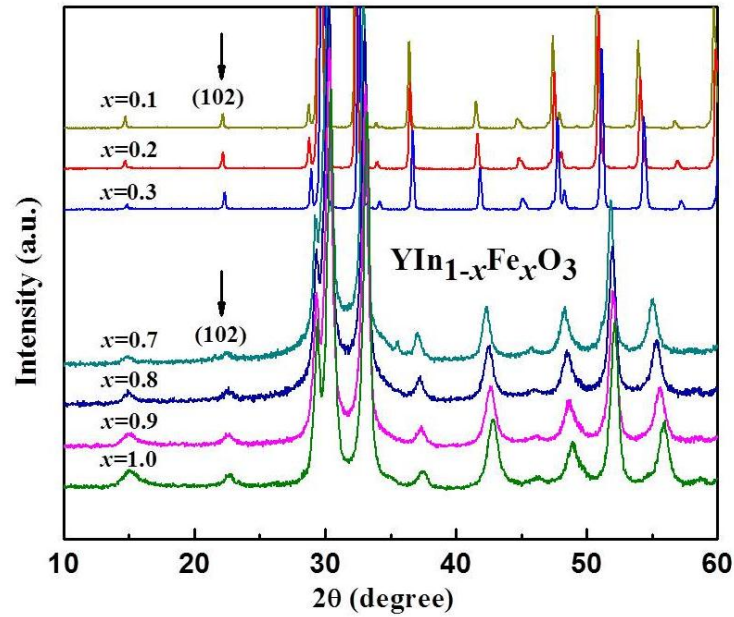


Figure 3.8 XRD patterns of the $\text{YIn}_{1-x}\text{Fe}_x\text{O}_3$ powder samples.

X-ray diffraction patterns of Fe-rich and In-rich $\text{YIn}_{1-x}\text{Fe}_x\text{O}_3$ samples are compared in figure 3.8. The broadening of the peaks for the Fe-rich samples is due to the small crystallite size of about 20 nm. All patterns of both Fe-rich and In-rich $\text{YIn}_{1-x}\text{Fe}_x\text{O}_3$ samples show the superstructure peaks indicative of the ferrielectric structure with space group $\text{P6}_3\text{cm}$ which is shown in figure 3.9.

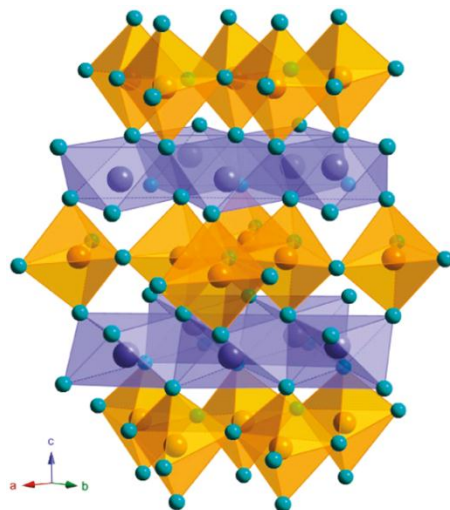


Figure 3.9 Hexagonal $\text{YIn}_{1-x}\text{Fe}_x\text{O}_3$ powders with ferroelectric structure (Y: blue spheres; In, Fe: dark yellow spheres; O: turquoise spheres).

Another form of hexagonal structure with formula ABO_3 is paraelectric structure which has the space group $\text{P6}_3/\text{mmc}$. Two structures are very similar to each other but the paraelectric structure has a center of symmetry. Thus lattice parameter is smaller ($a \sim 3.7 \text{ \AA}$ and $c \sim 10.7 \text{ \AA}$) compared to that of ferrielectric one ($a \sim 6.1 \text{ \AA}$ and $c \sim 11.4 \text{ \AA}$). The origin of ferrielectricity is the distortion of the BO_5 trigonal bipyramids and the bond distance change along with it. The direction of distortion is able to change and ferrielectricity is observed. The X-ray pattern of the ferrielectric structure exhibits a (102) reflection peak which is absent from the paraelectric structure.

In order to look into the morphology of samples and make comparison between the difference between the two synthesis methods, SEM was employed to get the image at the nanometer scale. The SEM images are illustrated in figure 3.10. $\text{YIn}_{0.1}\text{Fe}_{0.9}\text{O}_3$ represents the samples prepared by sol-gel method whereas $\text{YIn}_{0.9}\text{Fe}_{0.1}\text{O}_3$ is symbolic for samples made by solid state reactions. The different in particle size is

apparent from the image. The particle bears a precipitation from solution and is evenly spread on the gel frame in the sol gel method. And it involves a burnt out of organic chelating reagent. Thus the particle size is much smaller and the surface is more porous.

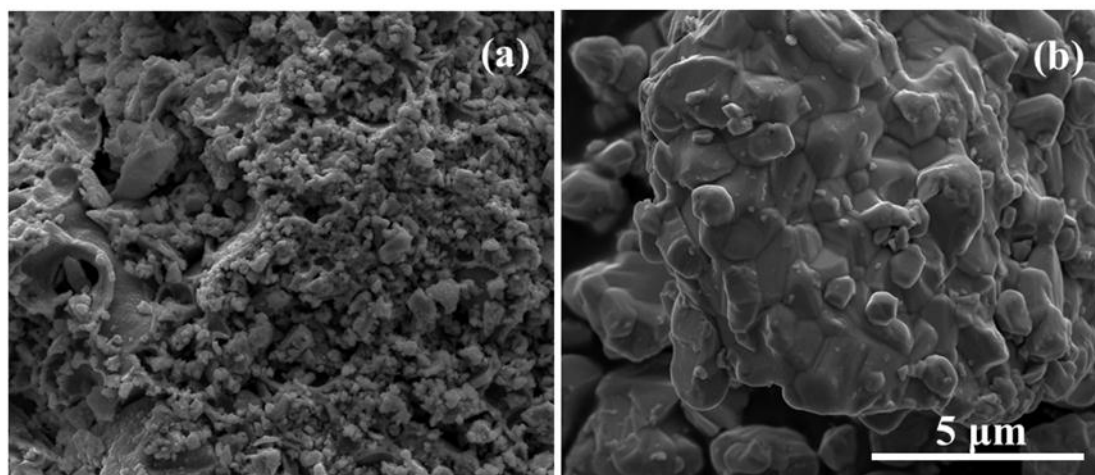


Figure 3.10 Morphology of $\text{YIn}_{1-x}\text{Fe}_x\text{O}_3$ powders by SEM. (a) $x = 0.9$; (b) $x = 0.1$. Scale is the same for a and b .

Neutron diffraction data for hexagonal YFeO_3 had previously been refined for both the ferrielectric and paraelectric structures, but only refined parameters based on the paraelectric form were reported [28]. Both forms gave good fits to the neutron diffraction data, but the X-ray pattern of YFeO_3 (Fig.3.8) clearly shows the (102) peak that arises from the ferrielectric form. Electron diffraction studies of hexagonal RFeO_3 phases ($\text{R} = \text{Eu} - \text{Lu}$) have also confirmed this ferrielectric structure [34].

Neutron data was taken for $\text{YIn}_{0.8}\text{Fe}_{0.2}\text{O}_3$ and $\text{YIn}_{0.2}\text{Fe}_{0.8}\text{O}_3$ samples. And the neutron fit is illustrated in figure 3.11. Our low temperature neutron diffraction

patterns of YFeO_3 show new peaks that can be indexed with the same unit cell used for the room temperature structure, but they violate the space group of the room temperature structure. These new peaks are presumably due to magnetic ordering.

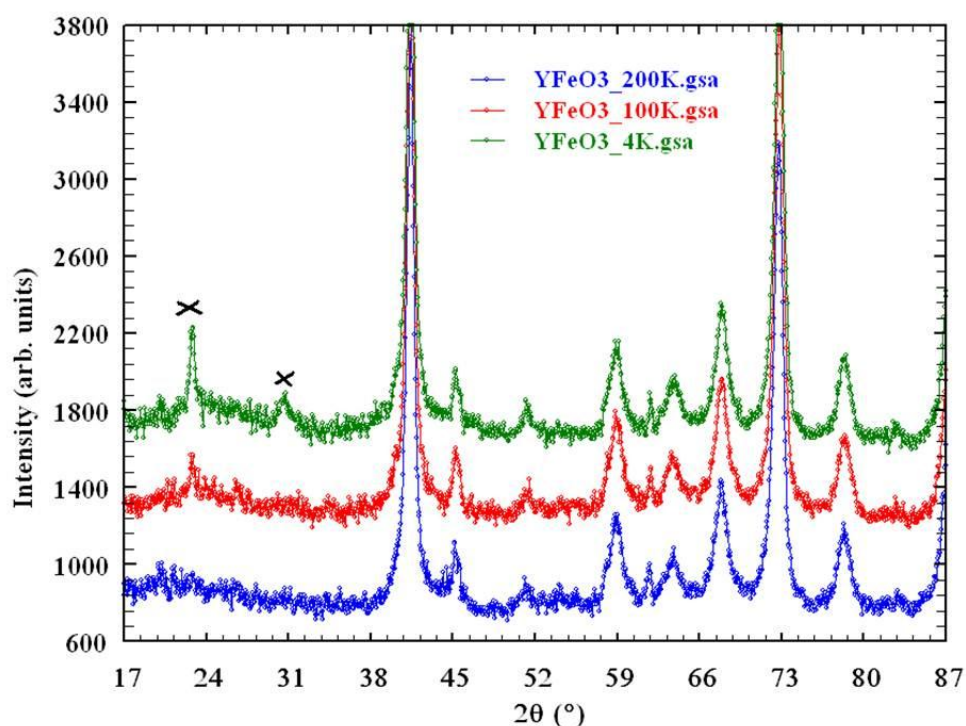


Figure 3.11 Low temperature neutron powder diffraction patterns of YFeO_3 . Peaks due to magnetic ordering are labeled with crosses.

Refinements using GSAS software were done for both X-ray and neutron diffraction data. La Bail method was used to acquire cell edges. The hexagonal unit cell edges vs. x are shown in figure 3.12. The shaded area indicates discontinuity of the lattice parameters due to missing phases with intermediate x values. The refinement results from X-ray and neutron diffraction agreed well with each other. Both a and c cell edges experienced a decrease with the increase of Fe content. This is

due to the smaller ionic radius of Fe (0.58 Å) compared to In (0.8 Å) in the similar coordination [35].

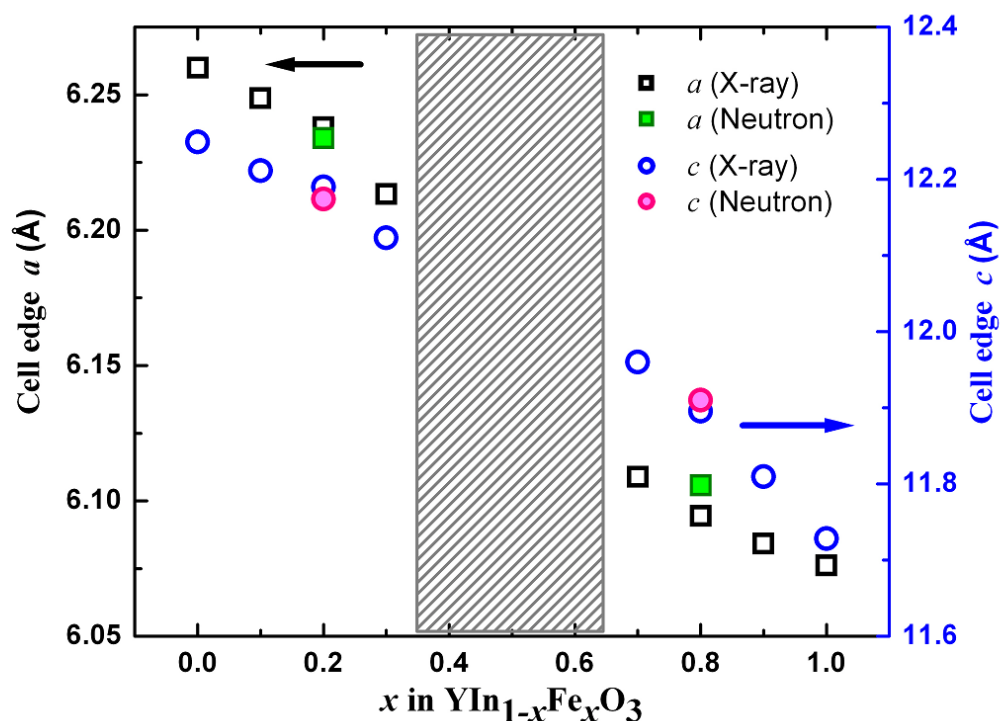
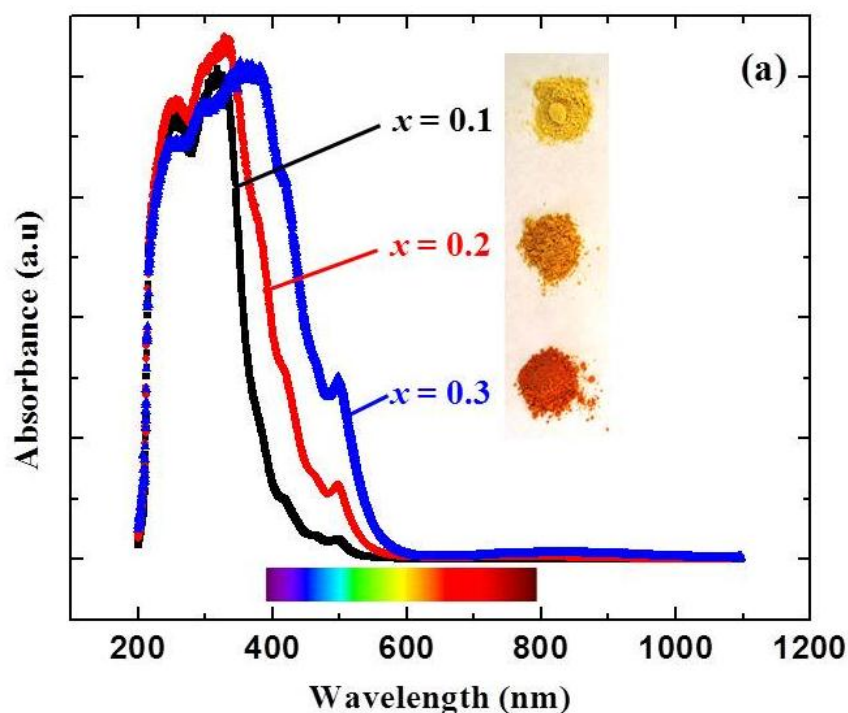


Figure 3.12 Hexagonal lattice parameters vs x in $\text{YIn}_{1-x}\text{Fe}_x\text{O}_3$. Both X-ray (open symbols) and neutron data (solid symbols) are plotted.

All the samples showed interesting bright colors, especially the In-rich side. Diffuse reflectance spectra were taken for all the samples and shown in figure 3.13. Pure YInO_3 reflects all the photons in the visible region and exhibits white color. Small amount of Fe doping creates absorption peak around 550 nm, which is the region of yellow and orange. For Fe-rich side sample, the absorption peaks are further broadened and covers all the visible range and results in a brown color. The colors of oxides containing Fe have been extensively studied, which is in part due to the

widespread use of various iron oxides as pigments [36, 37]. For oxides containing Fe^{3+} there is strong optical absorption in the near UV based on a $\text{Fe}^{3+}\text{-O}^{2-}$ charge transfer transition. This peak typically extends far enough into the visible to give a yellow color. The lower energy $d\text{-}d$ transitions are forbidden, but they become allowed for various reasons. One of the most important reasons is that in solids the d states broaden into bands. Therefore, a $d\text{-}d$ transition is no longer restricted to occurring on one Fe atom. Thus, the $d\text{-}d$ transitions become allowed as d states broaden into bands. This broadening increases as Fe-Fe distances decrease and as Fe concentration increases. In figure 3.2.3.7 we see the impact on color as the Fe concentration increases. For $x = 0.1$ the Fe is so dilute that the color is essentially all due to the $\text{Fe}^{3+}\text{-O}^{2-}$ charge transfer transition. As the Fe concentration increases color derived from the lower energy $d\text{-}d$ transitions becomes increasingly more evident.'



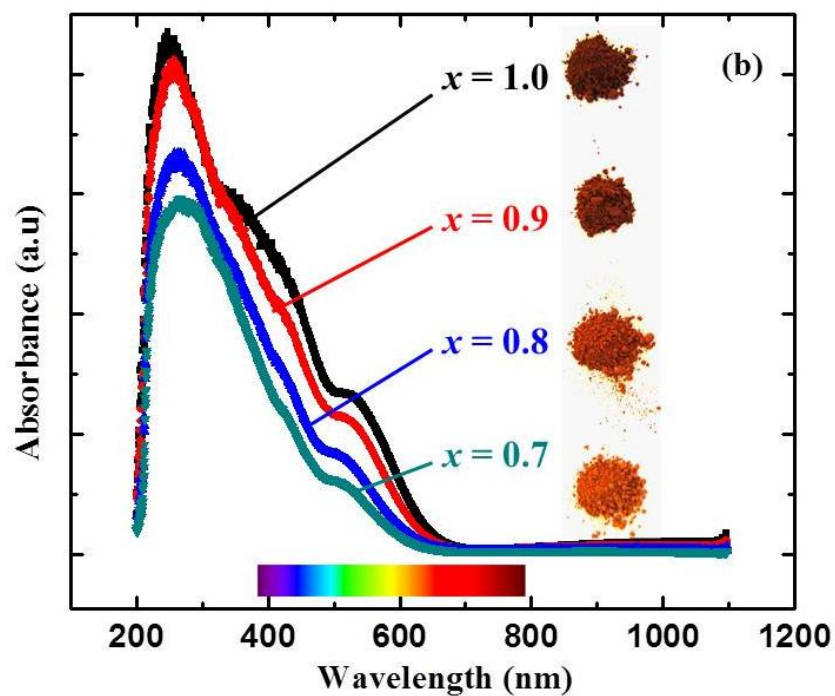


Figure 3.13 Diffuse-reflectance spectra for $\text{YIn}_{1-x}\text{Fe}_x\text{O}_3$ with colors of the samples with varying x . Spectra for $x=0$ (hexagonal YInO_3 ; white color) are shown for comparison.

ACMS was utilized to investigate the magnetic behaviors for the solid solution $\text{YIn}_{1-x}\text{Fe}_x\text{O}_3$. Plots of magnetic susceptibility are in figure 3.14. All samples showed paramagnetic behaviors in the measured temperature range.

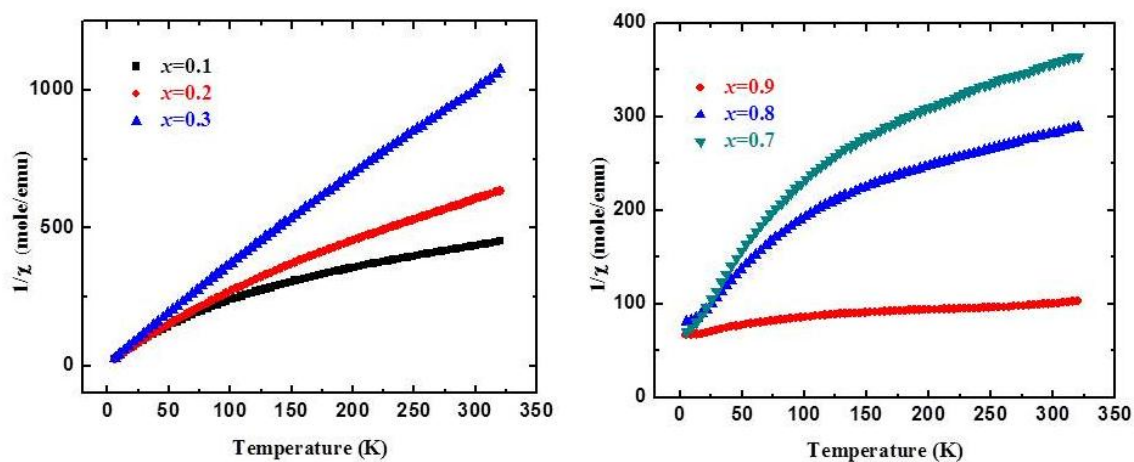


Figure 3.14 Inverse magnetic susceptibility of $\text{YIn}_{1-x}\text{Fe}_x\text{O}_3$ for $x = 0.1, 0.2, 0.3$ (left) and $x = 0.7, 0.8, 0.9$ (right).

The magnetic data of YFeO_3 is illustrated in figure 3.15. A transition appeared in the low temperature region (about 25K) which is due to the magnetic ordering. This result supported the low temperature neutron data which also showed extra peaks at 4K. (Figure 3.15)

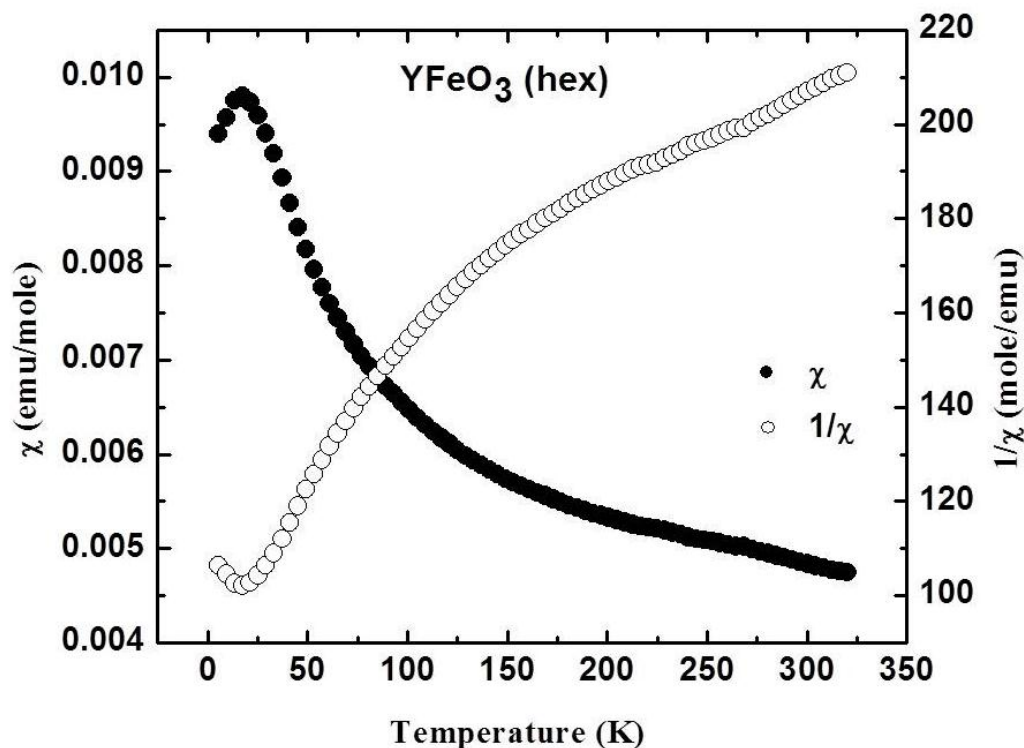


Figure 3.15 Magnetic susceptibility and inverse magnetic susceptibility of YFeO_3 .

Because Curie-Weiss Law was obeyed, linear fit was done for the high temperature region and observed magnetic moment was calculated from the slope. And the results of fitting these data to the Curie-Weiss law are summarized in Table 3.1. Calculations were done based on different oxidation states and coordination. The experimental moments are in reasonable agreement with the moments expected from high spin Fe^{3+} . The negative Weiss constants of all the compounds indicate the magnetic frustration which is illustrated in figure 3.16. The absolute value of Weiss constant increases as Fe content is increased and this is due to the higher concentration of Fe^{3+} ions.

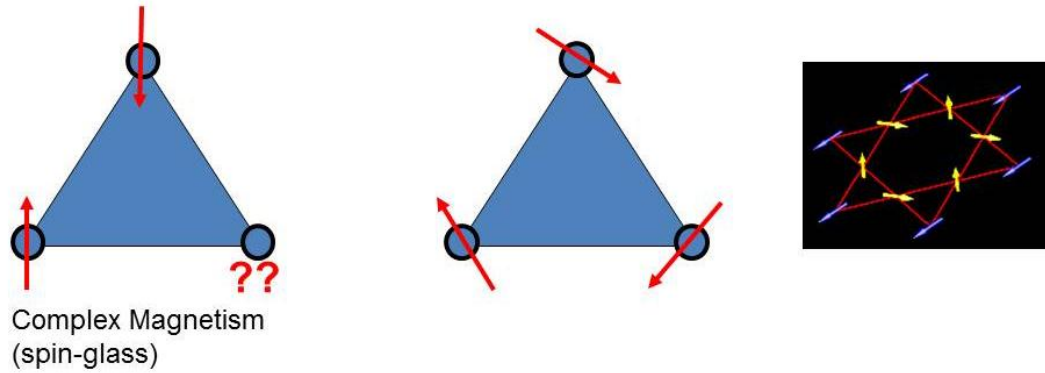


Figure 3.16 Illustration of magnetic frustration in triangular lattice [38].

Table 3.1 Magnetic data of hexagonal $\text{YIn}_{1-x}\text{Fe}_x\text{O}_3$.

x	Magnetism	θ_w	C	$\mu(\text{calc})$	$\mu(\text{obs})$
0.1	AFM	-25.68	0.324	1.872	1.610
0.2	AFM	-96.73	0.655	2.646	2.291
0.3	AFM	-223.82	1.197	3.243	3.097
0.7	AFM	-426.77	2.030	4.144	4.032
0.8	AFM	-489.91	2.787	4.736	4.725
0.9	AFM	-950.39	3.403	5.616	5.239
1.0	AFM	-650.23	4.613	5.916	6.078

For compounds which contain iron, Mössbauer spectroscopy is an efficient approach to study the local environment and valence of iron, thus provide more information about the structure. So Mössbauer spectra were collected for all the samples. In order to obtain spectra with reliable signal of the In-rich samples, trace amount of $\text{Fe}^{57}_2\text{O}_3$ was added to the precursors to enhance the signal. The data with the fit was illustrated in figure 3.17 and figure 3.17. $\text{YIn}_{0.3}\text{Fe}_{0.7}\text{O}_3$ was shown as a representative of Fe-rich site while $\text{YIn}_{0.7}\text{Fe}_{0.3}\text{O}_3$ was for In-rich site. From the

summary of Mössbauer table for both In-rich side and Fe-rich side samples, Fe exhibited as Fe^{3+} and is situated in the five-fold coordination. This result agreed well with the magnetic data which stated the oxidation state of Fe is 3+.

Table 3.2 Mössbauer parameters of $\text{YIn}_{0.3}\text{Fe}_{0.7}\text{O}_3$.

DIS	δ (mm/s)	Γ (mm/s)	$\Delta^* / \Delta_{\text{max}}$ (mm/s)	Distribution width	%	Site
1	0.298	0.30	1.56/1.83	$0.2 < \Delta < 2.4$	47	Fe^{3+} [5]
2	0.300	0.30	1.59/1.60	$0.5 < \Delta < 2.5$	53	Fe^{3+} [5]

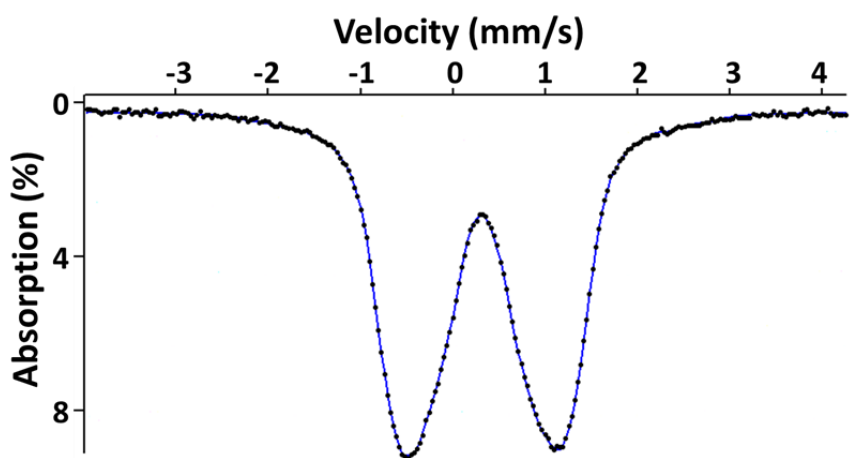


Figure 3.17 Mössbauer spectrum of $\text{YIn}_{0.3}\text{Fe}_{0.7}\text{O}_3$.

Table 3.3 Mössbauer parameters of $\text{YIn}_{0.7}\text{Fe}_{0.3}\text{O}_3$.

DIS	δ (mm/s)	Γ (mm/s)	$\Delta^* / \Delta_{\text{max}}$ (mm/s)	Distribution width	%	Site
1	0.303	0.25	1.59/1.60	$1.2 < \Delta < 2.1$	100	Fe^{3+} [5]

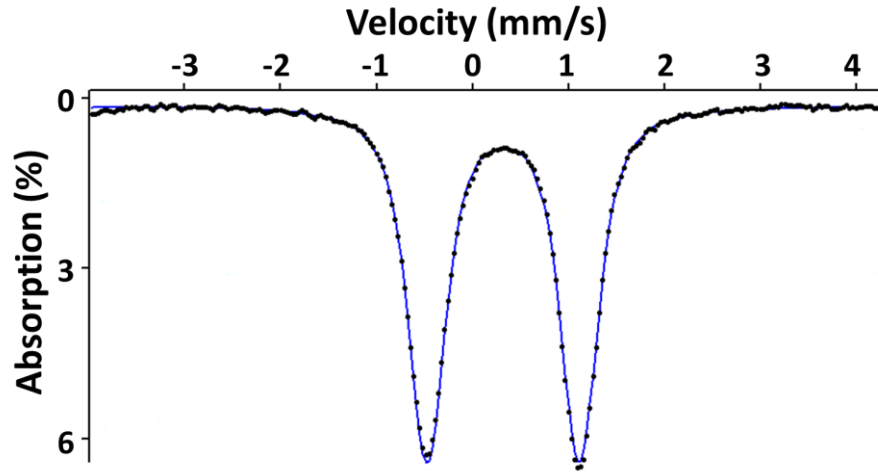


Figure 3.18 Mössbauer spectrum of $\text{YIn}_{0.7}\text{Fe}_{0.3}\text{O}_3$.

When looking at the Mossbauer spectrum for YFeO_3 which is illustrated in figure 3.19, two Fe sites was observed. The presumed structure for hexagonal YFeO_3 has only one site for Fe. This is true for both the paraelectric and ferrielectric versions of this structure. However, Mössbauer studies for hexagonal EuFeO_3 and YbFeO_3 find 2 different types of Fe [39]. Preliminary Mössbauer studies on our $\text{YIn}_{1-x}\text{Fe}_x\text{O}_3$ samples also show 2 Fe sites for Fe rich samples but only one Fe site for In rich samples [40].

Table 3.4 Mössbauer parameters of YFeO_3 .

DIS	δ (mm/s)	Γ (mm/s)	Δ^* / Δ_{\max} (mm/s)	Distribution width	%	Site
1	0.301	0.30	1.93 / 2.14	$0.60 < \Delta < 2.5$	78	Fe^{3+} [5]
2	0.329	0.30	1.37 / 0.90	$0.4 < \Delta < 2.1$	22	Fe^{3+} [5]

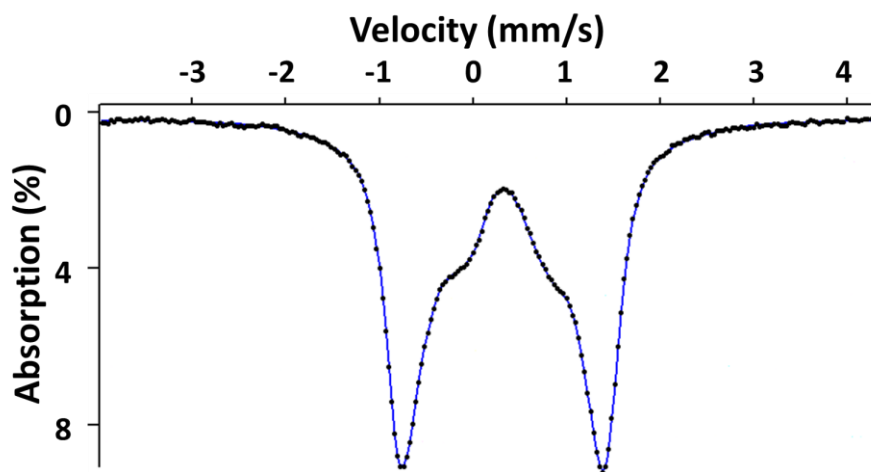


Figure 3.19 Mössbauer spectrum of YFeO_3 .

For the Fe-rich side samples, sol-gel method which involved the aqueous atmosphere was utilized. And the synthesis temperature was moderate (700°C) in the process. Thus it is possible that Fe is bonded with some hydroxyl groups and gives rise to another peak in Mössbauer spectrum. It has been reported that hexagonal YInO_3 prepared by sol-gel method went through overall water splitting [41]. However, TGA data (figure 3.20) with temperature up to 1000°C for both side samples did not show any difference. They both exhibited tiny gaining in weight through the heating process.

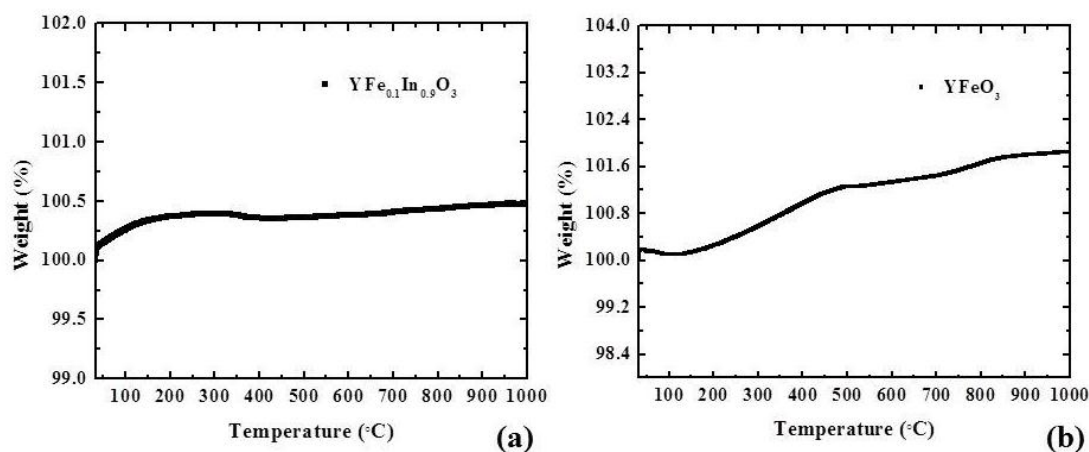


Figure 3.20 Thermal Gravimetric Analysis of $\text{YFe}_{0.1}\text{In}_{0.9}\text{O}_3$ (a) and YFeO_3 (b). The heating rate is $300^\circ\text{C}/\text{h}$ in both figures.

An obvious difference in the $\text{YIn}_{1-x}\text{Fe}_x\text{O}_3$ system between the In-rich and Fe-rich samples is the crystallite size. It would seem that the explanation of the two Fe sites might be related to the small crystallites of the Fe rich samples. It is well established that phase transitions occurring as a function of temperature can be influenced by crystallite size when the size becomes very small. This has been extensively studied in the case of ZrO_2 both experimentally and theoretically [42]. The normal room temperature ZrO_2 structure is monoclinic, but this structure transforms to a tetragonal structure at about 1000°C . The tetragonal form of ZrO_2 is, however, stable at room temperature when crystallites are smaller than 30 nm [42].

A possibility then for our small, Fe-rich $\text{YIn}_{1-x}\text{Fe}_x\text{O}_3$ crystallites is that they are a mixture of the paraelectric and ferrielectric forms. The paraelectric form has a regular trigonal bipyramidal coordination for Fe. In the ferrielectric form, the three basal plane Fe-O distances are not all equal and the two apical Fe-O distances are not

equal. The two different Fe sites in our Fe-rich samples could then arise from the two different phases of the same composition.

Removing the layer of O in the Fe plane (B layer) creates the delafossite structure, where the M cation then has a two-fold linear coordination. The delafossite structure is known in two modifications, which differ only in the stacking sequence. These are known as the 2H and 3R forms. For some compounds with the delafossite structure such as ScCuO_2 both the 2H and 3R forms are known. Intergrowth between the 2H and 3R forms is common and can be regarded as stacking faults [34]. Such stacking faults have been observed in thin films of hexagonal LuFeO_3 [43]. A very high concentration of stacking faults might also explain the two Fe environments observed by Mössbauer studies.

3.2.4 Conclusion

In summary, different characterizations such as structural, magnetic, optical properties were applied to investigate solid solution $\text{YIn}_{1-x}\text{Fe}_x\text{O}_3$. We found that all the single phase compounds in this system exhibited ferrielectric hexagonal structure with space group $\text{P6}_3/\text{mmc}$. Additionally, we have shown that an intense and bright yellow-orange color occurs through all the samples even though the color of YInO_3 end member is white. The color tolerates high temperature and is stable to acidic and basic conditions. We concluded that the origin of the color is from the $d-d$ transition of Fe^{3+} .

in trigonal bipyramidal coordination. And our work provides an approach to develop stable, environmental friendly color pigments.

3.3 Effect of Iron substitution in YAlO_3 ceramics

3.3.1 Introduction

The investigation of the solid solution $\text{YAl}_{1-x}\text{Fe}_x\text{O}_3$ was originated from study of $\text{YIn}_{1-x}\text{Fe}_x\text{O}_3$. The samples which show the most intensive color contains fairly high amount of In^{3+} , which is an element which is relatively rare in the earth. And this is considered as the obstacle for the pigment to be applied in the industry. It will be a giant improvement if indium can be substituted for a cheaper element while the color is still maintained. And this has triggered us to introduce aluminum to this field as aluminum is situated in the same group as indium and YAlO_3 with hexagonal structure was reported [44]. And Mn^{3+} was successfully substituted for the Al^{3+} site in the previous work [45]. Thus the purpose of this part of work was the preparation and characterization of solid solution $\text{YAl}_{1-x}\text{Fe}_x\text{O}_3$.

Phase diagram of Y-Al-O has been discussed intensively and different compositions and structures occur. Between Y_2O_3 and Al_2O_3 end members, there are three compositions: $\text{Y}_3\text{Al}_5\text{O}_{12}$ (YAG), YAlO_3 (YAP), and $\text{Y}_4\text{Al}_2\text{O}_9$ (YAM) [46]. $\text{Y}_3\text{Al}_5\text{O}_{12}$ is considered as thermo-optic materials which can be functioned as the laser host materials. And rare earth ions were introduced to enhance the luminescent

behavior [47, 48]. $\text{Y}_4\text{Al}_2\text{O}_9$ is a promising material as a phosphor host matrix [49]. For YAlO_3 , three forms exist: orthorhombic, cubic and hexagonal. Orthorhombic YAlO_3 phase was discovered long back and the structure can be described as an orthorhombic unit cell as the true crystallographic cell with four distorted perovskite units. The structure belonged to the space group Pbnm and Al^{3+} is six-fold coordinated [50]. It was intensively studied as the host for fluorescence materials [51]. At elevated temperature, cubic YAlO_3 phase was observed as an intermediate phase. Hexagonal phase YAlO_3 is metastable phase compared to the other two phases. The only synthesis method reported is sol-gel process. And the structure (figure 3.21) belongs to the space group $\text{P6}_3/\text{mmc}$ which is paraelectric. The AlO_5 trigonal bipyramidal layers are separated by YO_6 octahedral layers.

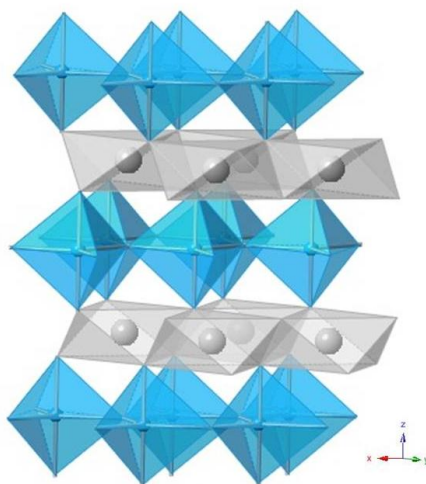


Figure 3.21 Illustration of YAlO_3 with paraelectric structure. Al is indicated in blue sphere; Y is demonstrated by grey sphere and O is omitted.

The Y-O bond distance is uniform thus there is an inversion center in this structure. The evolution of the symmetry shrinks the unit cell on the basal plane. The

non-centric form is distorted thus causing an increase in the cell edge a , compared to the non-centric form, by a factor of 3, thus changing Z from 2 to 6. Figure 3.22 demonstrated the comparison between the two structures from c-axis projection.

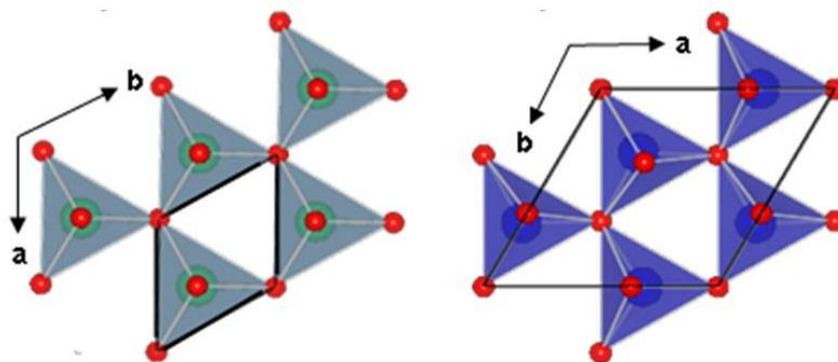


Figure 3.22 Paraelectric YAlO_3 (left) and ferrielectric YMnO_3 (right) [45].

Though the orthorhombic and cubic YAlO_3 was studied comprehensively, the structure of hexagonal YAlO_3 was incomplete and remained to be a mystery. And formation of solid solution with other elements is rarely reported. Dy^{3+} doped hexagonal YAlO_3 was reported for white light emission study [52]. Thus it is still a vast field to be explored. The research in this chapter focuses on the solid solution of $\text{YAl}_{1-x}\text{Fe}_x\text{O}_3$ and its characterization.

3.3.2 Synthesis

Sol-gel method was utilized to get the single phase for all the samples in $\text{YAl}_{1-x}\text{Fe}_x\text{O}_3$ ($x \leq 0.4$, $x \geq 0.7$). All the samples were prepared starting with solutions. The reactants were $\text{Y}(\text{NO}_3)_3 \cdot 6\text{H}_2\text{O}$ (Alfa Aesar, $\geq 99.9\%$), $\text{Al}(\text{NO}_3)_3 \cdot 3\text{H}_2\text{O}$ (Alfa Aesar,

$\geq 99.99\%$) and $\text{Fe}(\text{NO}_3)_3 \cdot 9\text{H}_2\text{O}$ (Aldrich, $\geq 99.99\%$). Appropriate quantities were dissolved in deionized water. The orange colored solution was heated to $60\text{ }^\circ\text{C}$, and citric acid (Mallinckrodt) was added to the solution in a molar ratio of 2:1 citric acid to Y. The pH of the solution was then adjusted to 7 using aqueous $\text{NH}_3 \cdot \text{H}_2\text{O}$. After heating for several hours at $90\text{ }^\circ\text{C}$ a viscous green gel formed. This gel was heated at $250\text{ }^\circ\text{C}$ for 2 hours. The dark brown powder obtained was then ground and served as a precursor.

For Al-rich $\text{YAl}_{1-x}\text{Fe}_x\text{O}_3$ samples, small amount of the precursor was contained in the platinum boat and heated at high temperature ($\sim 900\text{ }^\circ\text{C}$) for a short time (5-10 minutes). After that, the platinum boat was taken out and quenched to room temperature. For Fe-rich $\text{YAl}_{1-x}\text{Fe}_x\text{O}_3$ samples, the precursor was contained in the ceramic boat and heated at $700\text{ }^\circ\text{C}$ or higher in air for 18 hours.

3.3.3 Result and discussion

Sol-gel method was employed to synthesize all the samples in $\text{YAl}_{1-x}\text{Fe}_x\text{O}_3$. Single phase samples are achieved with $x \leq 0.4$, $x \geq 0.7$ in this solid solution. Samples in the intermediated range were heated at various temperatures. However, only amorphous phase appeared in the X-ray diffraction pattern. The X-ray diffraction plot for all the single phase was shown in figure 3.23. Trace amount of yttrium aluminum garnite (YAG) impurity exhibited in the X-ray pattern of Al-rich side samples. For the samples of Fe-rich side, the (102) reflection peak indicating ferrielectric structure

appeared in the XRD pattern. The intensity of the (102) peak decreased with the increase of Al content. And that reflection peak disappeared in the samples with aluminum value higher than 0.7.

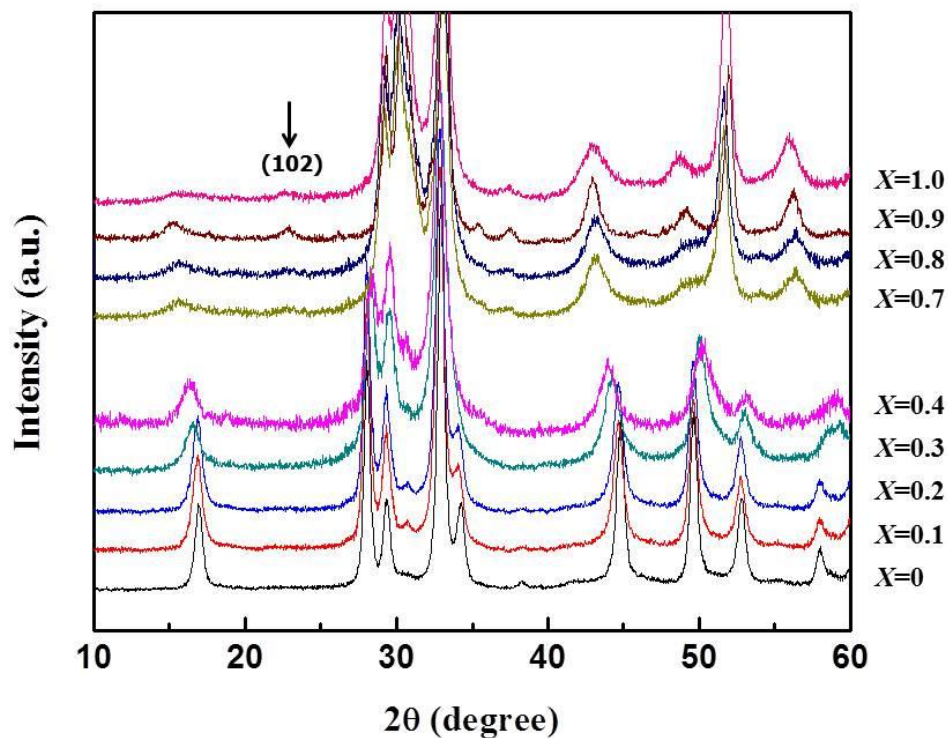


Figure 3.23 XRD patterns of the $\text{YAl}_{1-x}\text{Fe}_x\text{O}_3$ powder samples.

As all the samples were prepared through the sol-gel process, the peaks were broadened due to the small size of particles. And this will make it difficult to refine the XRD patterns and the structure information from Reitveld methods will not be reliable. Thus only La Bail fit was conducted for all the samples to get the value of cell parameters and cell volumes (Figure 3.24). The shaded area showed discontinuity of the lattice parameters due to missing phases with intermediate x values. Cell parameter

a of samples with ferrielectric structure ($x = 0.7-1.0$) was divided by $\sqrt{3}$ to be compared with samples with paraelectric structure ($x = 0-0.4$). The cell edge a is decreasing with an increase of x value. The Al-O bond distance on the basal plane has the biggest value among all the YMO_3 ($M=\text{Fe, Mn, In, Ga}$) hexagonal groups despite the fact that Al^{3+} has the smallest ionic radius among these elements. And lattice parameter c is increasing with more Fe content.

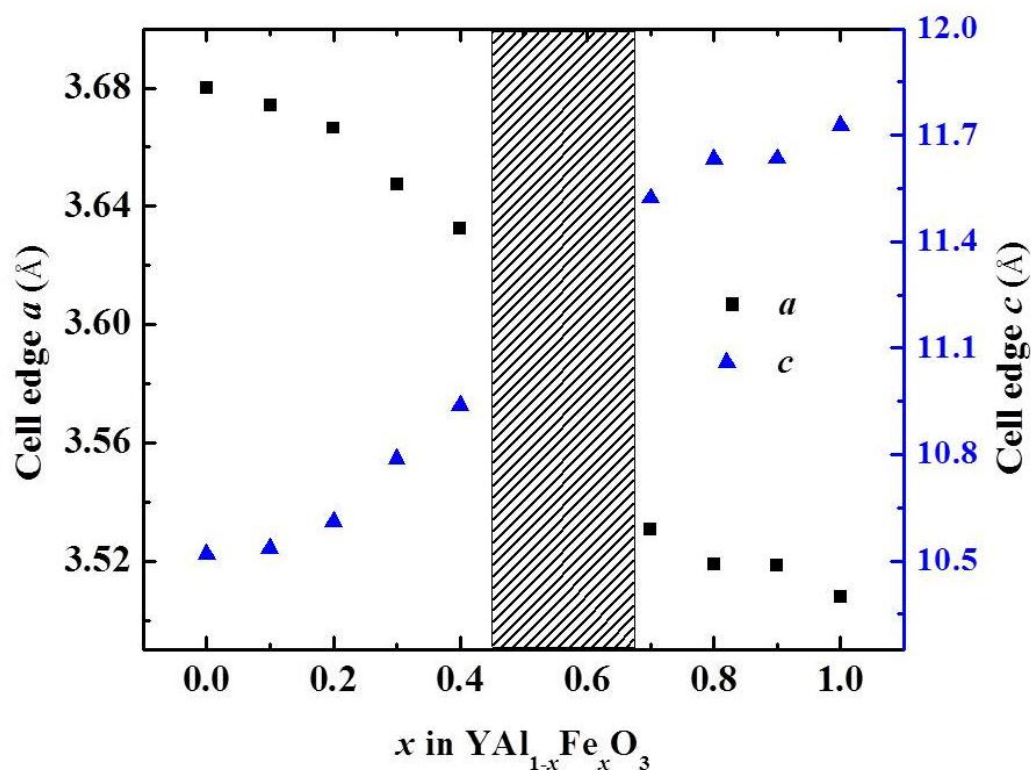


Figure 3.24 Hexagonal lattice parameters vs x in $\text{YAl}_{1-x}\text{Fe}_x\text{O}_3$.

Generally, the cell volume (illustrated in figure 3.25) also expanded systematically towards the Fe-rich side. The volume gap between $x = 0.4$ and $x = 0.7$ sample may be rooted in the structure transform from paraelectric structure to

ferrielectric structure. The simultaneous occurrence of the two phases can be another possibility which lead to this fluctuation of cell volume. As the peaks are broadened and the resolution of the X-ray patterns is not high enough to separate these two phases.

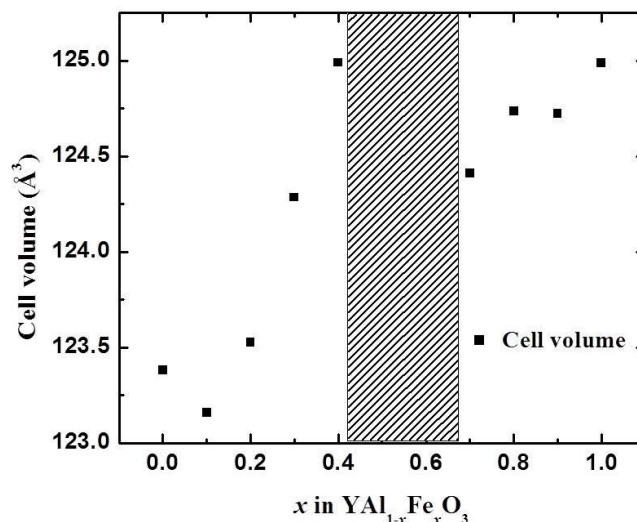


Figure 3.25 Cell volume vs. x in $\text{YAl}_{1-x}\text{Fe}_x\text{O}_3$.

The color of pure hexagonal YAlO_3 is white. The spectrum shows reflectance through the entire visible region. And the absorption peak in the ultraviolet region is from charge transfer. Small amount of Fe doping into the YAlO_3 tuned the color to be pale yellow. And $d-d$ transition creates small absorbance of photon at around 500 nm in the blue color absorption in the visible region, which lies in the yellow color region. The color became darker with the increase of the Fe content and finally changed to brown which is the color of hexagonal YFeO_3 . The color of the samples is shown in figure 3.26 and UV-Vis spectrum is illustrated.

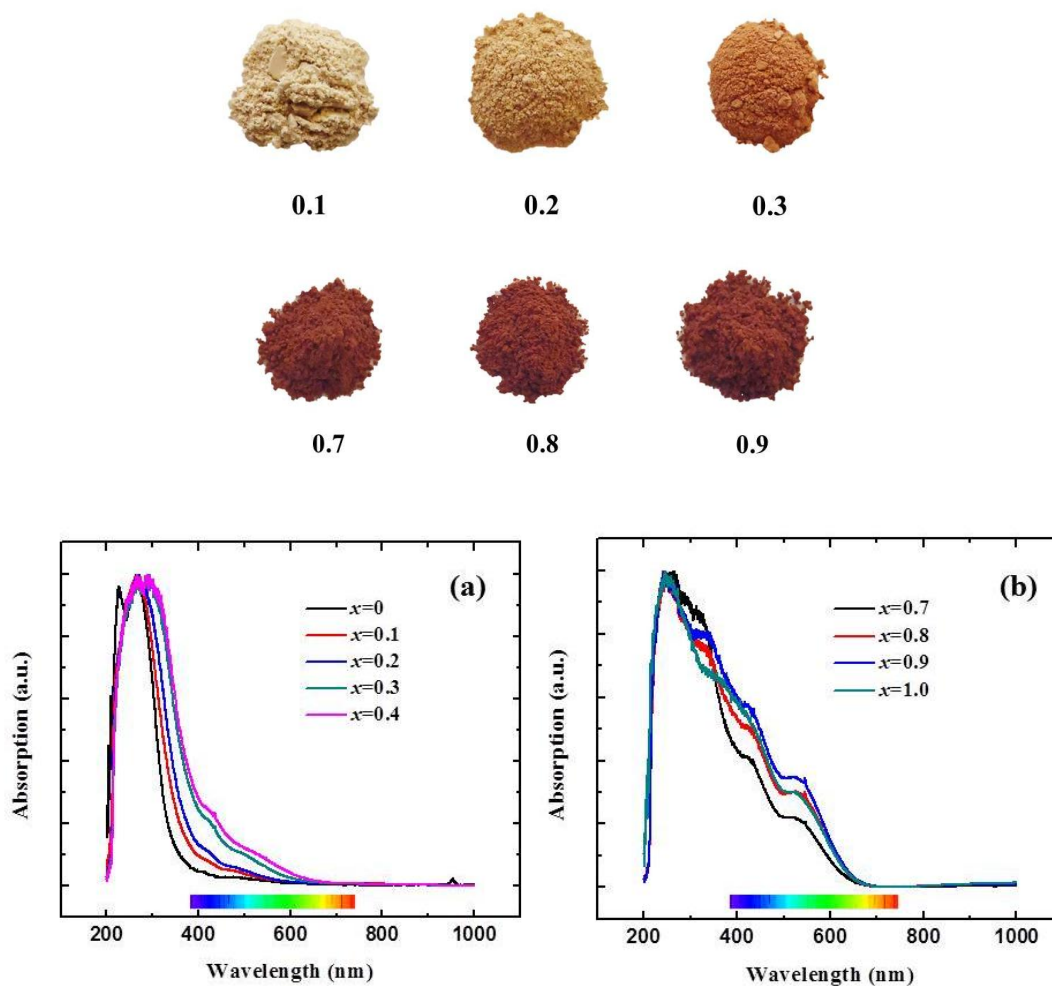


Figure 3.26 Pictures (above) (value for Fe content is below the sample) and diffuse-reflectance spectra (below) for $\text{YAl}_{1-x}\text{Fe}_x\text{O}_3$ with colors of the samples with varying x . Spectra for $x = 0$ (hexagonal YAlO_3 ; white color) are shown for comparison.

Though the samples exhibit yellow to brown colors, the colors are not comparable to the brightness of the colors presented in the $\text{YIn}_{1-x}\text{Fe}_x\text{O}_3$ samples. This is possibly due to the ionic radius difference between Al^{3+} and In^{3+} . As apical distance is crucial in color resulted from TBP site [20].

Magnetic data was collected to address the oxidation state of Fe ions. Inverse susceptibility data is illustrated in figure 3.27. And all samples exhibited paramagnetic

behavior in the temperature range measured, and it is more obvious in the Al-rich side compounds which are more diluted. For sample on the Fe-rich side, possibility of magnetic frustration presents as the geometry of Fe on the basal plane is triangular, in which not all the spin-wise interactions can be satisfied [53, 54].

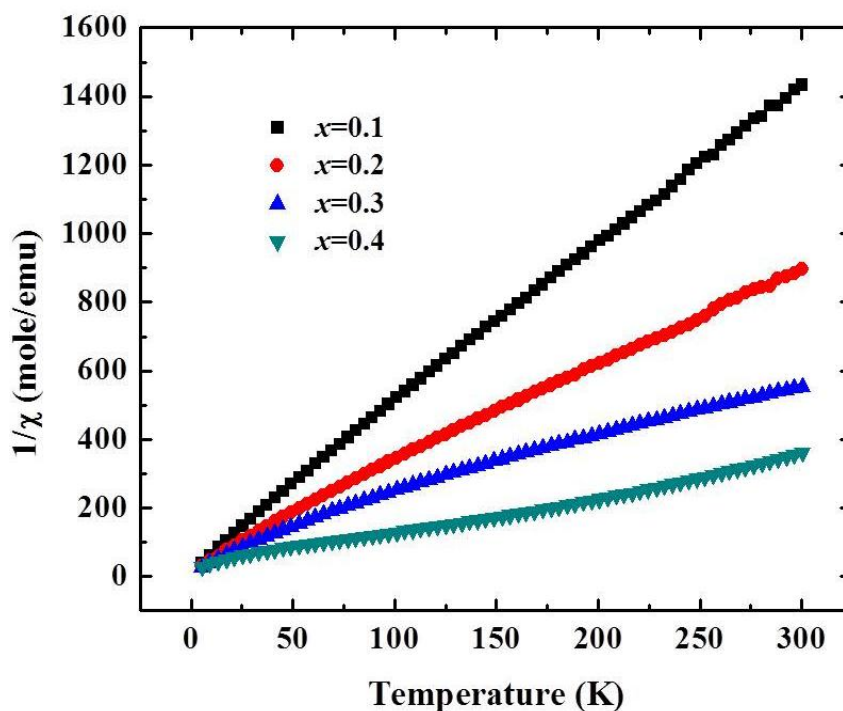


Figure 3.27 Inverse magnetic susceptibility versus temperature plot for $\text{YAl}_{1-x}\text{Fe}_x\text{O}_3$.

From the linear paramagnetic range of the inverse magnetic susceptibility plot, all the factors are calculated and the magnetic moment can be estimated. The negative Weiss constant indicates that all the compounds are antiferromagnetic but the antiferromagnetic ordering is not observed in the measured temperature range. The values of different Fe contents in this solid solution are listed in table 3.5 and compared with value calculated from Fe^{3+} high spin case (spin-only). Generally, the

magnetic moments increase with the elevating Fe content. However, unlike the $\text{YIn}_{1-x}\text{Fe}_x\text{O}_3$ system, the magnetic moments are lower than the theoretical values. The particle size of the compound was reported to affect the magnetic behavior and the value of magnetic moment in yttrium iron garnet (YIG) prepared by sol-gel method [55]. So it is possible that the magnetic moments of samples in this system are also shifted by the size of the particle. In addition, effect of the existence of the amorphous phase is not able to be excluded. Attempts of annealing the sample were conducted to make samples more crystalline and eliminate the amorphous phase. However, impurity of YAG appeared in a much higher intensity. Thus the mass of the hexagonal phase may not be represented by the total weight of the sample. And this may lead to the change in the magnetic susceptibility value. Thus, Fe may still be in an oxidation state of 3+ and a high spin case.

Table 3.5 Summary of magnetic data of $\text{YAl}_{1-x}\text{Fe}_x\text{O}_3$.

x	Curie Constant	θ_w	μ_B (experimental)	μ_B (calculated)
0.1	0.214	-4.21	1.314	1.871
0.2	0.349	-15.71	1.678	2.646
0.3	0.699	-89.49	2.374	3.240
0.4	0.730	41.21	2.426	3.742
0.7	1.280	-268.69	3.213	4.950
0.9	0.559	-394.03	3.876	5.612

3.3.4 Conclusion

Solid solution $\text{YAl}_{1-x}\text{Fe}_x\text{O}_3$ with $x \leq 0.4$, $x \geq 0.7$ was successfully synthesized for the first time. Low temperature sol-gel process was utilized to prepare the single phase samples. X-ray diffraction data confirmed that the structure of all the samples was hexagonal. However, the Fe-rich side samples grouped in the ferrielectric structure while Al-rich side samples in paraelectric structure. All the samples showed colors from white (YAlO_3) to yellow to brown (YFeO_3).

3.4 References

1. W. Kinase; K. Harada. *Ferroelectrics*, 283, 39-47, 2003
2. H. Miyazawa; E. Natori; S. Miyashita; T. Shimoda; F. Ishii; T. Oguchi. *Jpn. J. Appl. Phys.* 39, 5679-5682, 2000.
3. T. A. Vanderah. “*Chemistry of Superconductor Materials Preparation, Chemistry, Characterization and Theory.*” Noyes Publications. 1992
4. D. Damjanovic. *Rep. Prog. Phys.* 61, 1267, 1998
5. V. M. Goldshmidt. *Skr. Nor. Vidensk. Akad. Oslo.* 2, 1926.
6. N. Ramadass. *Mater. Sci. Eng.*, 36, 231-239, 1978.
7. Brewer, L. *Science*. 161, 115, 1968.
8. D. M. Giaquinta; H-C. zui Loye. *Chem. Mater.* 6, 365-372, 1994.
9. G. A. Smolenskii, et. al. *J. Appl. Phys.*, 35, 915-17, 1964.
10. I. G. Ismailzade, S. A. Kizhaev. *Fiz. Tverd. Tela.* 7, 298-301, 1965.
11. T. Katsufuji; S. Mori; M. Masaki; Y. Moritomo; N. Yamamoto; H. Takagi. *Phys. Rev. B.*, 64, 104419, 2001.
12. H. Yakel; W. Koehler; E. Bertaut; F. Forrat. *Acta. Aryst.* 16, 957, 1963.
13. B. B. Van Aken; A. Meetsma; T. M. Palstra. *Acta. Aryst.* c57, 230, 2001.
14. I. G. Ismailzade; S. A. Kizhaev. *Sov. Phys-Sol. State.* 7, 236, 1965.
15. C. W. F. T. Pistorius; G. J. J. Kruger. *Inorg. Nucl. Chem.* 38, 1471, 1976.
16. N. Floros; J. T. Rijssenbeek; A. B. Martinson; K. R. Poeppelmeier. *Solid State Sci.* 4, 1495, 2002.
17. D. A. Vander Griend; S. Malo; K. T. Wang; K. R. Poeppelmeier. *J. Am. Chem. Soc.* 122, 7308, 2000.

18. S. Malo; A. Maignan; S. Marin; M. Hervieu; K. R. Poeppelmeier; B. Raveau. *Solid. State. Sci.* 7, 1492, 2005.
19. B. B. Van Aken; T. T. M. Palstra; A. Filippetti; N. A. Spaldin. *Nat. Mater.* 3, 164, 2004.
20. A. E. Smith; H. Mizoguchi; K. Dlaney; N. A. Spaldin; A. W. Sleight; M. A. Subramanian. *J. Am. Chem. Soc.* 131, 17086, 2009.
21. H. Mizoguchi; A. W. Sleight; M. A. Subramanian. *Inorg. Chem.* 50, 10, 2011.
22. A. E. Smith; A. W. Sleight; M. A. Subramanian. *Mater. Res. Bull.* 46, 1, 2011.
23. S. L. Samal; W. Green; S. E. Lofland; K. V. Ramanujachary; D. Das; A. K. Ganguli. *J. Solid. State. Chem.* 181, 61-66, 2008.
24. C. W. F. T. Pistorius; G. J. Kruger. *J. inorg, nucl. Chem.* 38, 1471-1475, 1976.
25. A. W. Sleight. *Progress in Solid State Chemistry.* 37, 251-261, 2009.
26. O. Yamaguchi; H. Takemura; M. Yamashita; A. J. Hayashida. *Electrochem. Soc.* 1991, 138, 1492;
27. D. Du Boulay; E. N. Maslen; V. A. Streltsov; N. Ishizawa. *Acta. Crystallogr.* B51, 921, 1995.
28. J. Li; U.G. Singh; T.D. Schladt; J.K. Stalick; S.L. Scott; R. Seshadri. *Chem. Mater.* 20, 6567, 2008.
29. M. Sugawara; N. Kikukawa; N. Ishikawa; N. Kayano; T. Kimura. *J. Aerosol Sci.* 29, 675-686, 1998.
30. A. S. Hudson. *J. Phys. D.* 3, 251-68, 1970
31. K. J. Haralambous; Z. Loizos; N. Spyrellis. *Mater. Lett.* 11, 133-41, 1991
32. L. Wu; J. C. Yu; L. Zhang; X. Wang; S. Li. *J. Solid. State. Chem.* 177, 3666-3674, 2004.
33. M. Inoue; T. Nishikawa; T. Nakamura; T. Inui. *J. Am. Ceram. Soc.* 80, 2157-60, 1997.
34. A.A. Bossak; I.E. Graboy; O.Y. Gorbenko; A.R. Kaul; M.S. Kartavtseva; V.L. Svetchnikov; H.W. Zandbergen; *Chem. Mater.* 16, 1751, 2004.
35. R. D. Shannon. *Acta Cryst.* A32, 751-767, 1976.
36. U. Schwertmann, R.M. Cornell “*Iron Oxides in the Laboratory, Preparation and Characterization*” Wiley-VCH, New York, 2000.
37. J. Torrent; V. Barrón. “*Encyclopedia of Surface and Colloid Scienc,*” Marcel Dekker, New York, 1438-1446, 2002.
38. Dr. Subramanian. Solid State Chemistry class.
39. Y. Mizoguchi; H. Onodera; H. Yamauchi; M. Kagawa; Y. Syono; T. Hirai. *Mater. Sci. Eng.* A217/218, 164, 1996.
40. Alain Wattiaux, private communication.
41. N. Arai; N. Saito; N. Nishiyama; Y. Shimodaira; H. Kobayashi. *Chem. Letters.* 37 1, 2008.
42. R.C. Garvie. *J. Phys. Chem.* 69, 1238, 1965.
43. J. Li; A. Yokochi; A.W. Sleight. *Solid. State. Sci.* 6, 831, 2004.
44. E. F. Bertaut; J. Mareschal. *Compt. Rend.* 257, 867-70, 1963.
45. A. E. Smith. Thesis. Oregon State University. 2010
46. W. Y. Ching; Y. Xu. *Phys. Rev. B.* 59, 12815, 1999

47. R. L. Aggarwal; D. J. Ripin; J. R. Ochoa; T. Y. Fan. *J. Appl. Phys.* 98, 103514, 2005
48. M. Veith; S. Mathur; A. Kareiva; M. Jilavi; M. Zimmer; V. Huch. *J. Mater. Chem.* 9, 3069-3079, 1999
49. Y. Rabinovitch; O. K. Moune; D. Tetard; M. D. Faucher. *J. Phys. Chem. A.* 108, 8244-8255, 2004
50. S. Geller; E. Wood. *Act. Cryst.* 9, 563, 1956.
51. M. J. Weber. *J. Appl. Phys.* 44, 7, 1973.
52. Y. Ji; J. Cao; Z. Zhu; J. Li; Y. Wang; C. Tu. *J. Lumin.* 132, 702-706, 2012.
53. S. Nakatsuji; Y. Nambu; H. Tonomura; S. Sakai; S. Jonas; C. Broholm; H. Tsunetsugu; Y. Qiu; Y. Maeno. *Science.* 309, 1697, 2005.
54. H. T. Diep. *Frustrated Spin System.* World Scientific Publishing Co. Pte. Ltd., 2004.
55. R. D. Sánchez; J. Rivas; P. Vaquero; M. A. López-Quintela; D. Caeiro. *J. Magn. Mater.* 247, 92-98, 2002.

Chapter 4

Structure and Physical Properties of $\text{Ba}_2\text{In}_{2-x}\text{M}_x\text{O}_{5+x}$ Brownmillerite-type Structure System (M=Mn, Fe)

Abstract

Solid solution of $\text{Ba}_2\text{In}_{2-x}\text{Mn}_x\text{O}_{5+x}$ ($x = 0.1-0.7$) and $\text{Ba}_2\text{In}_{2-x}\text{Fe}_x\text{O}_{5+y}$ ($x = 0.1-1.5$) were successfully synthesized and characterized. Study on X-ray diffraction data and neutron diffraction data proves that the structure of all the compounds is brownmillerite-type. A transform from orthorhombic to tetragonal, and finally to cubic is observed for both solid solution. The optical, magnetic were characterized and thermogravimetric analysis was conducted.

In the solid solution $\text{Ba}_2\text{In}_{2-x}\text{Mn}_x\text{O}_{5+x}$ ($x = 0.1-0.7$), magnetic measurements confirm that Mn in as prepared samples is substituting as Mn^{5+} for all values of x with observed paramagnetic spin-only moments close to values expected for two unpaired electrons. A transform in the structure is observed from X-ray diffraction and neutron diffraction data. Neutron diffraction structure refinements show Mn^{5+} occupies tetrahedral sites for orthorhombic ($x = 0.1$) and tetragonal ($x = 0.2$) phases. For $\text{Mn} \geq 0.3$ samples, neutron refinements show the phases are cubic with disordered cations and oxygen vacancies. And this is the first known compound with Mn^{5+} easily stabilized in the oxides at room temperature. All the single phase samples exhibit bright colors as well. The colors of the phases change from light yellow ($x = 0$) to intense turquoise ($x=0.1$), to green ($x = 0.2, 0.3$) or dark green ($x \geq 0.4$).

$\text{Ba}_2\text{In}_{2-x}\text{Fe}_x\text{O}_{5+y}$ ($x = 0.1-1.5$) system was prepared and characterized. X-ray diffraction, neutron diffraction, TGA and ACMS were utilized to investigate the properties of this solid solution. Structure transition from orthorhombic to cubic is observed which is similar to $\text{Ba}_2\text{In}_{2-x}\text{Mn}_x\text{O}_{5+y}$ system. The magnetic moment falls in between Fe^{3+} and Fe^{4+} which indicate a mixed valence of Fe ions. Weight loss shown in TGA data and Mössbauer spectra confirm the existence of Fe^{4+} . Small amount of Fe dopant tunes the color to green. And the color becomes darker with the increase of Fe content and finally shows black.

4.1 Introduction

Perovskites (ABO_3) can tolerate a lot of distortion and vacancies. Thus it is considered as a potential material for oxygen ion conductors. Substitution of A or B site with ions which is in lower oxidation state will steadily decrease the content of oxygen. Ti^{4+} in SrTiO_3 , for example, can be substituted by Al^{3+} and oxygen vacancies are introduced [1]. If $1/6$ of the oxygen atoms are missing from perovskites, the structure transform to brownmillerite structure which acquires the formula of $\text{A}_2\text{B}_2\text{O}_5$. In the brownmillerite structure, the BO_4 tetrahedral layer is created by removing two oxygen atoms from the BO_6 octahedra. Thus it can be viewed as a layer structure with one layer of BO_6 octahedra and one layer of BO_4 tetrahedra, and the two layers are stacking alternatively. The structure of perovskite and brownmillerite is illustrated in figure 4.1.

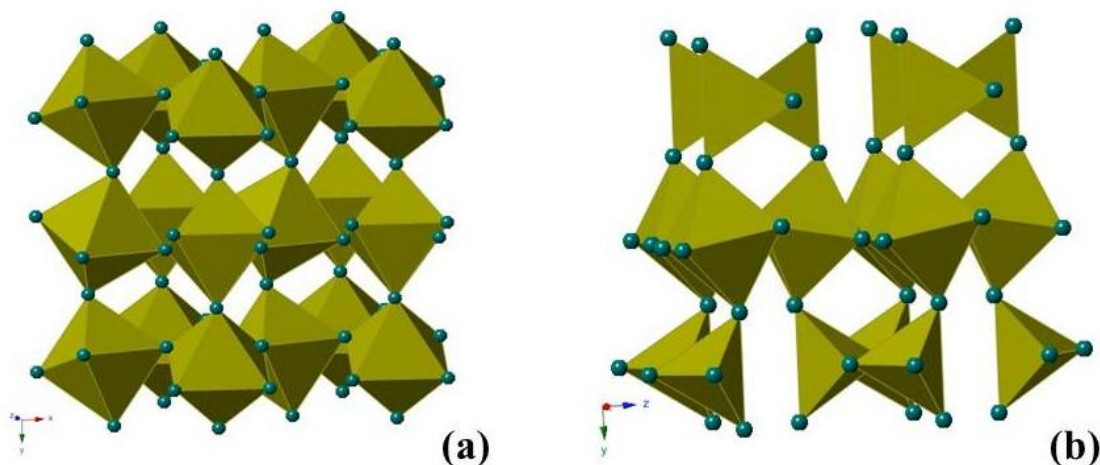


Figure 4.1 Structure of YFeO_3 perovskite structure (a) and $\text{Ca}_2\text{Fe}_2\text{O}_5$ brownmillerite structure (b).

Many related structures existed in between the perovskite and brownmillerite. The structure of compounds between perovskite and brownmillerite can be summarized. It can be considered as a sequence of $(n - 1)$ BO_6 octahedra sheets alternating with one sheet consisting of parallel chains of BO_4 tetrahedra. In other way, it can be viewed as an ordering of BO_4 tetrahedra in rows along the $[101]$ direction in between $(n - 1)$ layers of BO_6 octahedra in perovskite-like structure. The general formula can be expressed as $\text{A}_n\text{B}_n\text{O}_{3n-1}$. Brownmillerite and perovskite structures has the value of $n = 2$ and $n = \infty$, respectively [2, 3]. The structural evolution from $\text{A}^{2+}\text{B}^{4+}\text{O}_3$ to $\text{A}^{2+}\text{B}^{3+}\text{O}_5$, has been summarized as one branch of “perovskite space” as shown in Fig. 4.2 [4].

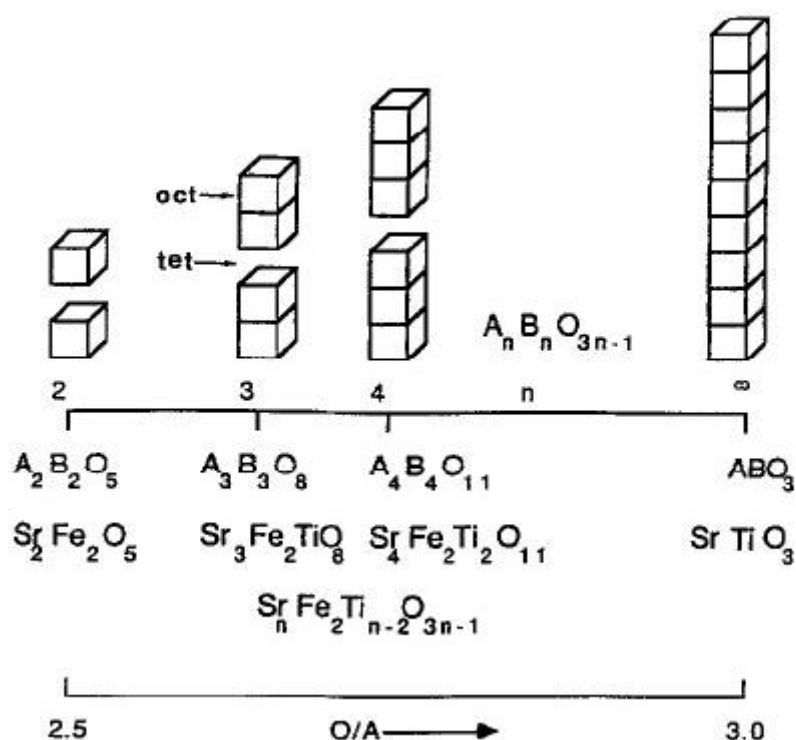


Figure 4.2 stacking sequence in perovskite-brownmillerite family: “Perovskite space” in the oxygen-deficient axis, $2.5 < \text{O/A} < 3.0$ [4].

The brownmillerite-type oxides have different structures based on the extent of oxygen disorder. The lattice belongs to orthorhombic unit cell if all the oxygen vacancies are ordered. Above a transition temperature T_d , which is the characteristic order-disorder temperature, all the oxygen vacancies are disordered and the tetrahedral sheets no longer exist. The unit cell is evolved to cubic. And maximum ionic conductivity is expected at this state [5]. Tetragonal unit cell is normally observed in between these two states and can be viewed as an intermediate state.

$\text{Ba}_2\text{In}_2\text{O}_5$ and related compounds have been intensively studied due to their high O^{2-} ionic conductivity, which can potentially be applied in areas such as solid oxide fuel cells and electrolytes [6]. $\text{Ba}_2\text{In}_2\text{O}_5$ adopts a brownmillerite-type structure, which can be considered to be a defect perovskite structure with alternating layers of octahedra and tetrahedra. A version of the brownmillerite structure is shown in figure 4.3.

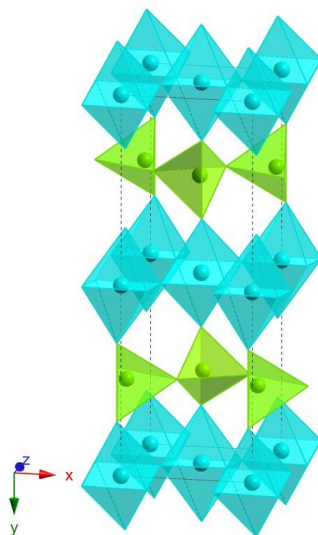


Figure 4.3 The *Pnma* version of the brownmillerite structure where the two chains shown have different configurations. Octahedra are turquoise and tetrahedral are green.

The tetrahedra share corners to form continuous chains along the shortest axis. There are, however, two different configurations possible for these chains. Simple ordering of chain configurations typically leads to structures described in space groups *I2mb* or *Pnma* (Fig.4.4). Complex chain ordering can occur, and complete disorder of chain configurations gives space group *Icmm*. The most recent structure refinements for $\text{Ba}_2\text{In}_2\text{O}_5$ have rejected space groups *I2mb* and *Pnma* in favor of *Icmm* [7, 8]. Thus, the two configurations of the tetrahedral chains are considered to be disordered. However, electron microscopy for $\text{Ba}_2\text{In}_2\text{O}_5$ shows a very complex superstructure indicating that the configurations of the chains are ordered [7]. This superstructure is ignored in the published refinements. Thus, the details of the $\text{Ba}_2\text{In}_2\text{O}_5$ structure with regard to the layers containing the tetrahedra are unknown. At high temperatures $\text{Ba}_2\text{In}_2\text{O}_5$ adopts the ideal cubic perovskite structure with no long range order of the O

vacancies. A tetragonal structure for $\text{Ba}_2\text{In}_2\text{O}_5$ has been reported to occur as an intermediate between the orthorhombic and cubic structures [6].

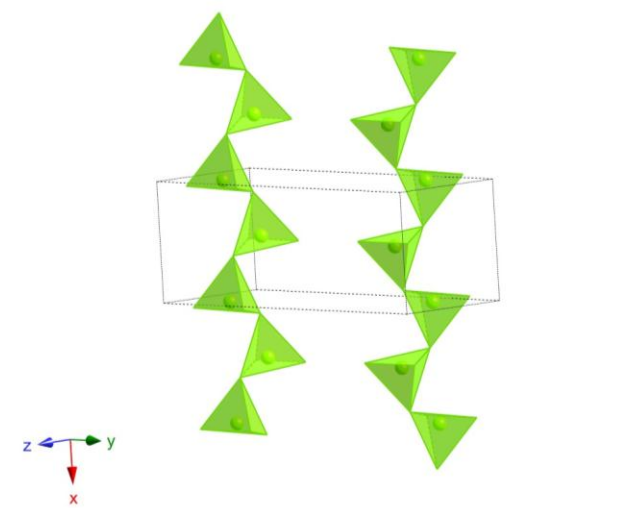


Figure 4.4 Chains of tetrahedra along the a axis in the $Pnma$ orthorhombic structure

Substitutions of Zr for In can stabilize the cubic structure at room temperature [6]. Kobayashi et al. reported the substitution for In of all the first row transition elements [9]. Such substitutions generally increased the symmetry to tetragonal or cubic. Ionic conductivity was reported for all substitutions, but no information was provided on the color or magnetic properties. Compounds of the type $\text{A}(\text{MO}_4)_3 \cdot x(\text{Mn}^{5+}\text{O}_4)_x\text{X}$ with $\text{A} = \text{Ba}, \text{Sr}, \text{Ca}$; $\text{M} = \text{P}, \text{As}, \text{V}$; $\text{X} = \text{Cl}, \text{OH}, \text{F}$ are known to exhibit a turquoise color at low x changing to green at higher values of x . The origin of this color is a valley in the visible absorption at a wavelength of about 540 nm.

4.2 Intense Turquoise and Green Colors in Brownmillerite-type Oxides Based on Mn^{5+} in $\text{Ba}_2\text{In}_{2-x}\text{Mn}_x\text{O}_{5+x}$

4.2.1 Introduction

Recent discovery [10, 11] of oxides with exceptional blue colors based on Mn^{3+} in trigonal bipyramidal coordination has prompted us to explore Mn in other oxide hosts. Inorganic compounds containing Mn^{5+} are known to show strong optical absorption producing turquoise to green colored compounds [12, 13]. However, Mn^{5+} is generally not stable in oxides where high pressure O_2 is routinely employed just to stabilize a Mn oxidation state of 4+ as in BaMnO_3 [14]. However, $\text{Ba}_2\text{In}_2\text{O}_5$ brownmillerite structure is a possible host for Mn^{5+} because Ba^{2+} has relatively large ionic radii and is quite electropositive. Thus Mn in high oxidation state will be easily maintained in this case. The oxygen content will shift from the ideal formula of brownmillerite and the excess oxygen atoms may create five-fold coordination as shown in figure 4.5.

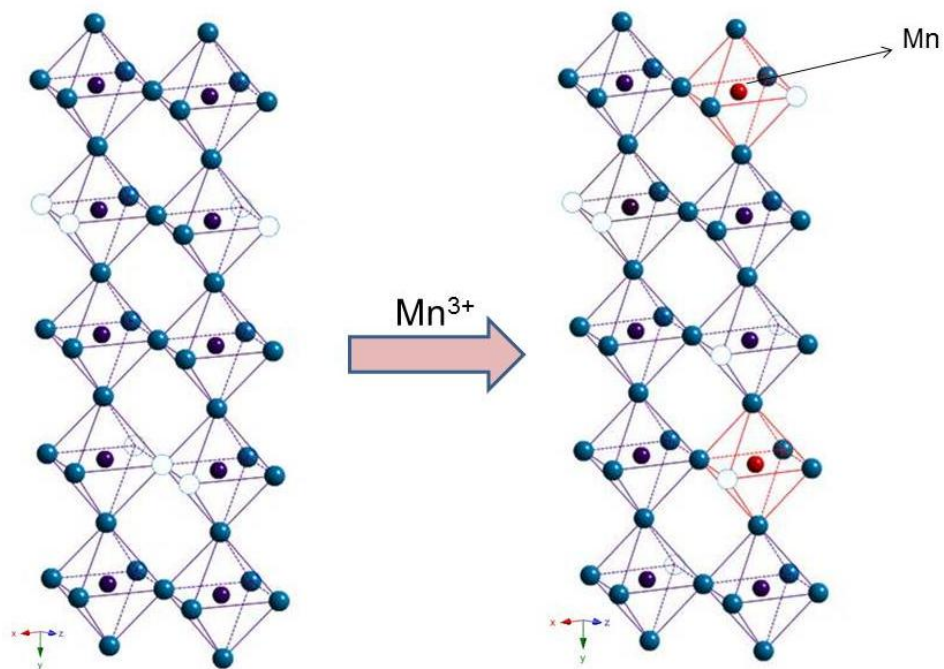


Figure 4.5 The formation of five-fold coordination in $\text{Ba}_2\text{In}_{2-x}\text{Mn}_x\text{O}_{5+x}$ system.

4.2.2 Synthesis

A solid state method was used for the synthesis of all the $\text{Ba}_2\text{In}_{2-x}\text{Mn}_x\text{O}_{5+y}$ samples. A stoichiometric mixture of BaCO_3 (Baker Analyze, >99%), In_2O_3 (Stanford Materials, >99.99%), and Mn_2O_3 (JMC, >98%) was thoroughly ground together in an agate mortar. The powder mixtures were then pressed into pellets with applied pressure of 1 psi. The pellets were heated at 1200 °C for 12 hours in air, reground, pelletized again, and finally heated at 1300 °C for another 12 hours. Powder samples were reduced in H_2/N_2 gas mixture (5% H_2) at 500 °C for 4 hours.

4.2.3 Result and discussion

Single-phase $\text{Ba}_2\text{In}_{2-x}\text{Mn}_x\text{O}_{5+x}$ samples were successfully prepared at 1300 °C in air with x up to 0.7. Figure 4.6 illustrated the XRD patterns of the solid solution. For the samples with a higher Mn content, impurity peaks appeared in the XRD patterns.

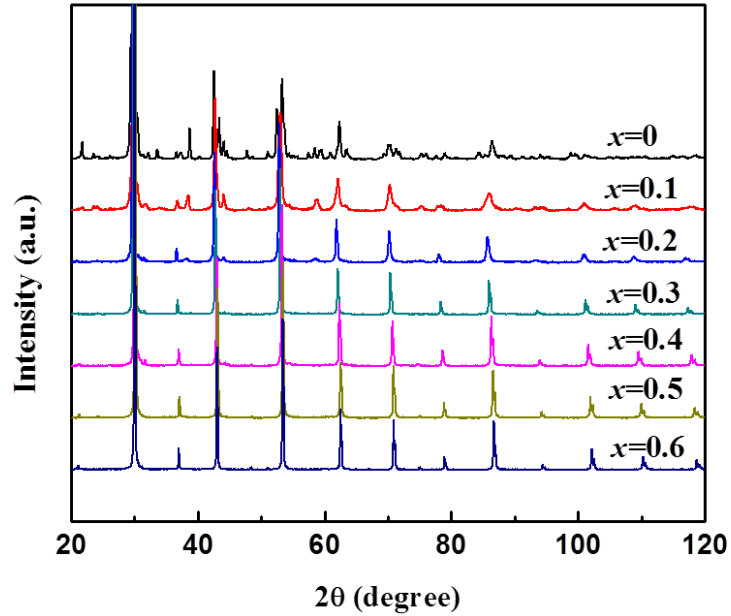


Figure 4.6 Powder X-ray diffraction patterns of $\text{Ba}_2\text{In}_{2-x}\text{Mn}_x\text{O}_{5+x}$ samples ($x = 0 - 0.6$).

Both X-ray and neutron powder diffraction data were collected to analyze the structure of the phases. The orthorhombic symmetry of $\text{Ba}_2\text{In}_2\text{O}_5$ is maintained for $x = 0.1$. The symmetry has increased to tetragonal for $x = 0.2$. Cubic symmetry with a unit cell expected for the ideal perovskite structure is indicated for samples with $x = 0.3$ to 0.7. The peaks associated with the O vacancy ordering and the two sites for In (Mn)

have disappeared for the cubic patterns. This symmetry evolution is consistent with that reported [9]. The unit cell edges vs. x are given in figure 4.7. For the orthorhombic $x = 0.0$ and 0.3 phases, a and c are divided by $\sqrt{2}$ and b is divided by 4. For the tetragonal phase with $x = 0.2$, a is divided by $\sqrt{2}$ and c is divided by 4. This allows a direct comparison with the values for the cubic phases. The open squares are unit cell parameters from low temperature (12 K) neutron data. A decrease in lattice parameter is observed from the refinement data as Mn is smaller than In exclusively for various oxidation states.

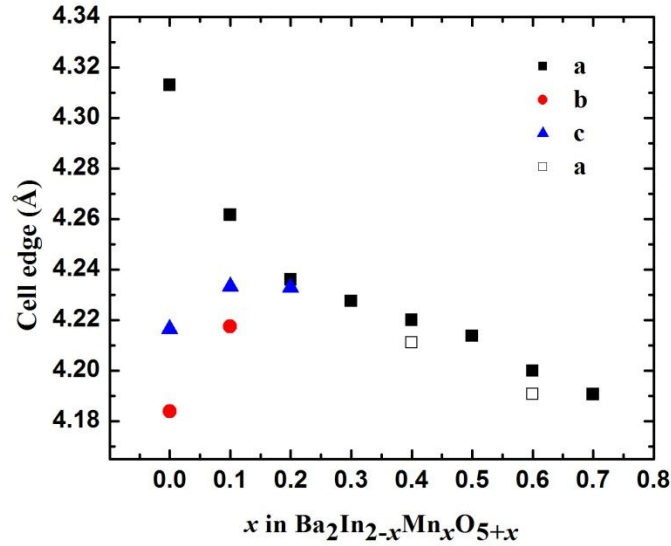


Figure 4.7 Cell edges for Ba₂In_{2-x}Mn_xO_{5+x} phases as a function of x .

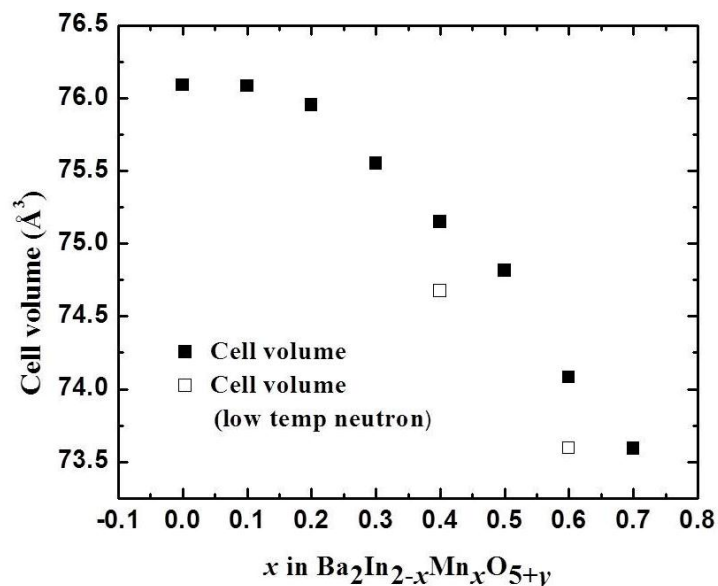


Figure 4.8 Cell volume for Ba₂In_{2-x}Mn_xO_{5+x} phases as a function of x .

The cell volume vs. x figure (figure 4.8) also provides a steady decrease curve. For the orthorhombic and tetragonal phases, pseudo-cubic cell edges from figure 4.7 were used for calculation. This allows a direct comparison with the values for the cubic phases. The open squares are unit cell parameters from low temperature (12 K) neutron data. Structure with ordered vacancies normally has bigger cell volume than disordered structures. And this can explain the existence of the small plateau formed from the points with orthorhombic and tetragonal structures.

Magnetic susceptibility data for a temperature range of 5-300K was collected on PPMS using ACMS mode. The inverse susceptibility data was plotted in figure 4.9. All the samples showed paramagnetic behavior.

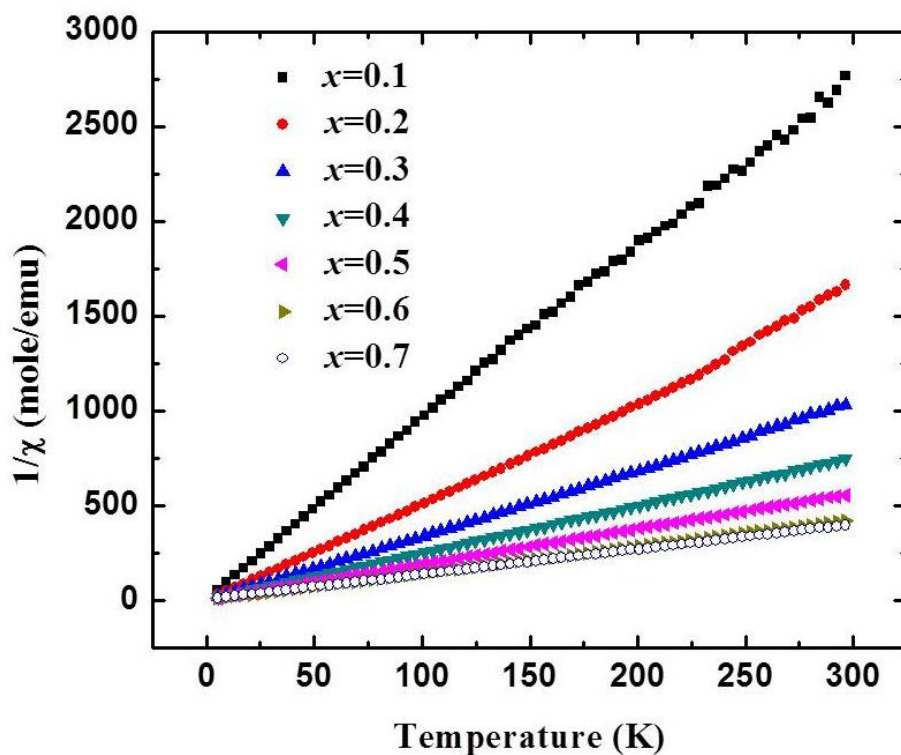


Figure 4.9 Inverse magnetic susceptibility of $\text{Ba}_2\text{In}_{2-x}\text{Mn}_x\text{O}_{5+y}$ for $x = 0.1-0.7$.

Various temperature ranges were used for the calculation of Curie and Weiss constants. For samples with $x = 0.1 - 0.3$, 5-300K was the temperature range as in such dilute system, Curie Law should be obeyed rather than Curie-Weiss Law. The small intercept from the linear regression supported this method. For samples with x higher than 0.3, 150-300K temperature range was taken for calculation. The Curie and Weiss Constants were derived from the slope and intercept of the straight line region of inverse magnetic susceptibility versus temperature. A summary of results is given in Table 4.1.

Table 4.1 Summary of magnetic data (as prepared) (Observed magnetic moments (μ_B , Bohr magnetons) per Mn for $\text{Ba}_2\text{In}_{2-x}\text{Mn}_x\text{O}_{5+x}$ as prepared)

As prepared $\text{Ba}_2\text{In}_{2-x}\text{Mn}^{5+}_x\text{O}_{5+x}$			
x	Magnetic moment	Curie constant	Intercept
0.2	2.80	0.19	0.91
0.3	2.74	0.28	9.55
0.4	2.84	0.40	0.33
0.5	2.94	0.53	-1.22
0.6	3.06	0.69	3.88
0.7	2.97	0.76	-5.02

Expected spin-only moments (μ_B): 5.92(Mn^{2+}), 4.90(HS Mn^{3+}), 3.87(Mn^{4+}), 2.83(Mn^{5+}), and 1.73(Mn^{6+}).

The expected spin-only moment (μ_B) for Mn^{3+} (high spin) is 4.90. The experimental value is way lower than the theoretical value. And this indicates two unpaired electrons per Mn for all samples as prepared, for which the expected spin-only moment is 2.83. Low spin Mn^{3+} is predicted to be possible in transition metal oxides [15]. However, only theoretical calculation exists in LiMnO_2 and no example could be found in brownmillerite-type structure oxides [16]. Mn^{5+} , by contrast, is known to be existed in oxides and produce turquoise color [12, 13]. The oxidation state of Mn in any possible Mn containing impurity phase would be lower than 5+ and would therefore increase the susceptibility to values higher than we observe. Thus, in the $\text{Ba}_2\text{In}_{2-x}\text{Mn}_x\text{O}_{5+x}$ formula the x values are essentially the same in samples as prepared. However, the O content is variable for these samples. The formula will shift to higher oxygen content with Mn at an oxidation state of 5+. Thus the sample will be reduced and lose oxygen in the reduced atmosphere. TGA was conducted for all the samples. The sample was placed in the alumina crucible in TGA furnace and heated to

1000 °C in N₂. All the samples showed weight loss through the heating process and small weight gain in the cooling process. The percentage mass vs. temperature plot of Ba₂In_{1.5}Mn_{0.5}O_{5.5} is illustrated in figure 4.10 as an example.

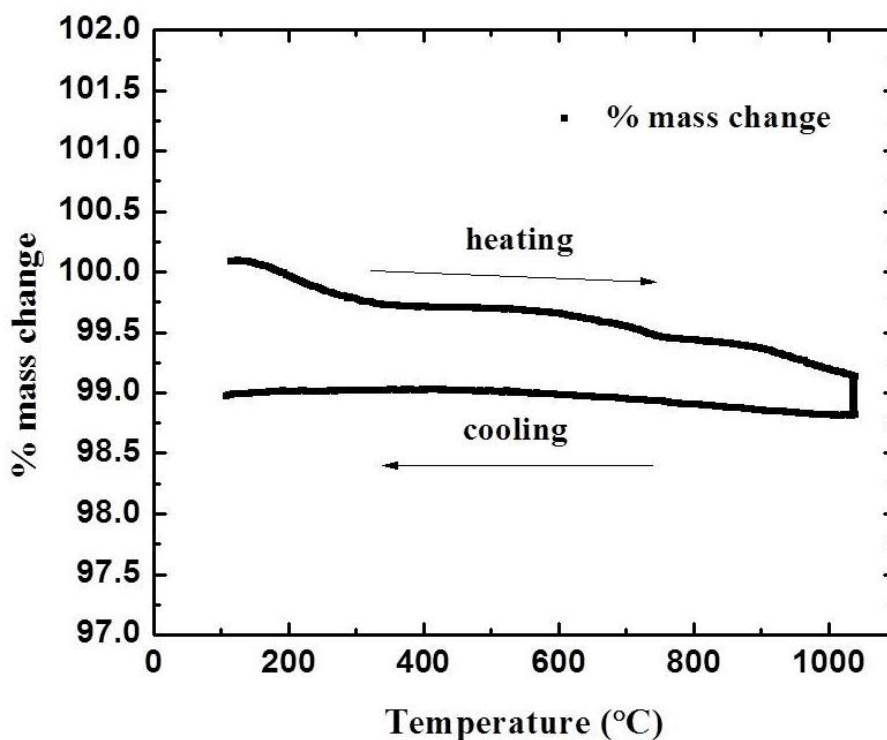


Figure 4.10 Thermal Gravimetric Analysis of Ba₂In_{1.5}Mn_{0.5}O_{5.5} with a heating rate of 5 °C/min, and the maximum temperature is 1000 °C in N₂ atmosphere.

The weight loss is shown in the heating and dwelling process. This may be due to the reduction of Mn⁵⁺. And the small weight gain in the cooling process indicates possible pick up of oxygen atoms. The mass gained is smaller than the lost, as absorbing oxygen is more energy and time consuming.

Though TGA data showed weight loss (<1%), it is less than the calculated value with all Mn⁵⁺ reduced to Mn³⁺ (1.42%). Thus, the sample was weighed and reduced in H₂/N₂ at 500 °C. Different time periods of dwelling were tried and the mass

kept dropping as heating time became longer. After 4 hours, the mass remained constant indicating all the Mn^{5+} species were converted to Mn^{3+} . The mass loss is 1.7%, which is close to the theoretical value. The refinement of reduced sample gave a lattice parameter of 4.192 Å, smaller than that of as prepared which is 4.211 Å. This is reasonable as the structure lost oxygen and shrank. Samples with Mn content of 0.2 and 0.3 also went through this reduction process. Magnetic susceptibility was measured for all the reduced samples and the summary of magnetic data is in table 4.2. The values of as-prepared samples are given to be compared. Apparently, the magnetic moment moves higher and is close to Mn^{3+} high spin value. This is consistent with the mass loss.

Table 4.2 Summary of magnetic data (as prepared and after reduction).

	As prepared (Ba₂In_{2-x}Mn⁵⁺_xO_{5+x})			After reduction (Ba₂In_{2-x}Mn³⁺_xO₅)		
<i>x</i>	Magnetic moment	Curie constant	Intercept	Magnetic moment	Curie constant	Intercept
0.2	2.80	0.19	0.91	4.99	0.62	-9.59
0.3	2.74	0.28	9.55	4.94	0.90	-13.44
0.4	2.84	0.40	0.33	-	-	-
0.5	2.94	0.53	-1.22	5.11	1.62	-17.23
0.6	3.06	0.69	3.88	-	-	-
0.7	2.97	0.76	-5.02	-	-	-

Expected spin-only moments (μ_B): 5.92(Mn^{2+}), 4.90(HS Mn^{3+}), 3.87(Mn^{4+}), 2.83(Mn^{5+}), and 1.73(Mn^{6+}).

Thus, a more general formula for the phases we have investigated would be $\text{Ba}_2\text{In}_{2-x}\text{Mn}_x\text{O}_{5+x}$ where the extra oxygen content can be as high as x for samples with Mn^{5+} and as low as 0.0 in phases containing Mn^{3+} . We have not conducted a complete study of O content for $\text{Ba}_2\text{In}_{2-x}\text{Mn}_x\text{O}_{5+y}$ phases under various conditions, but we

believe that the value of excess oxygen content is always less than that of x at the 1300 °C synthesis temperature with y increasing as the samples are cooled.



Figure 4.11 Colors of powders for $\text{Ba}_2\text{In}_{2-x}\text{Mn}_x\text{O}_{5+x}$ samples, left to right, $x = 0, 0.1, 0.2$ and 0.3 .

The color of $\text{Ba}_2\text{In}_2\text{O}_5$ is pale yellow. Small amount of Mn tunes the color to turquoise and bright green. As more Mn is dissolved in this system, the color becomes darker green finally merges to black. The colors and diffuse reflectance spectra of the as prepared $\text{Ba}_2\text{In}_{2-x}\text{Mn}_x\text{O}_{5+x}$ phases are shown in figures 4.11 and 4.12. Spectra for $x=0$ ($\text{Ba}_2\text{In}_2\text{O}_5$: white color) is shown for comparison. The light yellow color of the pure $\text{Ba}_2\text{In}_2\text{O}_5$ is due to tailing of a band edge into the visible region. As Mn is substituted for In, a turquoise to green color develops. The color originates from additional optical absorption at both the high and low energy regions of the visible spectrum (Fig. 4.2.3.7). As x increases the absorption minimum in the middle of the visible region is increasingly filled in, and samples with x higher than 0.3 become darker and finally appear black for $x = 0.7$, even though the minimum in the visible spectrum persists.

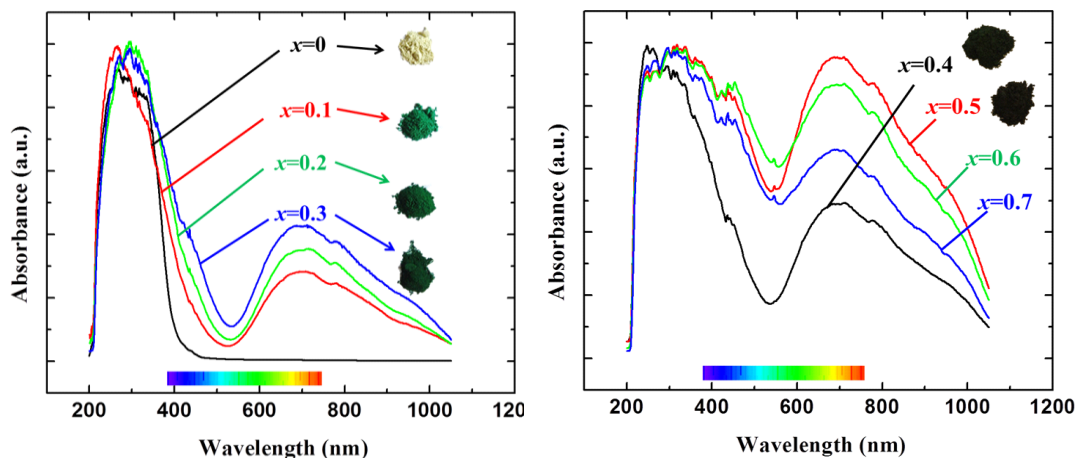


Figure 4.12 Diffuse reflectance spectra for $\text{Ba}_2\text{In}_{2-x}\text{Mn}_x\text{O}_{5+x}$ with colors of the sample with varying x .

Reinen [13] observed green to blue color in the compounds with Mn (V) sitting in the tetrahedral site. The reflectance spectra exhibited peaks which are contributed from charge transfer and d-d transition. The diffuse spectrum of the reference and the energy levels are illustrated in figure 4.13. The figure on the left showed energies of the spin- and symmetry-allowed transitions (D_{2d}). The energies were calculated with the parameters $\Delta = 14350$ (10600) cm^{-1} , $B = 500$ cm^{-1} for the tetrahedral angles 113.6° and 118.5° (116.5°). The angle 113.6° refers to the geometry of the PO_4^{3-} tetrahedra. The right figure illustrates the term diagram of Mn (V) in Td symmetry, in a compressed DM geometry. The figure is schematic and demonstrates only nearest excited states. And the consideration of spin-orbit coupling is included.

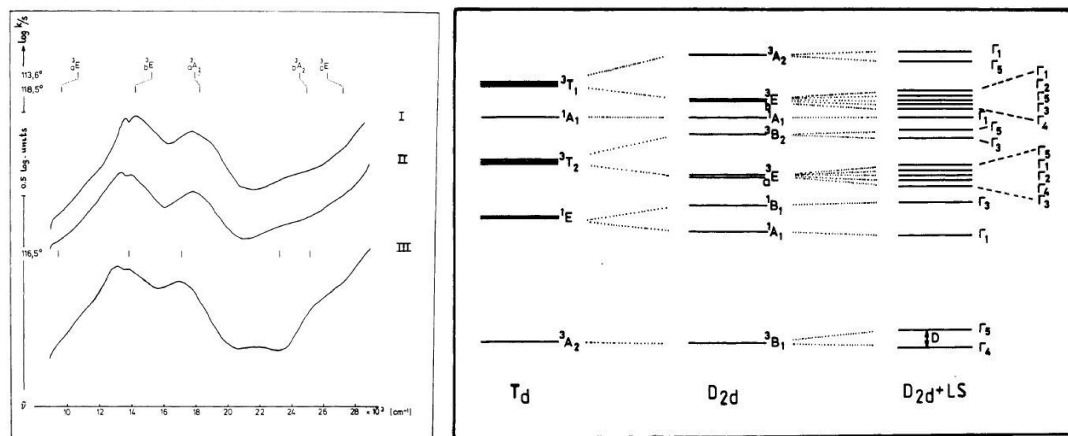
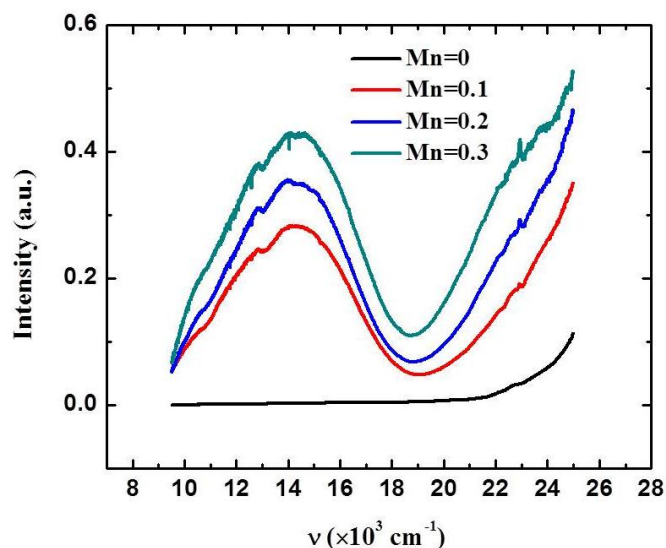


Figure 4.13 Reflection spectra of Mn (V)-doped (1 mol 7%) spodiosite-type compounds $\text{Ca}_2(\text{PO}_4)\text{Cl}$ (I), $\text{Ca}_2(\text{VO}_4)\text{Cl}$ (II), and $\text{Sr}_2(\text{VO}_4)\text{Cl}$ (111). (Reproduction of reference 13)

For the prepared samples, the x-axis is converted to wave number to compare to the reference (figure 4.14). Similar peaks were observed at 13000 and 15000 cm^{-1} and the shift compared to the reference may relate to different states and host. The reduced samples, which were black powder, did not exhibit any peak in the range mentioned above. And this is a clue that Mn^{5+} disappeared in the reduced phases.



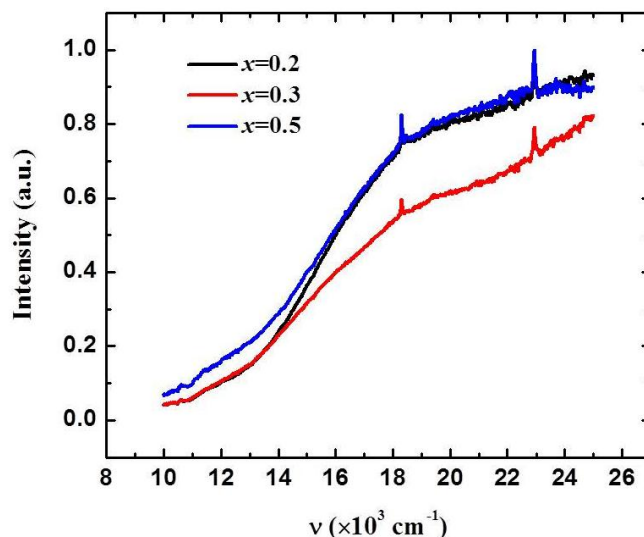


Figure 4.14 Reflection spectra of $\text{Ba}_2\text{In}_{2-x}\text{Mn}_x\text{O}_{5+x}$ for as prepared samples (above) and reduced samples (below).

All the structural studies were based on the Rietveld fitting of neutron diffraction patterns. Two independent studies have recently concluded that the most appropriate space group to describe the room temperature structure of $\text{Ba}_2\text{In}_2\text{O}_5$ is *Icmm* [7, 8]. This space group was found to be suitable for our Rietveld refinements of orthorhombic $\text{Ba}_2\text{In}_{1.9}\text{Mn}_{0.1}\text{O}_{5.1}$. Substitution of Mn for In occurs almost exclusively on the tetrahedral site. Refinement of the occupancy for the O site indicates a small increase in O content as Mn is substituted for In. Comparison between $\text{Ba}_2\text{In}_2\text{O}_5$ and Mn = 0.1 sample was summarized in Table 4.3. And further details are in Figure 4.15 and table 4.4.

Table 4.3 Structural summary for orthorhombic $\text{Ba}_2\text{In}_{2-x}\text{Mn}_x\text{O}_{5+x}$ phases*.

	$\text{Ba}_2\text{In}_2\text{O}_5^7$	$\text{Ba}_2\text{In}_{1.9}\text{Mn}_{0.1}\text{O}_{5.1}$
<i>a</i>	6.099	6.027

b	16.73	16.88
c	5.962	5.984
In – O1 ($\times 4$)	2.136	2.124
In – O2 ($\times 2$)	2.315	2.268
In/Mn2 – O2 ($\times 2$)	2.018	1.981
In/Mn2 – O3	2.065	1.956
In/Mn2 – O3	2.117	2.112

* All standard deviations are less than ± 1 for the last digit. The crystal structure of $\text{Ba}_2\text{In}_{1.9}\text{Mn}_{0.1}\text{O}_{5.1}$ was refined in space group $Icmm$.

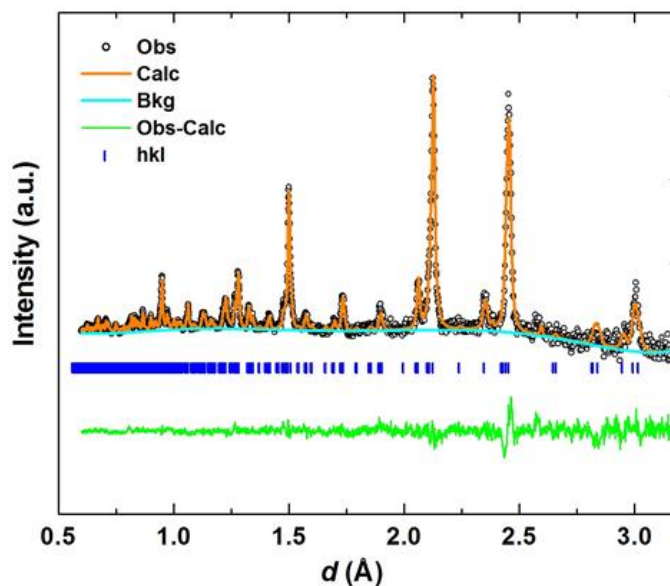


Figure 4.15 TOF neutron data of orthorhombic $\text{Ba}_2\text{In}_{1.9}\text{Mn}_{0.1}\text{O}_{5.1}$ are shown with Rietveld fit. The observed pattern displayed is from the highest-resolution bank (Bank 2) with d-spacing range 0.60 – 3.2 Å.

Table 4.4 TOF Neutron structural refinement of orthorhombic $\text{Ba}_2\text{In}_{1.9}\text{Mn}_{0.1}\text{O}_{5.1}$

General information	
Space group	$Icmm$
a (Å)	6.0265(5)
b (Å)	16.878(2)
c (Å)	5.9835(4)

$V(\text{\AA}^3)$				608.60(6)		
$R_p(\%)$				3.01		
$wR_p(\%)$				1.78		
Atomic coordinates and occupancy						
		x	y	z	occupancy	$U_{\text{iso}}(\text{\AA}^2)$
Ba	Ba	0.501(2)	0.6117(2)	0	1.00	0.0060(4)
In	In1	0	0	0	1.00	0.0012(1)
	In2	0.544(2)	1/4	0.466(2)	0.45(1)	0.0026(2)
Mn	Mn2	0.544(2)	1/4	0.466(2)	0.05(1)	0.0026(2)
O	O1	1/4	0.9967(6)	1/4	1.00	0.0100
	O2	0.005(3)	0.1344(3)	0	1.00	0.0442
	O3	0.669(2)	1/4	0.166(2)	0.57(2)	0.0357
Anisotropic thermal displacement parameters						
	$U_{11}(\text{\AA}^2)$	$U_{22}(\text{\AA}^2)$	$U_{33}(\text{\AA}^2)$	$U_{12}(\text{\AA}^2)$	$U_{13}(\text{\AA}^2)$	$U_{23}(\text{\AA}^2)$
O1	0.005(1)	0.022(2)	0.003(1)	0	-0.004(1)	0
O2	0.076(6)	0.035(3)	0.022(3)	0.004(8)	0	0
O3	0.06(1)	0.011(4)	0.031(5)	0	0.050(5)	0

Our Rietveld refinements of tetragonal $\text{Ba}_2\text{In}_{1.8}\text{Mn}_{0.2}\text{O}_{5.2}$ were conducted in space group $I4/mcm$. Refinement details are available in Table 4.5 and figure 4.16. The unit cell is now metrically very close to cubic (Figure 4.6), but diffraction peaks indicating a departure from the ideal cubic perovskite structure remain. Our Rietveld refinements indicate that Mn resides again almost exclusively in the “tetrahedral layer” and is displaced about 0.5 Å off the 4-fold axis. The increase in O content of this layer increases the average coordination number of In; thus, the average In displacement in this layer relative to the ideal perovskite site is smaller than for phases with $x = 0.0$ and 0.1. The displacement factors for all O atoms are large and indicate disorder extending beyond the “tetrahedral layer.”

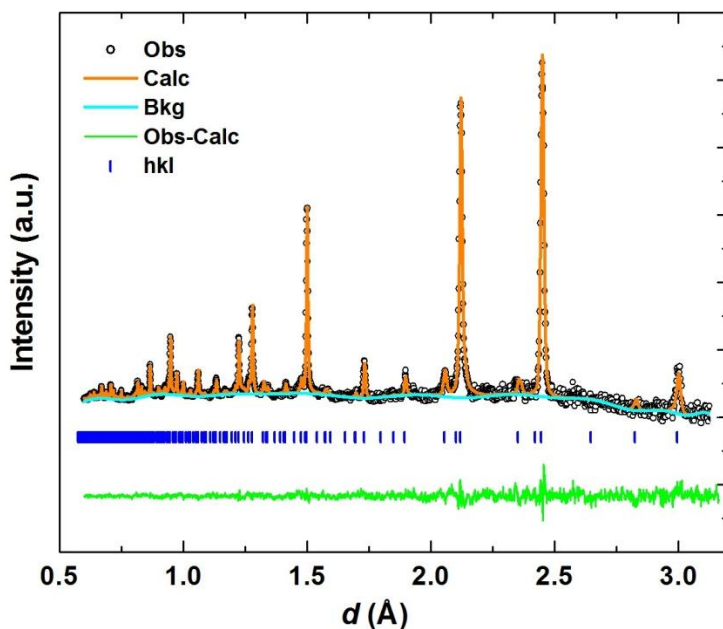


Figure 4.16 TOF neutron data of tetragonal $\text{Ba}_2\text{In}_{1.8}\text{Mn}_{0.2}\text{O}_{5.2}$ are shown with Rietveld fit. The observed pattern displayed is from the highest-resolution bank (Bank 2) with d-spacing range 0.60 – 3.2 Å.

Table 4.5 TOF neutron structural refinement of tetragonal $\text{Ba}_2\text{In}_{1.8}\text{Mn}_{0.2}\text{O}_{5.2}$

General information						
Space group			<i>I4/mcm</i>			
<i>a</i> (Å)			5.9896(4)			
<i>b</i> (Å)			5.9896(4)			
<i>c</i> (Å)			16.949(2)			
<i>V</i> (Å ³)			608.05(2)			
R _p (%)			2.64			
wR _p (%)			1.54			
Atomic coordinates and occupancy						
		<i>x</i>	<i>y</i>	<i>z</i>	occupancy	<i>U</i> _{iso} (Å ²)
Ba	Ba	0	1/2	0.6310(5)	1.00	0.0226
In	In1	0	0	0	0.76(1)	0.0379
	In2	0	0	1/4	1.00	0.0207
Mn	Mn1	0.087(4)	-0.031(4)	0	0.06(1)	0.011(2)
O	O1	1/4	1/4	1/4	1.00	0.0395
	O2	0.73(1)	0.23(1)	0	0.62(2)	0.0902

	O3	0	0	0.1213(6)	1.00	0.0427
Anisotropic thermal displacement parameters						
	$U_{11}(\text{\AA}^2)$	$U_{22}(\text{\AA}^2)$	$U_{33}(\text{\AA}^2)$	$U_{12}(\text{\AA}^2)$	$U_{13}(\text{\AA}^2)$	$U_{23}(\text{\AA}^2)$
Ba	0.018(2)	0.018(2)	0.032(5)	0.004(5)	0	0
In1	0.050(9)	0.050(9)	0.01(1)	0	0	0
In2	0.004(3)	0.004(3)	0.05(1)	0	0	0
O1	0.015(2)	0.015(2)	0.098(9)	-0.013(2)	0.016(5)	-0.016(5)
O2	0.126(9)	0.126(9)	0.020(8)	0.120(9)	0	0
O3	0.051(4)	0.051(4)	0.026(5)	0	0	0

The thermal parameters were refined and the ellipsoids for atoms are plotted in figure 4.17. The vertical four-fold axes go through both In1 and In2. The size and shape of the ellipsoids indicate the range of positional parameters caused by the disorder. The ellipsoids for In1 atoms indicate strong displacements perpendicular to the *c* axis; however, Mn atoms (shown for only one site) are displaced much more, as would be expected for Mn to achieve a tetrahedral environment. The displacements of Mn off the four-fold axis are in the direction expected. Refinement of the Mn content at this site is in good agreement with the overall Mn content, indicating that essentially all Mn is displaced as shown. The O-2 site is 66% occupied, and its ellipsoid shape is consistent with various positions for this O in forming a tetrahedral environment around Mn and some In1 as well as forming an octahedral environment around some In-1. The ellipsoids for Ba and O-1 are close to normal but somewhat large due the disorder. The ellipsoid shapes for In-2 and O-3 indicate that the disorder is no longer confined to the tetrahedral layer. This would be expected as the cell edges become metrically close to cubic. When we have well-formed chains of tetrahedra in this structure, they occur along either the *a* or *b* axis. The cell edge along which chains

form shrinks causing a reduction in symmetry from tetragonal to orthorhombic. The tetragonal symmetry we observe for $\text{Ba}_2\text{In}_{1.8}\text{Mn}_{0.2}\text{O}_{5.2}$ thus indicates that the chains are no longer extended along just one direction. The chains have been disrupted by the Mn substitution and the extra O. Now we have only chain fragments that have an equal probability of occurring along the a or the b axis.

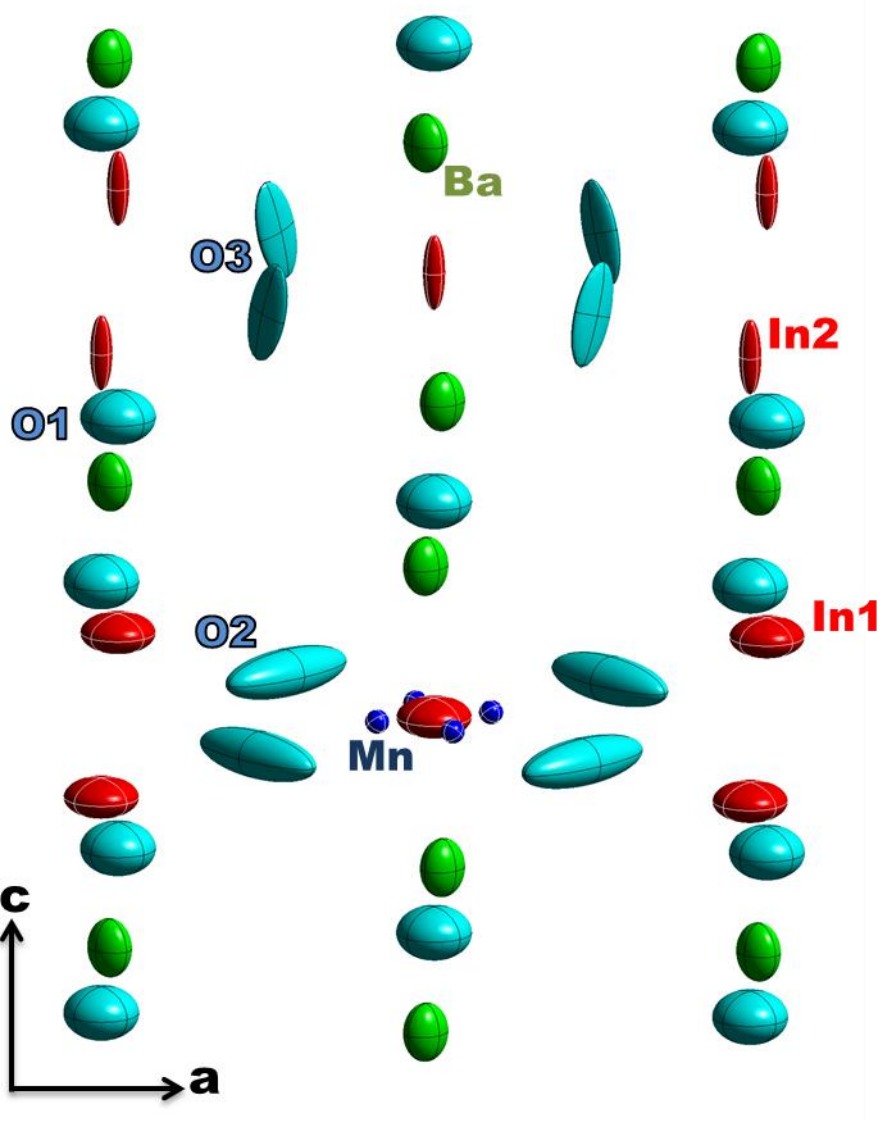


Figure 4.17 Ellipsoids for tetragonal $\text{Ba}_2\text{In}_{1.8}\text{Mn}_{0.2}\text{O}_{5.2}$: green Ba, red In, blue Mn and turquoise O.

Rietveld refinements for cubic $\text{Ba}_2\text{In}_{2-x}\text{Mn}_x\text{O}_{5+x}$ phases with $x = 0.4, 0.5$ and 0.6 were conducted in the $Pm3m$ space group for the ideal perovskite structure with just one In/Mn site. The superstructure peaks present in patterns with $x = 0.0, 0.1$ and 0.2 are now absent. The cubic cell edges decrease with increasing Mn substitution (Figure 4.7) because Mn is smaller than In regardless of the Mn oxidation state. Details of the Rietveld refinements are in table 4.6 and figure 4.18.

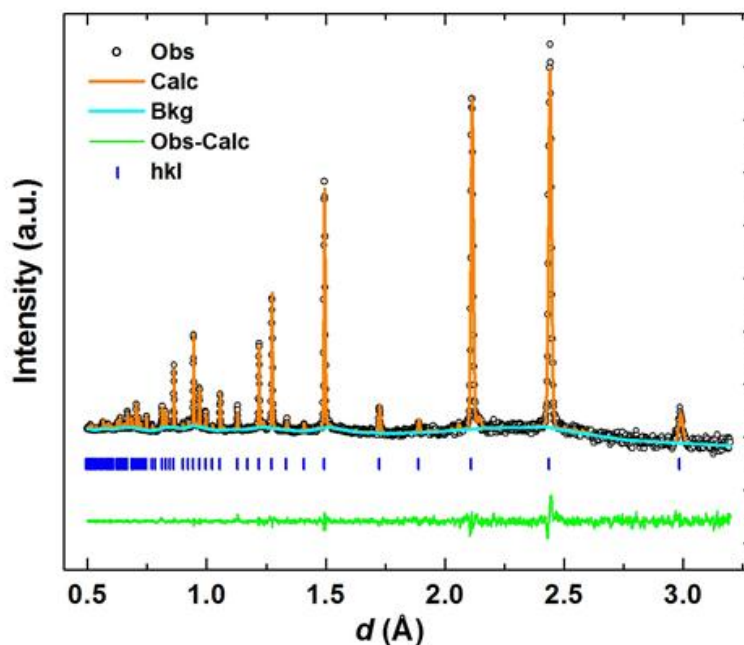


Figure 4.18 TOF neutron data of cubic $\text{Ba}_2\text{In}_{1.6}\text{Mn}_{0.4}\text{O}_{5.4}$ are shown with Rietveld fit. The observed pattern displayed is from the highest-resolution bank (Bank 2) with d-spacing range $0.60 - 3.2 \text{ \AA}$.

Table 4.6 TOF neutron structural refinement of cubic $\text{Ba}_2\text{In}_{1-x}\text{Mn}_x\text{O}_{5+x}$ samples

Mn x	Mn Occupancy	Cell a (\AA)	wR_p (%)	R_p (%)
0.40	0.36(1)	4.2208(1)	1.60	2.80
0.50	0.46(1)	4.2136(1)	5.73	4.89
0.60	0.56(1)	4.1998(1)	2.41	3.99
Mn x	Ba	In/Mn	O	

	$U_{\text{iso}} (\text{\AA}^2)$	$U_{\text{iso}} (\text{\AA}^2)$	$U_{11} (\text{\AA}^2)$	$U_{22} (\text{\AA}^2)$
0.40	0.0211(3)	0.0068(4)	0.0189(6)	0.0427(4)
0.50	0.0188(4)	0.0024(8)	0.0281(9)	0.0404(6)
0.60	0.0241(4)	0.0034(7)	0.028(1)	0.0404(6)

In summary, our conclusions concerning the oxidation states of Mn in as prepared and reduced $\text{Ba}_2\text{In}_{2-x}\text{Mn}_x\text{O}_{5+x}$ samples are based primarily on magnetic susceptibility. Given the dilution of Mn, these conclusions should be reliable. The colors we observe for as prepared $\text{Ba}_2\text{In}_{2-x}\text{Mn}_x\text{O}_{5+x}$ phases are those expected for Mn^{5+} , thus adding support to this Mn oxidation state. A small level of mixed valency for Mn in both as prepared and reduced samples is likely. At our 1300 °C calcination temperature Mn^{5+} seems unlikely, but oxidation of our samples during cooling will be facilitated by the established high O^{2-} mobility in these phases. The most likely coordination of Mn^{5+} by O is tetrahedral, and we find a strong preference of Mn for the “tetrahedral layer” in both orthorhombic $\text{Ba}_2\text{In}_{1.9}\text{Mn}_{0.1}\text{O}_{5.1}$ and tetragonal $\text{Ba}_2\text{In}_{1.8}\text{Mn}_{0.2}\text{O}_{5.2}$.

EPR of $\text{Ba}_2\text{In}_{1.98}\text{Mn}_{0.02}\text{O}_{5.02}$ was recorded at 10 K with 328.8 GHz and the spectrum is shown in figure 4.19. The top part is experimental curve while the bottom blue line is the magnified experimental spectrum with the central line cut off. The red curve exhibits simulated pattern with $g_x = 1.973$, $g_y = 1.965$, $g_z = 1.968$, $D = 1.608 \text{ cm}^{-1}$, $E = 0.495 \text{ cm}^{-1}$. The resonances at 5.4 and at 9.6 T are due to frozen oxygen [17].

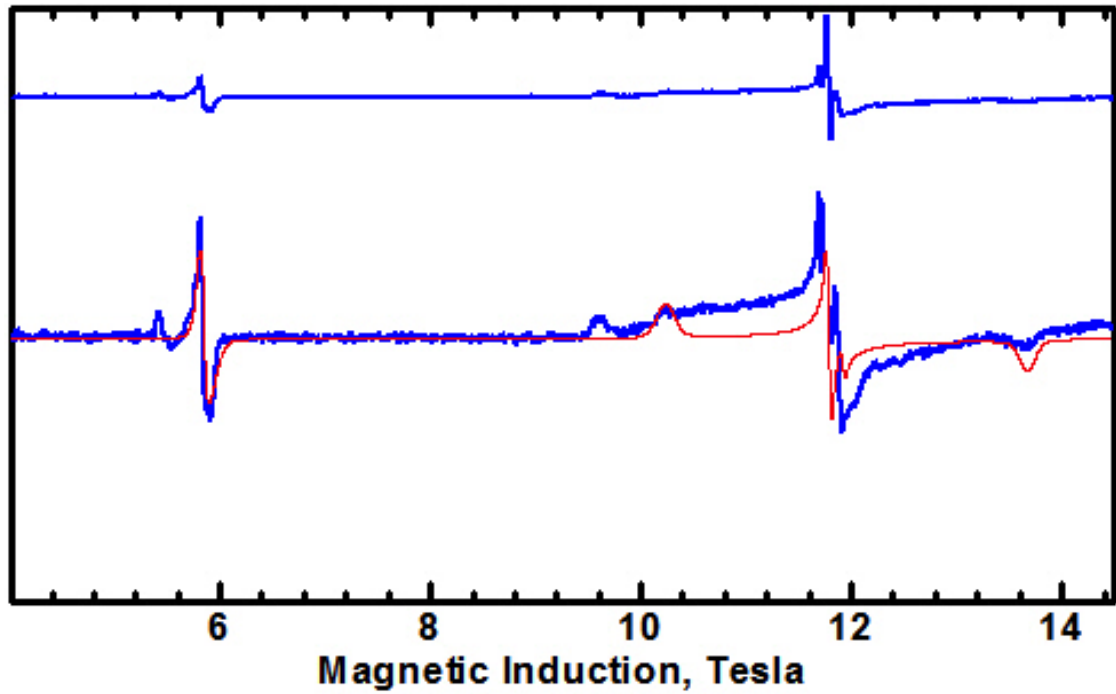


Figure 4.19 High-field EPR spectra for $\text{Ba}_2\text{In}_{1.98}\text{Mn}_{0.02}\text{O}_{5.02}$.

The EPR spectra were relatively difficult to obtain, showing line broadening due to metal-metal interactions at higher Mn concentrations, while the diluted samples were prone to microwave saturation effects. The best spectra were obtained for the $\text{Ba}_2\text{In}_{1.98}\text{Mn}_{0.02}\text{O}_{5.02}$ sample at 10 K. The spectra could be interpreted using the spin Hamiltonian

$$\hat{H}_S = \mu_B \mathbf{B} \cdot \{\mathbf{g}\} \cdot \hat{\mathbf{S}} + D \{ \hat{\mathbf{S}}_z^2 - S(S+1)/3 \} + E (\hat{\mathbf{S}}_x^2 - \hat{\mathbf{S}}_y^2)$$

assuming that they were due to the spin state $S = 1$. The spin Hamiltonian parameters were $g_x = 1.973$, $g_y = 1.965$, $g_z = 1.968$, $D = 1.608 \text{ cm}^{-1}$, $E = 0.495 \text{ cm}^{-1}$. The g values are consistent with a less than half-filled d subshell. Large D and E parameters render standard X or Q-Band EPR inapplicable to this problem. Since E is close to $D/3$, the sign of D cannot be determined and is actually irrelevant [17].

No simulation is possible assuming other spin states other than $S = 1$. For example, when $S = 2$ is assumed then a D three times smaller must be taken to get the outermost lines (at ~ 10.2 and ~ 13.7 Tesla), but then the 'forbidden' transition (at 5.86 T in experiment) will be calculated at a magnetic field too high and will be much less intense. The conclusion that Mn is present as Mn^{5+} is thus unambiguous.

4.2.4 Conclusion

Solid solution $\text{Ba}_2\text{In}_{2-x}\text{Mn}_x\text{O}_{5+x}$ ($x = 0.1-0.7$) was successfully synthesized by solid state reaction. All the single phases showed intense color from turquoise to green and finally dark green. These color compounds could be applied in the pigment industry as they are durable, environmental friendly. Mn appeared in 5+ in all the phases and this was confirmed by magnetic susceptibility data as well as the EPR study. The neutron refinement indicated that all the Mn^{5+} substitution occurred in the tetrahedral sites.

4.3 Study on Brownmillerite-type solid solution $\text{Ba}_2\text{In}_{2-x}\text{Fe}_x\text{O}_{5+y}$

4.3.1 Introduction

Our recent discovery of intense turquoise and green colors in brownmillerite-type oxides $\text{Ba}_2\text{In}_{2-x}\text{Mn}_x\text{O}_{5+x}$ has showed that Mn with higher oxidation state in tetrahedral site will give rise to bright colors. It would be interesting to investigate the other transition metal ions in $\text{Ba}_2\text{In}_2\text{O}_5$ oxygen deficient host. Fe^{3+} can be stabilized in both tetrahedral and octahedral coordination as seen in Fe_3O_4 spinel. Fe^{4+} was also found in tetrahedral sites in some oxides in various structures, including brownmillerite-type structure $\text{CaAl}_{0.5}\text{Fe}_{0.5}\text{O}_{2.5+\delta}$ [18, 19]. The similarity between Fe and Mn is seen in trigonal bipyramidal coordination in our recent studies [10, 20]. And this has prompted us to introduce Fe into the brownmillerite-type structure.

Barium ferrite ($\text{Ba}_2\text{Fe}_2\text{O}_5$), the other end member in this solid solution, has been investigated comprehensively since the Ba-Fe-O₂ system was studied by Gallagher [21]. Since then, the structure of $\text{Ba}_2\text{Fe}_2\text{O}_5$ has been intensely studied. Gallagher suggested it has orthorhombic unit cell and is a brownmillerite structure similar to YFeO_3 and $\text{Sr}_2\text{Fe}_2\text{O}_5$. Several works [22, 23] have been done utilizing Mössbauer spectroscopy, HREM and CIP. The structure of $\text{Ba}_2\text{Fe}_2\text{O}_5$ is described as monoclinic unit cell with cubic superstructure. The difficulty of structure determination rooted in the complicity of superstructures. Fe obtains various oxidation states in oxides which exhibit perovskite related structures. The common states are 3+ and 4+ as in $\text{BaFeO}_{2.5-3.0}$ and oxoperovskites [24]. Only a few oxides are known to present Fe^{4+} , BaFeO_3 [25] and Na_4FeO_4 [26] are examples. Fe^{5+} is relatively rare and the reason of existence is due to the disproportionation of Fe^{4+} into Fe^{3+} and Fe^{5+} [27].

And the possibility of Fe in high oxidation state is desired. As it may bring interesting colors if Fe is doped into $\text{Ba}_2\text{In}_2\text{O}_5$ as we explained in $\text{Ba}_2\text{In}_{2-x}\text{Mn}_x\text{O}_{5+x}$ system.

4.3.2 Synthesis

A solid state method was used for the synthesis of all the $\text{Ba}_2\text{In}_{2-x}\text{Fe}_x\text{O}_{5+y}$ samples. A stoichiometric mixture of BaCO_3 (Baker Analyze, >99%), In_2O_3 (Stanford Materials, >99.99%), and Fe_2O_3 (JMC, >98%) was thoroughly ground together in an agate mortar. The powder mixtures were then pressed into pellets with applied pressure of 1 psi. The pellets were heated at 1200 °C for 12 hours in air, reground, pelletized again, and finally heated at 1300 °C for another 12 hours.

4.3.3 Result and discussion

Conventional solid state reactions were used to prepare the samples in solid solution $\text{Ba}_2\text{In}_{2-x}\text{Fe}_x\text{O}_{5+y}$. Single phase samples were achieved with $x = 0.1-1.5$. For samples with x value higher than 1.5, extra peaks which cannot be indexed showed up. The X-ray plot of all the samples is shown in Figure 4.20. For Fe = 0.1-0.3 samples, the average structure can be described as orthorhombic. Upon an increase in Fe content, the orthorhombic distortion reduces gradually. The structure merged to a higher symmetry of cubic lattice for all the samples with higher Fe content. And

similar trend of lattice evolution was reported in other substitutions on both Ba and In sites [6, 17, 28].

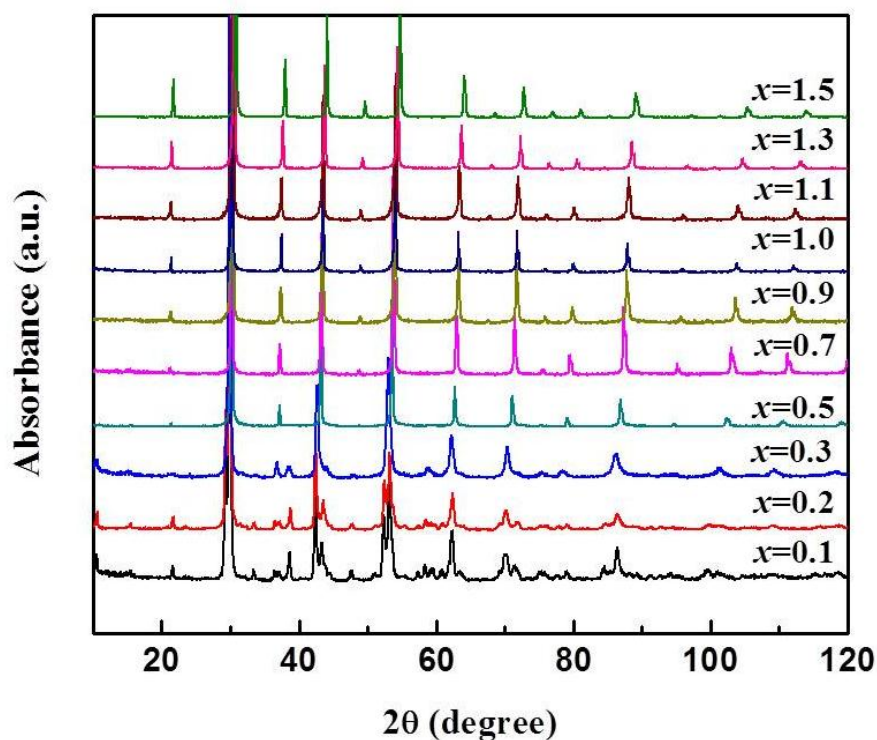


Figure 4.20 Powder X-ray diffraction patterns of $\text{Ba}_2\text{In}_{2-x}\text{Fe}_x\text{O}_{5+y}$ samples ($x = 0.1 - 1.5$).

Refinements of X-ray diffraction patterns are completed in GSAS software. Lattice parameters of orthorhombic phases are listed in table 4.7. The extent of the distortion is indicated in c/a ratio [29]. And it is obvious that the c/a ratio moves towards 1, which shows the increase of the symmetry. Lattice parameters of all the single phase samples are plotted with increasing Fe content in figure 4.21. For orthorhombic phases ($x = 0 - 0.3$), a and c are divided by $\sqrt{2}$ and b is divided by 4. This allows a direct comparison with the values for the cubic phases. Lattice parameter from neutron data is indicated in hollow symbols. The cell volume (figure

4.22) decreased with increase of Fe content. And this is reasonable as Fe is smaller in ionic size than In regardless of the value for oxidation state.

Table 4.7 Structural parameters of $\text{Ba}_2\text{In}_{2-x}\text{Fe}_x\text{O}_{5+y}$ solid solution

x	a (Å)	b (Å)	c (Å)	c/a
0	6.099	16.737	5.962	0.978
0.1	6.095	16.752	5.972	0.980
0.2	6.086	16.652	5.974	0.982
0.3	6.098	16.851	5.981	0.981

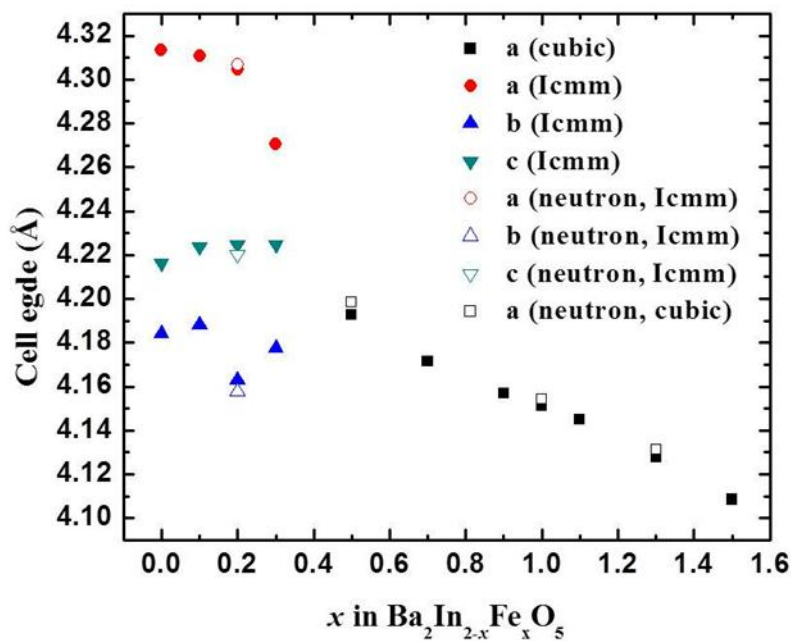


Figure 4.21 Cell edges for $\text{Ba}_2\text{In}_{2-x}\text{Fe}_x\text{O}_{5+y}$ phases as a function of x .

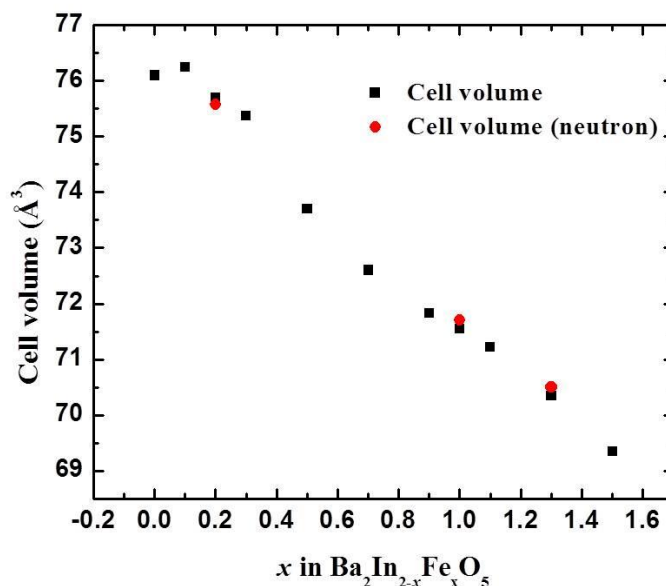


Figure 4.22 Cell volume data for Ba₂In_{2-x}Fe_xO_{5+y} phases. The volume of orthorhombic phases are multiplication of the converted *a*, *b* and *c* value.

Time of flight neutron diffraction data were collected in ORNL for compositions with $x = 0.2, 0.5, 1.0, 1.3$ and 1.5 . The $x = 0.2$ sample is orthorhombic while all the others exhibit cubic patterns. Rietveld refinement using GSAS software was conducted. The Rietveld fit of Ba₂In_{1.8}Fe_{0.2}O_{5+y} employing space group *Icmm* is illustrated in figure 4.23. The noise in the background of the low angle region makes the refinement difficult to be converged and the intensity of some of the superstructure peaks are similar to the background level. The refinement indicates that Fe ions mainly occupy the tetrahedral sites and this was observed in the Ba₂In_{2-x}Mn_xO_{5+x} solid solutions. And the refined oxygen occupancy is close to 5.

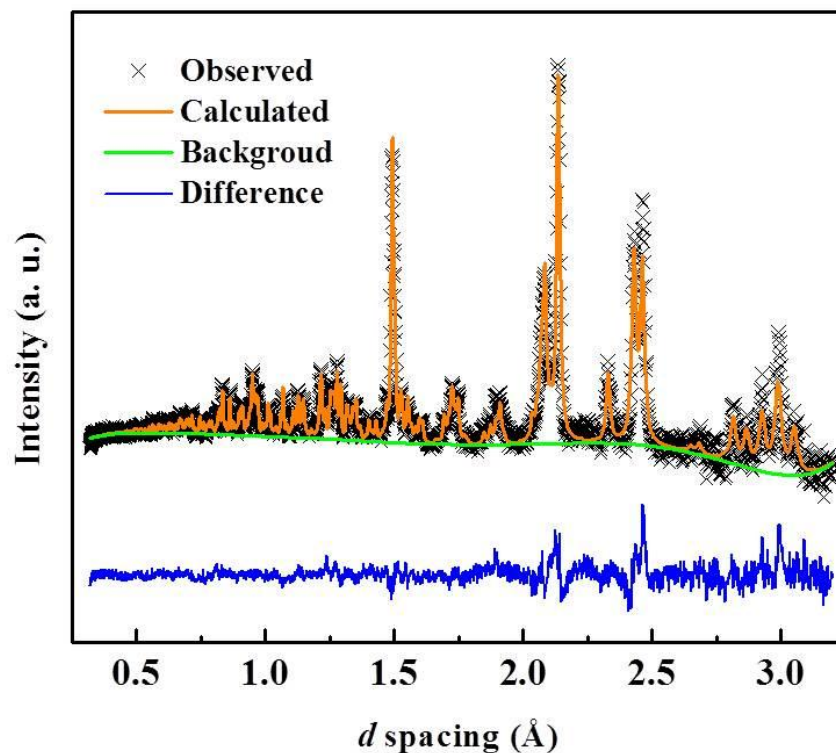


Figure 4.23 TOF neutron data of orthorhombic $\text{Ba}_2\text{In}_{1.8}\text{Fe}_{0.2}\text{O}_{5+y}$ are shown with Rietveld fit. The observed pattern displayed is from the highest-resolution bank (Bank 2) with d -spacing range 0.60 – 3.2 Å.

For all the other cubic compositions, cubic space group $Pm\bar{3}m$ was employed to conduct the refinement. $\text{Ba}_2\text{In}_{1.5}\text{Fe}_{0.5}\text{O}_{5+y}$ with Rietveld fit was illustrated in figure 4.24 as an example of all the cubic phases. Only one site of In/Fe occurs in the ideal cubic perovskite structure. The peaks indicating superstructure presents in the orthorhombic phase are now absent due to the evolution of structure symmetry. The refined cell edges are in agreement with the X-ray refinement results (figure 4.3.3.3) and a decrease of cell volume as well as cell edge exhibited with the increase of Fe content.

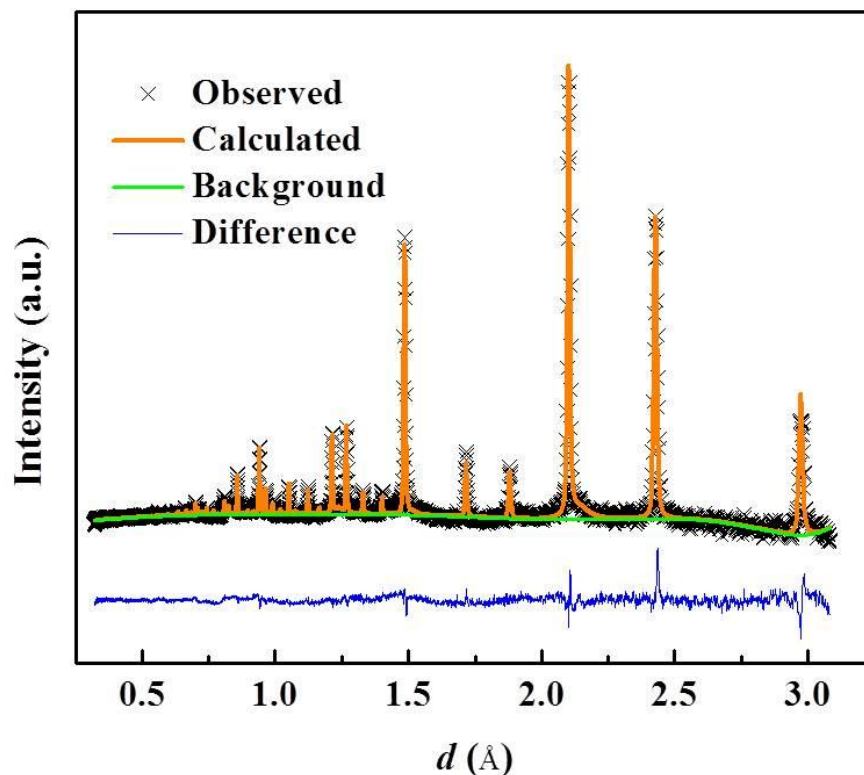


Figure 4.24 TOF neutron data of cubic $\text{Ba}_2\text{In}_{1.5}\text{Fe}_{0.5}\text{O}_{5+y}$ are shown with Rietveld fit. The observed pattern displayed is from the highest-resolution bank (Bank 2) with d-spacing range 0.60 – 3.2 Å.

The color of $\text{Ba}_2\text{In}_2\text{O}_5$ is pale yellow. Small amount of Fe ($x=0.1-0.3$) changed the color to green, and for samples with higher Fe content the colors are all black. Figure 4.25 shows the plot of absorbance for Fe = 0.1, 0.2, 0.3 samples. The color of the pure $\text{Ba}_2\text{In}_2\text{O}_5$ is from the tailing of a band edge into the visible region. As Fe is doped into the system, another absorption hump showed up in the region of 500 nm and 700nm. And this is due to the d-d transition of the d electrons in Fe. With higher Fe content, the hump became higher and merged into the band edge in the high energy region and this made the sample almost showed black color.

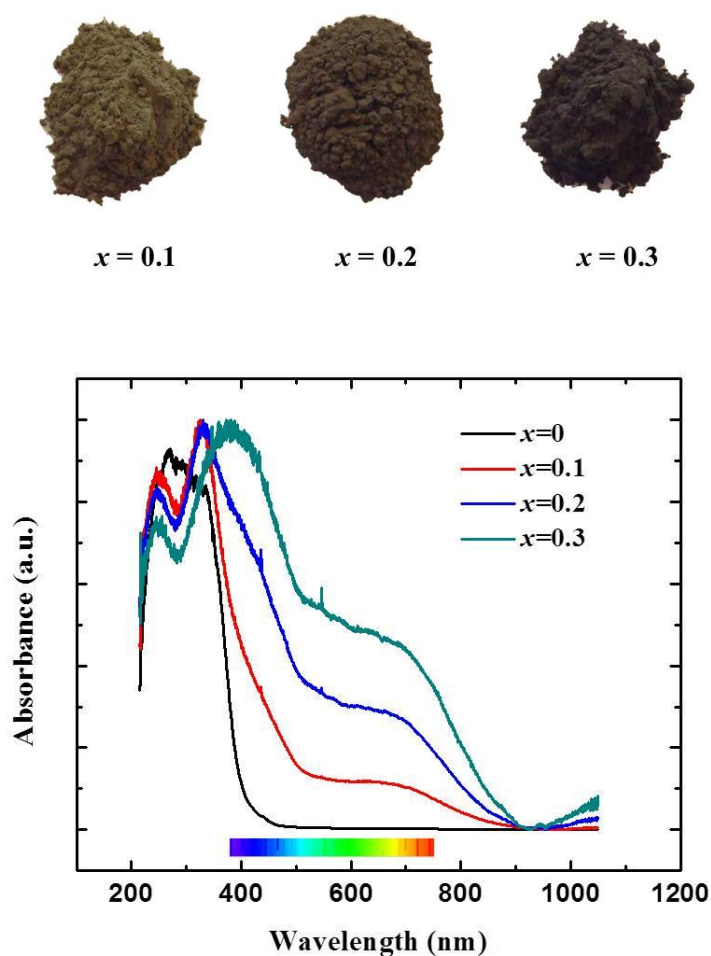


Figure 4.25 Pictures of prepared samples (above) and diffuse reflectance spectra (below) for $\text{Ba}_2\text{In}_{2-x}\text{Fe}_x\text{O}_{5+y}$ samples. Spectra for $x = 0$ ($\text{Ba}_2\text{In}_2\text{O}_5$; pale yellow color) is shown for comparison.

Inverse magnetic susceptibility vs. temperature figure is shown in Figure 4.26. All samples showed paramagnetic behavior. Inverse magnetic susceptibility data ranging from 150K to 320K was taken to fit for Curie-Weiss law. Calculated magnetic moments are listed in Table 4.8. The experimental magnetic moments are much lower than expected Fe^{3+} high spin value, and this is similar to the solid solution $\text{Ba}_2\text{In}_{2-x}\text{Mn}_x\text{O}_{5+x}$. In this system, magnetic moment values in between different oxidation

states rather than equals to one oxidation states exactly, which indicates the existence of mixed valency. The possibility of Fe^{5+} is excluded by the Mössbauer spectroscopy. As Fe^{5+} will show negative isomer shift in the spectrum, and this is not observed from our Mössbauer spectra. For the samples with $x = 0.1$ -1.1, experimental value was between the value of Fe^{3+} and Fe^{4+} low spin value, and this is an indication of a mixture of these two oxidation states. Though for samples with high Fe content ($x = 1.3$ and 1.5), the observed value is closest to Fe^{5+} , Mossbauer study did not see any existence of Fe^{5+} .

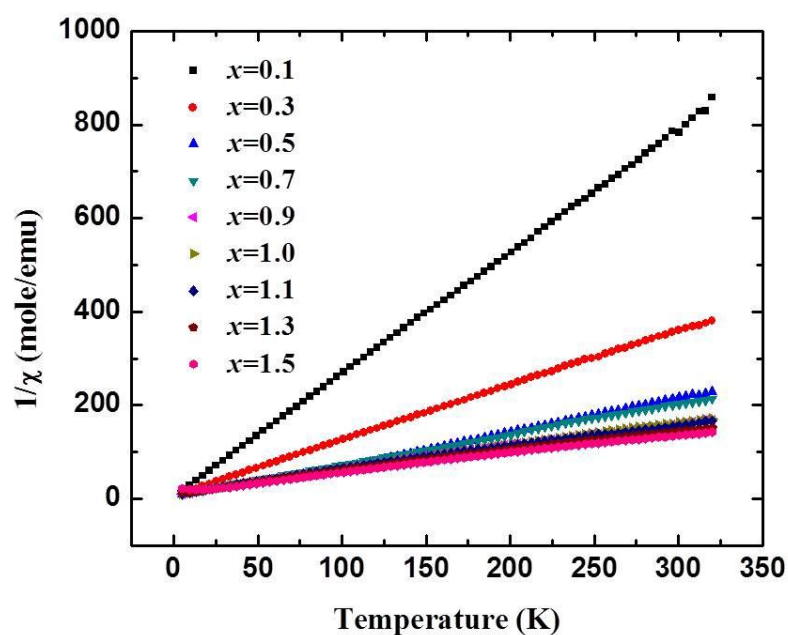


Figure 4.26 Inverse magnetic susceptibility data of $\text{Ba}_2\text{In}_{2-x}\text{Fe}_x\text{O}_{5+y}$ for $x = 0.1$ -1.5.

Table 4.8 Magnetic moments of $\text{Ba}_2\text{In}_{2-x}\text{Fe}_x\text{O}_{5+y}$ for $x = 0.1-1.5$

x	μ_B (obs)	$\mu_B \text{Fe}^{3+}$ (high spin)	$\mu_B \text{Fe}^{4+}$ (high spin)	$\mu_B \text{Fe}^{4+}$ (low spin)
0.1	1.716	1.872	1.549	0.894
0.3	2.680	3.243	2.683	1.549
0.5	3.372	4.183	3.464	2.000
0.7	3.699	4.950	4.099	2.366
0.9	4.227	5.613	4.648	2.683
1.0	4.328	5.916	4.899	2.828
1.1	4.277	6.205	5.138	2.967
1.3	4.794	6.745	5.586	3.225
1.5	4.878	7.246	6.000	3.464

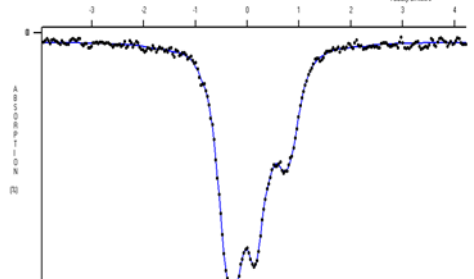
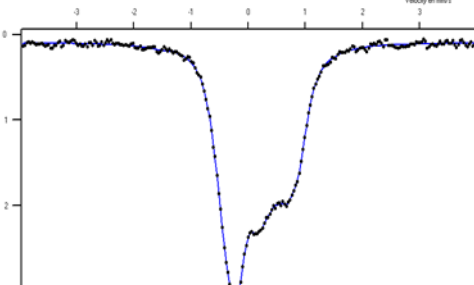
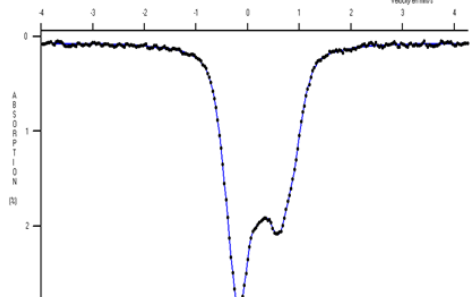
Mössbauer spectroscopy was employed to clarify the oxidation state and the valence of Fe in this solid solution. The spectra were recorded from 4.2 K to 293 K. The calculation of the spectra was carried out in two steps using two computer programs. A first method of calculation was used to adjust the spectra using Lorentzian profile lines. The position, amplitude and width of each line are parameters that can be refined. This first approach allows us to deduce the experimental hyperfine parameters of iron sites. A second method of calculation was used to strip the spectra in terms of distribution of hyperfine parameters $P(\Delta)$ and $P(B)$ by the method of Hesse and Rubartsch [30]. This method is often used for disordered compounds in

which there is a wide distribution of possible environments that results in the experimental spectrum by lines of large width and the shape can deviate from a Lorentzian profile.

Samples with Fe content equals to 0.1, 0.3, 0.5, 1.0 and 1.5 were analysed with Mössbauer spectroscopy. Generally, the mixed valency of $\text{Fe}^{3+}/\text{Fe}^{4+}$ was observed within all the samples [31]. The ratio of these two species differs, though. The mixed valency is also confirmed by the lower magnetic moment obtained from magnetic data. The resolution of the compounds with low Fe content ($x=0.1$ and 0.3) is very low due to the dilution of Fe ions. The Mössbauer spectra of all the samples and the calculated distribution are illustrated in table 4.9.

Table 4.9 Summary of Mössbauer data of $\text{Ba}_2\text{In}_{2-x}\text{Fe}_x\text{O}_{5+y}$

x	Experimental spectrum	Calculated distribution	% Fe^{4+}															
0.1		<table><tr><th>DIS</th><th>δ (mm/s)</th><th>%</th><th>Fe^{3+}</th><th>Fe^{4+}</th></tr><tr><td>D1</td><td>0.25</td><td>47</td><td>34</td><td>13</td></tr><tr><td>D2</td><td>0.13</td><td>53</td><td>22</td><td>31</td></tr></table>	DIS	δ (mm/s)	%	Fe^{3+}	Fe^{4+}	D1	0.25	47	34	13	D2	0.13	53	22	31	44
DIS	δ (mm/s)	%	Fe^{3+}	Fe^{4+}														
D1	0.25	47	34	13														
D2	0.13	53	22	31														
0.3		<table><tr><th>DIS</th><th>δ (mm/s)</th><th>%</th><th>Fe^{3+}</th><th>Fe^{4+}</th></tr><tr><td>D1</td><td>0.19</td><td>37</td><td>21</td><td>16</td></tr><tr><td>D2</td><td>-0.01</td><td>63</td><td>0</td><td>63</td></tr></table>	DIS	δ (mm/s)	%	Fe^{3+}	Fe^{4+}	D1	0.19	37	21	16	D2	-0.01	63	0	63	79
DIS	δ (mm/s)	%	Fe^{3+}	Fe^{4+}														
D1	0.19	37	21	16														
D2	-0.01	63	0	63														

0.5		<table><tr><th>DIS</th><th>δ (mm/s)</th><th>%</th><th>Fe³⁺</th><th>Fe⁴⁺</th></tr><tr><td>D1</td><td>0.21</td><td>19</td><td>12</td><td>7</td></tr><tr><td>D2</td><td>0.16</td><td>22</td><td>11</td><td>11</td></tr><tr><td>D3</td><td>-0.04</td><td>59</td><td>0</td><td>59</td></tr></table>	DIS	δ (mm/s)	%	Fe ³⁺	Fe ⁴⁺	D1	0.21	19	12	7	D2	0.16	22	11	11	D3	-0.04	59	0	59	77
DIS	δ (mm/s)	%	Fe ³⁺	Fe ⁴⁺																			
D1	0.21	19	12	7																			
D2	0.16	22	11	11																			
D3	-0.04	59	0	59																			
1		<table><tr><th>DIS</th><th>δ (mm/s)</th><th>%</th><th>Fe³⁺</th><th>Fe⁴⁺</th></tr><tr><td>D1</td><td>0.20</td><td>33</td><td>19</td><td>14</td></tr><tr><td>D2</td><td>0.16</td><td>34</td><td>17</td><td>17</td></tr><tr><td>D3</td><td>-0.04</td><td>33</td><td>0</td><td>33</td></tr></table>	DIS	δ (mm/s)	%	Fe ³⁺	Fe ⁴⁺	D1	0.20	33	19	14	D2	0.16	34	17	17	D3	-0.04	33	0	33	64
DIS	δ (mm/s)	%	Fe ³⁺	Fe ⁴⁺																			
D1	0.20	33	19	14																			
D2	0.16	34	17	17																			
D3	-0.04	33	0	33																			
1.5		<table><tr><th>DIS</th><th>δ (mm/s)</th><th>%</th><th>Fe³⁺</th><th>Fe⁴⁺</th></tr><tr><td>D1</td><td>0.25</td><td>35</td><td>25</td><td>10</td></tr><tr><td>D2</td><td>0.19</td><td>28</td><td>16</td><td>12</td></tr><tr><td>D3</td><td>0.09</td><td>37</td><td>10</td><td>27</td></tr></table>	DIS	δ (mm/s)	%	Fe ³⁺	Fe ⁴⁺	D1	0.25	35	25	10	D2	0.19	28	16	12	D3	0.09	37	10	27	49
DIS	δ (mm/s)	%	Fe ³⁺	Fe ⁴⁺																			
D1	0.25	35	25	10																			
D2	0.19	28	16	12																			
D3	0.09	37	10	27																			

The existence of Fe⁴⁺ is confirmed by both magnetism and Mössbauer spectra. Presumably, the weight loss due to the oxygen content change should appear in the TGA data. The TGA graph of the Ba₂InFeO_{5+y} sample is shown in figure 4.27. A weight loss occurred in the low temperature heating region (<500°C). The parent Ba₂In₂O₅ was reported to experience a structure transition in the moisture atmosphere at low temperature, and this structure transition is reflected in the TGA data as a weight loss [32, 33]. Thus the weight loss in this region could be possibly addressed to the structure transition. Through the dwelling process which is labeled in the figure, a slight mass decrease around 0.3% percent presents, and this could be considered as the

oxygen content change. The accurate theoretical weight loss is not able to be calculated because of the mixed valency. However, the change in the valance of Fe is still proved from TGA data. A small weight gain is exhibited in the cooling process. And it is probably because the compound picked up oxygen atoms slowly to equilibrium at room temperature.

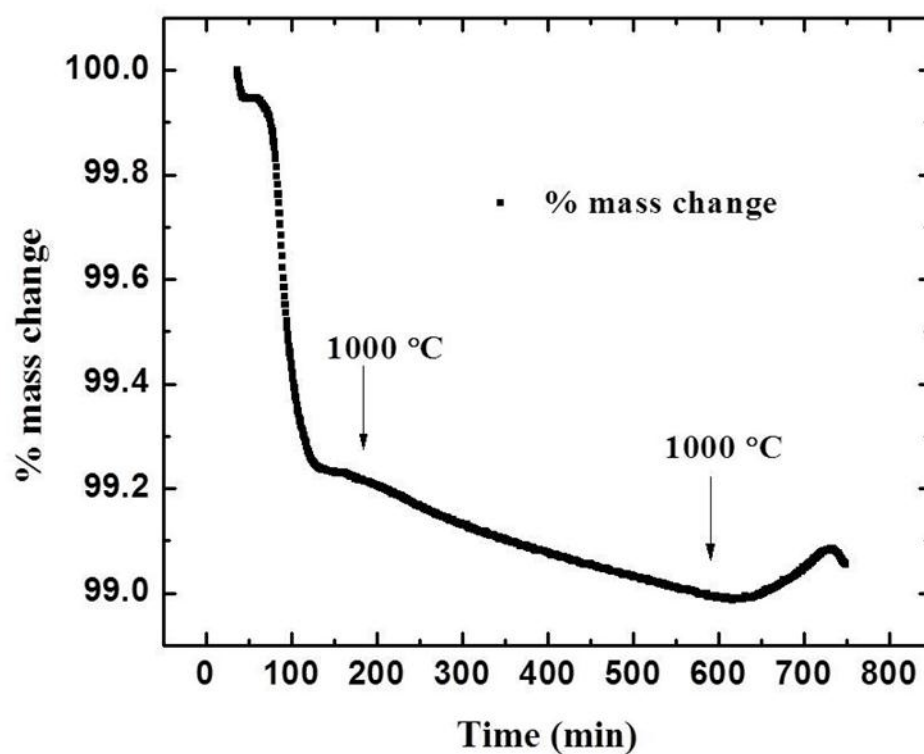


Figure 4.27 Thermogravimetric Analysis of $\text{Ba}_2\text{InFeO}_{5+y}$ in N_2 atmosphere with the maximum temperature of 1000 °C.

Though mixed valence is observed here from magnetic moment, high conductivity is not exhibited as in other compounds. With higher Fe content, an increase in electrical conductivity is exhibited. The $\text{Ba}_2\text{In}_{0.5}\text{Fe}_{1.5}\text{O}_{5+y}$ sample has the highest conductivity around 120,000 ohms by two probe measurement, which is too

high to be considered as a good conductor. The coordination of Fe is disordered thus it is difficult to build a chain to carry the electrons.

4.3.4 Conclusion

The solid solution $\text{Ba}_2\text{In}_{2-x}\text{Fe}_x\text{O}_{5+y}$ ($x = 0.1-1.5$) was successfully prepared by solid state reactions. The structure exhibited a transition from orthorhombic to cubic. The refinement of the orthorhombic $\text{Ba}_2\text{In}_{1.8}\text{Fe}_{0.2}\text{O}_{5+y}$ showed that the substitution of In occurred mostly in the tetrahedral sites. The oxidation state of Fe is a mixed valence of Fe^{3+} and Fe^{4+} , and this conclusion was confirmed by magnetic susceptibility, Mössbauer spectra and TGA data. For samples with low Fe content, we observed the dark green color. When the Fe content is higher than 0.5, the color appeared to be black.

4.4 References

1. T. Takahashi. “*Physics of Electrolytes*”, 2nd edition, Academic Press, New York, 1972.
2. J. C. Grenier; N. Ea; M. Pouchard; P.J. Hagenmuller. *Solid State Chem.* 58, 243, 1985
3. J.C. Grenier; M. Pouchard; P. Hagenmuller. “*Reactivity of Solids*”, Elsevier, Amsterdam, 1982.
4. D.M. Smyth. *Cryst. Latt. Def. Amorph. Mat.* 18, 355, 1989.

5. G. B. Zhang; D. M. Smyth. *Solid State Ionics*. 82, 161-172, 1995.
6. J. B. Goodenough; J. E. Ruiz-diaz; Y. S. Zhen. *Solid State Ionics*. 44, 21, 1990.
7. P. Berastegui; S. Hull; F. J. Garc ía-Garc ía; S.-G. Eriksson. *J. Solid State Chem*. 164, 119-130, 2002.
8. S. A. Speakman; J. W. Richardson; B. J. Mitchell; S. T. Misture. *Solid State Ionics*. 149, 247-259, 2002.
9. T. Kobayashi; A. Hasesaka; M. Hibino; T. Yao. *Transaction of the Materials Research Society of Japan*. 33, 1077-1080, 2008.
10. A. E. Smith; H. Mizouguchi; K. Dlaney; N. A. Spaldin; A.W. Sleight; M. A. Subramanian. *J. Am. Chem. Soc*. 131, 17086, 2009.
11. H. Mizoguchi; A. W. Sleight; M. A. Subramanian. *Inorg. Chem*. 50, 10, 2011.
12. D. A. Grisafe; F. A. Hummel. *J. Solid. State. Chem*. 2, 167-175, 1970.
13. H. Lachwa; D. Reinen. *Inorg. Chem*. 28, 1044-1053, 1989.
14. B. L. Chamberland; A. W. Sleight; J. F. Weiher; *J. Solid State Chem*. 1, 506-511, 1970.
15. D. K. Singh; B. Kamble; A. Singh. *Phys. Rev. B*. 81, 064430, 2010.
16. Z. Huang; F. Du; C. Wang; D. Wang; G. Chen. *Phys. Rev. B*. 75, 054411, 2007.
17. L. A. Pardi; J. Krzystek; J. Telser; L. C. Brunel. *J. Magn. Reson*. 146, 375-378, 2000; A. K. Hassan; L. A. Pardi; J. Krzystek; A. Sienkiewicz; P. Goy; M. Rohrer; L.-C. Brunel. *J. Magn. Reson*. 142, 300, 2000.
18. M. Pardavi-Horvath; P. E. Wigen. *J. Appl. Phys*. 63, 3110, 1998.
19. J. C. Waerenborgh; D. P. Rojas; N. P. Vyshatko; A. L. Shaula; V. V. Kharton; I. P. Marozau; E. N. Naumovich. *Mater. Lett*. 57, 4388-4393, 2003.
20. P. Jiang; J. Li; A. W. Sleight; M. A. Subramanian. *Inorg. Chem*. 50, 5858-5860, 2011.
21. P. K. Gallagher; J. B. MacChesney; D. N. E. Buchanan. *J. Chem. Phys*. 43, 516, 1965
22. M. Parras; F. Fournes; J.-C. Grenier; M. Pouchard; M. Vallet; J. M. Calbet; P. Hagenmuller. *J. Solid. State. Chem*. 88, 261-268, 1990.
23. X.D. Zhou; S. Hovmoller; M. Parras; J.M. Gonzalez-Calbet; M. Vallet-Regi. J. C. Grenier. *Acta. Cryst*. 49, 27-35, 1993
24. H. D. Zhou; J. B. Goodenough. *J. Solid. State. Chem*. 178, 3679-3685, 2005.
25. W. W. Malinofsky; H. Kedesdy. *J. Am. Chem. Soc*. 76, 3090-3091, 1954.
26. Y. D. Perfiliev; V. K. Sharma. *Ferrates: Synthesis, Properties, and Applications in Water and Wastewater Treatment*. American Chemical Society, 2008.
27. M. Takano; N. Nakanishi; Y. Takeda; S. Naka. *Journal De Physique*, 3, C2-313, 1979.
28. K. Kakinuma; H. Yamamura; H. Haneda; T. Atake. *J. Therm. Anal. Calorim*. 57, 737-743, 1999
29. I. V. Spesivtseva; N. A. Kochetova; E. M. Gorbunova; I. E. Animitsa. *Russ. J. Phys. Chem. A*. 85, 1689-1694, 2011.
30. J. Hesse; A. Rubartsch. *J. Phys. E. Sci. Instrum*. 7, 526, 1974.
31. Dr. Wattiax, private communication.

32. S. B. Adler; J. A. Reimer; J. Baltisberger; U. Werner. *J. Am. Chem. Soc.* 116, 675-681, 1994.
33. T. Schober; J. Friedrich; F. Krug. *Solid State Ionics*. 99, 9-13, 1997.

Chapter 5

Study on $\text{LnCu}_{0.5}\text{Ti}_{0.5}\text{O}_3$ hexagonal system (Ln=Y, Tb-Lu)

Abstract

The impurity of $\text{YCu}_{0.5}\text{Ti}_{0.5}\text{O}_3$ was removed by shift the ratio of Cu and Ti from the starting stoichiometry to $\text{YCu}_{0.6}\text{Ti}_{0.4}\text{O}_{3-\delta}$. Structure study of $\text{YCu}_{0.6}\text{Ti}_{0.4}\text{O}_{3-\delta}$ derived that the oxygen content of hexagonal phase was less than the ideal formula. Thus the change in the cation site will balance the oxidation state. Optical and magnetic properties were also measured and compared. This change in oxygen content was further studied in the Mn-doped system. And the effect of stoichiometric difference in the Mn-doped samples was not as obvious as the initial compound. The disorder in the cation site enhanced the tolerance of the structure on the aspect of oxygen content.

The hexagonal phases $\text{LnCu}_{0.5}\text{Ti}_{0.5}\text{O}_3$ (Ln = Y, Tb-Lu) phases were prepared by the traditional solid state reactions. The prepared compounds were reduced at high temperature in the reduction atmosphere created by the H_2/N_2 gas mixture. Study on the structure and properties changes by reduction was conducted by X-ray diffraction, optical measurement, magnetic measurement and thermalgravimetric analysis. And we observed some evidence of the presence of Cu^+ in the reduced phase by these characterization methods.

5.1 Introduction

Transition metal oxides have been studied thoroughly for various properties. Multiferroicity is one interesting subject in material research and has potential to be utilized in vast fields of applications. The multiferroic material is the material exhibits both ferroelectric and ferromagnetic behavior. A ferroelectric material exhibits a stable and reversible electrical polarization that is manifested by cooperative atomic displacements. The ferromagnetic crystal shows a steady and switchable magnetization that arises from the quantum mechanical phenomenon of exchange [1]. Abundant examples can be found with ferroelectric or ferromagnetic property, however, materials with the coexistence of both effects are very rare [2-4]. The magnetism phenomena derive from the finite number of unpaired d electrons (spin). Ferroelectric materials have polar unit cell, mostly favored by d^0 electronic configuration. The structure is necessary to be non-centrosymmetric to obtain a finite macroscopic electric polarization. Both of these properties are normally provided by the transition metal ions. However, most ferroelectric materials are composed of cations without a finite d -occupancy. Thus, the most effective way is to explore a non-centrosymmetric material with two different types of transition metal ions: one with unpaired electrons and the other acquiring a d^0 configuration. In this way, the coexistence of magnetism and ferroelectricity is achieved in the different sub-lattice [5].

One possible candidate is RMnO_3 group ($\text{R}=\text{Y}$, Ho-Lu) which expresses both ferroelectricity and magnetic order. To be mentioned, this system exhibits antiferromagnetic behavior rather than ferromagnetic. However, the magnetic ferroelectric coupling can be expected. The structure is hexagonal which belongs to the space group $P6_3cm$. The ferroelectric character is manifested by the MnO_5 trigonal bipyramids together with the displacement of Y^{3+} ions [6].

Two different cations can occupy the trigonal bipyramidal sites while the ferroelectric structure is still maintained. The crystal field stabilization energy of the d^9 electronic configuration of Cu^{2+} also favors the TBP site. Compounds with Cu^{2+} and some other transition metal ions which have the d^0 configuration have been proved to be existed [7]. Ti^{4+} is one cation which is able to be stabilized in the five-fold coordination. $\text{LnCu}_{0.5}\text{Ti}_{0.5}\text{O}_3$ system was reported to be successfully prepared, with space group $P6_3cm$. The Cu^{2+} and Ti^{4+} cations are dispersed randomly on the trigonal bipyramids layers [8]. The illustration of the structure is in figure 5.1. A structure refinement of $\text{ErCu}_{0.5}\text{Ti}_{0.5}\text{O}_3$ was reported. In the Cu/TiO_5 trigonal bipyramids, the metal-oxygen bond distance on the apical plane is shorter than that of the basal plane. So the possible coupling between electrical and magnetic effect would be expected.

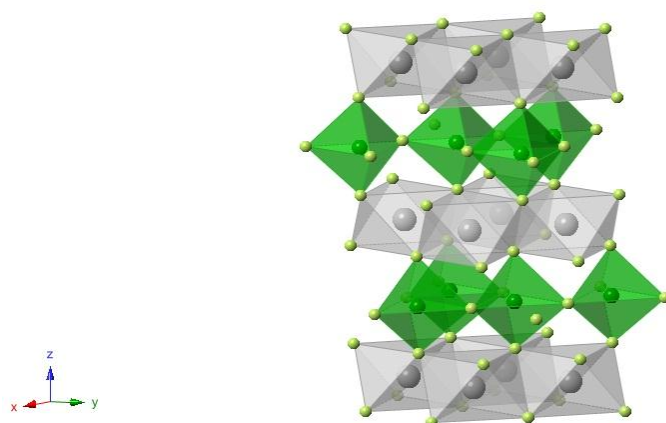


Figure 5.1 Illustration of ferrielectric structure of $\text{YCu}_{0.5}\text{Ti}_{0.5}\text{O}_3$. Grey sphere: Y^{3+} ; Green sphere: $\text{Cu}^{2+}/\text{Ti}^{4+}$; light green sphere: O^{2-} .

Despite the potential in multiferroic property, $\text{LnCu}_{0.5}\text{Ti}_{0.5}\text{O}_3$ system also exhibits excellence in other physical properties such as dielectric property [9]. One interesting physical property of the $\text{LnCu}_{0.5}\text{Ti}_{0.5}\text{O}_3$ ($\text{Ln} = \text{Er}, \text{Lu}, \text{Y}$) is that all the compounds exhibit green color. The earlier studies on the color pigments had manifested the uniqueness of TBP coordination in producing colors [10]. Thus, $\text{LnCu}_{0.5}\text{Ti}_{0.5}\text{O}_3$ is an attractive host to investigate optical properties besides the multiferroic properties. Study on the solid solutions between $\text{YCu}_{0.5}\text{Ti}_{0.5}\text{O}_3$ and YMO_3 where $\text{M} = \text{Mn}, \text{Cr}, \text{Fe}, \text{Al}, \text{Ga}$ and In has been carried out thoroughly [11]. Further study on the structure by means of neutron diffraction will be interesting.

5.2 Study on structure and properties of the compounds $\text{YCu}_{0.6}\text{Ti}_{0.4}\text{O}_{3-\delta}$, $\text{YMn}_{0.5}\text{Cu}_{0.25}\text{Ti}_{0.25}\text{O}_3$ and $\text{YMn}_{0.5}\text{Cu}_{0.3}\text{Ti}_{0.2}\text{O}_3$.

5.2.1 Introduction

Though various heating time and rate was tried in the preparation process, the reported X-ray patterns of $\text{LnCu}_{0.5}\text{Ti}_{0.5}\text{O}_3$ always indicate a small fraction of $\text{Y}_2\text{Ti}_2\text{O}_7$ pyrochlore impurity [8]. And the intensity peak of the pyrochlore differed with different Ln ions. However, similar condition was not observed with other $\text{LnCu}_{0.5}\text{M}_{0.5}\text{O}_3$ ($\text{M}=\text{V}, \text{Mo}$) compounds [12, 13]. And the reason of the occurrence of the pyrochlore phase is not yet explained. It is necessary to notice that initial oxides are weighed with equal amount of Cu and Ti content. However, impurities with only Ti content appeared in the X-ray patterns. Apparently some Cu is “missing” in the synthesis process. Thus, it may be helpful to exclude the impurities by shifting the stoichiometry of Cu and Ti from the starting materials. The purpose of this part of work is to prepare the single phase YMO_3 compounds with Cu and Ti occupying the M site. The effect of shifted stoichiometry on the Mn-doped samples is examined as well. And we observe the least impurity peak with the composition of $\text{YCu}_{0.6}\text{Ti}_{0.4}\text{O}_{3-\delta}$. Comparisons on the Mn-doped samples are also included.

5.2.2 Synthesis

A solid state method was used for the synthesis of the $\text{YCu}_{0.5}\text{Ti}_{0.5}\text{O}_3$ related compounds, $\text{YMn}_{0.5}\text{Cu}_{0.25}\text{Ti}_{0.25}\text{O}_3$ and $\text{YMn}_{0.5}\text{Cu}_{0.3}\text{Ti}_{0.2}\text{O}_3$ samples. A stoichiometric mixture of Y_2O_3 (Baker Analyze, >99%), In_2O_3 (Stanford Materials, >99.99%), TiO_2 (Aldrich, >99.99%) and CuO (Aldrich, >99.99%) was weighed and thoroughly ground

together in an agate mortar. The powder mixtures were then pressed into pellets with applied pressure of 1 psi. The pellets were heated at 1050 °C for 12 hours in air. This procedure was repeated several times until the intensity of impurity peaks no longer decreases in the X-ray patterns.

5.2.3 Results and discussion

The $\text{YCu}_{0.5}\text{Ti}_{0.5}\text{O}_3$ sample was prepared in conventional solid state route and impurity of $\text{Y}_2\text{Ti}_2\text{O}_7$ was identified as reported (figure 5.2). Thus, extra Cu content served as an attempt to eliminate the impurity. However, extra peaks indicating Cu containing compounds appeared in the X-ray pattern. So we fixed the total amount of Cu and Ti to be one but shifted the ratio of these two elements. Several compositions have been tried and the X-ray pattern of $\text{YCu}_{0.6}\text{Ti}_{0.4}\text{O}_{3-\delta}$ presents to be the cleanest. The X-ray patterns of $\text{YCu}_{0.6}\text{Ti}_{0.4}\text{O}_{3-\delta}$ and $\text{YCu}_{0.5}\text{Ti}_{0.5}\text{O}_3$ are compared in figure 5.2. It can be seen that the $\text{Y}_2\text{Ti}_2\text{O}_7$ impurity peak intensity is much lower in the pattern of $\text{YCu}_{0.6}\text{Ti}_{0.4}\text{O}_{3-\delta}$. However, the (102) reflection peak which indicates the ferroelectric structure also becomes lower. Refinements of X-ray diffraction patterns were conducted and the lattice parameters a and c are listed in table 5.1. The similarity in the lattice parameters indicates the hexagonal structure is similar in both cases.

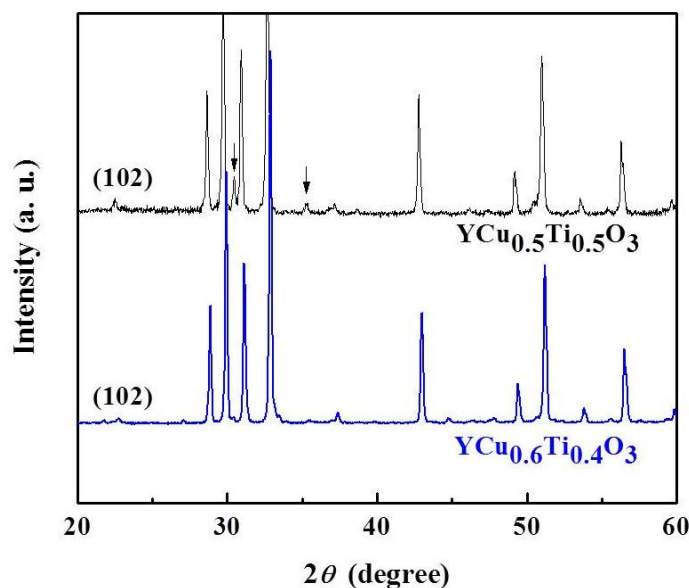


Figure 5.2 X-ray patterns of $\text{YCu}_{0.5}\text{Ti}_{0.5}\text{O}_{3-\delta}$ and $\text{YCu}_{0.6}\text{Ti}_{0.4}\text{O}_3$. $\text{Y}_2\text{Ti}_2\text{O}_7$ pyrochlore impurity peaks are indicated in arrow.

Table 5.1 Lattice parameters summary of $\text{YCu}_{0.5}\text{Ti}_{0.5}\text{O}_{3-\delta}$ and $\text{YCu}_{0.6}\text{Ti}_{0.4}\text{O}_3$

	Cell edge a (Å)	Cell edge c (Å)
$\text{YCu}_{0.5}\text{Ti}_{0.5}\text{O}_3$	6.172(1)	11.48(2)
$\text{YCu}_{0.6}\text{Ti}_{0.4}\text{O}_{3-\delta}$	6.176(5)	11.48(0)

* Values of $\text{YCu}_{0.5}\text{Ti}_{0.5}\text{O}_3$ is from reference [8].

The structure of $\text{YCu}_{0.6}\text{Ti}_{0.4}\text{O}_{3-\delta}$ is further studied by neutron diffraction to address the positions, occupancies of the atoms especially for oxygen. The Rietveld refinement fit by GSAS software is illustrated in figure 5.3. Trace amount of YCu_2O_5 was observed and refined as the second phase. And the parameters of the major $\text{P6}_3\text{cm}$ phase from Rietveld refinement are summarized in table 5.2. The Cu/Ti ratio is refined as 0.585/0.415 which is close to the ratio of the input. The oxidation states of the cations and anions are balanced as oxygen deficiency was found in O-3 and O-4 sites.

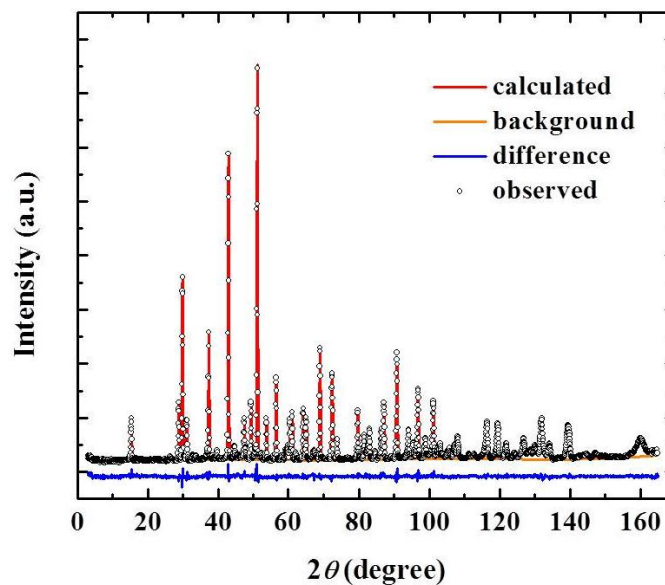


Figure 5.3 NIST constant wavelength neutron diffraction data of $\text{YCu}_{0.6}\text{Ti}_{0.4}\text{O}_{3-\delta}$ is shown with Rietveld fit.

Table 5.2 NIST Neutron structural refinement of $\text{YCu}_{0.6}\text{Ti}_{0.4}\text{O}_{3-\delta}$

General information					
Space group			P6 ₃ cm		
<i>a</i> (Å)			6.1764(3)		
<i>c</i> (Å)			11.480(7)		
<i>V</i> (Å ³)			379.27(6)		
R _p (%)			4.05		
wR _p (%)			5.12		
Atomic coordinates and occupancy					
		<i>x</i>	<i>y</i>	<i>z</i>	occupancy
Cu	Cu	0.306(4)	0	0.003(7)	0.58(5)
Ti	Ti	0.306(4)	0	00.003(7)	1.00
Y	Y1	1/3	2/3	0.268(8)	1.00
	Y2	0	0	0.244(9)	1.00
O	O1	0.348(6)	0	0.168(6)	1.00
	O2	0.673(9)	0	0.340(5)	1.00
	O3	0	0	0.020(9)	0.96(9)
	O4	1/3	2/3	0.501(0)	0.97(6)

According to the refinement results, the structure is presumably oxygen deficient when synthesized by conventional solid state reactions. We increased the content of Cu further more and tried to make the compound $\text{YCu}_{0.7}\text{Ti}_{0.3}\text{O}_{3-\delta}$. However, the $\text{Y}_2\text{Ti}_2\text{O}_7$ impurity showed up in the X-ray diffraction pattern. And this gave us a clue that the oxygen content favors the Cu/Ti ratio to be around 6/4. The oxygen deficiency is commonly seen in octahedral site such as in perovskite structure [14, 15]. In the case of tetrahedral sites, examples are also reported [16, 17]. However, few references were found in the trigonal bipyramidal site. And based on our research in $\text{YCu}_{0.6}\text{Ti}_{0.4}\text{O}_{3-\delta}$, the appearance of impurity in other $\text{LnCu}_{0.5}\text{Ti}_{0.5}\text{O}_3$ may be rationalized. The percentage of the $\text{Y}_2\text{Ti}_2\text{O}_7$ impurity varies with different Ln ions. The thickness of the TBP layers is correlated to the ionic radii and electronegativity. The amount of oxygen atoms held in the TBP layer will be different for all the Ln ions. Thus, the intensities of impurity peaks are different in $\text{LnCu}_{0.5}\text{Ti}_{0.5}\text{O}_3$ with various Ln ions.

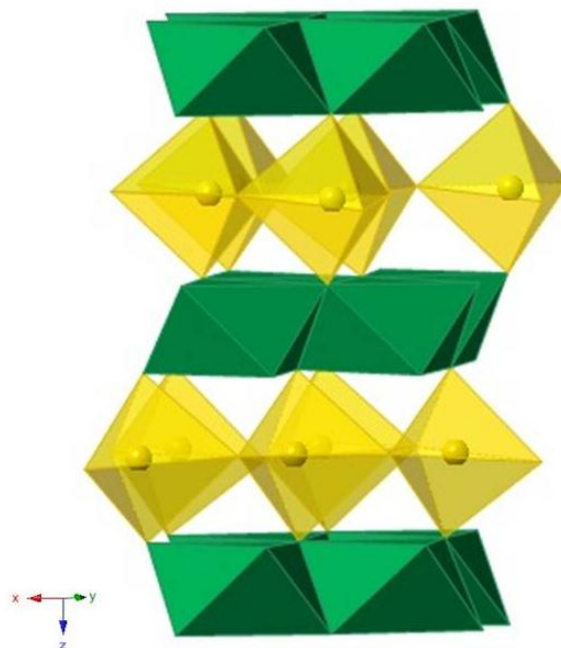


Figure 5.4 Structure of $\text{YCu}_{0.6}\text{Ti}_{0.4}\text{O}_{3-\delta}$. Cu/Ti ions are indicated with yellow sphere; Y ions are represented by green octahedras; O ions are omitted.

Figure 5.4 illustrates the structure from the refinement results. The structure of $\text{YCu}_{0.6}\text{Ti}_{0.4}\text{O}_{3-\delta}$ is ferroelectric $P6_3cm$ layered structure. Cu and Ti are randomly distributed in the trigonal bipyramidal layers and intercalated with the distorted YO_6 octahedral layers. Figure 5.5 shows the thermal ellipsoids version of the structure. The oxygen atoms (O-1 and O-2) in the octahedral layers exhibit uniform unisotropic thermal distribution. The oxygen atoms on the basal plane (O-3 and O-4) have much bigger range of distribution, and oxygen vacancies were identified at these positions in the neutron refinements (table 5.2.3.2).

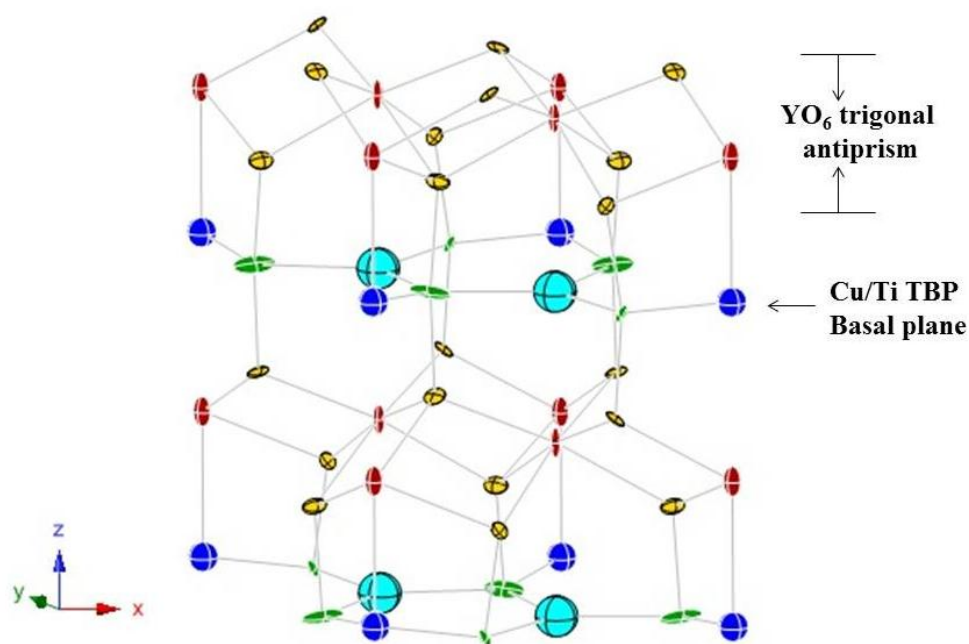


Figure 5.5 Thermal ellipsoid of $\text{YCu}_{0.6}\text{Ti}_{0.4}\text{O}_{3-\delta}$. Cu/Ti: green sphere; O-1 and O-2: yellow sphere; Y: red sphere; O-3: blue sphere; O-4: light blue sphere.

Both compositions exhibit green color, but $\text{YCu}_{0.6}\text{Ti}_{0.4}\text{O}_{3-\delta}$ appeared darker green in color. This may be because small amount of $\text{Y}_2\text{Ti}_2\text{O}_7$, which is a white compound, is removed. The diffuse reflectance spectra are shown below in figure 5.6. The main difference lies in the peak in the high energy region which is resulted in charge transfer. It is reported that $\text{Y}_2\text{Ti}_2\text{O}_7$ has a reflection peak at around 350 nm [18]. So the absorbance peak at 400 nm is possibly rooted in the combination of the two compounds. And this makes the absorbance valley for green color even sharper. Thus the color of $\text{YCu}_{0.5}\text{Ti}_{0.5}\text{O}_3$ with $\text{Y}_2\text{Ti}_2\text{O}_7$ impurity is brighter than $\text{YCu}_{0.6}\text{Ti}_{0.4}\text{O}_{3-\delta}$ sample.

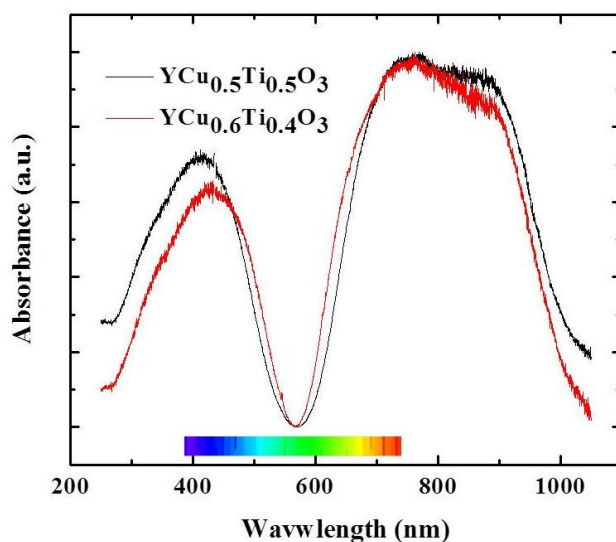


Figure 5.6 Diffuse reflectance spectra of $\text{YCu}_{0.5}\text{Ti}_{0.5}\text{O}_3$ and $\text{YCu}_{0.6}\text{Ti}_{0.4}\text{O}_3$.

Magnetic susceptibility data is taken on PPMS using ACMS mode and the result is plotted in figure 5.7. Both samples showed paramagnetic behavior down to 5K. The magnetic moment is calculated from the linear region (150-300K) of inverse susceptibility plot. The magnetic moment of the $\text{Cu} = 0.6$ sample is slightly higher than that of $\text{Cu} = 0.5$ sample. The results are summarized in table 5.3. The value derived from the Curie-Weiss law is close enough to the expected value. However, there is no clue for the coordination of Cu^{2+} from the magnetic data as only one unpaired electron is in the d-shell. The large negative value of the intercept indicates the frustration originated from the triangular lattice. Similar results were observed from the $\text{YIn}_{1-x}\text{Fe}_x\text{O}_3$ system.

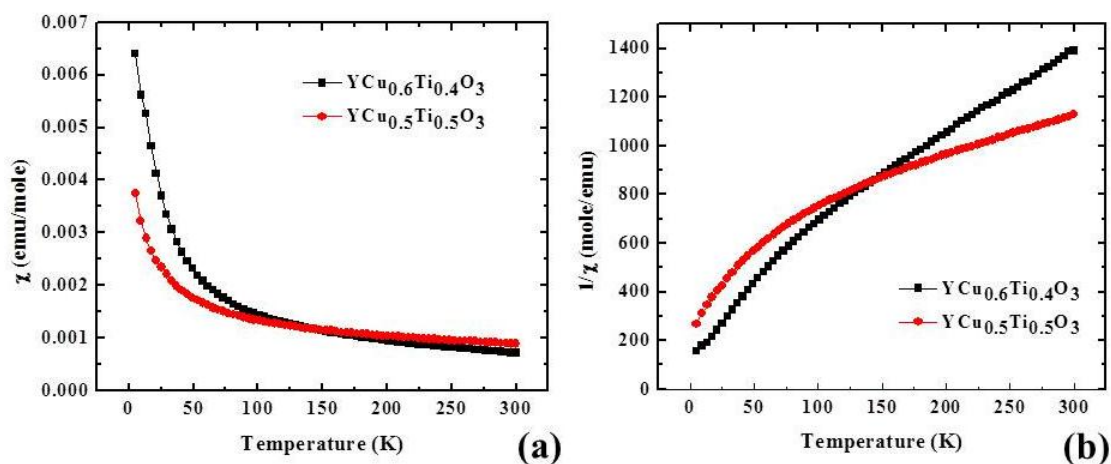


Figure 5.7 Magnetic susceptibility (a) and inverse susceptibility (b) versus temperature plot of $\text{YCu}_{0.6}\text{Ti}_{0.4}\text{O}_{3-\delta}$ and $\text{YCu}_{0.5}\text{Ti}_{0.5}\text{O}_3$.

Table 5.3 Summary of magnetic data of $\text{YCu}_{0.5}\text{Ti}_{0.5}\text{O}_3$ and $\text{YCu}_{0.6}\text{Ti}_{0.4}\text{O}_3$

	Temperature range	μ_B (experimental value)	μ_B (expected value)	Curie constant	Intercept
$\text{YCu}_{0.5}\text{Ti}_{0.5}\text{O}_3$	150-300K	1.425	1.225	0.252	-147.8
$\text{YCu}_{0.6}\text{Ti}_{0.4}\text{O}_3$	150-300K	1.640	1.342	0.334	-131.09

It has been reported that the full solid solution can be formed between YMnO_3 and $\text{YCu}_{0.5}\text{Ti}_{0.5}\text{O}_3$ [11]. So $\text{Mn} = 0.5$ sample was picked up to investigate the effect of dopant on different Cu/Ti ratio compounds. The regular composition $\text{YMn}_{0.5}\text{Cu}_{0.25}\text{Ti}_{0.25}\text{O}_3$ and the new composition $\text{YMn}_{0.5}\text{Cu}_{0.3}\text{Ti}_{0.2}\text{O}_3$ are synthesized by the conventional solid state reactions. The X-ray patterns are illustrated in figure 5.8. The two compositions showed similar patterns, and only trace amount of $\text{Y}_2\text{Ti}_2\text{O}_7$ is observed in the $\text{YMn}_{0.5}\text{Cu}_{0.25}\text{Ti}_{0.25}\text{O}_3$ and can be neglected. The reason of the impurity

disappearance is not addressed yet. But it is possible that the disorder on the cation site may create the order for the anion sites [19].

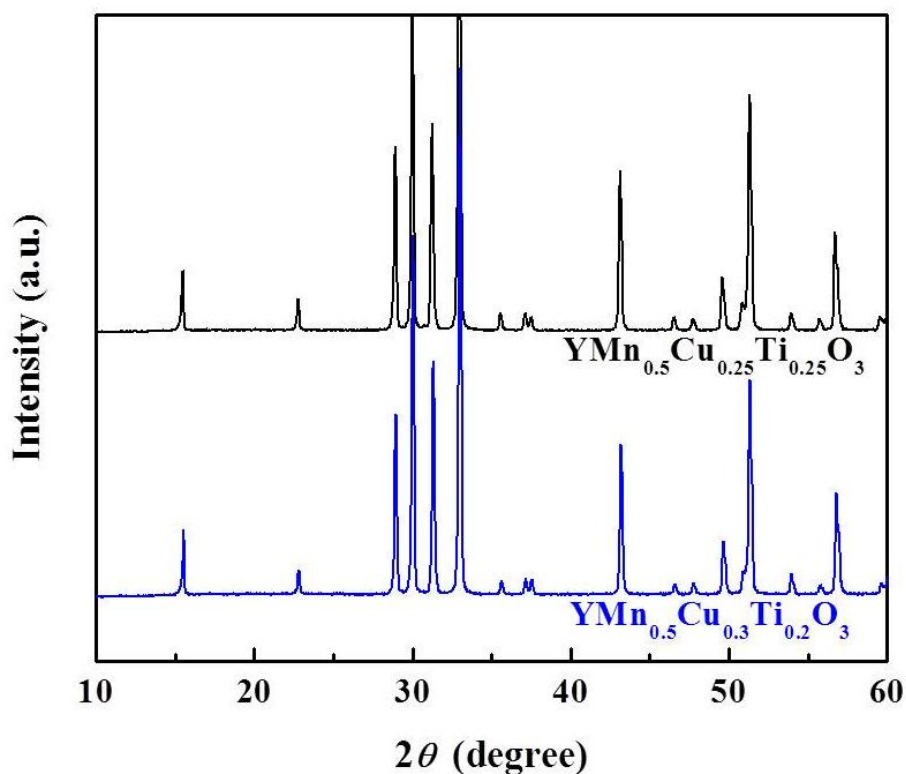


Figure 5.8 XRD patterns of $\text{YMn}_{0.5}\text{Cu}_{0.25}\text{Ti}_{0.25}\text{O}_3$ and $\text{YMn}_{0.5}\text{Cu}_{0.3}\text{Ti}_{0.2}\text{O}_3$.

All the samples showed black colors. Magnetic measurements for the samples are collected in PPMS. The difference between the two samples in the magnetic data is very small (figure 5.9) as Mn^{3+} contributes more in the magnetic moment in the compound. And this overweighs the small shift from Cu^{2+} . They all exhibit antiferromagnetic behaviors in the measured temperature range. The magnetic moment from the Curie-Weiss fit confirms that Mn is 3+ in high spin. However, no conclusion about the coordination could be addressed as tetrahedral, octahedral and

TBP coordination all gives the same magnetic moment. The details of magnetic data are summarized in table 5.4.

Table 5.4 Summary of magnetic data of $\text{YMn}_{0.5}\text{Cu}_{0.3}\text{Ti}_{0.2}\text{O}_3$ and $\text{YMn}_{0.5}\text{Cu}_{0.25}\text{Ti}_{0.25}\text{O}_3$

	Temp. range	μ_B (calculated value)	μ_B (expected value)*	Curie constant	Weiss constant
$\text{YMn}_{0.5}\text{Cu}_{0.3}\text{Ti}_{0.2}\text{O}_3$	150-300K	3.425	3.592	1.454	-169.89
$\text{YMn}_{0.5}\text{Cu}_{0.25}\text{Ti}_{0.25}\text{O}_3$	150-300K	3.485	3.571	1.506	-175.85

* The expected magnetic moment assumes Mn^{3+} in high spin state.

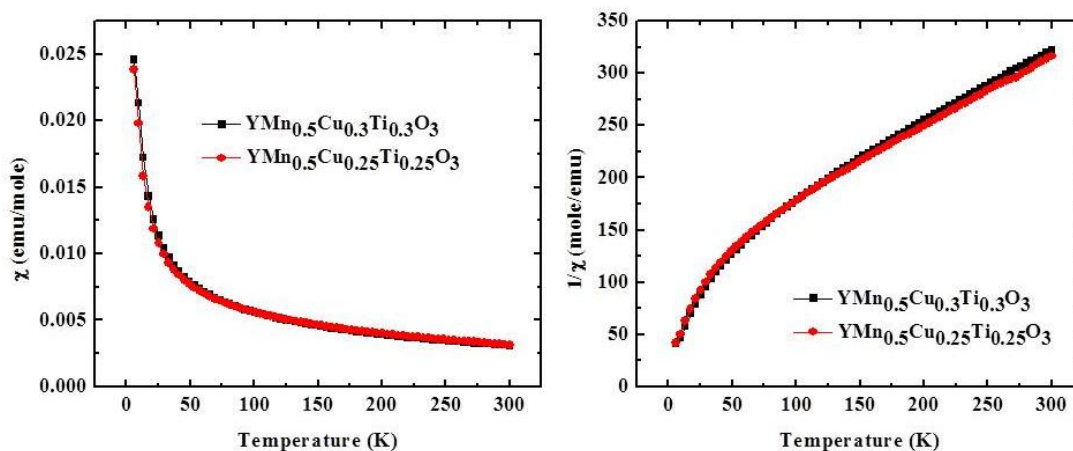


Figure 5.9 Magnetic susceptibility and inverse magnetic susceptibility versus temperature for $\text{YMn}_{0.5}\text{Cu}_{0.3}\text{Ti}_{0.2}\text{O}_3$ and $\text{YMn}_{0.5}\text{Cu}_{0.25}\text{Ti}_{0.25}\text{O}_3$.

Neutron diffraction data were also collected. Tiny amount of $\text{Y}_2\text{Ti}_2\text{O}_7$ pyrochlore phase was observed and refined as a second phase. However, the three atoms on the same site make it difficult to be refined. And currently we are still trying to finish the Rietveld refinement.

5.2.4 Conclusion

The single phase hexagonal structure $\text{YCu}_{0.6}\text{Ti}_{0.4}\text{O}_{3-\delta}$ was successfully prepared and characterized. The synthesis condition favored oxygen deficiencies and the shift in the Cu/Ti ratio balanced the oxidation state. Single phase $\text{YCu}_{0.6}\text{Ti}_{0.4}\text{O}_{3-\delta}$ showed darker green color compared to the sample reproduced from the reported $\text{YCu}_{0.5}\text{Ti}_{0.5}\text{O}_3$. And magnetic data showed an increasement of the magnetic moment, which indicated a higher amount of Cu content. Mn dopants on the Cu/Ti site clearly stabilized the structure and future work will be focused on the structure analysis based on neutron diffraction data.

5.3 Study on the reduction of $\text{LnCu}_{0.5}\text{Ti}_{0.5}\text{O}_3$ (Ln=Y, Eu-Lu)

5.3.1 Introduction

Hexagonal oxides of $\text{LnCu}_{0.5}\text{Ti}_{0.5}\text{O}_3$ (Ln=Tb-Lu, Y) group in ferroelectric structure $\text{P6}_3\text{cm}$ are very attractive for the simultaneous presence of ferroelectricity and magnetism. Despite multiferroic properties, comprehensive study on the physical properties such as dielectric has been carried out [9]. And it has been realized that the special trigonal bipyramidal coordination give rise to the unique and intense colors [11]. However, the information on the details of TBP coordination is lack. And this is no known example with TBP coordination which is conductive. It may be helpful to

relate the TBP oxides to the similar conductive layered compounds to further investigate the structure as well as physical properties.

Delaffosite structure is considered in this work. Compounds with delaffosite structure are served as the transit conductor oxide [20-22]. The delaffosite structure, which has the formula of ABO_2 is illustrated in figure 5.10. The A cation has two oxygen near neighbors and is linear coordinated. And B cation is located in the regular octahedral interstices. $CuYO_2$ is one example, which has the space group $P6_3/mmc$. This is a ferrielectric structure in which the YO_6 octahedras are not tilted.

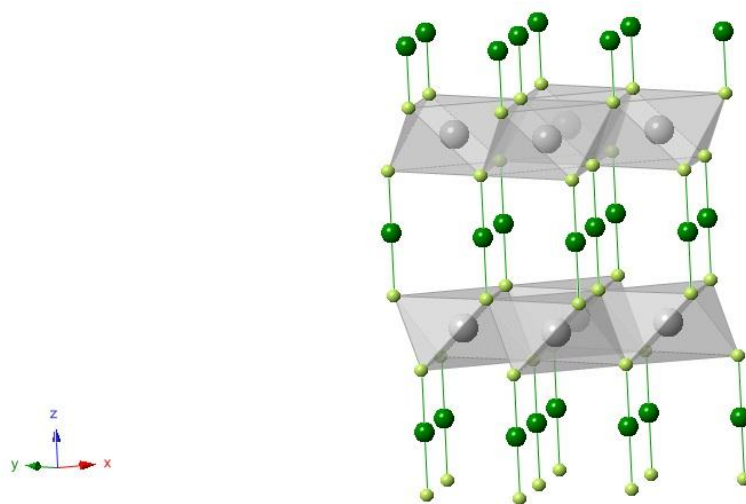


Figure 5.10 Illustration of the structure of delaffosite $CuYO_2$ (grey sphere: Y^{3+} ; green sphere: Cu^{2+} ; yellow sphere: O^{2-})

Similarity between hexagonal $YCu_{0.5}Ti_{0.5}O_3$ and $CuYO_2$ is obvious as they are all layered structures. The difference lies in the oxygen content in the interstitial layers which reside between the octahedral layers. Thus, if oxygen atoms can be removed from the TBP interlayers, the valence of Cu atoms will be decreased and the presence of Cu^+ may be possible. If the linear coordination is created, the electrons are

then able to transport through the O-Cu-O bonds as in the delafossite structure. This may even create conductivity because of the mixed valency similar to YBCO [23].

Reduction on DyMnO_3 revealed that the change in oxygen will affect the structure [24]. Thus study on the reduction of $\text{LnCu}_{0.5}\text{Ti}_{0.5}\text{O}_3$ ($\text{Ln}=\text{Y, Tb-Lu}$) system will be inspiring in structural transition as well as physical property change. Work of this part utilized H_2/N_2 gas mixture as a reduction atmosphere for $\text{YCu}_{0.5}\text{Ti}_{0.5}\text{O}_3$. We saw evidence of the change in valence of Cu atoms and we observed conductivity from the reduced samples.

5.3.2 Synthesis

A solid state method was used for the synthesis of the $\text{YCu}_{0.5}\text{Ti}_{0.5}\text{O}_3$ related compounds. A stoichiometric mixture of Y_2O_3 (Baker Analyze, >99%), In_2O_3 (Stanford Materials, >99.99%), and CuO (Aldrich, >99.99%) was weighed and thoroughly ground together in an agate mortar. The powder mixtures were then pressed into pellets with applied pressure of 1 psi. The pellets were heated at 1050 °C for 12 hours in air. This procedure was repeated several times until least impurity in the X-ray patterns.

5.3.3 Results and discussions

All the $\text{LnCu}_{0.5}\text{Ti}_{0.5}\text{O}_3$ (Ln=Y, Tb-Lu) phases prepared by solid state reactions, green colors are observed. $\text{YCu}_{0.5}\text{Ti}_{0.5}\text{O}_3$ sample was picked up to study the effect of dwell time and reduction temperature. Various reduction conditions were explored to find out the most desired condition. Small amount of sample was placed on the ceramic crucible and inserted to the center of a tube furnace for several hours at 400 °C, while a 5% H_2/N_2 gas mixture went through the sealed tube. Different dwell time periods were attempted and the X-ray patterns are plotted in the figure below. The shortest time period tested was 4 hours and we see clear change in diffraction peaks in the powder X-ray pattern compared to the initial phase. There is mere any change in the peak positions for different heating time. However, the intensity decrease and peaks are broadening as the duration time is increasing. So 4 hours dwell time is considered as the most desired.

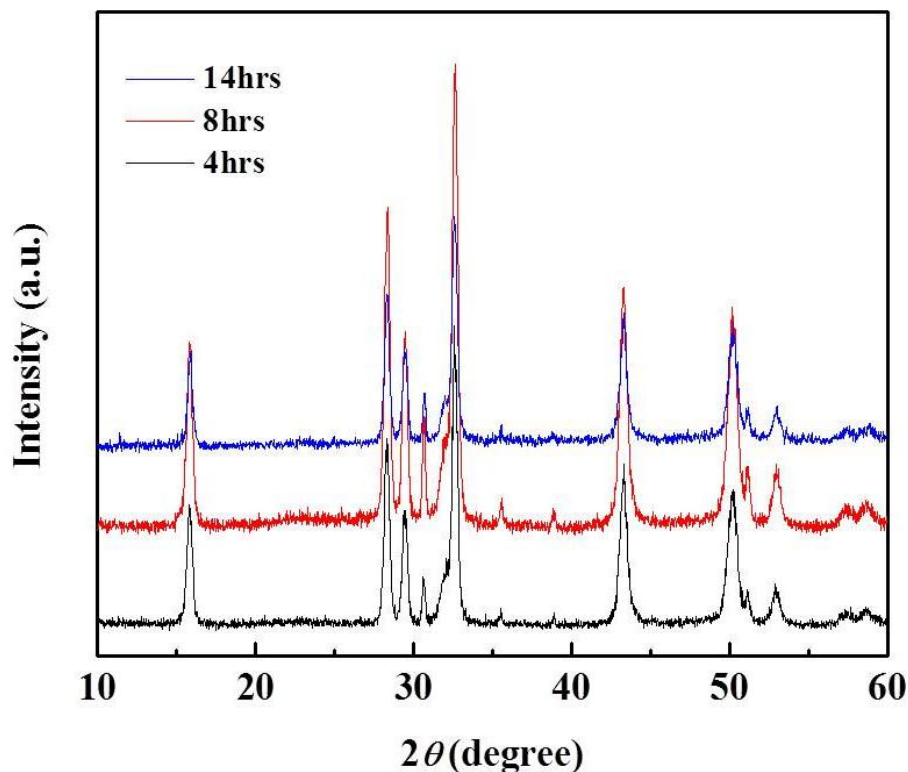


Figure 5.11 X-ray pattern of $\text{YCu}_{0.5}\text{Ti}_{0.5}\text{O}_3$ reduced at $400\text{ }^{\circ}\text{C}$ for various time periods.

The reduction process was conducted at elevating temperatures for four hours and X-ray patterns were shown in figure 5.12. At low temperature ($150\text{--}200\text{ }^{\circ}\text{C}$), the collected patterns of the reduced phases are the same as the sample as prepared. And the colors of the reduced samples are still green. The peaks broadened at $200\text{ }^{\circ}\text{C}$ which can be considered as an indication of H_2/N_2 reacting with the compounds. Though the peaks are shifted and broadened, the structure still belongs to hexagonal structure. The compounds lose the bright green color and appear to be brown/black. The hexagonal structure is still maintained while temperature is raised. When reduced at $500\text{ }^{\circ}\text{C}$, the X-ray pattern no longer exhibits hexagonal structure, and the compound decomposes.

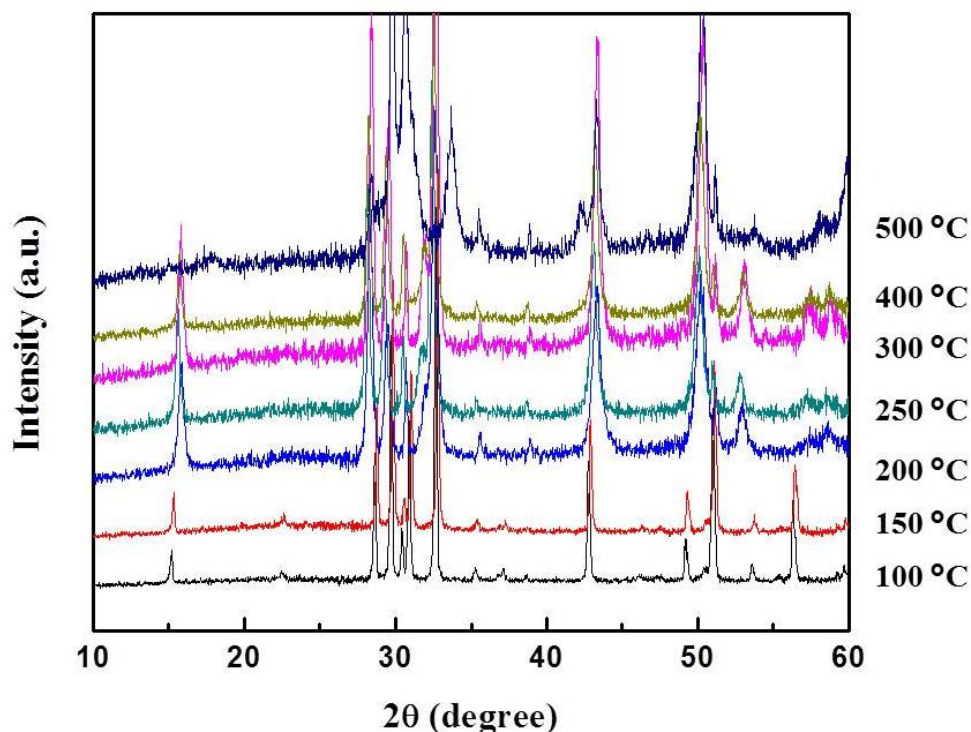


Figure 5.12 X-ray patterns of $\text{YCu}_{0.5}\text{Ti}_{0.5}\text{O}_3$ sample reduced at various temperatures.

La Bail fits for samples reduced at various temperatures were completed using GSAS software. When the reduction temperature is above 200 °C, the (102) reflection peak symbolic for ferroelectric structure disappeared. Thus the structure transformed to $\text{P6}_3/\text{mmc}$ ferrielectric structure. The cell parameters calculated from the refinement are plotted in the figure 5.13 and all the values are from the fitting with $\text{P6}_3/\text{mmc}$ ferrielectric structure. The cell edge value has a fairly big difference between the refined value and the reported CuYO_2 structure. From the figures, the giant change in lattice parameters occurred at 200 °C. Cell edge a increases while c decreases. The increase in cell edge a is possibly due to the removal of oxygen atoms on the basal plane in the TBP layers. As all the cations are experiencing more Colombic repulsion

interactions. And the combination of the two cell edge changes resulted in a slight increase in the cell volume.

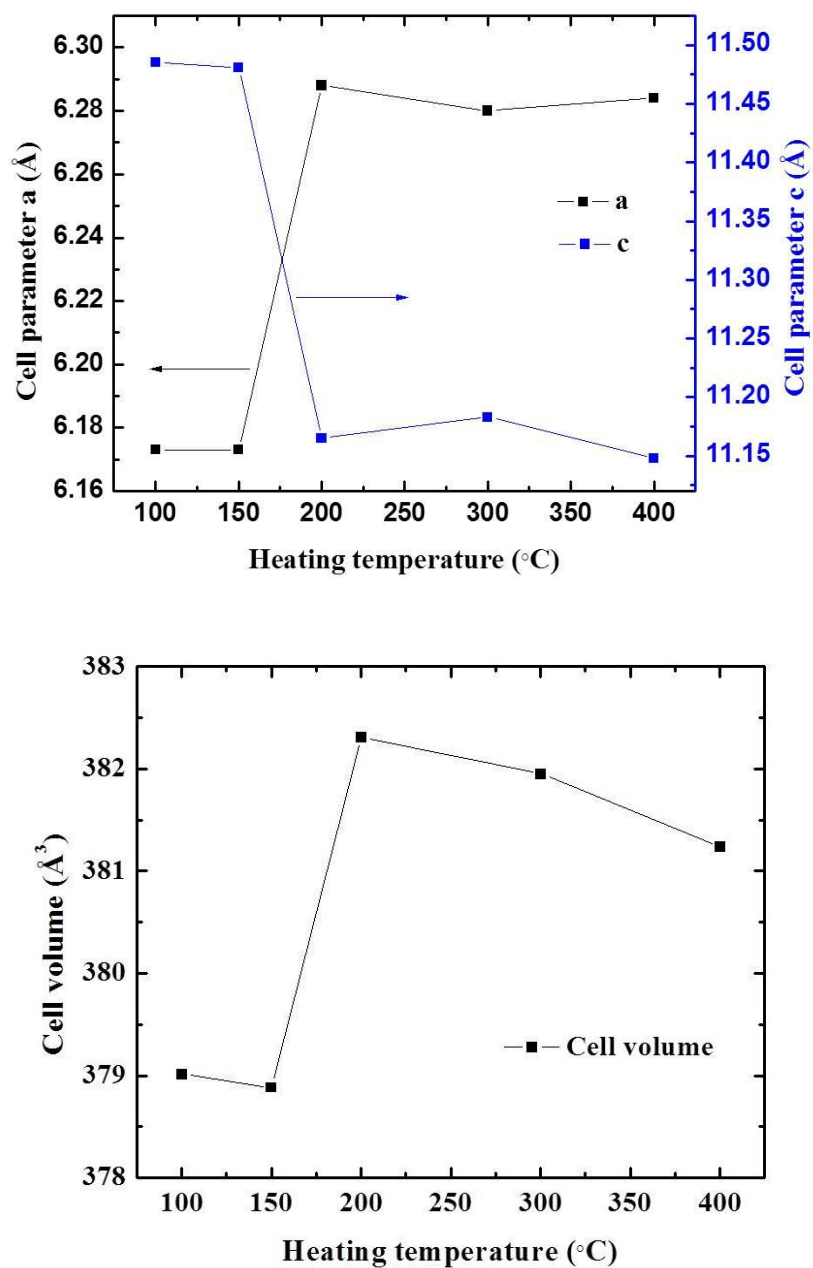


Figure 5.13 Cell edges a and c (above figure) and cell volume (below figure) at various reduction temperature.

It is attractive to investigate whether oxygen can be inserted back into the structure. So the reverse procedure was conducted: the synthesis condition was taken and the reduced phase was put to the bulk furnace as a powder form, and heated at 1050 °C for 12 hours. The product after this step appeared green color again and the X-ray pattern was the same as the initial green samples as prepared. Refinements were done for all the three phases and the cell parameters are summarized in table 5.5. And this reduction-oxidation procedure can be repeated for several times.

Table 5.5 Cell edges of $\text{YCu}_{0.5}\text{Ti}_{0.5}\text{O}_3$ for different treatment

Cell edge	As prepared phase	Reduced phase	Re-oxidized phase
<i>A</i>	6.195Å	6.284Å	6.187Å
<i>C</i>	11.501Å	11.148Å	11.498Å

* The cell edge *a* of the reduced compound is multiplied by square root 3 to make comparison with the other two samples as prepared.

The same reduction process (4 hours reducing at 400 °C) was applied for the other $\text{LnCu}_{0.5}\text{Ti}_{0.5}\text{O}_3$ (Ln=Y, Tb-Lu) compounds. Similar change in X-ray patterns as well as color was observed. The colors of the $\text{LnCu}_{0.5}\text{Ti}_{0.5}\text{O}_3$ samples as prepared are all green, and the reduced phases are all brown/black color. The color comparison between the two phases for all the $\text{LnCu}_{0.5}\text{Ti}_{0.5}\text{O}_3$ samples is demonstrated in figure 5.14.

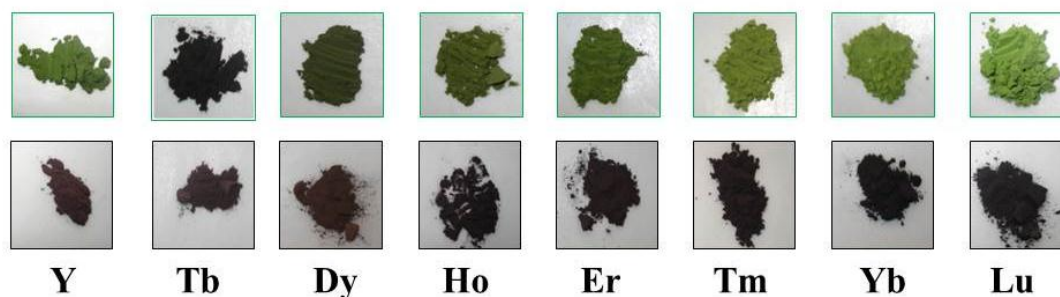


Figure 5.14 Colors of $\text{LnCu}_{0.5}\text{Ti}_{0.5}\text{O}_3$ ($\text{Ln} = \text{Y, Tb-Lu}$) before and after reduction.

Accompanied with the color change, conductivity was observed in some samples after reduction. The conductivity measurement was conducted by two probe measurement because the sample after reduction was too fragile to be centered for four probe measurement. La Bail fit was applied for the X-ray patterns of all the samples and the cell edges are summarized in table 5.6 as well as conductivity.

Table 5.6 Summary of cell edges and conductivity of $\text{LnCu}_{0.5}\text{Ti}_{0.5}\text{O}_3$ (Tb - Lu, Y) for samples as prepared and reduced

	Y	Tb	Dy	Ho	Er	Tm	Yb	Lu
a (Å)	6.20	6.26	6.19	6.17	6.15	6.11	6.09	6.06
(as prepared)								
c (Å)	11.50	11.46	11.48	11.49	11.52	11.50	11.50	11.53
(as prepared)								
a (Å)	6.29	6.42	6.32	6.28	6.24	6.19	6.15	6.11
(reduced)								
c (Å)	11.19	11.07	11.17	11.20	11.29	11.39	11.42	11.48
(reduced)								
Conductivity*	5-7Ω	1Ω	2-3Ω	60-300Ω	6-150Ω	N/A	N/A	N/A

* All conductivity values are measured by two probe measurement.

The cell edges of the $\text{LnCu}_{0.5}\text{Ti}_{0.5}\text{O}_3$ ($\text{Ln} = \text{Y, Tb-Lu}$) series are plotted with ionic radii of Ln^{3+} in figure 5.15. The cell edges of the initial green phases are indicated in green squares whereas the reduced brown phases in black squares. Cell

edge a increases while cell edge c decreases with the increasing ionic radii. And similar trend is observed in the reduced phase. So all samples follow the similar trend through the reduction process.

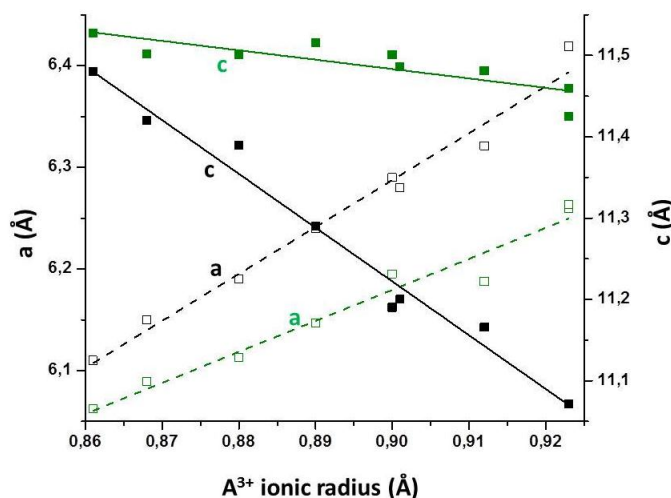


Figure 5.15 Cell edge a and c versus ionic radius of Ln^{3+} ($\text{Ln}=\text{Y}, \text{Tb-Lu}$) (green: initial phase; black: reduced phase)

The origin of the color in $\text{LnCu}_{0.5}\text{Ti}_{0.5}\text{O}_3$ is the crystal field transition of Cu^{2+} which is the only ion with unfilled d shells. The special TBP coordination also attributes to the intense green color. Thus, the change in color may indicate the change in the valence of Cu. If Cu^{2+} is reduced to Cu^+ , it acquires the d^{10} electronic configuration in which the $d-d$ transition become forbidden in this compound. The crystal field splittings of Cu^{2+} in octahedral and TBP sites are explained in the figure below.

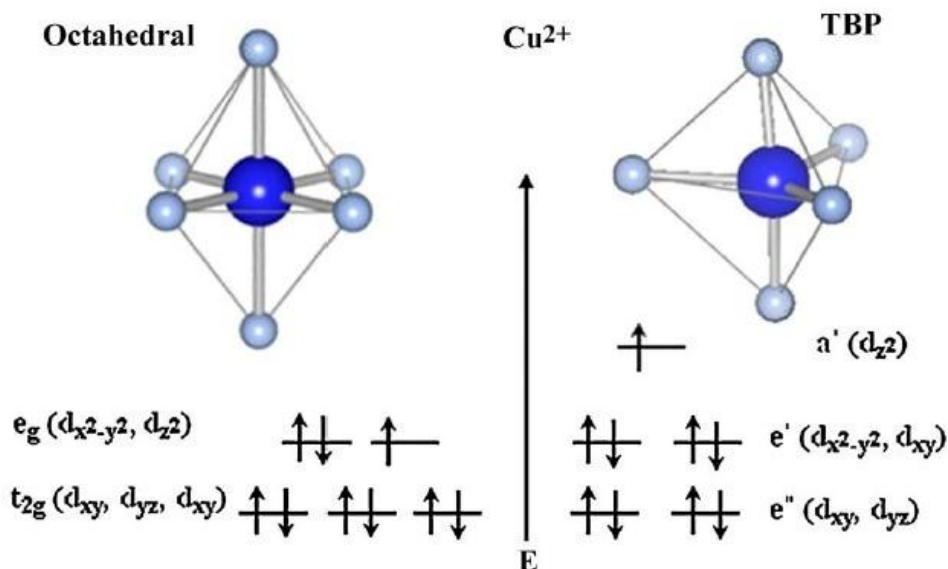


Figure 5.16 Cu^{2+} in octahedral coordination and TBP coordination (reproduction of reference 10).

The diffuse reflectance spectra data was collected from the fiber optics measurement set up for all the samples before and after reduction. Figure 5.17 illustrated the UV-Visible spectrum for $\text{YCu}_{0.5}\text{Ti}_{0.5}\text{O}_3$ as the representative of the series. The green phase is from two absorption peaks in high energy and low energy regions. The absorption peak which lies in the high energy region is from the charge transfer tailing into the visible region. As Y^{3+} and Ti^{4+} do not have d electrons, the bigger and broader peak in the low energy region is due to the $d-d$ transition from Cu^{2+} . The transition between d electrons becomes allowed as TBP is not centrosymmetric coordination. However, in the reduced phase, the peak indicating $d-d$ transition is disappeared and results in the brown color of the compound. One possible explanation is that the major part of Cu^{2+} is reduced to Cu^+ and thus the peak in at around 700-1000 nm region disappears in the spectra. Cu^+ doped highly transmitting glasses

present absorption in the high energy region which is explained by the band transition [25]. So it is reasonable to address the absorption peak around 400-600 nm region to Cu^+ .

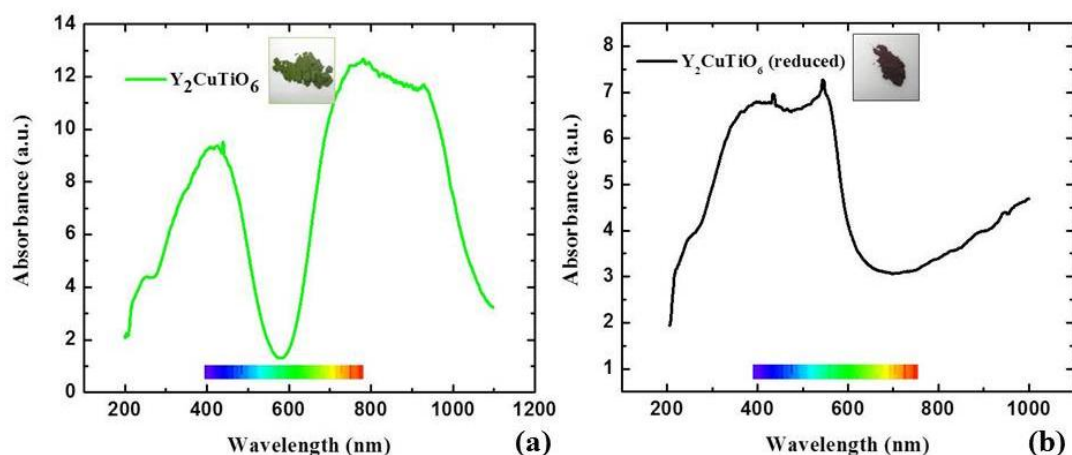


Figure 5.17 Diffuse reflectance spectra of $\text{YCu}_{0.5}\text{Ti}_{0.5}\text{O}_3$ as prepared (left) and reduced in H_2/N_2 gas mixture (right).

Magnetic data also support the change in oxygen content and the existence of Cu^+ . As Cu^{2+} has one unpaired electron and exhibits paramagnetic behavior whereas Cu^+ has d^{10} configuration and shows diamagnetic behavior. Thus the magnetic moment will be distinguished in magnetic data. For the $\text{LnCu}_{0.5}\text{Ti}_{0.5}\text{O}_3$ ($\text{Ln}=\text{Tb-Lu, Y}$), Y^{3+} and Lu^{3+} are the best samples to state the difference before and after reduction. As the other Ln^{3+} ions takes a bigger portion in magnetic moment and they may shadow the change due to the oxidation state change in Cu^{2+} .

Table 5.7 Calculated magnetic moment of $\text{LnCu}_{0.5}\text{Ti}_{0.5}\text{O}_3$ ($\text{Ln}=\text{Tb-Lu, Y}$)

	Y	Tb	Dy	Ho	Er	Tm	Yb	Lu
Electronic configuration	$4d^0$	$4f^8$	$4f^9$	$4f^{10}$	$4f^{11}$	$4f^{12}$	$4f^{13}$	$4f^{14}$

Theoretical magnetic moment	1.22	9.80	10.72	10.72	9.66	7.66	4.70	1.22
--	------	------	-------	-------	------	------	------	------

The magnetic susceptibility data is shown in figure 5.18. The decrease in the magnetic moment is obvious. And for the reduced samples, when the temperature is above 150K, the standard deviation of the measurement is greater than the measured. Thus the values are no longer reliable and omitted in the figure. The fit for Curie-Weiss law was done for the initial $\text{YCu}_{0.5}\text{Ti}_{0.5}\text{O}_3$ phase and the data was taken from the linear part of the inverse magnetic susceptibility versus temperature plot. The value from the plot is $1.30\mu\text{B}$ which is very close to the theoretical value which is $1.22\mu\text{B}$.

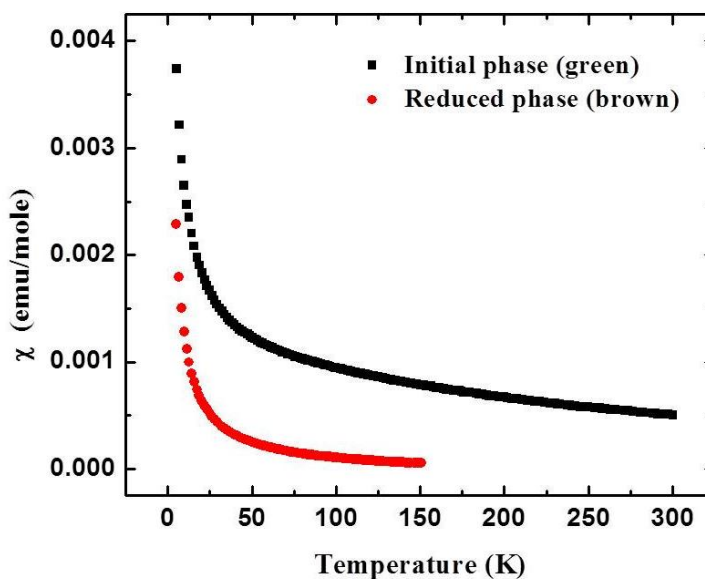


Figure 5.18 Magnetic susceptibility versus temperature plot of $\text{YCu}_{0.5}\text{Ti}_{0.5}\text{O}_3$ as prepared (indicated in black square) and reduced (indicated in red dot).

The most evident proof of the oxygen content change is the weight loss during this reduction process. $\text{YCu}_{0.5}\text{Ti}_{0.5}\text{O}_3$ was heated up to $400\text{ }^{\circ}\text{C}$ in 5% H_2/N_2 gas and

held at peak temperature for 6 hours in TGA. The weight was recorded and plotted in figure 5.19. About 1.2% weight loss is observed when the temperature was held at 400 °C. ideally, if all the Cu^{2+} is reduced to Cu^{+} , the formula will be $\text{YCu}_{0.5}\text{Ti}_{0.5}\text{O}_{2.75}$. And a weight loss of 2.07% is accompanied with this reduction. The variance between the two values is possibly due to the difficulty in diffusion.

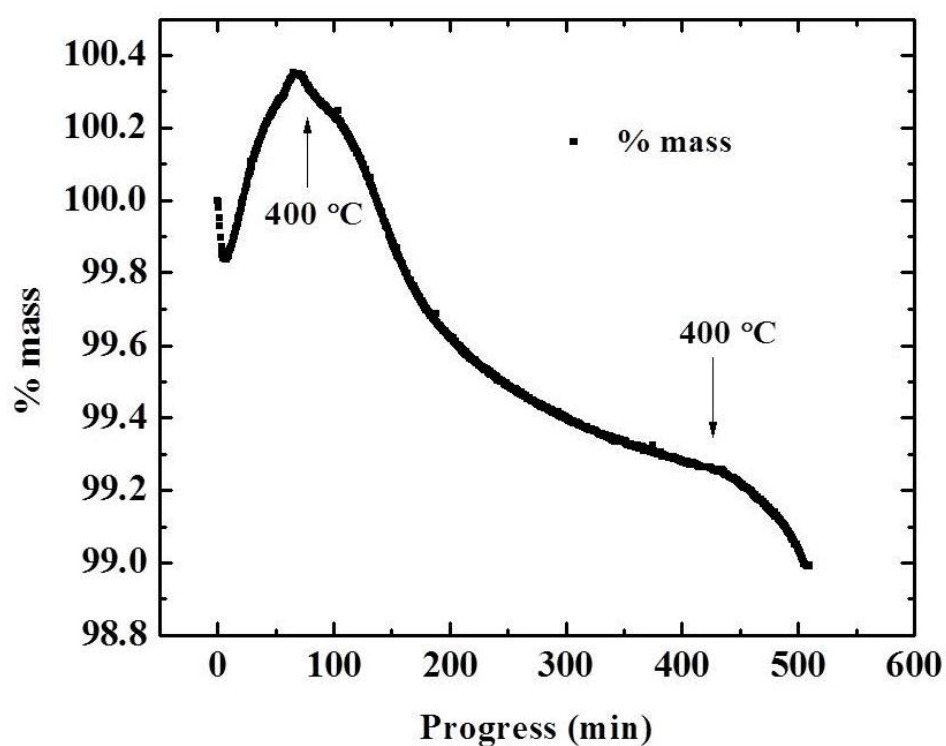


Figure 5.19 Thermal Gravimetric Analysis of $\text{YCu}_{0.5}\text{Ti}_{0.5}\text{O}_3$ in H_2/N_2 gas mixture. The maximum temperature is 400 °C with a heating rate of 5°C/h and 6 hours dwell time.

5.3.4 Conclusion

The $\text{LnCu}_{0.5}\text{Ti}_{0.5}\text{O}_3$ with $\text{Ln}=\text{Y}, \text{Tb-Lu}$ compounds were prepared by conventional solid state reaction. The reduction process in H_2/N_2 gas mixture was conducted and studied. We observed color as well as structure change. And evidence from diffuse reflectance spectra, magnetic measurements, TGA data proved the presence of Cu^+ . So the coordination of CuO_5 trigonal bipyramids was changed in the reducing process. Further work on the structure of the reduced sample will be completed.

5.4 References

1. W. Eerenstein; N. D. Mathur; J. F. Scott. *Nature*. 442, 17, 2006.
2. N.A. Hill. *J. Phys. Chem. B*. 104, 6694, 2000.
3. S. Cheoung; M. Mostovoy. *Nature. Mater.* 6, 13, 2007.
4. R. Ramesh, N.A. Spaldin. *Nature. Mater.* 6, 21, 2007.
5. D. Choudhury; A. Hazarika; A. Venimadhav; C. Kakarla; K. Delaney; P. Sujatha Devi; P. Mondal; R. Nirmala; J. Gopalakrishnan; N. A. Spaldin; U. V. Waghmare; D. D. Sarma. *Phys. Reiv. B*. 82, 13, 2010.
6. B. B. Van Aken; T. M. Thomas; A. F. Palstra; N. A. Spaldin. *Nature. Mater.* 3, 2004
7. M. T. Anderson; K. B. Greenwood, G.A. Taylor, K.R. Poeppelmeier, *Prog. Solid. State. Chem.* 22, 197, 1993.
8. N. Floros; J. T. Rijssenbeek; A. B. Martinson; K. R. Poeppelmeier. *Solid. State. Sci.* 4, 1495–1498, 2002.
9. K. Singh; N. Kumar; B. Singh; S. D. Kaushik; N. K. Gaur; S. Bhattacharva; S. Rayaprol; C. Simon. *J. Supercond. Nov. Magn.* 24, 1829-1838, 2011
10. A. E. Smith; H. Mizoguchi; K. Dlaney; N. A. Spaldin; A. W. Sleight; M. A. Subramanian. *J. Am. Chem. Soc.* 131, 17086, 2009.
11. A. E. Smith, A. W. Sleight, M.A. Subramanian, *Mater. Res. Bul.* 46, 1-5, 2011
12. D. A. Vander Griend; S. Malo; S. J. Barry; N. M. Dabbousch; K. R. Poeppelmeier; V. P. Dravid. *Solid. State. Sci.* 3, 569-579, 2001.

13. D. A. Vander Griend; S. Boudin; V. Caignaert; K. R. Poeppelmeier; Y. Wang; V. P. Dravid; M. Azuma; M. Takano; Z. Hu; J. D. Jorgensen. *J. Am. Chem. Soc.* 121, 4787-4792, 1999.
14. M. T. Anderson; J. T. Vaughey; K. R. Poeppelmeier. *Chem. Mater.* 5, 151-165, 1993.
15. J. Li; Y. Duan; H. He; D. Song. *J. Alloys. Compounds.* 315, 259-264, 2001.
16. E. mamontov; T. Egami; R. Brezny; M. Koranne; S. Tyagi. *J. Phys. Chem. B.* 104, 11110-11116, 2000.
17. H. W. Brinkman; W. J. Briels; H. Verweij. *Chem. Phys. Lett.* 247, 386-390, 1995.
18. R. Abe; M. Higashi; K. Sayama; Y. Abe; H. Sugihara. *J. Phys. Chem. B.* 110, 2219-2226, 2006.
19. C. P épin; P. A. Lee. *Phys. Rev. Lett.* 81, 2779, 1998.
20. R. D. Shannon; D. B. Rogers; T. Prewitt. *Inorg. Chem.* 10, 4, 1971.
21. R. Nagarajan; N. Duan; M. K. Javarai; J. Li; K. A. Vanaja; A. Yokichi; A. draeseke. *Inter. J. Inorg. Mater.* 3, 265-270, 2001.
22. M. A. Marquardt; N. A. Ashmore; D. P. Cann. *Thin Solid Films.* 496, 146-156, 2006.
23. J. Yperman; A. D. Backer; A. Vos; D. Franco; J. Mullens; L. C. Van Poucke. *Anal. Chim. Acta.* 273, 511-519, 1993.
24. S. Remsen; B. Dabrowski; O. Chmaissem; J. Mais; A. Szewczyk. *J. Solid State Chem.* 184, 2306-2314, 2011.
25. S. Gomez; I. Urria; R. Valiente; F. Rodriguez. *J. Phys.: Condens. Matter.* 22, 295505, 2010.

Chapter 6

Structural and magnetic property study on the cation vacancy system: $\text{YMn}_x\text{Ti}_y\text{O}_{3-\delta}$ ($y = 0.1-0.4$)

Abstract

Solid solution $\text{YMn}_x\text{Ti}_y\text{O}_{3-\delta}$ ($y = 0.1-0.4$) was successfully prepared through conventional solid state approach. All the samples showed hexagonal structure. But the structure transition from ferroelectric $P6_3cm$ to ferrielectric $P6_3/mmc$ occurred when Ti amount is higher than 0.2. Based on the neutron diffraction refinement, the lattice expanded in the ab plane but contracted through the c axis direction.

6.1 Introduction

The $AMnO_3$ group compounds where A is a trivalent rare earth cation (Y^{3+} , Ln^{3+}) have been investigated for their wide applications in the material industry [1, 2]. The compounds in this group present two different types of structures: perovskite and hexagonal. And this can be justified by the size of the A ion. For compounds with a bigger A^{3+} such as La and Ce-Dy, the perovskite-like phase is more stable [3]. These compounds are special interesting in many properties such as the colossal magnetoresistance effect and it could be applied as the catalyst in organic reactions [4, 5]. If the ionic radius of Ln^{3+} is smaller (Y, Ho-Lu), hexagonal phase appears to be the most stable phase [6, 7]. In the $LnMnO_3$ family, $YMnO_3$ attracted a lot of research interest due to the relative abundance of yttrium over the other lanthanide elements. The hexagonal $YMnO_3$ is more stable than the perovskite phase for the ambient synthesis condition. But perovskite phase can be achieved if the preparation process is adjusted. Recent study has showed that perovskite phase can be stabilized by pulsed laser deposition of thin films [8].

Hexagonal $YMnO_3$ receives special research interest. The structure experiences the ferroelectric ordering at around 910K. And this indicates the coupling between ferroelectric and antiferromagnetic orders in this compound [9]. The simultaneous occurrence of ferroelectricity and antiferromagnetism is very rare among all the transition metal oxides. This property makes it a potential material for multiferroic applications. The hexagonal $YMnO_3$ is layered structure which belongs to space group $P6_3cm$ [7, 10]. The structure is illustrated in figure 6.1. The compound

exhibits layered structure with corner shared MnO_5 trigonal bipyramidal layers separated by YO_6 trigonal antiprism layer.

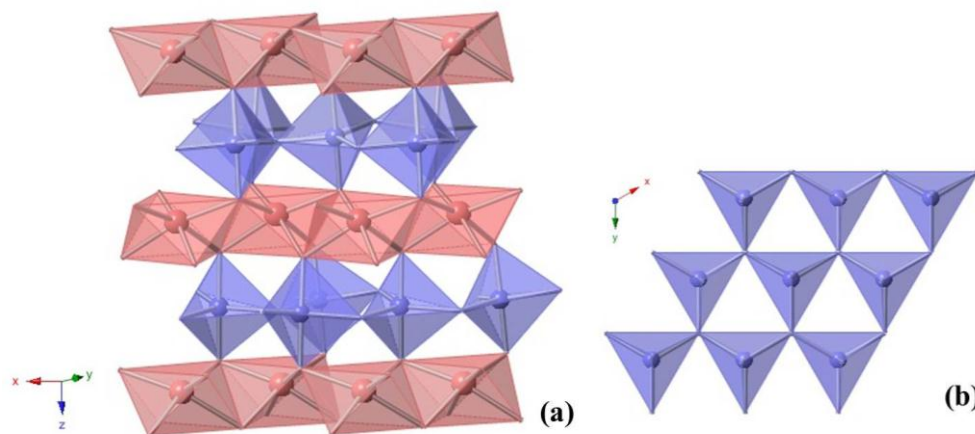


Figure 6.1 Illustration of the structure of YMnO_3 (a): Mn^{3+} is indicated in blue sphere; Y^{3+} is represented by red sphere. The figure on the right (b) is the MnO_5 trigonal bipyramidal layer from c axis direction.

Several metals have been tried to be substituted for Y site in search of functional materials. YMnO_3 - CaMnO_3 solid solution has been reported and electric conductivity was enhanced due to the mixed valence created [11]. Van Aken group reported that it is possible to substitute the tetravalent Zr^{4+} ions to the Y site in the YMnO_3 structure. And mixed valency of Mn^{2+} - Mn^{3+} was created rather than the conventional Mn^{3+} - Mn^{4+} [12].

For the Mn site, a lot of research has been done to substitute trivalent metal ions such as Fe^{3+} , Cr^{3+} , Al^{3+} [13]. However, these substitutions were all limited in content and none of them formed full range solid solution. Recent studies of bright blue color observed from YInO_3 - YMnO_3 solid solution revealed that the trigonal bipyramidal coordination will give rise to the special physical properties [14]. It is

known that the YMnO_3 structure is able to tolerate some oxygen vacancies at high temperature [15, 16]. Yet no reference has been found on substitution of a tetravalent or higher valent ion into the Mn site because rarely the tetravalent ions can be stabilized in the TBP site. Ti^{4+} was known to be in trigonal bipyramidal coordination [17]. Thus it will be interesting to study the $\text{YMn}_x\text{Ti}_y\text{O}_{3-\delta}$ system if the hexagonal phase is formed.

6.2 Synthesis

A solid state method was used for the synthesis of the $\text{YMn}_x\text{Ti}_y\text{O}_{3-\delta}$ compounds. A stoichiometric mixture of Y_2O_3 (Baker Analyze, >99%), In_2O_3 (Stanford Materials, >99.99%), Mn_2O_3 (JMC, >98%) and CuO (Aldrich, >99.99%) was weighed and thoroughly ground together in an agate mortar. The powder mixtures were then pressed into pellets with applied pressure of 1 psi. The pellets were heated at 1200 °C for 12 hours in air. The pellet was taken out and grounded again. The sample went through the same pelletizing process and another 12 hours heating at 1300 °C.

6.3 Results and discussion

Compounds with various contents of Mn and Ti were tried and four of them showed single phase in X-ray diffraction pattern. The single phased compounds are $\text{YMn}_{0.87}\text{Ti}_{0.1}\text{O}_{3-\delta}$, $\text{YMn}_{0.73}\text{Ti}_{0.2}\text{O}_{3-\delta}$, $\text{YMn}_{0.6}\text{Ti}_{0.3}\text{O}_{3-\delta}$ and $\text{YMn}_{0.3}\text{Ti}_{0.4}\text{O}_{3-\delta}$. The X-ray

patterns are shown in figure 6.2. The X-ray pattern of YMnO_3 was shown for comparison. The hexagonal structure is maintained for all the compositions. However, the structure transformed from ferroelectric space group $P6_3cm$ to ferrielectric space group $P6_3/mmc$. As when Ti content is higher than 0.2, the (102) reflection peak which indicates the ferroelectric superstructure disappeared in the X-ray patterns.

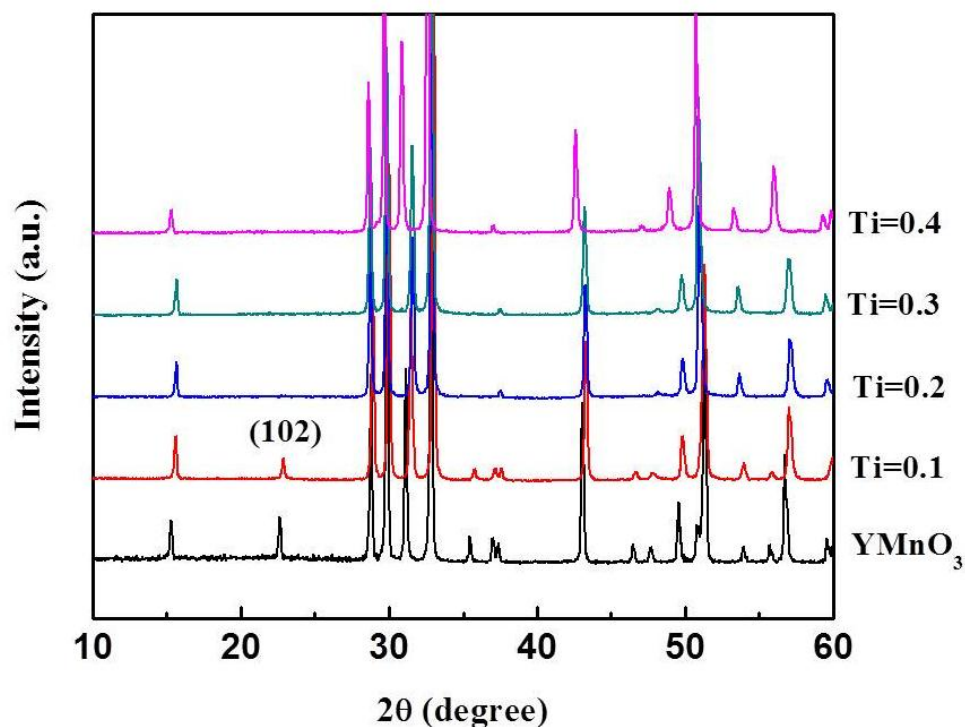


Figure 6.2 X-ray patterns of $\text{YMn}_x\text{Ti}_y\text{O}_{3-\delta}$ ($y = 0-0.4$).

Neutron diffraction data was collected for the detailed study of the structure. The structure model used for $\text{YMn}_{0.87}\text{Ti}_{0.1}\text{O}_{3-\delta}$ was ferrielectric space group $P6_3cm$ while all the other samples were refined with paraelectric space group $P6_3/mmc$. Figure 6.3 is shown for the La Bail fit of the neutron diffraction pattern of $\text{YMn}_{0.73}\text{Ti}_{0.2}\text{O}_{3-\delta}$.

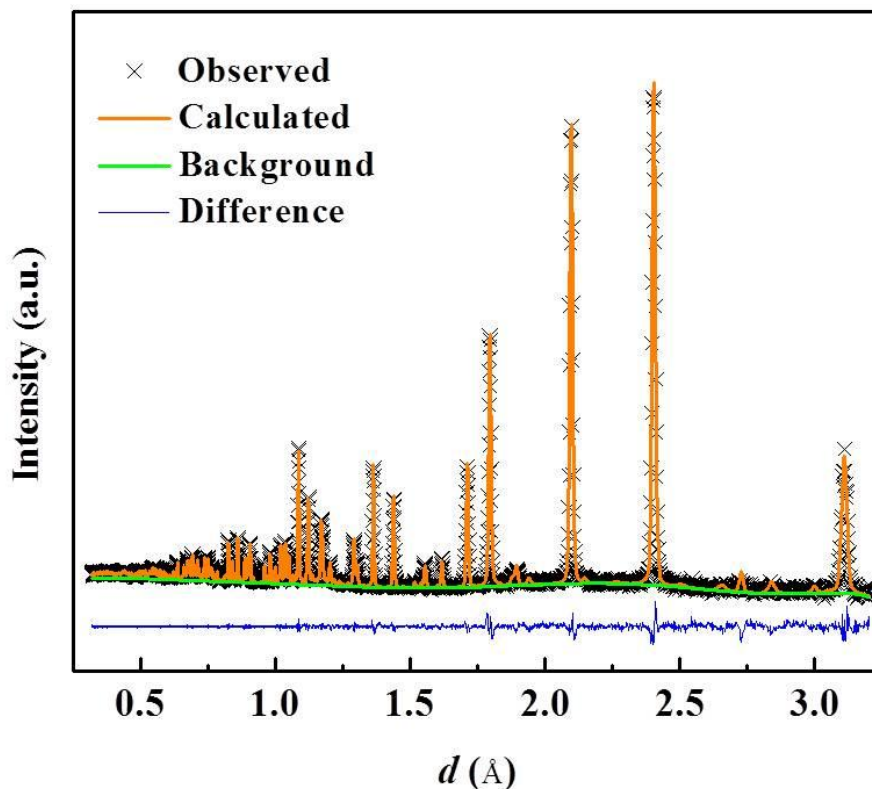


Figure 6.3 TOF neutron data of $\text{YMn}_{0.73}\text{Ti}_{0.2}\text{O}_{3-\delta}$ are shown with La Bail fit. The observed pattern displayed is from the highest-resolution bank (Bank 2) with d -spacing range 0.60 – 3.2 Å.

The refined lattice parameters a and c are plotted in figure 6.4. The lattice parameter a of the larger non-centrosymmetric cell is divided by square root 3 to compare with the other compounds in the serie. Generally, cell edge a increases with the elevating amount of Ti. This is possibly due to the absence of oxygen atoms. The repulsive force is enhanced by removing the ions with opposite charge. Thus the lattice is enlarged in the direction of a . For the vertical parameter c , small amount of Ti makes it decreased as both cations and anions are removed from the TBP layer.

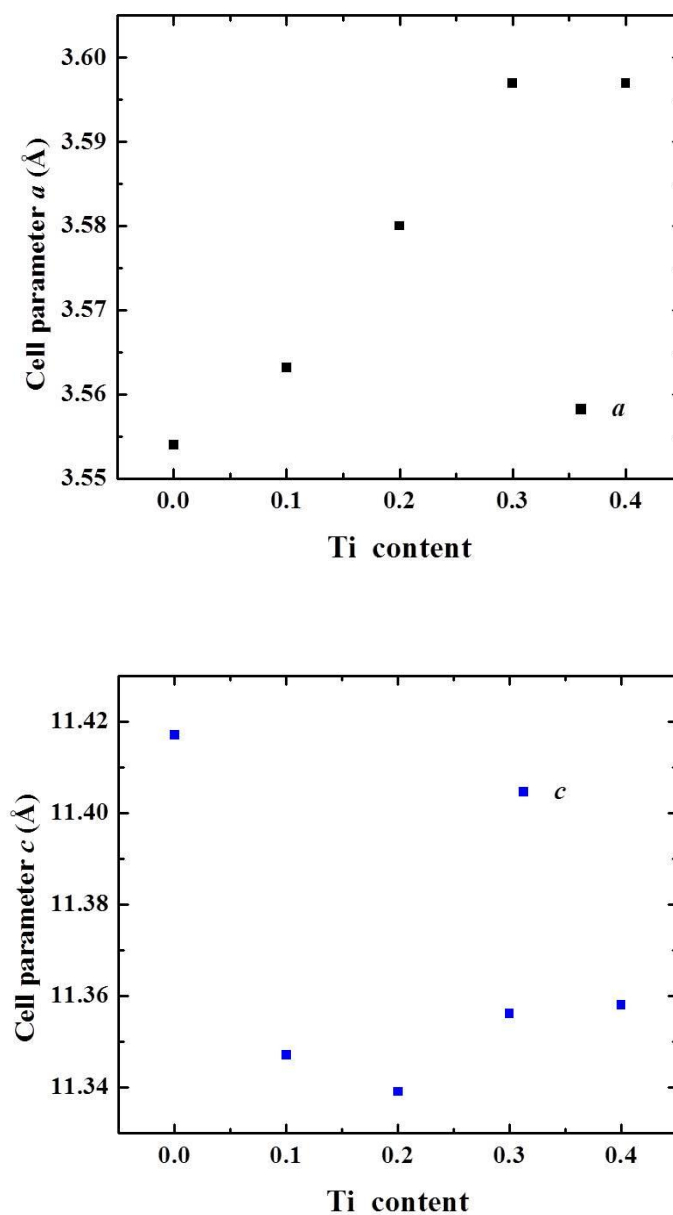


Figure 6.4 Lattice parameter a (above) and c (below) versus the Ti content. The value of YMnO_3 is from neutron diffraction data of reference 18.

Magnetic data was collected from PPMS on the ACMS mode. The inverse magnetic susceptibility versus temperature data for all the samples is plotted in figure 6.5. All the samples exhibit paramagnetic behavior in the temperature range measured.

For $Ti = 0.1$ and 0.2 sample, the low temperature magnetic susceptibility data showed a curvature which may indicate the antiferromagnetic ordering.

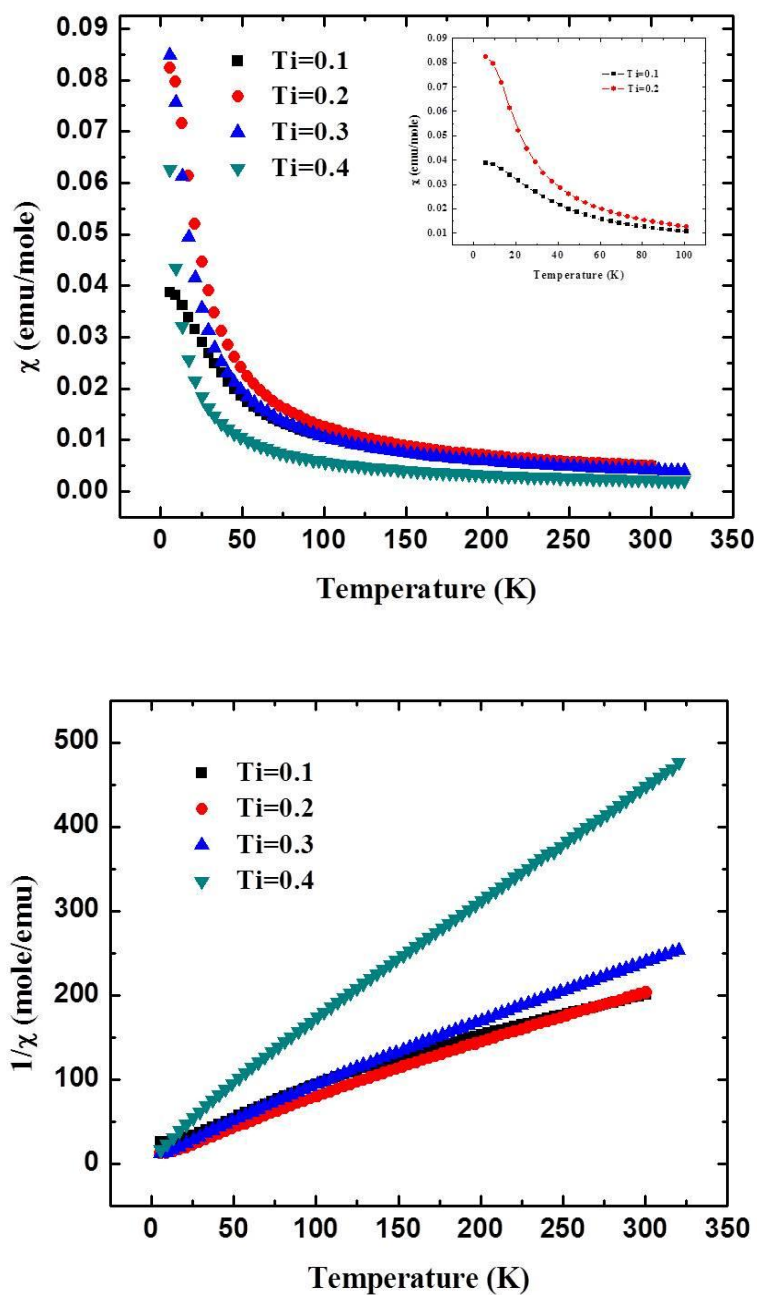


Figure 6.5 Magnetic susceptibility (above) and inverse magnetic susceptibility (below) versus temperature for $YMn_xTi_yO_{3-\delta}$.

Magnetic moments of different compounds were calculated from the linear region of the inverse magnetic susceptibility plot. The summary of magnetic data is in table 6.1. The experimental magnetic moments are close but a little lower than the expected value from spin only case. The further explanation of the magnetic data will rely on the result from Rietveld refinements which is in progress.

Table 6.1 Summary of magnetic data of $\text{YMn}_x\text{Ti}_y\text{O}_{3-\delta}$

y	Curie constant	θ_w (K)	μ_B (experimental)	μ_B Mn^{3+} (HS)
0.1	2.074	-112.6	4.090	4.561
0.2	1.707	-43.98	3.711	4.178
0.3	1.447	-37.04	3.417	3.780
0.4	0.764	-33.93	2.482	2.678

All the theoretical values are calculated from the spin only condition.

6.4 Conclusion

The hexagonal $\text{YMn}_x\text{Ti}_y\text{O}_{3-\delta}$ ($y = 0.1-0.4$) system which has vacancies on the cation site was successfully synthesized by solid state reactions. Two space groups were employed to refine the structure as the transition from ferroelectric to ferrielectric structure appeared when Ti content is higher than 0.2. The lattice experienced an expansion in the a value and a contraction in the c value. All the samples showed black color. And the magnetic data showed that all the samples

exhibited paramagnetic behavior in the temperature range and the oxidation state of Mn is 3+. Future work will be focused on the Rietveld refinement of the neutron diffraction data. The refined oxygen occupancy will shed light on the explanation of this cation vacant system as well as the magnetic data interpretation.

6.5 References

1. C. N. R. Rao; A. K. Cheetham. *Science*. 272, 369-370.
2. G. H. Jonker; J. H. van Santen. *Physica*. 16, 599-600, 1950.
3. T. Mori; N. Kamegashira; K. Aoki; T. Shishido; T. Fukuda. *Mater. Lett.* 54, 238-243, 2002.
4. C. N. R. Rao; A. K. Cheetham; R. Mahesh. *Chem. Mater.* 8, 2421-2432, 1996.
5. B. Levasseur; S. Kaliaguine. *J. Solid State Chem.* 181, 2953-2963, 2008.
6. H. K. Yakel; W. C. Koehler; E. F. Bertaut; E. F. Forrat. *Acta. Cryst.* 16, 957, 1963.
7. E. S. Stampler; W. C. Sheets; W. Prellier; T. J. Marks; K. R. Poeppelmeier. *J. Mater. Chem.* 19, 4375-4381, 2009.
8. P. A. Salvador; T. Doan; B. Mercey; B. Raveau. *Chem. Mater.* 10, 2592-2595, 1998.
9. Z. J. Huang; Y. Cao; Y. Y. Sun; Y. Y. Xue; C. W. Chu. *Phys. Rev. B*. 56, 1997
10. B. B. van Aken; A. Meetsma; T. T. M. Palstra. *Acta. Cryst.* C57, 230-232, 2001.
11. C. Moure; M. Villegas; J. F. Fernandez; J. Tartaj; P. Duran. *J. Mater. Sci.* 34, 2565, 1999
12. B. B. van Aken; J-W. G. Bos; R. A. de Groot; T. T. M. Palstra. *Phys. Rev. B*. 63, 125127, 2001.
13. I. H. Ismailzade; G. A. Smolenskii; V. I. Nesterenko; F. A. Agaev. *Phys. Status Solid A*. 5, 83, 1971.
14. A. E. Smith; H. Mizoguchi; K. Dlaney; N. A. Spaldin; A. W. Sleight; M. A. Subramanian. *J. Am. Chem. Soc.* 131, 17086, 2009.
15. Th. Lonkai; D. Hohlwein; J. Ihringer; W. Prandl. *Appl. Phys. A*. 74, S843-S845, 2002.
16. T. Atsumi; T. Ohgushi; H. Namikata; N. Kamegashira. *J. Alloy. Compd.* 252, 67-70, 1997.
17. M. T. Anderson; K. B. Greenwood; G. A. Taylor; K. R. Poeppelmeier. *Prog. Solid State Chem.* 22, 197-233, 1993.
18. M. Janoschek; B. Roessli; L. Keller; S. N. Gvasaliya; K. Conder; E. Pomjakushina. *J. Phys.: Condens. Matter*. 17, 1, 2005.

General conclusion and future work

In general, transition metal oxides present a variety of different properties such as electronic properties, magnetic properties, and optical properties. In this thesis, all the compositions are crystallized in two structures: AMO_3 hexagonal structure and $\text{A}_2\text{B}_2\text{O}_5$ brownmillerite structure. Structure studies based on neutron diffraction and X-ray diffraction were conducted for all the single phase compounds. Magnetic and other property measurements served as analytical approach and they also provide insights of potential applications of the materials. Discussion on the optical property especially the color is especially focused. This work exhibits the importance of material research as the future of color pigments and electronic devices is dependent on the development of novel materials with improved properties.

We discussed the design, preparation, structure and some physical properties of novel materials. The compounds in $\text{YM}_{1-x}\text{Fe}_x\text{O}_3$ family showed interesting colors when $\text{M} = \text{In}, \text{Al}$. And the materials could be utilized in color pigment industry as they have great advantages such as stability in acid/base and high temperature. The structure is hexagonal with In/Fe/Al in the trigonal bipyramidal coordination. The structure study revealed that the intense color is originated from the special coordination. Magnetic and Mössbauer study showed that the Fe^{3+} species existed exclusively in all the single phase compounds. Based on what we have learned, a lot of candidates such as Co, Cr could be explored to be substituted in the trigonal bipyramidal coordination.

The brownmillerite-type compounds $\text{Ba}_2\text{In}_{2-x}\text{M}_x\text{O}_{5+x}$ ($\text{M} = \text{Mn}, \text{Fe}$) were synthesized and studied by comprehensive characterization methods. Some of the compositions exhibit intense colors from turquoise to green. And the colors could be applied in the color pigment field. And we concluded that the origin of the color is Mn^{5+} in the tetrahedral sites based on neutron diffraction data. Magnetic data also confirmed the higher oxidation state of Mn species. For Fe-containing compounds, a mixed valence of Fe^{3+} and Fe^{4+} was observed in magnetic measurements and Mössbauer spectra. Thus only a small fraction of the compounds presented color. As we knew that the higher oxidation state in tetrahedral sites in brownmillerite structure would bring intense colors, in the future some transition metals with possible high oxidation states such as Cr could be desolved in this parent compound and may bring interesting colors. Manipulation with the lattice parameters will also tune the color as the color is sensitive to bond angles and lengths. Thus, substitution of large cations on Ba site could be possible design for new color pigments.

In this thesis, we also discussed about structure study of $\text{YCu}_{0.6}\text{Ti}_{0.4}\text{O}_{3-\delta}$ and the structure was studied through neutron diffraction. It was observed that the structure preferred oxygen vacancies in the synthesis condition. The reduction was carried out for the $\text{LnCu}_{0.5}\text{Ti}_{0.5}\text{O}_3$ ($\text{Ln} = \text{Tb-Lu}, \text{Y}$). It was found that the color changed from green to black. And magnetic data implied that Cu^{2+} was reduced to Cu^+ . Conductivity was observed from some of the samples due to the mixed valence state. The future work on this project can be focused on the neutron study of the reduced samples as

neutron diffraction can calculate the oxygen vacancies and locate the atom positions.

All these will help to confirm the oxidation state of the Cu.

The cation vacant system $\text{YMn}_x\text{Ti}_y\text{O}_3$ was successfully prepared and characterized. All the compounds showed hexagonal structure, but a transition from ferrielectric to paraelectric is observed in the X-ray and neutron diffraction patterns. Further study on the structure including the Rietveld refinement of neutron diffraction patterns will be helpful to have an accurate understanding of this system.

Bibliography

- J. Mannhart; J. G. Bednorz; K. A. Müller; D. G. Schlom, *Zeitschrift für Physik B* 83, 307-311.
- C.N.R. Rao; B. Reveau. *Transition Metal Oxides: Structure, Properties, and synthesis of Ceramic Oxides*, 2nd edition, John Wiley & Sons: New York, 1998.
- Dr. Subramanian lecture: *Solid State Chemistry*.
- A. R. West. *Solid State Chemistry and Its Applications*. John Wiley & Sons Ltd. 1985.
- R. E. Williams. *Science*. 161, 276-277, 1968.
- J. D. Dunitz; L. E. Orgel. *J. Phys. Chem. Solids*. 3, 318-323. 1957.
- L. Pauling. *J. Am. Chem. Soc.* 51, 1010-1026, 1929.
- J. K. Burdett; T. J. McLarnan. *J. Am. Chem. Soc.* 104, 5229-5230, 1982.
- A.R.West. *Basic Solid State Chemistry*. 2nd edition, John Wiley & Sons, LTD.
- D.M. Smyth. *Cryst. Lattice Defects Amorph. Mater.* 18, 355, 1989.
- P. A. Cox. *The Electronic Structure and Chemistry of Solids*. Oxford University Press, 1987.
- S. Cattarin; F. Decker. *Electrodes: Semiconductor Electrodes*. Elsevier, 2009.
- J. Nishizawa. *Mater. Sci. in Semiconductore Processing*. 6, 249-252, 2003.
- Y. Tokura. *Colossal Magneto-resistive Oxides*. Gordon and Breach Science Publishers, 2000
- E. De Grave; A. Govaert; D. Chambaere; G. Robbrecht. *Physica B+C*. 96, 103-110, 1979.
- R. J. Harrison; A. Putnis. *Phys. Chem. Minerals*. 26, 322-332, 1999.
- P.W. Selwood. *Magnetochemistry*. Interscience Publishers, Inc, New York, 1943.
- J.B. Goodenough. *Magnetism and the Chemical Bond*. John Wiley & Sons, New York, 1963
- http://en.wikipedia.org/wiki/Lenz%27s_law.
- Michael M. Schieber. *Experimental Magnetochemistry Nonmetallic Magnetic Materials*. John Willey & Sons, Inc, New York, 1967
- P. G. Radaelli; D. E. Cox; M. Marezio; S-W. Cheong. *Phys. Rev. B*. 55, 3015, 1997.
- V. Cannella; J. A. Mydosh. *Phys. Rev. B*. 6, 4220, 1972.
- R. J. Elliott. *Phy. Rev.* 124, 346, 1961.
- C. M. Hurd. *Contemp. Phys.* 23, 469-493, 1982.
- J. Kanamori. *J. Phys. Chem. Solids* 10, 87-98, 1959.
- D. N. Aristov. *Phys. Rev. B*. 55, 8064, 1997
- P. W. Anderson. *Phys. Rev.* 79, 350, 1950.
- J. B. Goodenough; A. L. Loeb. *Phys. Rev.* 98, 391, 1955.
- J. Kanamori. *J. Phys. Chem. Solids*. 10, 87, 1959.
- C-W Nan; M. I. Bichurin; S. Dong; D. Viehland; G. Srinivasan. *J. Appl. Phys.* 103, 031101, 2008.
- M. Gajek; M. Bibes; S. Fusil; K. Bouzehouane; J. Fontcuberta; A. Barthélémy; A. Fert. *Nature Mater.* 6, 296-302, 2007.
- E. Coates. *J. Soc. Dyers. Colour.* 83, 95, 1967.

- Richard J. D. Tilley. *Colour and the Optical Properties of Materials*. Second Edition, John Wiley and Sons, Ltd., Publication,
- M. V. Orna. *J. Chem. Educ.* 55, 478, 1978.
- K. Nassau. *Am. Mineral.* 63, 219-229, 1978.
- K. Z. Prizbram. *Physik.* 20, 196, 1923.
- E. Robinowitch. *Rev. Mod. Phys.* 14, 127, 1942.
- M. B. Robin. *Inorg. Chem.* 1, 337-342, 1962.
- Y. -J. Liu; J. A. Cowen; T. Kaplan; D. C. DeGroot; J. Schindler; C. R. kannewurf; M. G. Kanatzidis. *Chem. Mater.* 7, 1616-1624, 1995
- R. V. Morris; H. V. Lauer, Jr; C. A. Lawson; E. K. Gibson, Jr; G. A. Nace; C. Stewart. *J. Geophys. Res.* 90, 3126-3144, 1985.
- P. E. Lippens; M. Lannoo. *Phys. Rev. B.* 39, 10935-10942, 1989.
- S. Huey. *Color Eng.* 9, 20, 1971.
- A. Montali; C. bastiaansen; P. Smith; C. Weder. *Nature.* 392, 261-264, 1998.
- W. D. Kingery; H. K. Bowen; D. R. Uhlmann. *Introduction to Ceramics*. 2nd ed.; John Wiley & Sons: New York, 1976
- M.A. Subramanian; D. Li; N. Duan; B.A. Reisner; A.W. Sleight. *J. Solid State Chem.* 151, 323, 2000.
- T. M. Tritt; M. A. Subramanian, *Mat. Res. Soc. Bul.* 31, 188-194, 2006.
- S.O. Kasap. *Thermoelectric Effects in Metals: Thermocouples*. An e-booklet, 1997-2001.
- G.D. Mahan; J.O. Sofo. *Proc. Natl. Acad. Sci.* 19, 7436, 1996.
- Dr. Subramanian, lecture on thermoelectric materials.
- B. Lamp. "Instrumental Analysis." Truman State University.
http://www2.truman.edu/~blamp/chem322/pdf/chapter%201%20_93%20corrections_.pdf. Accessed May 2010.
- Anthony R. West, *Solid State Chemistry and Its Applications*, John Wiley & Sons, New York, 1984.
- A.C. Larson, R.B. Von Dreele, "General Structure Analysis System (GSAS)," Los Alamos National Laboratory Report LAUR 86-784, 2004.
- B.H. Toby, EXPGUI, a graphical user interface for GSAS, *J. Appl. Cryst.* 34, 210, 2001.
- B.D. Cullity, S.R. Stock. *Elements of X-Ray Diffraction*, 3rd edition; Prentice Hall; New Jersey, 2001.
- NIST Center of Neutron Research, <http://www.ncnr.nist.gov/instruments/bt1/>.
- A.E. Smith, Ph.D. thesis, Oregon State University, 2010.
- Quantum Design. *Physical Property Measurement System Hardware and Operations Manual*, 2nd Edition, Quantum Design, 1999.
- Quantum Design. <http://www.qdusa.com/products/ppms.html>.
- R. Kykyneshi. M.S. Thesis, Oregon State University, Corvallis, OR, 2004.
- M. El. Sherif, O. A. Bayoumi, T. Z. N. Sokkar, *Color Res. App.* 22, 32, 1997.
- Introduction to Mössbauer Spectroscopy: Part 1. *Royal Soc. Chem.* www.rsc.org.
- R. L. Mössbauer, *Z. Phys.* 151, 124, 1958.

- J. P. Suchet, *Crystal Chemistry and Semiconduction in Transition Metal Binary Compounds*, Academic Press, New York and London, 1971.
http://en.wikipedia.org/wiki/Mossbauer_spectroscopy.
- J. Hesse and A. Rubartsch, *J. Phys. E. Sci. instrum.*, 7, 526, 1974.
- A. Wattaix, private conversation.
- T. Takahashi. “*Physics of Electrolytes*”, 2nd edition, Academic Press, New York, 1972.
- J. C. Grenier; N. Ea; M. Pouchard; P.J. Hagemuller. *Solid State Chem.* 58, 243, 1985
- J.C. Grenier; M. Pouchard; P. Hagemuller. “*Reactivity of Solids*”, Elsevier, Amsterdam, 1982.
- D.M. Smyth. *Cryst. Latt. Def. Amorph. Mat.* 18, 355, 1989.
- G. B. Zhang; D. M. Smyth. *Solid State Ionics.* 82, 161-172, 1995.
- J. B. Goodenough; J. E. Ruiz-díaz; Y. S. Zhen. *Solid State Ionics.* 44, 21, 1990.
- P. Berastegui; S. Hull; F. J. Garc á-Garc á; S.-G. Eriksson. *J. Solid State Chem.* 164, 119-130, 2002.
- S. A. Speakman; J. W. Richardson; B. J. Mitchell; S. T. Misture. *Solid State Ionics.* 149, 247-259, 2002.
- T. Kobayashi; A. Hasesaka; M. Hibino; T. Yao. *Transaction of the Materials Research Society of Japan.* 33, 1077-1080, 2008.
- H. Mizoguchi; A. W. Sleight; M. A. Subramanian. *Inorg. Chem.* 50, 10, 2011.
- D. A. Grisafe; F. A. Hummel. *J. Solid. State. Chem.* 2, 167-175, 1970.
- H. Lachwa; D. Reinen. *Inorg. Chem.* 28, 1044-1053, 1989.
- B. L. Chamberland; A. W. Sleight; J. F. Weiher; *J. Solid State Chem.* 1, 506–511, 1970.
- D. K. Singh; B. Kamble; A. Singh. *Phys. Rev. B.* 81, 064430, 2010.
- Z. Huang; F. Du; C. Wang; D. Wang; G. Chen. *Phys. Rev. B.* 75, 054411, 2007.
- L. A. Pardi; J. Krzystek; J. Telser; L. C. Brunel. *J. Magn. Reson.* 146, 375-378, 2000;
- A. K. Hassan; L. A. Pardi; J. Krzystek; A. Sienkiewicz; P. Goy; M. Rohrer; L.-C. Brunel. *J. Magn. Reson.* 142, 300, 2000.
- M. Pardavi-Horvath; P. E. Wigen. *J. Appl. Phys.* 63, 3110, 1998.
- J. C. Waerenborgh; D. P. Rojas; N. P. Vyshatko; A. L. Shaula; V. V. Kharton; I. P. Marozau; E. N. Naumovich. *Mater. Lett.* 57, 4388-4393, 2003.
- P. Jiang; J. Li; A. W. Sleight; M. A. Subramanian. *Inorg. Chem.* 50, 5858-5860, 2011.
34. P. K. Gallagher; J. B. MacChesney; D. N. E. Buchanan. *J. Chem. Phys.* 43, 516, 1965
- M. Parras; F. Fournes; J-C. Grenier; M. Pouchard; M. Vallet; J. M. Calbet; P. Hagemuller. *J. Solid. State. Chem.* 88, 261-268, 1990.
- X.D. Zhou; S. Hovmoller; M. Parras; J.M. Gonzalez-Calbet; M. Vallet-Regi. J. C. Grenier. *Acta. Cryst.* 49, 27-35, 1993
- H. D. Zhou; J. B. Goodenough. *J. Solid. State. Chem.* 178, 3679-3685, 2005.
- W. W. Malinofsky; H. Kedesdy. *J. Am. Chem. Soc.* 76, 3090-3091, 1954.
- Y. D. Perfiliev; V. K. Sharma. *Ferrates: Synthesis, Properties, and Applications in Water and Wastewater Treatment*. American Chemical Society, 2008.
- M. Takano; N. Nakanishi; Y. Takeda; S. Naka. *Journal De Physique*, 3, C2-313, 1979.

- K. Kakinuma; H. Yamamura; H. Haneda; T. Atake. *J. Therm. Anal. Calorim.* 57, 737-743, 1999
- I. V. Spesivtseva; N. A. Kochetova; E. M. Gorbunova; I. E. Animitsa. *Russ. J. Phys. Chem. A.* 85, 1689-1694, 2011.
- J. Hesse; A. Rubartsch. *J. Phys. E. Sci. Instrum.* 7, 526, 1974.
- Dr. Wattiax, private communication.
- S. B. Adler; J. A. Reimer; J. Baltisberger; U. Werner. *J. Am. Chem. Soc.* 116, 675-681, 1994.
- T. Schober; J. Friedrich; F. Krug. *Solid State Ionics.* 99, 9-13, 1997.
- W. Eerenstein; N. D. Mathur; J. F. Scott. *Nature.* 442, 17, 2006.
- N.A. Hill. *J. Phys. Chem. B.* 104, 6694, 2000.
- S. Cheoung; M. Mostovoy. *Nature. Mater.* 6, 13, 2007.
- R. Ramesh, N.A. Spaldin. *Nature. Mater.* 6, 21, 2007.
- D. Choudhury; A. Hazarika; A. Venimadhav; C. Kakarla; K. Delaney; P. Sujatha Devi; P. Mondal; R. Nirmala; J. Gopalakrishnan; N. A. Spaldin; U. V. Waghmare; D. D. Sarma. *Phys. Rev. B.* 82, 13, 2010.
- B. B. Van Aken; T. M. Thomas; A. F. Palstra; N. A. Spaldin. *Nature. Mater.* 3, 2004
- M. T. Anderson; K. B. Greenwood, G.A. Taylor, K.R. Poeppelmeier, *Prog. Solid. State. Chem.* 22, 197, 1993.
- N. Floros; J. T. Rijssenbeek; A. B. Martinson; K. R. Poeppelmeier. *Solid. State. Sci.* 4, 1495-1498, 2002.
- K. Singh; N. Kumar; B. Singh; S. D. Kaushik; N. K. Gaur; S. Bhattacharva; S. Rayaprol; C. Simon. *J. Supercond. Nov. Magn.* 24, 1829-1838, 2011
- A. E. Smith, A. W. Sleight, M.A. Subramanian, *Mater. Res. Bul.* 46, 1-5, 2011
- D. A. Vander Griend; S. Malo; S. J. Barry; N. M. Dabbousch; K. R. Poeppelmeier; V. P. Dravid. *Solid. State. Sci.* 3, 569-579, 2001.
- D. A. Vander Griend; S. Boudin; V. Caignaert; K. R. Poeppelmeier; Y. Wang; V. P. Dravid; M. Azuma; M. Takano; Z. Hu; J. D. Jorgensen. *J. Am. Chem. Soc.* 121, 4787-4792, 1999.
- M. T. Anderson; J. T. Vaughey; K. R. Poeppelmeier. *Chem. Mater.* 5, 151-165, 1993.
- J. Li; Y. Duan; H. He; D. Song. *J. Alloys. Compounds.* 315, 259-264, 2001.
- E. mamontov; T. Egami; R. Brezny; M. Koranne; S. Tyagi. *J. Phys. Chem. B.* 104, 11110-11116, 2000.
- H. W. Brinkman; W. J. Briels; H. Verweij. *Chem. Phys. Lett.* 247, 386-390, 1995.
- R. Abe; M. Higashi; K. Sayama; Y. Abe; H. Sugihara. *J. Phys. Chem. B.* 110, 2219-2226, 2006.
- C. P  pin; P. A. Lee. *Phys. Rev. Lett.* 81, 2779, 1998.
- R. D. Shannon; D. B. Rogers; T. Prewitt. *Inorg. Chem.* 10, 4, 1971.
- R. Nagarajan; N. Duan; M. K. Javarai; J. Li; K. A. Vanaja; A. Yokichi; A. draeseke. *Inter. J. Inorg. Mater.* 3, 265-270, 2001.
- M. A. Marquardt; N. A. Ashmore; D. P. Cann. *Thin Solid Films.* 496, 146-156, 2006.
- J. Yperman; A. D. Backer; A. Vos; D. Franco; J. Mullens; L. C. Van Poucke. *Anal. Chim. Acta.* 273, 511-519, 1993.

- S. Remsen; B. Dabrowski; O. Chmaissem; J. Mais; A. Szewczyk. *J. Solid State Chem.* 184, 2306-2314, 2011.
- S. Gomez; I. Urria; R. Valiente; F. Rodriguez. *J. Phys.: Condens. Matter.* 22, 295505, 2010.
- C. N. R. Rao; A. K. Cheetham. *Science.* 272, 369-370.
- G. H. Jonker; J. H. van Santen. *Physica.* 16, 599-600, 1950.
- T. Mori; N. Kamegashira; K. Aoki; T. Shishido; T. Fukuda. *Mater. Lett.* 54, 238-243, 2002.
- C. N. R. Rao; A. K. Cheetham; R. Mahesh. *Chem. Mater.* 8, 2421-2432, 1996.
- B. Levasseur; S. Kaliaguine. *J. Solid State Chem.* 181, 2953-2963, 2008.
- H. K. Yakel; W. C. Koehler; E. F. Bertaut; E. F. Forrat. *Acta. Cryst.* 16, 957, 1963.
- E. S. Stampler; W. C. Sheets; W. Prellier; T. J. Marks; K. R. Poeppelmeier. *J. Mater. Chem.* 19, 4375-4381, 2009.
- P. A. Salvador; T. Doan; B. Mercey; B. Raveau. *Chem. Mater.* 10, 2592-2595, 1998.
- Z. J. Huang; Y. Cao; Y. Y. Sun; Y. Y. Xue; C. W. Chu. *Phys. Rev. B.* 56, 1997
- B. B. van Aken; A. Meetsma; T. T. M. Palstra. *Acta. Cryst. C* 57, 230-232, 2001.
- C. Moure; M. Villegas; J. F. Fernandez; J. Tartaj; P. Duran. *J. Mater. Sci.* 34, 2565, 1999
- B. B. van Aken; J-W. G. Bos; R. A. de Groot; T. T. M. Palstra. *Phys. Rev. B.* 63, 125127, 2001.
- I. H. Ismailzade; G. A. Smolenskii; V. I. Nesterenko; F. A. Agaev. *Phys. Status Solid A.* 5, 83, 1971.
- Th. Lonkai; D. Hohlwein; J. Ihringer; W. Prandl. *Appl. Phys. A.* 74, S843-S845, 2002.
- T. Atsumi; T. Ohgushi; H. Namikata; N. Kamegashira. *J. Alloy. Compd.* 252, 67-70, 1997.
- M. T. Anderson; K. B. Greenwood; G. A. Taylor; K. R. Poeppelmeier. *Prog. Solid State Chem.* 22, 197-233, 1993.
- M. Janoschek; B. Roessli; L. Keller; S. N. Gvasaliya; K. Conder; E. Pomjakushina. *J. Phys.: Condens. Matter.* 17, 1, 2005.